Computer Simulation of Entanglements in Viscoelastic Polymer Melts

Johan Padding

2003

Ph.D. thesis
University of Twente

Twente University **Press**

Also available in print:
http://www.tup.utwente.nl/

COMPUTER SIMULATION OF ENTANGLEMENTS IN VISCOELASTIC POLYMER MELTS

Promotion committee:

Prof.dr. G.J. Vancso	University of Twente (chairman)
Prof.dr. J. Feijen	University of Twente (secretary)
Prof.dr. W.J. Briels	University of Twente (thesis supervisor)
Dr. M.A. van der Hoef	University of Twente (referee)
Prof.dr. J. Mellema	University of Twente
Prof.dr. J.J.M. Slot	University of Twente / DSM Research
Prof.dr. K. Kremer	Max Planck Institut für Polymerforschung, Mainz, Germany
Prof.dr. G. ten Brinke	University of Groningen
Prof.dr. B. Smit	University of Amsterdam

Twente University **Press**

Publisher: Twente University Press,
P.O. Box 217, 7500 AE Enschede, The Netherlands, www.tup.utwente.nl

Cover illustration: M.C. Escher's "Dragon" © 2002 Cordon Art - Baarn - Holland. All rights reserved. (reproduced with permission no. B-02/467)

Print: Océ Facility Services, Enschede

Typeset in LaTeX, by the author

ISBN 9036518644

COMPUTER SIMULATION OF ENTANGLEMENTS IN VISCOELASTIC POLYMER MELTS

PROEFSCHRIFT

ter verkrijging van
de graad van doctor aan de Universiteit Twente,
op gezag van de rector magnificus,
prof. dr. F.A. van Vught,
volgens besluit van het College voor Promoties
in het openbaar te verdedigen
op vrijdag 24 januari 2003 te 15.00 uur

door
Johannes Tiemen Padding
geboren op 20 juli 1975
te Steenwijk

Dit proefschrift is goedgekeurd door:
Prof. dr. W.J. Briels (promotor)

“Convictions are more dangerous enemies of truth than lies.”

-

Friedrich Nietzsche

Contents

About the author

Johannes Tiemen Padding was born on July 20th 1975 in Steenwijk (the Netherlands). He attended the Rijksscholengemeenschap Jan Hendrik Tromp Meester in Steenwijk at atheneum B level from 1987 until 1993. In 1993 he moved to Enschede to study Applied Physics at the University of Twente. In 1997, as a practical training period, he spent four months at the University of Uppsala in Sweden. Under the guidance of Prof. Kersti Hermansson, he wrote a program to optimize the geometry of molecular crystals using quantum chemical calculations. Back in Enschede he started his graduation work in the Chemical Physics group of Prof. Dick Feil, under the guidance of (then) Dr. Wim Briels. He graduated cum laude in 1998 with a Master's thesis on simulations of entangled polymer melts. After graduation he started his Ph.D. work in the new Computational Chemistry group of Prof. Wim Briels, which transformed to the Computational Dispersion Rheology group in 2001.

Parts of this work have been presented at the 'IVth Liquid Matter Conference' in Granada (Spain), the workshop on 'Linking Different Length and Time Scales in (Macro-) Molecular systems' in Dresden (Germany), the 'IVth International Discussion Meeting on Relaxations in Complex Systems' in Hersonissos, Crete (Greece), and the 'Jülich Soft Matter Days 2002' in Kerkrade (the Netherlands).

During his Ph.D. period he participated in winterschools on Theoretical Chemistry and Spectroscopy and on Macroscopic Physical Chemistry, both in Han-sur-Lesse (Belgium). As a part of the Ph.D. position the author has been teaching practical classes on classical and quantum mechanics, chemical physics, and statistical thermodynamics.

List of publications

- J.T. Padding and W.J. Briels,
  A time-integrated estimate of the entanglement molecular weight in polymer melts in agreement with the one determined by time-resolved measurements,
  Submitted to Macromolecules.

- J.T. Padding and W.J. Briels,
  Time and length scales of polymer melts studied by coarse-grained molecular dynamics simulations,
  J. Chem. Phys. **117**(2), 925 (July 8, 2002).

- M.A.I. Schutyser, J.T. Padding, F.J. Weber, W.J. Briels, A. Rinzema, and R. Boom,
  Discrete particle simulations predicting mixing behavior of solid substrate particles in a rotating drum fermenter,
  Biotechnol. Bioeng. **75**(6), 666 (December 20, 2001).

- J.T. Padding and W.J. Briels,
  Uncrossability constraints in mesoscopic polymer melt simulations: Non-Rouse behavior of $C_{120}H_{242}$,
  J. Chem. Phys. **115**(6), 2846 (August 8, 2001).

- J.T. Padding and W.J. Briels,
  Zero-shear stress relaxation and long time dynamics of a linear polyethylene melt: A test of Rouse theory,
  J. Chem. Phys. **114**(19), 8685 (May 15, 2001).

1 Introduction

"The year is 1839. It is a time of dizzying developments in chemistry. Chemists are just starting to synthesize innumerable new molecules. They try a little bit of everything, they react everything with everything else. One among them, Charles Goodyear, promped by sheer curiosity, takes the sap from the hevea tree - a sort of whitish, milky juice - and decides to boil it with sulfur. He has no idea what latex is. He only knows that it contains carbon and hydrogen. The very concept of a long-chained molecule is totally unknown to him or any other chemist. But he continues to experiment and obtains a sort of blackish substance, deformable and yet resilient: natural rubber. This rubber remains, more than a century and a half later, one of the pillars of man's industrial activity. Yet, in Goodyear's time no chemist had any interest in this type of product. Why? When a nineteenth-century chemist tried to synthesize a new material, he attempted to react two known compounds on each other. He expected to obtain a molecule containing at most a few tens of atoms, about the same number as the starting materials. He was not prepared to find a compound whose every molecule contains a million atoms! Besides, he lacked the tools to determine whether he had made one product or a mixture of several. The standard practice then was to purify the product of the reaction by crystallization or sequential distillation until one obtained a pure substance. The main criterion for purity was the melting point. If the compound obtained is pure, it has a well-defined melting point. If it is a mixture, the melting process starts and ends over a range of temperatures.
As it happens, long-chained molecules have no well-defined melting point. They do not crystallize unambiguously and, when heated up, they behave somewhat like amorphous glass. The solid starts softening before liquefying, and the transition from solid to liquid takes place over a rather extended temperature range. Given the purity criteria of nineteenth-centure chemistry, these molecules were doomed, and the chemists of the time had no reason to show any interest in them." [28]

1.1 A (very) brief history of polymers

The above story was brought by Pierre-Gilles de Gennes on his journey through the high schools of France after receiving his Nobel prize in physics. The purpose of the story was to warn against too much reliance on laws, doctrines, and rules. In this particular case of polymer research, it was not until 80 years after Goodyears discovery that the concept of long-chained molecules was accepted by the community of chemists and physicists. It happened thanks to Hermann Staudinger, who succeeded around 1920 to synthesize relatively long molecules (some 20 units, rather than 1000 or a million units). Chains of this length are still short enough to be crystallized and to have a well-defined melting point. From that point on, gradually, by means of successive operations, Staudinger prepared ever longer chains. These chains remained well-defined, even though their melting point becomes increasingly fuzzy. From all this, he concluded that it is possible to make very long molecules. Yet Staudinger was also a bit a victim of the doctrines of his time, as he assumed that these macromolecules looked like small rigid rods, up to about a micrometer in length.

It was another 20 years before the atomic physicist and physical chemist Richard Kuhn was able to show, using the concept of entropy in statistical mechanics, that the amazing elasticity of rubber can be explained by the very flexibility of the macromolecules. [70]

1.2 Flexibility and uncrossability

Richard Kuhns description of a polymer as a coiling, flexible thread is valid because in each monomer (the building block of a polymer) there is at least one torsion angle that can adopt multiple values, all within reach of thermally activated motions. For example, the torsion angle in the C-C backbone of polyethylene has three possible values (one *trans* and two *gauche*). [44] This means that the number of possible conformations of a polymer is astronomical, in the order of $3^{(n-3)}$ for a polyethylene chain containing n CH_2 groups. This number is somewhat overestimated, because repulsive interactions between the atoms prevent overlap between different parts of a chain. For a polymer *in vacuo*, or a dilute solution of polymers in a good solvent, this leads to somewhat swollen conformations. In a polymer melt, i.e. a liquid of undiluted polymer, these so-called excluded volume effects are effectively screened, [13] and the random coil conformation is retained.

As a result of the flexibility of polymer chains, their dynamic behavior is quite complicated. In polymer melts, and also in concentrated polymer solutions, the situation is aggravated by the fact that each chain is interacting with many other chains. The effect of these intermolecular interactions is best revealed by the peculiar flow behavior of these materials: they are very viscous and have surprising elastic properties. In uncrosslinked polymers, these elastic properties manifest themselves temporarily, but still sometimes on very long time scales (hours). So, despite the fact that they are not crosslinked (as in a rubber), dense polymer systems act temporarily as rubber-like networks. The cause of this, of course, is the fact that the chains are intertwined and can not penetrate through each other: they are "entangled". These entanglements survive for some non-negligible time. Another interesting observation is that the magnitude of the elastic effect is rather independent of chain length,

but it occurs only when the chains are longer than a certain threshold. The aim of the research presented in this thesis is to explain this peculiar dynamic behavior of polymer melts, and to derive the threshold chain length from the characteristics of a specific polymer species.

1.3 Theories of entanglement

Many attempts have already been made to explain the entanglement phenomenon. The usual procedure is to propose a microscopic model, calculate the consequences for various dynamic properties, and compare the outcome with experiment (if available). Theoretical treatments of this sort can be divided in two groups. [73] First, there are the cooperative motion models, where the focus is on the increased friction experienced by a test chain because it drags other chains or chain segments along with it over finite distances. The resulting motion of a test chain is isotropic over all length scales, and the friction enhancement is in general a function of both test chain and surrounding chain molecular weight. A major difficulty in such an approach is the specification of the location and duration of entanglements, because the exact nature of an entanglement is not known. Examples are the mode-coupling approach by Ngai and co-workers [88–90] and the phenomenological theory of Skolnick and co-workers. [127] But also the generalized Langevin equation models fall into this category. These models often do try to address the inherent multiple-chain nature of an entanglement, or at least the viscoelastic nature of the effective field felt by a test chain. Examples are the Ronca model [117], the Renormalized Rouse (mode-coupling) formalism by Schweizer [122, 123], and more recently the Twice-Renormalized Rouse formalism by Fatkullin. [36]

The second group includes the reptative motion models, in which the primary result of entanglement is the constraining of a test chain to longitudinal, i.e., anisotropic motion along its own contour. The test chain is often envisioned as being confined to a fictitious “tube” with diameter equal to the entanglement spacing. The reptation model was introduced by De Gennes [24, 25] and further refined by Doi and Edwards [30]. The main task of the tube is to constrain the chain along the lateral direction. It has been shown that other models exist which use this same ingredient, but without explicitly introducing a tube. [56, 60] The main point of concern with these theories is that although the test chain is treated explicitly, only some mean field approximation is applied to represent the surrounding chains. This makes the calculation of certain quantities which to a large extent depend on intermolecular correlation functions somewhat questionable. To name one example, it appears that viscoelasticity is largely based on collective multi-chain modes. Therefore calculation of the stress tensor should include intermolecular interactions. [35, 37, 43, 46]

At the time of writing (2002) it remains a matter of debate which theory provides the best description of polymer melt dynamics. Some experiments seem to agree with the reptation model, [120] while others disagree. [34, 36] In this thesis we will use an alternative technique to study the dynamics of polymer melts: computer simulations.

1.4 Simulations

By the use of computers, a range of increasingly complex polymer models can be solved. It will be instructive to shortly review the different approaches that have already been undertaken.

1.4.1 Microscopic simulations

On the very detailed level, molecular dynamics (MD) simulations can be performed, in which each atom of the polymer chain is represented separately (see Fig. 1.1a). The atoms are modelled as interacting particles and they are moving according to Newton's laws. Bulk behavior is simulated by applying periodic boundary conditions to the simulation box. Typical MD simulations cover the motion of a few thousand of atoms over a period of a few nanoseconds; on current computers such a run would take a day or two to complete. There are limitations, however, to the length of polymers that can be simulated this way, for two reasons: First, the typical size of the polymer grows as $\sqrt{n}$, where n is the number of monomers in a chain. If a polymer is not allowed to interact with itself via the periodic boundaries, the volume of the box must increase as $n^{3/2}$. Second, the longest relaxation time of a polymer chain scales very fast, approximately as n^3. To obtain a well-equilibrated system, and also to measure certain long-time correlation functions, the simulation must be performed for at least as long as this time scale.[1] It should come as no surprise that, up to now, atomistically detailed MD simulations have only been performed for relatively short chains, with lengths of the order of 100 monomers.

1.4.2 Coarse-grained simulations

In order to increase the time and length scales accessible in the simulations of polymers, detailed atomistic models are often replaced by coarse-grained models. The coarse-graining of polymers, and subsequent analysis of the dynamic data, can be performed in two ways: bottom-up or top-down. In the bottom-up approach, the interactions between the coarse-grained sites (called blobs in this thesis) are derived from the underlying atomistic interactions by suitable averaging techniques. [2, 7, 45, 86, 137] This results in an effective potential as well as friction and random forces. When the degree of coarse-graining is sufficiently large, the effective potential usually becomes very soft. This allows the bonds between the blobs to cross each other (see Fig. 1.1b) and greatly accellerates the equilibration process in polymer systems. On the other hand, the resulting dynamics is very unrealistic (too fast), because in reality bonds cannot cross each other. Therefore, when primary interest lies with the dynamics of the polymer system, the atomistic details must somehow be re-introduced in the blobs (this is called "reverse-mapping") and the simulations must be continued in the ordinary MD fashion.

In the other (top-down) approach a certain interaction model is chosen beforehand. In such a "generic" polymer model, the interactions are chosen such that bond crossings will

1 The equilibration time can be reduced considerably by use of special sampling techniques, such as End-Bridging Monte Carlo. [77]

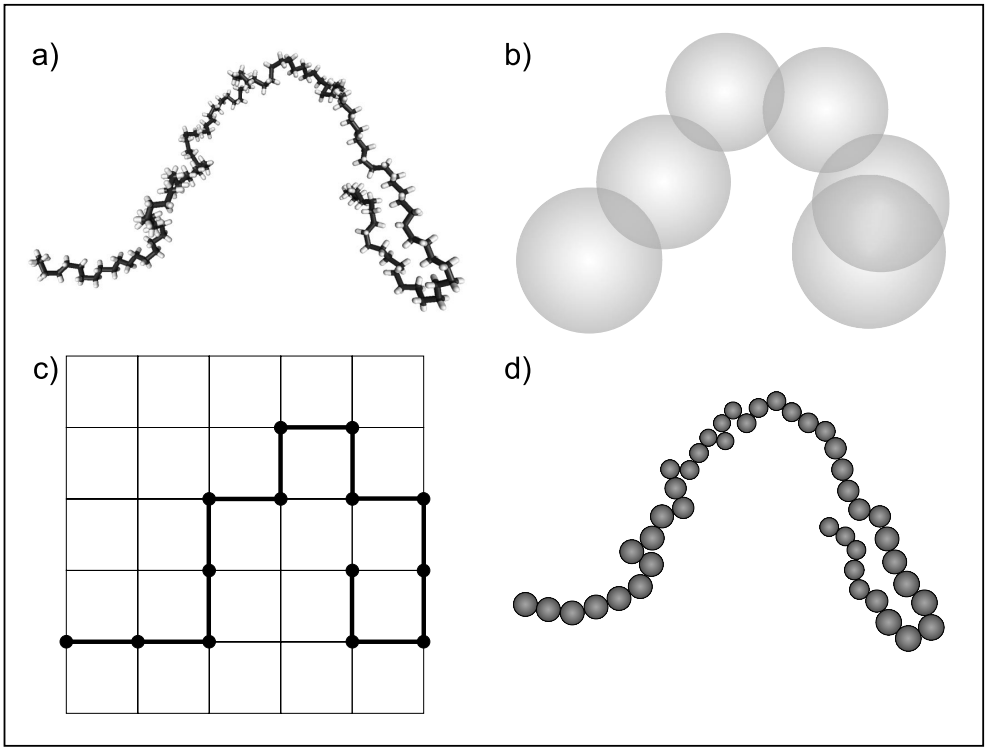

Figure 1.1: Different polymer simulation models. *a*) Atomistically detailed model. *b*) Coarse model, obtained by coarse-graining the atomistically detailed model (bottom-up approach). When many atoms are combined into one new particle, the effective interactions between the particles become so soft that bond crossings can no longer be prevented. *c*) Lattice model. Advantage is the great speed with which a computer can simulate such a model and the relative easy with which bond crossings can be prevented. *d*) Coarse model, in which the interaction model has been chosen beforehand (generic polymer model; top-down approach). Usually these interactions are chosen such that bond crossings are energetically unfavorable (in this example a string of hard spheres). The actual values for the model parameters may be estimated *a posteriori* by mapping on experimental data.

be forbidden or at least energetically unfavorable. In contrast to the bottom-up approach, the model parameters are usually not derived from an underlying atomistic model. Examples of this kind are the Monte Carlo simulations of polymers on a diamond lattice by Termonia [135] and Kremer [64], Monte Carlo simulations on a square lattice by Shaffer [125, 126] (see Fig. 1.1c), and the hard chain simulations of Smith *et al.* [130, 131] and Gao and Weiner [47, 48] (see Fig. 1.1d). An exception may be the work on the (Monte Carlo) bond fluctuation model, in which attempts have been made to map real polymer systems onto the abstract model. [11, 63, 136]

In most top-down models, there exists a possibility to estimate the time and length scales occurring in the simulation *a posteriori*. A well-studied example is the polymer model of Kremer, Grest and co-workers, [66, 107] in which the polymer segments are modeled as relatively hard (Lennard-Jones) beads, connected by finite extensible non-linear springs. The simulations are performed in reduced units, i.e., lengths, masses, and energies are related to the size σ, mass m, and interaction energy ε of the Lennard-Jones beads. The universal trends shown by these simulations are consistent with a crossover to reptation at large chain lengths, although it is clear that the crossover is broad. The crucial test, of course, comes when simulation results are compared with experimental results. In order to make such a comparison, numerical values for the model parameters are needed. Kremer and Grest suggested mapping the simulated persistence and entanglement lengths on those of real polymers. [66] The crucial issue here is to estimate the entanglement length, which is not a trivial thing to do, as will become clear in *Chapter 5* of this thesis.

1.4.3 Simulations performed in this work

The polymer simulation model presented in this thesis distinguishes itself from the above simulation models because it combines two approaches. (i) The model will be based on an undulging atomistic model (bottom-up), therefore encompassing time and length scales in a much more realistic way than can be achieved in the top-down approach. (ii) A method is introduced to detect and prevent bond crossings, which ensures realistic dynamics of the polymer chains. As already mentioned, in most other bottom-up approaches, the dynamics of the coarse-grained model is unrealistic because bond crossings are possible.

Notice that in all top-down models the uncrossability is explicitly introduced, for example by confining the chain on a lattice and exclude multiple occupation of one lattice site or by means of the bond fluctuation model. [67, 125] Lattice models have their limitations by being typically confined to rather low densities and by tending to overestimate the diffusivity at intermediate time scales.

1.5 A short outline of this thesis

This thesis reports on atomistic and coarse-grained simulations of polyethylene melts. We will compare the results with both experimental and theoretical predictions. Two of the best known theories of the dynamics of polymer melts are the Rouse model (for unentangled polymer melts) and the aforementioned tube model (for entangled polymer melts). We discuss

these theories in some detail in *Chapter 2*.

In *Chapter 3* we present atomistic molecular dynamics simulations of a melt of $C_{120}H_{242}$ chains. Such chains are not yet long enough to be seriously entangled, so the dynamic results can be compared with Rouse model predictions. On the other hand, we expect that these chains are long enough to have polymer-like configurations and interactions. This is necessary to be able to correctly derive the coarse-grained interaction parameters for simulation of longer polymers.

The method with which the coarse-grained interactions are derived from the atomistic simulations is described in *Chapter 4*. In this chapter, we also explain the implementation of the uncrossability constraint, and apply it to the coarse-grained version of the $C_{120}H_{242}$ melt. We will show the importance of the uncrossability of bonds, even for chains which are unentangled. Only when the bonds can not cross each other do the results of the coarse-grained simulations agree with the results of the atomistic molecular dynamics simulations.

In *Chapter 5* the coarse-grained model is studied for a range of chain lengths, from C_{80} to C_{1000}. We will study various dynamical quantities, such as the diffusivity, dynamic structure factor, shear relaxation modulus and the viscosity, and compare the outcome with experiment and various theories.

In *Chapter 6* we will show that different experimental techniques, which measure different kinds of dynamical quantities, can consistently lead to the same value for the entanglement molecular weight. For this, however, it is necessary to release the strict relationship between the entanglement molecular weight and the value of the plateau modulus.

The nonlinear flow properties of the coarse-grained model are investigated in *Chapter 7* by means of nonequilibrium simulations. Both transient (start-up) effects and the stationary state will be discussed. Moreover, we will give some attention to the validity of certain rheological “rules”, such as the stress-optical rule and the Cox-Merz rule.

At the end of this thesis, the results are summarized in both English and Dutch. We will focus on the advantages and disadvantages of the current polymer model and we will suggest improvements of the coarse-graining procedure.

2 Theory

In this chapter, we will describe in some detail the two predominant theories for the dynamics of chains in polymer melts: the Rouse model and the tube model. The former is supposed to describe the dynamics of relatively low-weight linear polymers. The latter describes the dynamics of very long chains which are forced to move anisotropically inside effective tubes formed by entanglements with surrounding chains. These theories will be tested against simulation results in the subsequent chapters.

2.1 Introduction

Much of the static and dynamic behavior of monodisperse, linear polymer melts can be explained by models which are surprisingly simple. [30] This is possible because the global, large scale properties of polymers do not depend on the chemical details of the monomers, except for some species-dependent "effective" parameters. For example, one can measure the end-to-end vector, defined as

$$\mathbf{R}_e = \mathbf{r}_n - \mathbf{r}_1, \tag{2.1}$$

where $\mathbf{r}_1$ and $\mathbf{r}_n$ are the positions of the first and last monomers respectively. If the end-to-end vector is measured for a large number of polymers in a melt, one will find that the distribution of end-to-end vectors is Gaussian and that the root mean squared end-to-end distance scales with the square root of the number of monomers, $\sqrt{\langle R_e^2 \rangle} \propto \sqrt{n}$, irrespective of the chemical details. This scaling is characteristic for a random walk: after taking n consecutive steps, each in a random direction, the end point will on average be separated only $\sqrt{n}$ steps from the starting point. Of course, in a real polymer the vectors connecting consecutive monomers do not take up random orientations. However, if enough (say λ) consecutive monomers are combined into one segment with position $\mathbf{R}_i$, the vectors connecting the segments ($\mathbf{R}_i - \mathbf{R}_{i-1}$, $\mathbf{R}_{i+1} - \mathbf{R}_i$, etc.) become independent of each other, see Fig. 2.1. If the number of segments $N = n/\lambda$ is large enough, the end-to-end vectors, according to the central limit theorem in

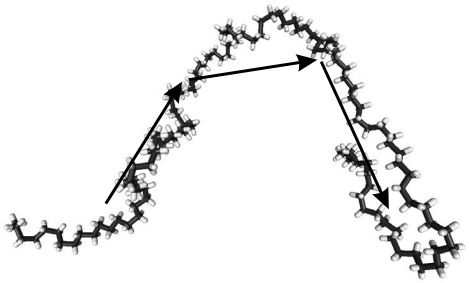

Figure 2.1: If enough consecutive monomers are combined into one segment, the vectors connecting these segments become independent of each other. In this example a polyethylene chain is represented by segments of $\lambda = 30$ monomers. The vectors connecting the centers of mass of these segments are depicted as black arrows.

statistics, will be Gaussianly distributed. Furthermore, on the global scale of segments the mean square end-to-end distance will be given by

$$\langle R_e^2 \rangle = Nb^2, \tag{2.2}$$

i.e. the local structure of the polymer appears only through the effective (or statistical) bond length b. Therefore, if one is interested in the global static properties of polymers, one can start from the simplest model available, consistent with a Gaussian end-to-end distribution. This model is one in which every bond vector itself is Gaussianly distributed. Such a "Gaussian chain" is often represented by a mechanical model of segments connected by ideal, harmonic springs with a spring constant k equal to

$$k = \frac{3k_BT}{b^2}, \tag{2.3}$$

where k_B is Boltzmann's constant and T the temperature. With this choice for the spring characteristics, at equilibrium, the Boltzmann distribution of the bonds between the segments will be Gaussian and the end-to-end distance will obey Eq. (2.2). Of course the Gaussian chain is only a static model of a polymer. In the rest of this chapter we will focus on dynamical models.

2.2 The Rouse model

The simplest dynamical model of a polymer is the Rouse model. In this model it is assumed that the surrounding particles (polymers and/or solvent molecules) merely constitute a stochastic background, and corresponding friction, to a Gaussian chain. [118] This means that both entanglements and hydrodynamic interactions are assumed to be unimportant. When this model is applied to dilute polymeric solutions it gives rather bad results, indicating the importance of hydrodynamic interactions. However, when applied to polymeric melts the model is found to be much more appropriate, because in polymeric melts the friction may be thought of as being caused by the motion of the chain relative to the rest of the material, which to a first approximation may be taken at rest. Propagation of a velocity field like in a normal liquid is highly improbable, meaning that hydrodynamic interactions are screened. [13, 30] A prerequisite is that the polymer chains are not very long, otherwise entanglements with surrounding chains will highly constrain the molecular motions.

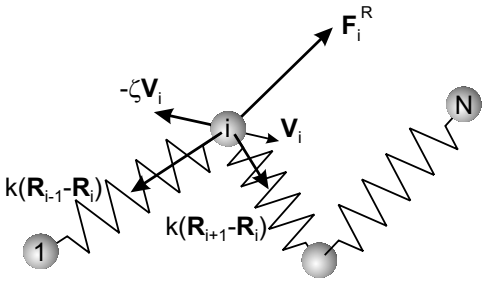

Figure 2.2: Schematic picture of a Rouse chain. A segment i experiences harmonic interaction forces with its bonded neighbours. Intermolecular interactions are approximated by a friction force $-\zeta \mathbf{V}_i$, where $\mathbf{V}_i$ is the velocity, and a random force $\mathbf{F}_i^R$.

2.2.1 Equations of motion

In the Rouse model, the friction force on each segment is assumed proportional to its velocity and directed opposite to its velocity. The constant of proportionality, the friction coefficient ζ, is assumed to be independent of the position of the segment in the medium. The segment will also experience a stochastic, or random, force $\mathbf{F}^R(t)$. In view of the chaotic character of the stochastic forces, the following assumption seems to be appropriate:

$$\left\langle \mathbf{F}^R(t) \right\rangle = \mathbf{0}. \tag{2.4}$$

In Fig. 2.2 the forces acting on a segment i in a Rouse chain are summarized. The resulting equations of motion are the following Langevin equations:

$$\zeta \frac{d\mathbf{R}_1}{dt} = -\frac{3k_BT}{b^2}\left(\mathbf{R}_1 - \mathbf{R}_2\right) + \mathbf{F}_1^R, \tag{2.5}$$

$$\zeta \frac{d\mathbf{R}_i}{dt} = -\frac{3k_BT}{b^2}\left(2\mathbf{R}_i - \mathbf{R}_{i-1} - \mathbf{R}_{i+1}\right) + \mathbf{F}_i^R, \tag{2.6}$$

$$\zeta \frac{d\mathbf{R}_N}{dt} = -\frac{3k_BT}{b^2}\left(\mathbf{R}_N - \mathbf{R}_{N-1}\right) + \mathbf{F}_N^R. \tag{2.7}$$

Eq. (2.6) applies when $i = 2, \ldots, N-1$. Notice that, in writing down these equations, the inertial effects have been neglected. The Rouse model, by its formulation, applies only to large time and length scales. In the diffusive limit, i.e., for times $t > M/\zeta$, where M is the mass of a segment, inertial effects may be ignored.

It is assumed that the segments are slow compared with the stochastic variables. This means that memory effects can be ignored and that the autocorrelation of the stochastic force can be approximated by a δ-function (Markov approximation). The equipartition theorem states that, for large times, the expectation value for the kinetic energy of a segment should go to $\frac{3}{2}k_BT$. On integration of the equation of motion of a single segment, this premises leads to the following relation between the cartesian α and β components of the stochastic forces and the friction coefficient (fluctuation-dissipation theorem):

$$\left\langle F_{i\alpha}^R(t) F_{j\beta}^R(t') \right\rangle = 2k_BT\zeta\delta_{ij}\delta_{\alpha\beta}\delta(t-t'). \tag{2.8}$$

2.2.2 Normal modes

The equations of motion, Eqs. (2.5) - (2.7) can be solved by transforming to the normal coordinates,

$$\mathbf{X}_k = \frac{1}{N}\sum_{i=1}^{N} A_{ki}\mathbf{R}_i \qquad (k = 0,\ldots,N-1), \tag{2.9}$$

where A_{ki} is defined as

$$A_{ki} = \cos\left[\frac{k\pi}{N}(i-1/2)\right]. \tag{2.10}$$

In this expression a term 1/2 is included to assure that the Langevin equations are consistent at the boundaries of the chain. [62] The inverse of Eq. (2.9) expresses the segment coordinates in terms of the normal coordinates,

$$\mathbf{R}_i = \mathbf{X}_0 + 2\sum_{k=1}^{N-1} \mathbf{X}_k A_{ki}. \tag{2.11}$$

The equations of motion in normal coordinates read

$$\zeta\frac{d\mathbf{X}_k}{dt} = -\frac{3k_BT}{b^2}4\sin^2\left[\frac{k\pi}{2N}\right]\mathbf{X}_k + \mathbf{F}_k, \tag{2.12}$$

$$\left\langle F_{0\alpha}(t)F_{0\beta}(t')\right\rangle = 2k_BTN^{-1}\zeta\delta_{\alpha\beta}\delta(t-t'), \tag{2.13}$$

$$\left\langle F_{k\alpha}(t)F_{k\beta}(t')\right\rangle = k_BTN^{-1}\zeta\delta_{\alpha\beta}\delta(t-t') \qquad (k\neq 0). \tag{2.14}$$

Eqs. (2.13) and (2.14) were obtained from Eq. (2.8) by defining

$$\mathbf{F}_k = \frac{1}{N}\sum_{i=1}^{N} A_{ki}\mathbf{F}_i^R, \tag{2.15}$$

and using the property

$$\frac{1}{N}\sum_{i=1}^{N} A_{ki} = \delta_{k,0} \qquad (0\leq k<2N). \tag{2.16}$$

The normal modes $\mathbf{X}_k$ are usually called the Rouse modes. The zeroth mode describes the motion of the center of mass, $\mathbf{X}_0 = \mathbf{R}^{\mathrm{cm}}$; all other modes are associated with internal motions of the chain, mode k roughly corresponding with motion of a subchain of size N/k. In the next chapters, the Rouse mode analysis will be applied to more realistic linear chains. The Rouse modes are then used as generalized coordinates, which can be introduced to analyze the dynamical properties of any dynamical model, not necessarily the Rouse model. With this objective in mind, measurable properties will in the rest of this section first be given in general terms of Rouse mode amplitudes and correlation functions, and then be evaluated explicitly for the Rouse model.

The equation of motion of the center of mass can readily be solved:

$$\zeta \frac{d\mathbf{R}^{\mathrm{cm}}}{dt} = \zeta \frac{d\mathbf{X}_0}{dt} = \mathbf{F}_0, \tag{2.17}$$

$$\mathbf{R}^{\mathrm{cm}}(t) = \mathbf{R}^{\mathrm{cm}}(0) + \zeta^{-1} \int_0^t d\tau \mathbf{F}_0(\tau). \tag{2.18}$$

So the mean square displacement of the center of mass of the Rouse chain is equal to

$$\begin{aligned} \left\langle (\mathbf{R}^{\mathrm{cm}}(t) - \mathbf{R}^{\mathrm{cm}}(0))^2 \right\rangle &= \left\langle \zeta^{-2} \int_0^t d\tau \int_0^t d\tau' \mathbf{F}_0(\tau) \cdot \mathbf{F}_0(\tau') \right\rangle \\ &= \frac{6k_B T}{N\zeta} t, \end{aligned} \tag{2.19}$$

which is always proportional to time, with the well-known Einstein relation between the diffusion and friction coefficient: [32]

$$D = \frac{k_B T}{N\zeta}. \tag{2.20}$$

Notice that the diffusion coefficient scales inversely proportional to the length (and weight) of the polymer chain.

Within the Rouse model, according to Eq. (2.12), the Rouse modes are mutually orthogonal and the correlation functions for $k > 0$ are exponentially decaying:

$$\begin{aligned} \left\langle \mathbf{X}_k(t) \cdot \mathbf{X}_k(0) \right\rangle &\equiv \left\langle X_k^2 \right\rangle C_k(t) \\ &= \left\langle X_k^2 \right\rangle \exp\left(-t/\tau_k\right), \end{aligned} \tag{2.21}$$

$$\tau_k^{-1} = 4W \sin^2\left[\frac{k\pi}{2N}\right], \tag{2.22}$$

$$W = \frac{3k_B T}{\zeta b^2}, \tag{2.23}$$

where we have defined the normalized autocorrelation function $C_k(t)$ and the characteristic frequency W. In case $k \ll N$, the relaxation times τ_k can be approximated as

$$\tau_k \approx \frac{1}{\pi^2 W} \left(\frac{N}{k}\right)^2. \tag{2.24}$$

From the last equation it is clear that the lower Rouse modes, which represent motions with larger wavelengths, are also slower modes. The relaxation time of the slowest mode, $k = 1$, is sometimes referred to as the Rouse time τ_R.

The amplitudes of the Rouse modes can be calculated by rewriting the Boltzmann statistical weight of a chain configuration, using Eq. (2.11):

$$\begin{aligned} P(\mathbf{R}_1, \ldots, \mathbf{R}_N) &= \frac{1}{Z} \exp\left[-\frac{3}{2b^2} \sum_{i=2}^{N} \left(\mathbf{R}_i - \mathbf{R}_{i-1}\right)^2\right] \\ &= \frac{1}{Z} \exp\left[-\frac{12N}{b^2} \sum_{k=1}^{N-1} \mathbf{X}_k \cdot \mathbf{X}_k \sin^2\left(\frac{k\pi}{2N}\right)\right], \end{aligned} \tag{2.25}$$

where Z is a normalization constant (the partition function). Since the transformation to the Rouse coordinates is a linear transformation from one set of orthogonal coordinates to another, the corresponding Jacobian is simply a constant. The distribution of Rouse modes is therefore given by Eq. (2.25), and since it is a simple product of independent Gaussians, the amplitudes of the Rouse modes can easily be calculated:

$$\left\langle X_k^2 \right\rangle = \frac{b^2}{8N \sin^2\left(\frac{k\pi}{2N}\right)}. \tag{2.26}$$

In case $k \ll N$, the amplitudes can be approximated by

$$\left\langle X_k^2 \right\rangle \approx \frac{Nb^2}{2\pi^2}\frac{1}{k^2}. \tag{2.27}$$

Note the similarity between the scaling of the amplitudes and the scaling of the relaxation times with k of the Rouse modes. Using this similarity, it is easy to express the normalized autocorrelation of the end-to-end vector, Eq. (2.1), in terms of relaxation times only (this will be of use in *Chapter 3*). The end-to-end vector is, in terms of Rouse modes,

$$\mathbf{R}_e = -4 \sum_{k=\text{odd}}^{N-1} \mathbf{X}_k \cos\left(\frac{k\pi}{2N}\right), \tag{2.28}$$

and its autocorrelation function is

$$\left\langle \mathbf{R}_e(t) \cdot \mathbf{R}_e(0) \right\rangle = 16 \sum_{k=\text{odd}}^{N-1} \left\langle X_k^2 \right\rangle \cos^2\left(\frac{k\pi}{2N}\right) C_k(t). \tag{2.29}$$

The result will be dominated by k values which are very small compared with N. In the limit $N \gg 1$, and using Eqs. (2.26) and (2.22), the normalized autocorrelation for the Rouse model is given by

$$\frac{\left\langle \mathbf{R}_e(t) \cdot \mathbf{R}_e(0) \right\rangle}{\left\langle R_e^2 \right\rangle} = \frac{\sum_{k=\text{odd}} \tau_k e^{-t/\tau_k}}{\sum_{k=\text{odd}} \tau_k}. \tag{2.30}$$

2.2.3 Segmental motion

Important measurable dynamic properties of polymers are the dynamic structure factor and the mean square displacement of individual segments. Using Eq. (2.11) and the fact that different modes are not correlated, the mean square displacement of segment i can be expressed in terms of Rouse mode amplitudes and autocorrelation functions:

$$\left\langle \left(\mathbf{R}_i(t) - \mathbf{R}_i(0)\right)^2 \right\rangle = \left\langle \left(\mathbf{X}_0(t) - \mathbf{X}_0(0)\right)^2 \right\rangle + 8 \sum_{k=1}^{N-1} \left\langle X_k^2 \right\rangle \left[1 - C_k(t)\right] A_{ki}^2. \tag{2.31}$$

Averaging over all segments, and introducing Eqs. (2.19) - (2.21) and (2.26), the mean square displacement of a typical segment in the Rouse model is

$$g_{\text{seg}}(t) \quad = \quad \frac{1}{N} \sum_{i=1}^{N} \left\langle \left(\mathbf{R}_i(t) - \mathbf{R}_i(0)\right)^2 \right\rangle$$

$$= \quad 6Dt + 6D\sum_{k=1}^{N-1}\tau_k\left(1-e^{-t/\tau_k}\right). \tag{2.32}$$

Two limits may be distinguished. First, when t is very large, $t \gg \tau_R = \tau_1$, the first term in Eq. (2.32) will dominate, yielding $g_{\text{seg}}(t) \approx 6Dt$. This is consistent with the fact that the polymer as a whole diffuses with diffusion coefficient D. Secondly, when $t \ll \tau_R$ the sum over k in Eq. (2.32) will dominate. If $N \gg 1$ the relaxation times can be approximated by Eq. (2.24) and the sum can be replaced by an integral. Performing the integral, one obtains

$$g_{\text{seg}}(t) \approx \left(\frac{12b^2k_BT}{\pi\zeta}\right)^{1/2} t^{1/2} \qquad (t \ll \tau_R,\, N \gg 1). \tag{2.33}$$

So, at short times the mean square displacement of a typical Rouse segment is subdiffusive with an exponent 1/2, and is independent of the number of segments N in the chain.

The dynamic structure factor of a single chain is defined as

$$S(\mathbf{q},t) = \frac{1}{N}\sum_{i=1}^{N}\sum_{j=1}^{N}\left\langle \exp\left\{ i\mathbf{q}\cdot\left[\mathbf{R}_i(t)-\mathbf{R}_j(0)\right]\right\}\right\rangle. \tag{2.34}$$

Inserting Eq. (2.11) yields

$$\begin{aligned} S(q,t) \quad &= \quad \frac{1}{N}\exp\left\{-\frac{q^2}{6}\left\langle\left(\mathbf{X}_0(t)-\mathbf{X}_0(0)\right)^2\right\rangle\right\} \\ &\times\left\{\sum_{i=1}^{N}\sum_{j=1}^{N}\exp\left[-\frac{2q^2}{3}\sum_{k=1}^{N-1}\left\langle X_k^2\right\rangle\left(\left[A_{ki}-A_{kj}\right]^2+2A_{ki}A_{kj}\left[1-C_k(t)\right]\right)\right]\right\}, \end{aligned} \tag{2.35}$$

where it is assumed that the Rouse modes remain orthogonal and that the segmental displacements, and consequently the random displacements of the Rouse modes, are Gaussianly distributed. [101, 129] Inserting Eqs. (2.19) - (2.21) and (2.26), and using the property

$$\sum_{k=1}^{N-1}\frac{\left[A_{ki}-A_{kj}\right]^2}{\sin^2\left(\frac{k\pi}{2N}\right)} = 2N|i-j|, \tag{2.36}$$

the dynamic structure factor of a Rouse chain can be expressed as

$$\begin{aligned} S(q,t) \quad &= \quad \frac{1}{N}\exp\left\{-q^2Dt\right\} \\ &\times\left\{\sum_{i=1}^{N}\sum_{j=1}^{N}\exp\left[-\frac{q^2b^2}{6}|i-j|-2q^2D\sum_{k=1}^{N-1}A_{ki}A_{kj}\tau_k\left(1-e^{-t/\tau_k}\right)\right]\right\}. \end{aligned} \tag{2.37}$$

2.2.4 Shear relaxation and viscosity

Macroscopic viscosity and stress tensor

Suppose the fluid velocity on a macroscopic scale is described by the fluid velocity field $\mathbf{u}(\mathbf{r})$. The Navier-Stokes equation then reads

$$\rho\frac{D}{Dt}\mathbf{u} = \nabla\cdot\boldsymbol{\sigma}, \tag{2.38}$$

where $D/Dt \equiv \partial/\partial t + \mathbf{u}\cdot\nabla$ is the total derivative and $\boldsymbol{\sigma}$ is the stress tensor. Many fluids may be described by assuming that the stress tensor $\boldsymbol{\sigma}$ consists of a part, which is independent of the fluid velocity $\mathbf{u}$, and a part which depends linearly on the derivatives $\partial u_i/\partial r_j$. In hydrodynamics it is shown that the most general stress tensor having these properties reads

$$\boldsymbol{\sigma} = -\left\{P + \left(\frac{2}{3}\eta - \kappa\right)\nabla\cdot\mathbf{u}\right\}\mathbf{I} + \eta\left\{\nabla\mathbf{u} + (\nabla\mathbf{u})^T\right\}, \tag{2.39}$$

with $\mathbf{I}$ the unit tensor, P the pressure, and η and κ the shear and bulk viscosities, respectively. The shear viscosity (and other viscoelastic properties) can be studied by applying a shear flow, with fluid velocity components given by

$$u_x(\mathbf{r},t) = \kappa(t)\, r_y, \qquad u_y = 0, \qquad u_z = 0. \tag{2.40}$$

If the shear rate $\kappa(t)$ is small enough, the stress tensor depends linearly on $\kappa(t)$ and can be written as [30, 38]

$$\sigma_{xy}(t) = \int_{-\infty}^{t} d\tau G(t-\tau)\,\kappa(\tau), \tag{2.41}$$

where $G(t)$ is called the shear relaxation modulus. An important special case is stepwise shear, which is switched on at $t = 0$:

$$\kappa(t) = \dot{\gamma}\,\Theta(t), \tag{2.42}$$

$$\sigma_{xy}(t) = \dot{\gamma}\int_0^t d\tau G(t-\tau), \tag{2.43}$$

where $\Theta(t)$ is the Heaviside function and $\dot{\gamma}$ is the shear rate. Comparing Eq. (2.40) and the off-diagonal elements of Eq. (2.39), the viscosity can now be expressed as

$$\eta = \lim_{t\to\infty}\frac{\sigma_{xy}(t)}{\kappa(t)} = \lim_{t\to\infty}\int_0^t d\tau G(t-\tau) = \int_0^\infty d\tau G(\tau), \tag{2.44}$$

where the last two expressions are valid for small shear rates only. The limit $t\to\infty$ must be taken because during the early stages elastic stresses are built up.

Microscopic expressions for the viscosity and stress tensor

Eq. (2.44) is not yet very useful because the viscosity is not related to the microscopic properties of the molecular model. Microscopic expressions for transport properties such as the viscosity can be found by relating the relaxation of a macroscopic disturbance to spontaneous fluctuations in an equilibrium system. Close to equilibrium there is no way to distinguish between spontaneous fluctuations and deviations from equilibrium that are externally prepared. Since one cannot distinguish, according to the regression hypothesis of Onsager, [17] the regression of spontaneous fluctuations should coincide with the relaxation of macroscopic variables to equilibrium. A derivation for the viscosity and many other thermal transport coefficients can be found in Ref. [79]. The result for the viscosity is

$$\eta = \frac{V}{k_B T}\int_0^\infty d\tau \left\langle \sigma_{xy}^{\mathrm{micr}}(\tau)\,\sigma_{xy}^{\mathrm{micr}}(0)\right\rangle, \tag{2.45}$$

where V is the volume in which the microscopic stress tensor $\boldsymbol{\sigma}^{\text{micr}}$ is calculated. Eq. (2.45) is sometimes referred to as the Green-Kubo expression for the viscosity. Using Onsager's regression hypothesis, it is possible to relate also the integrand of Eq. (2.45) to the shear relaxation modulus $G(t)$ in the macroscopic world:

$$G(t) = \frac{V}{k_B T} \left\langle \sigma_{xy}^{\text{micr}}(t)\, \sigma_{xy}^{\text{micr}}(0) \right\rangle \tag{2.46}$$

The microscopic stress tensor in Eqs. (2.45) and (2.46) is defined as

$$\boldsymbol{\sigma}^{\text{micr}} = -\frac{1}{V} \sum_{i=1}^{N_{\text{tot}}} \left(M \mathbf{V}_i \mathbf{V}_i + \mathbf{R}_i \mathbf{F}_i \right), \tag{2.47}$$

where $\mathbf{V}_i$ and $\mathbf{F}_i$ are the velocity of and the force on particle i, respectively. The sum must be taken over all N_{tot} particles in the system. In most polymer melt systems the first (kinetic) part may be neglected because the stress is dominated by the interactions between the segments.

Calculation for the Rouse model

The above results suggest that the shear relaxation modulus and viscosity of the Rouse model can be obtained by two different approaches: either by applying an external shear field or by analyzing the relaxations in equilibrium. We will start with the first approach.

The idea is to apply a stepwise shear field, and evaluate the resulting stress using Eq. (2.47). [13, 30] As already mentioned, the sum over i in Eq. (2.47) must be taken over all particles of all chains in the system, i.e., the stress tensor is a collective property. In the Rouse model, however, there is no correlation between the dynamics of one chain and the other, so one may just as well analyze the stress of only one chain and make an ensemble average over all initial configurations. The microscopic stress tensor of a Rouse chain in a specific configuration, neglecting the kinetic contributions, is equal to

$$\boldsymbol{\sigma}^{\text{micr}} = \frac{1}{V} \frac{3 k_B T}{b^2} \left[\mathbf{R}_1 \left(\mathbf{R}_1 - \mathbf{R}_2 \right) + \sum_{i=2}^{N-1} \mathbf{R}_i \left(2\mathbf{R}_i - \mathbf{R}_{i-1} - \mathbf{R}_{i+1} \right) + \mathbf{R}_N \left(\mathbf{R}_N - \mathbf{R}_{N-1} \right) \right]. \tag{2.48}$$

Introducing the Rouse modes, Eq. (2.11), and using the properties $\sum_{i=1}^{N} A_{ki} A_{k'i} = \delta_{kk'} N/2$ and Eq. (2.16), the xy-component of the microscopic stress tensor of this configuration can be expressed in terms of the Rouse modes,

$$\sigma_{xy}^{\text{micr}}(t) = \frac{1}{V} \frac{3 k_B T}{b^2} 8N \sum_{k=1}^{N-1} X_{kx}(t)\, X_{ky}(t) \sin^2 \left(\frac{k\pi}{2N} \right). \tag{2.49}$$

To evaluate the stress tensor at time t, we must average $\sigma_{xy}^{\text{micr}}(t)$ over all initial configurations which have evolved under the conditions of Eqs. (2.40) and (2.42) To this end, we augment the Langevin equations, Eqs. (2.5) - (2.7), with terms of the form $\dot{\gamma} R_{iy} \hat{\mathbf{e}}_x$, representing the effects of a shear field. Transforming to normal coordinates, we obtain

$$\frac{d\mathbf{X}_k}{dt} = -\frac{1}{\tau_k} \mathbf{X}_k + \dot{\gamma} X_{ky} \hat{\mathbf{e}}_x + \mathbf{F}_k, \tag{2.50}$$

where τ_k and $\mathbf{F}_k$ are given by Eqs. (2.21) and (2.14), respectively. From this we find

$$\begin{aligned}\frac{d}{dt}\left\langle X_{kx}(t)X_{ky}(t)\right\rangle &= \left\langle \frac{dX_{kx}}{dt}(t)X_{ky}(t)\right\rangle + \left\langle X_{kx}(t)\frac{X_{ky}}{dt}(t)\right\rangle \\ &= -\frac{2}{\tau_k}\left\langle X_{kx}(t)X_{ky}(t)\right\rangle + \dot\gamma\left\langle X_{ky}(t)X_{ky}(t)\right\rangle \\ &\quad + \left\langle F_{kx}(t)X_{ky}(t)\right\rangle + \left\langle X_{kx}(t)F_{ky}(t)\right\rangle. \end{aligned} \tag{2.51}$$

It can be argued (see Ref. [13]) that the last two terms vanish. Moreover, for small values of $\dot\gamma$, $\left\langle X_{ky}(t)X_{ky}(t)\right\rangle$ may be approximated as one third of the equilibrium value $\left\langle X_k^2\right\rangle$. Using $\left\langle X_{kx}(0)X_{ky}(0)\right\rangle = 0$, we find from Eq. (2.51)

$$\left\langle X_{kx}(t)X_{ky}(t)\right\rangle = \int_0^t d\tau\,\dot\gamma\,\frac{1}{3}\left\langle X_k^2\right\rangle e^{-2(t-\tau)/\tau_k}. \tag{2.52}$$

We can now evaluate the average of Eq. (2.49) to get the stress at time t:

$$\sigma_{xy}(t) = \left\langle \sigma_{xy}^{\mathrm{micr}}(t)\right\rangle = \dot\gamma\int_0^t d\tau\frac{k_BT}{V}\frac{8N}{b^2}\sum_{k=1}^{N-1}\left\langle X_k^2\right\rangle \sin^2\left(\frac{k\pi}{2N}\right)e^{-2(t-\tau)/\tau_k}. \tag{2.53}$$

On comparison with Eq. (2.43), we recognize that the shear relaxation modulus of the Rouse model equals

$$G(t) = \frac{k_BT}{V}\frac{8N}{b^2}\sum_{k=1}^{N-1}\left\langle X_k^2\right\rangle \sin^2\left(\frac{k\pi}{2N}\right)e^{-2t/\tau_k} \tag{2.54}$$

$$= \frac{ck_BT}{N}\sum_{k=1}^{N-1}e^{-2t/\tau_k}, \tag{2.55}$$

where in the last line we have used the Rouse expectation value for $\left\langle X_k^2\right\rangle$, Eq. (2.26), and $c = N/V$ is the number density of segments.

In the other approach, explicit introduction of a shear field is not neccesary, as the fluctuations which occur naturally in the Rouse model can also be used to evaluate the stress relaxation. Combining Eqs. (2.49) and (2.26), the *xy*-component of the microscopic stress tensor of a Rouse chain in a specific configuration is

$$\sigma_{xy}^{\mathrm{micr}}(t) = \frac{3k_BT}{V}\sum_{k=1}^{N-1}\frac{X_{kx}(t)X_{ky}(t)}{\left\langle X_k^2\right\rangle}. \tag{2.56}$$

The correlation of the *xy*-component of the microscopic stress tensor at time $t = 0$ with the one at time $t = t$ is therefore

$$\sigma_{xy}^{\mathrm{micr}}(t)\,\sigma_{xy}^{\mathrm{micr}}(0) = \frac{(3k_BT)^2}{V^2}\sum_{k=1}^{N-1}\sum_{k'=1}^{N-1}\frac{X_{kx}(t)X_{ky}(t)}{\left\langle X_k^2\right\rangle}\frac{X_{k'x}(0)X_{k'y}(0)}{\left\langle X_{k'}^2\right\rangle}. \tag{2.57}$$

To obtain the shear relaxation modulus, according to Eq. (2.46), the ensemble average of Eq. (2.57) is needed, i.e. an average must be taken over all possible configurations at $t = 0$. Now, since the Rouse modes are Gaussian variables, all the ensemble averages of products of an odd number of $\mathbf{X}_k$'s are zero and the ensemble averages of products of an even number of $\mathbf{X}_k$'s can be written as a sum of products of averages of only two $\mathbf{X}_k$'s. [116] For the even term in Eq. (2.57) we find:

$$\begin{aligned}\left\langle X_{kx}(t)X_{ky}(t)X_{k'x}(0)X_{k'y}(0)\right\rangle &= \left\langle X_{kx}(t)X_{ky}(t)\right\rangle\left\langle X_{k'x}(0)X_{k'y}(0)\right\rangle \\ &+\left\langle X_{kx}(t)X_{k'y}(0)\right\rangle\left\langle X_{ky}(t)X_{k'x}(0)\right\rangle \\ &+\left\langle X_{kx}(t)X_{k'x}(0)\right\rangle\left\langle X_{ky}(t)X_{k'y}(0)\right\rangle. \end{aligned} \tag{2.58}$$

The first four ensemble averages are zero because, for a Rouse chain in equilibrium, there is no correlation between different cartesian components. The last two ensemble averages are nonzero only when $k' = k$, since the Rouse modes are mutually orthogonal. Using Eq. (2.21) and $\left\langle X_{kx}^2\right\rangle = \left\langle X_{ky}^2\right\rangle = \frac{1}{3}\left\langle X_k^2\right\rangle$, the shear relaxation modulus of a Rouse chain can be expressed as

$$G(t) = \frac{k_BT}{V}\sum_{k=1}^{N-1}\frac{\left\langle X_{kx}(t)X_{kx}(0)\right\rangle}{\frac{1}{3}\left\langle X_k^2\right\rangle}\frac{\left\langle X_{ky}(t)X_{ky}(0)\right\rangle}{\frac{1}{3}\left\langle X_k^2\right\rangle} = \frac{ck_BT}{N}\sum_{k=1}^{N-1}C_k^2(t). \tag{2.59}$$

This is equivalent to Eq. (2.55).

In *Chapter 3* the integral of the shear relaxation modulus up to time t will be compared with the result of the Rouse model, which equals

$$\eta^R(t) = \frac{ck_BT}{N}\sum_{k=1}^{N-1}\frac{\tau_k}{2}\left(1-e^{-2t/\tau_k}\right). \tag{2.60}$$

The limit of this integral for time to infinity is the viscosity. For $N \gg 1$ this can be approximated as

$$\eta^R \approx \frac{\pi^2}{12}\frac{ck_BT}{N}\tau_R. \tag{2.61}$$

So, because $\tau_R \propto N^2$, the viscosity of the Rouse model scales linearly with chain length N for constant segmental friction coefficient ζ. However, as will be shown in *Chapters 4* and *5*, a stronger N dependence is observed in real unentangled melts because the density and, more important, the segmental friction coefficient increase with increasing N.

2.3 The tube model

Studies of the mechanical properties of concentrated polymeric liquids and melts reveal a nontrivial molecular weight dependence of the viscosity and rubber-like elastic behavior on

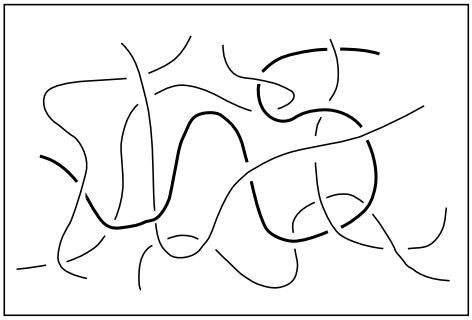

Figure 2.3: The motion of a long chain in a melt is severely constrained by entanglements with surrounding chains.

time scales which increase rapidly with chain length. The observed behavior is rather universal, independent of temperature or molecular species (as long as the polymer is linear and flexible), which indicates that the phenomena are governed by general features of polymers. [30] One of these general features, of course, is the fact that the bonds in polymer chains cannot cross each other. These topological interactions seriously affect the dynamical properties since they impose constraints on the motion of polymers, see Fig. 2.3 In the tube (or reptation) model, introduced by De Gennes [24, 25] and further refined by Doi and Edwards [30], the complicated topological interactions are simplified to an effective tube of constant contour length, surrounding each polymer chain. In order to move over large distances, the chain has to leave the tube by means of longitudinal, reptational, motions

The concept of a tube introduced above, clearly has only a statistical (mean field) meaning. The tube can change by two mechanisms. First by means of the motion of the central chain itself, by which the chain leaves parts of its original tube, and generates new parts. Secondly, the tube will reorganize because of motions of the chains which build up the tube. Also, the contour length of the tube is not constant, but fluctuating. It is generally believed that tube reorganizations of the second kind and contour length fluctuations are unimportant for extremely long chains. For the case of medium long chains, subsequent corrections can be made to account for the reorganization and fluctuation of tubes. Whether the tube picture is indeed correct for polymer solutions or melts still remains a matter for debate, but many experimental results suggest that reptation is the dominant mechanism for the dynamics of a chain in the highly entangled state. In this section we will give a mathematical description of the original tube model, in which tube fluctuations are ignored. Results for segmental motion and viscoelasticity will be derived. In the next section, the corrections dealing with reorganization and fluctuations of the tube will be discussed qualitatively.

2.3.1 Definition of the model

In the tube model, the chain fluctuates around the tube axis, which is also called the primitive chain. By some fluctuation the chain may store some excess mass in part of the tube. This mass may diffuse along the primitive chain and finally leave the tube. The chain thus creates a new piece of tube and at the same time destroys part of the tube on the other side, see Fig. 2.4. This reptative motion will determine the long time motion of the chain. The main concept of

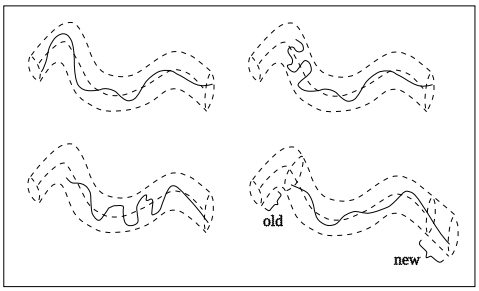

Figure 2.4: A reptating chain escaping from its tube.

the model is the primitive chain, while the details of the polymer itself are considered to be to a large extent irrelevant. For conveniency, the simple Rouse model (with parameters N, b and ζ as in the previous section) is chosen as the underlying basic chain.

The dynamics of the primitive chain is characterized by the following assumptions. (i) The contour length L of the primitive chain is assumed to be constant. The position along the primitive chain will be indicated by the continuous variable $s \in [0,L]$. (ii) The configurations of the primitive chain are assumed to be Gaussian, i.e.

$$\left\langle \left(\mathbf{R}(s) - \mathbf{R}\left(s'\right)\right)^2 \right\rangle = d\left|s - s'\right|, \tag{2.62}$$

where d is the step length of the primitive chain, or tube diameter. (iii) The primitive chain can move back and forth only along itself with diffusion coefficient $D_R = k_B T/(N\zeta)$, i.e. with the Rouse diffusion coefficient, because the motion of the primitive chain corresponds to the overall translation of the Rouse chain along the tube.

Apparently two new parameters have been introduced, the contour length L and the tube diameter d. Only one of them however is independent, because they are related by $Nb^2 = \left\langle R_e^2 \right\rangle = Ld$, i.e.,

$$L = \frac{Nb^2}{d}. \tag{2.63}$$

2.3.2 Segmental motion

In this subsection it will be shown that the mean square displacement of a typical segment in the tube model behaves like

$$g_{\text{seg}}(t) \propto \begin{cases} t^{1/2} & (t < \tau_e), \\ t^{1/4} & (\tau_e < t < \tau_R), \\ t^{1/2} & \left(\tau_R < t < \tau_d\right), \\ t^{1} & \left(t > \tau_d\right). \end{cases} \tag{2.64}$$

Here τ_R is the Rouse time which is equal to τ_1 in Eq. (2.22). The meaning of τ_e and τ_d will become clear in the remaining part of this section. The different time regimes in Eq. (2.64) will now be treated separately.

(i) $t < \tau_e$

At short times a Rouse segment does not know about any tube constraints. According to Eq. (2.33) then

$$g_{\text{seg}}(t) = \left(\frac{12b^2 k_B T}{\pi\zeta}\right)^{1/2} t^{1/2}. \tag{2.65}$$

Once the segment has moved a distance d, it will feel the constraints of the tube, and a new regime will set in. The time at which this happens is given by

$$\tau_e = \frac{\pi\zeta d^4}{12b^2 k_B T}. \tag{2.66}$$

Notice that this is independent of N.

(ii) $\tau_e < t < \tau_R$

On this time and length scale, the segment performs random motions, still constrained by the fact that the segment is part of a chain because $t < \tau_R$. Orthogonally to the primitive chain these motions do not lead to any displacement, because of the constraints implied by the tube. Only along the primitive chain the segments may diffuse free of any other constraints than the one implied by the fact that it belongs to a chain. The diffusion therefore is given by the 1-dimensional analogue of Eq. (2.65),

$$\left\langle (s_i(t) - s_i(0))^2 \right\rangle = \frac{1}{3}\left(\frac{12b^2 k_B T}{\pi\zeta}\right)^{1/2} t^{1/2}, \tag{2.67}$$

where $s_i(t)$ is the position of segment i along the primitive chain at time t. It is assumed that for times $t < \tau_R$ the chain as a whole does not move, i.e. that the primitive chain does not change. Using Eq. (2.62) then

$$g_{\text{seg}}(t) = d\left(\frac{12b^2 k_B T}{9\pi\zeta}\right)^{1/4} t^{1/4}, \tag{2.68}$$

where was assumed $\left\langle \left| s_i(t) - s_i(0) \right| \right\rangle \approx \left\langle (s_i(t) - s_i(0))^2 \right\rangle^{1/2}$.

(iii) $\tau_R < t < \tau_d$

The segment still moves along the primitive path. Now however $t > \tau_R$, which means that one should use the 1-dimensional analogue of the long time limit of Eq. (2.32), i.e.

$$\left\langle (s_i(t) - s_i(0))^2 \right\rangle = 2D_R t. \tag{2.69}$$

Again, assuming that the tube does not change appreciably during time t, one gets

$$g_{\text{seg}}(t) = d\left(\frac{2k_B T}{N\zeta}\right)^{1/2} t^{1/2}. \tag{2.70}$$

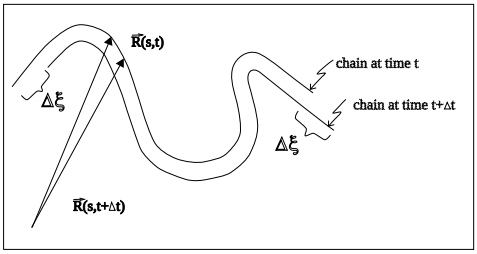

Figure 2.5: When the primitive chain moves a distance $\Delta\xi$ along its contour, the segment s comes to the point where the segment $s+\Delta\xi$ was at time t.

From this treatment it is clear that τ_d is the time it takes for the chain to create a tube which is uncorrelated with the old one.

(iv) $t > \tau_d$

This is the regime in which reptation dominates. On this time and length scale a definite value of s may be attributed to every segment. The goal then is to calculate

$$\varphi(s,t) = \langle(\mathbf{R}(s,t) - \mathbf{R}(s,0))^2\rangle, \tag{2.71}$$

where $\mathbf{R}(s,t)$ is the position of segment s at time t. In order to calculate $\varphi(s,t)$ it is useful to introduce

$$\varphi(s,s';t) = \langle(\mathbf{R}(s,t) - \mathbf{R}(s',0))^2\rangle, \tag{2.72}$$

i.e. the mean square distance between segment s at time t and segment s' at time zero. According to Fig. 2.5, for all s, except $s=0$ and $s=L$, the following relation is valid:

$$\varphi(s,s';t+\Delta t) = \langle\varphi(s+\Delta\xi,s';t)\rangle, \tag{2.73}$$

where $\Delta\xi$ according to the definition of the primitive chain is a stochastic variable. The average on the right hand side has to be taken over the distribution of $\Delta\xi$. Expanding the right hand side of Eq. (2.73) one gets

$$\begin{aligned}\langle\varphi(s+\Delta\xi,s';t)\rangle &= \varphi(s,s';t) + \langle\Delta\xi\rangle\frac{\partial}{\partial s}\varphi(s,s';t) + \frac{1}{2}\langle(\Delta\xi)^2\rangle\frac{\partial^2}{\partial s^2}\varphi(s,s';t) \\ &\approx \varphi(s,s';t) + D_R\Delta t\frac{\partial^2}{\partial s^2}\varphi(s,s';t).\end{aligned} \tag{2.74}$$

Introducing this into Eq. (2.73) and taking the limit for Δt going to zero, a diffusion equation results:

$$\frac{\partial}{\partial t}\varphi(s,s';t) = D_R\frac{\partial^2}{\partial s^2}\varphi(s,s';t). \tag{2.75}$$

In order to complete the description of reptation the boundary conditions going with this diffusion equation have to specified. These are given by

$$\varphi(s,s';t)|_{t=0} = d|s-s'|, \tag{2.76}$$

$$\frac{\partial}{\partial s}\varphi(s,s';t)|_{s=L} = d, \tag{2.77}$$

$$\frac{\partial}{\partial s}\varphi(s,s';t)|_{s=0} = -d. \tag{2.78}$$

The first of these is obvious. The second follows from

$$\begin{aligned}
\frac{\partial}{\partial s}\varphi(s,s';t)|_{s=L} &= 2\langle\frac{\partial \mathbf{R}(s,t)}{\partial s}|_{s=L}\cdot(\mathbf{R}(L,t)-\mathbf{R}(s',0))\rangle \\
&= 2\langle\frac{\partial \mathbf{R}(s,t)}{\partial s}|_{s=L}\cdot(\mathbf{R}(L,t)-\mathbf{R}(s',t))\rangle + 2\langle\frac{\partial \mathbf{R}(s,t)}{\partial s}|_{s=L}\cdot(\mathbf{R}(s',t)-\mathbf{R}(s',0))\rangle \\
&= 2\langle\frac{\partial \mathbf{R}(s,t)}{\partial s}|_{s=L}\cdot(\mathbf{R}(L,t)-\mathbf{R}(s',t))\rangle \\
&= \frac{\partial}{\partial s}\langle(\mathbf{R}(s,t)-\mathbf{R}(s',t))^2\rangle|_{s=L} \\
&= \frac{\partial}{\partial s}d|s-s'|_{s=L} = d.
\end{aligned} \tag{2.79}$$

Condition Eq. (2.78) follows from a similar reasoning.

The solution of Eqs. (2.75) to (2.78) is given without proof:

$$\begin{aligned}
\varphi(s,s';t) &= |s-s'|d + 2D_R\frac{d}{L}t \\
&\quad + 4\frac{Ld}{\pi^2}\sum_{k=1}^{\infty}\frac{1}{k^2}(1-e^{-tk^2/\tau_d})\cos\left(\frac{k\pi s}{L}\right)\cos\left(\frac{k\pi s'}{L}\right),
\end{aligned} \tag{2.80}$$

where

$$\tau_d = \frac{L^2}{\pi^2 D_R} = \frac{1}{\pi^2}\frac{b^4}{d^2}\frac{\zeta}{k_B T}N^3. \tag{2.81}$$

Notice that τ_d becomes much larger than τ_R for large N, see Eqs. (2.24) and (2.81). If the number of steps in a primitive chain is defined by

$$Z = \frac{Nb^2}{d^2} = \frac{L}{d}, \tag{2.82}$$

then the ratio between τ_d and τ_R is

$$\frac{\tau_d}{\tau_R} = 3Z. \tag{2.83}$$

Now taking the limit $s \to s'$ one gets

$$\langle(\mathbf{R}(s,t)-\mathbf{R}(s,0))^2\rangle = 2D_R\frac{d}{L}t + 4\frac{Ld}{\pi^2}\sum_{k=1}^{\infty}\cos^2\left(\frac{k\pi s}{L}\right)(1-e^{-tk^2/\tau_d})\frac{1}{k^2}. \tag{2.84}$$

For $t > \tau_d$ this results in diffusive behaviour with diffusion constant

$$D = \frac{1}{3}D_R\frac{d}{L} = \frac{1}{3}\frac{d^2}{b^2}\frac{kT}{\zeta}\frac{1}{N^2}. \tag{2.85}$$

Notice that this is proportional to N^{-2}, whereas the diffusion coefficient of the Rouse model was proportional to N^{-1}.

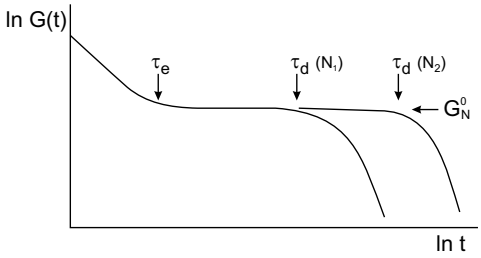

Figure 2.6: Schematic logarithmic plot of the time behavior of the shear relaxation modulus $G(t)$ as measured in a polymer melt; $N_1 < N_2$.

2.3.3 Shear relaxation and viscosity

Experimentally the shear relaxation modulus $G(t)$ of a polymer melt turns out to be like in Fig. 2.6. [30] Two regimes may be distinguished.

(i) $t < \tau_e$

At very short times the chain behaves like a 3-dimensional Rouse chain. Using Eq. (2.55),

$$\begin{aligned} G(t) &= \frac{c}{N} k_B T \sum_{k=1}^{N-1} \exp\left(-2k^2 t/\tau_R\right) \\ &\approx \frac{c}{N} k_B T \int_0^{\infty} dk \exp\left(-2k^2 t/\tau_R\right) \\ &= \frac{c}{N} k_B T \sqrt{\frac{\pi}{8}} \left(\frac{\tau_R}{t}\right)^{1/2}. \end{aligned} \tag{2.86}$$

which decays as $t^{-1/2}$. At $t = \tau_e$ this possibility to relax ends. The only way for the chain to relax any further is by breaking out of the tube.

(ii) $t > \tau_e$

The stress that remains in the system is caused by the fact that the chains are trapped in twisted tubes. By means of reptation the chain can break out of its tube. The newly generated tube contains no stess. So, it is plausible to assume that the stress at any time t is proportional to the fraction of the original tube that is still part of the tube at time t. This fraction is called $\Psi(t)$. So,

$$G(t) = G_N^0 \Psi(t). \tag{2.87}$$

On the reptation time scale, τ_e is practically zero, so it is allowed to set $\Psi(\tau_e) = \Psi(0) = 1$. To make a smooth transition from the Rouse regime to the reptation regime, Eqs. (2.86) and (2.87) are matched at $t = \tau_e$, yielding

$$G_N^0 = G(\tau_e) = \frac{c}{N} k_B T \sqrt{\frac{\pi}{8}} \left(\frac{\tau_R}{\tau_e}\right)^{1/2} = \frac{c}{\sqrt{2}\pi} k_B T \frac{b^2}{d^2}. \tag{2.88}$$

Notice that the plateau value G_N^0 is independent of the chain length N. The numerical prefactor of $1/\sqrt{2}\pi$ in Eq. (2.88) is not rigorous because in reptation theory the time τ_e, at which the Rouse-like modulus is supposed to be instantaneously replaced by the reptation-like modulus, is not defined in a rigorous manner. A calculation based on stress relaxation after a large step strain gives a numerical prefactor of $4/5$ [30], i.e.

$$G_N^0 = \frac{4}{5}\frac{ck_BTb^2}{d^2} = \frac{4}{5}\frac{ck_BT}{N_e}. \tag{2.89}$$

In the last equation we have defined the entanglement length N_e. In most experiments the entanglement length (or more precisely the entanglement molecular weight) is estimated from the value of the plateau modulus. We will return to this in *Chapter 5*.

$\Psi(t)$ will now be calculated. Take a look at

$$\left\langle \mathbf{u}\left(s',t\right)\cdot\mathbf{u}\left(s,0\right)\right\rangle \equiv \left\langle \frac{\partial \mathbf{R}\left(s',t\right)}{\partial s'}\cdot\frac{\partial \mathbf{R}\left(s,0\right)}{\partial s}\right\rangle. \tag{2.90}$$

The vector $\mathbf{u}(s',t)$ is the tangent to the primitive chain, at segment s' at time t. Because the primitive chain has been parametrized with the contour length, $\mathbf{u}\cdot\mathbf{u} = (\triangle\mathbf{R}\cdot\triangle\mathbf{R})/(\triangle s)^2 = 1$, i.e. the tangent has length 1. Then, using Eq. (2.72),

$$\begin{aligned} & \left\langle \mathbf{u}\left(s',t\right)\cdot\mathbf{u}\left(s,0\right)\right\rangle \\ = \; & -\frac{1}{2}\frac{\partial^2}{\partial s\partial s'}\varphi\left(s',s;t\right) \qquad (2.91)\\ = \; & d\delta\left(s-s'\right) - \frac{2d}{L}\sum_{k=1}^{\infty}\left(1-e^{-tk^2/\tau_d}\right)\sin\left(\frac{k\pi s}{L}\right)\sin\left(\frac{k\pi s'}{L}\right) \\ = \; & \frac{2d}{L}\sum_{k=1}^{\infty}e^{-tk^2/\tau_d}\sin\left(\frac{k\pi s}{L}\right)\sin\left(\frac{k\pi s'}{L}\right), \qquad (2.92) \end{aligned}$$

where was used:

$$\frac{2}{L}\sum_{k=1}^{\infty}\sin\left(\frac{k\pi s}{L}\right)\sin\left(\frac{k\pi s'}{L}\right) = \delta\left(s-s'\right). \tag{2.93}$$

Using this last equation, one also finds

$$\left\langle \mathbf{u}\left(s',0\right)\cdot\mathbf{u}\left(s,0\right)\right\rangle = d\delta\left(s-s'\right). \tag{2.94}$$

This equation states that there is no correlation between the tangents to the primitive chain at a segment s, and at another segment s'. If we look at $\langle \mathbf{u}(s',t)\cdot\mathbf{u}(s,0)\rangle$ as a function of s', at time t, we see that the original delta function has broadened and lowered. However, the tangent $\mathbf{u}(s',t)$ can only be correlated to $\mathbf{u}(s,0)$ by means of diffusion of segment s', during the time interval $[0,t]$, to the place where s was at time $t=0$, and still lies in the original tube. So, $\frac{1}{d}\langle \mathbf{u}(s',t)\cdot\mathbf{u}(s,0)\rangle$ is the probability density that, at time t, segment s' lies within the original tube at the place where s was initially. Integrating over s' gives us the probability

$\Psi(s,t)$ that at time t *any* segment lies within the original tube at the place where segment s was initially. In other words, the chance that the original tube segment s is still up-to-date, is

$$\begin{aligned}\Psi(s,t) &= \frac{1}{d}\int_0^L ds' \left\langle \mathbf{u}\left(s',t\right)\cdot\mathbf{u}\left(s,0\right)\right\rangle \\ &= \frac{4}{\pi}\sum_{k=1}^{\infty}\frac{1}{k}\sin\left(\frac{k\pi s}{L}\right)e^{-tk^2/\tau_d}. \end{aligned} \tag{2.95}$$

The fraction of the original tube that is still intact at time t, is therefore given by

$$\begin{aligned}\Psi(t) &= \frac{1}{L}\int_0^L ds\Psi(s,t) \\ &= \frac{8}{\pi^2}\sum_{k=\text{odd}}^{\infty}\frac{1}{k^2}e^{-tk^2/\tau_d}, \end{aligned} \tag{2.96}$$

where only terms with odd k occur in the sum. This formula shows why τ_d is the time needed by the chain to reptate out if its tube; for $t > \tau_d$, $\Psi(t)$ is falling to zero quickly. According to Eq. (2.81), this maximum relaxation time τ_d is proportional to N^3.

Finally, the viscosity of a system of reptating chains will be calculated. Using Eq. (2.44) one finds

$$\begin{aligned}\eta &= \int_0^{\infty} G(t)\,dt = G_N^0\frac{8}{\pi^2}\sum_{k=\text{odd}}^{\infty}\frac{1}{k^2}\int_0^{\infty} dt e^{-tk^2/\tau_d} \\ &= G_N^0\frac{8}{\pi^2}\tau_d\sum_{k=\text{odd}}^{\infty}\frac{1}{k^2}\int_0^{\infty} d\tau e^{-\tau k^2} \\ &= \frac{\pi^2}{12}G_N^0\tau_d. \end{aligned} \tag{2.97}$$

Since G_N^0 is independent of N, the viscosity, like τ_d, is proportional to N^3. This is close to, but underestimating, the experimentally observed scaling $\eta \propto N^{3.4}$. The discrepancy may be removed by introducing other relaxation modes in the tube model.

2.4 Other relaxation modes in the tube model

2.4.1 Contour length fluctuation

In the original tube model, described in the previous sections, the primitive chain was regarded as an inextensible string of contour length L. In reality, the contour length of a primitive chain can fluctuate in time. These fluctuations lead to significant reduction of the longest time scales in the dynamics of medium long chains,[1] as will be explained in this section.

The statistical distribution of contour lengths can be estimated by calculating the probability that a certain conformation of the primitive chain is realized. [30] This probability will be proportional to the number of conformations of the Rouse chain which are represented by

1 In this context, medium long chains are chains with contour lengths of only a few times the tube diameter.

that primitive chain. The simplest hypothesis is to constrain the Rouse chain within a straight tube of length L. Furthermore one has to take into account the multiplicity of states with the same contour length L. Combination of both effects leads to the following contour length distribution:

$$P(L) \propto \exp\left[-\frac{3}{2Nb^2}\left(L-\bar{L}\right)^2\right] \quad \text{for } \bar{L} \gg N^{1/2}b, \tag{2.98}$$

where $\bar{L} = Nb^2/d$ is the average contour length. Using Eq. (2.98), the average fluctuation in L can be calculated as:

$$\Delta\bar{L} = \left\langle \Delta L^2 \right\rangle^{1/2} = \left[\int_0^\infty dL P(L)\left(L-\bar{L}\right)^2\right]^{1/2} = \left(Nb^2/3\right)^{1/2}. \tag{2.99}$$

The *relative* fluctuations decrease with chain length,

$$\frac{\Delta\bar{L}}{\bar{L}} = \left(\frac{d^2}{3Nb^2}\right)^{1/2} = \left(\frac{d}{3L}\right)^{1/2} = \frac{1}{\sqrt{3Z}}, \tag{2.100}$$

justifying the inextensible string approximation when $Z \gg 1$, i.e. $\bar{L} \gg d$. However, when the chain is not extremely long, the fluctuations lead to a faster escape of the chain from the original tube than would be predicted in the original tube model. If the contour length fluctuation is neglected, the disentanglement time is proportional to the time necessary for the chain to move the distance $\bar{L}$, see Eq. (2.81),

$$\tau_d^{(\mathrm{NF})} = \frac{\bar{L}^2}{\pi^2 D_R}, \tag{2.101}$$

where the superscript (NF) stands for 'no fluctuation'. If there are fluctuations, the chain can disentangle from the tube when it has moved approximately the distance $\bar{L} - \Delta\bar{L}$, because the chain ends are fluctuating rapidly over the distance $\Delta\bar{L}$. So we estimate the disentanglement time as

$$\tau_d^{(\mathrm{F})} \approx \frac{\left(\bar{L}-\Delta\bar{L}\right)^2}{\pi^2 D_R}, \tag{2.102}$$

where the superscript (F) stands for 'fluctuation'. From these equations we can estimate:

$$\tau_d^{(\mathrm{F})} \approx \tau_d^{(\mathrm{NF})}\left(1-\frac{X}{\sqrt{Z}}\right)^2, \tag{2.103}$$

where X is a certain numerical constant. A more precise variational calculation for the Rouse model shows that X is larger than 1.47. [29] For this reason the effect of the contour length fluctuation is significant even if Z is as large as 100.

The contour length fluctuations may serve to explain the discrepancy between the observed scaling behavior of the viscosity, $\eta \propto N^{3.4}$, and the (pure) reptation prediction, $\eta \propto N^3$. As long as Z is not extremely large the disentanglement times, and therefore the viscosities, will be underestimated compared with the pure reptation predictions. This cross-over region

is very large and in this region an apparent exponent for the scaling of the viscosity is observed, which is larger than 3. It should be noted that for some time it was not clear why the self-diffusion coefficient could scale according to the pure reptation result, $D \propto N^{-2}$, while at the same time the viscosity and typical relaxation times felt the effects of contour length fluctuations. However, recent reinvestigation of available experimental diffusion coefficient data suggests that an exponent smaller than -2 can be observed for D as well, consistent with the viscosity scaling. [72]

2.4.2 Tube reorganization

Another limitation of the pure reptation picture is the assumption that the tube is fixed in the material and that conformational changes occur only at the tube ends. In reality, all polymer move and the tube of polymer *A* is not only renewed by reptation of *A* but also by "constraint release", as a result of the motion of other polymers. This effect can be modeled by double reptation, an idea introduced by des Cloizeaux, [19] in which an entanglement situated at the junction of two polymers *A* and *B* can be released by reptation of either *A* or *B*. A more detailed treatment of the double reptation model is outside the scope of the thesis, but we mention that all typical relaxation times decrease in comparison with pure reptation, and that additional relaxations occur in the shear stress relaxation modulus.

Tube reorganization effects, such as the constraint release, are especially important for polymers with a broad molecular weight distribution, because the presence of short chains speeds up relaxation of longer ones, and vice versa. In the next chapters we will only consider monodisperse polymer melts, in which case most difficulties of the pure reptation theory can be resolved by including the contour length fluctuations.

3 United atom simulations of zero-shear stress relaxation and long time dynamics of $C_{120}H_{242}$: A test of Rouse theory

Results of united atom molecular dynamics simulations of a n-$C_{120}H_{242}$ melt at 450 K are presented. It is shown that the results of mean square displacement, dynamic structure factor, end-to-end vector autocorrelation and shear relaxation modulus can consistently be described by the Rouse model with a single set of fit parameters, provided the length scales involved are larger than the statistical segment length $b \approx 1.2$ nm. On smaller length scales the stiffness of the chain becomes prominent, and the results deviate increasingly from the Rouse predictions. The shear relaxation modulus $G(t)$ is determined from the stress autocorrelation function from both atomic and molecular points of view. The integrals $\int G(t)dt$ are found to be identical after 1 ps and a Rouse description is shown to coincide for time scales larger than 0.4 ns. Compared to experimental values, the measured diffusion coefficient is overestimated by 63% and the viscosity is underestimated by 38%, consistent with molecular dynamics simulations of small molecules.[*]

3.1 Introduction

A melt of polyethylene (PE) can be viewed as a prototype of a large spectrum of different polymer species, which all have the common feature that they are long and linear. Both its simple chemical structure and its technological relevance have made PE the favorite subject of modeling and simulation efforts on computers. However, the level of sophistication and atomic detail is always limited by the computational cost which can become quite enormous because of the large time and length scales involved in dynamic properties of polymers. For instance, atomic simulations of melts of very long (thousands of monomers) chains are still out of reach of current-day computer power. Coarse grained models have been applied to overcome this problem, and some are quite successful in reproducing experimentally observed scaling laws of polymer melt properties, such as the diffusion coefficient and viscosity. However, quantitative agreement with experiment is usually better when atomic simulations

[*] The work described in this chapter previously appeared in J. Chem. Phys. **114**(19), 8685 (2001). [96]

are applied. Therefore, the results of atomic simulations are important to check the validity of coarse grained models and to calculate the parameters occurring in these models.

In this chapter we report diffusion, dynamic structure factor, zero-shear relaxation modulus, and viscosity results of atomic molecular dynamics (MD) simulations of a melt of *n*-$C_{120}H_{242}$ chains. Several other studies have been reported on simulations of melts of polymers of comparable size. [14, 51, 52, 82–85, 100, 101] They all suggest that individual properties of these melts can well be described by the Rouse model. [118] In this chapter we will test whether the Rouse model can be used to predict the time correlation functions of a comprehensive set of physical processes by using one single set of parameters. At the same time our results provide a benchmark for the coarse grained modelling of $C_{120}H_{242}$ in *Chapter 4*.

Paul and co-workers have performed molecular dynamics simulations of a melt of *n*-$C_{100}H_{202}$ chains. [100, 101] They found that translational and rotational diffusion of the chains can consistently be described by the Rouse model, but that systematic deviations show up in the internal dynamics of the chains. Also, subdiffusive behavior was observed in the chain dynamics, not predicted by the Rouse model. Similar results were found by Harmandaris *et al.* for chains in polydisperse blends. [51] Mondello and co-workers investigated a number of chain lengths between C_{10} and C_{66}. [82, 83] By use of the Green-Kubo (GK) relation they were able to calculate the zero-shear viscosity η_0 for chains up to C_{16} by integrating the zero-shear stress relaxation curves obtained from equilibrium molecular dynamics simulations (EMD). They were not able to determine the viscosity by this method for chains longer than C_{16}. The reason for this, as was already shown by Cui and co-workers for the case of liquid decane, [22] is that the integration time must be at least as long as the longest relaxation time, which increases enormously with chain length. A more direct method to estimate the viscosity is provided by the nonequilibrium molecular dynamics (NEMD) technique in which a shear flow is imposed on the system. By measuring relevant components of the stress tensor, the viscosity may be determined as a function of shear rate. Using this method, Mondello *et al.* showed that η_0 of medium long chains may be estimated from the longest relaxation time measured in EMD simulations by invoking the Rouse model. [82, 83] They found that the estimates are in good agreement with extrapolated NEMD results (within 20%). Moore *et al.* have performed NEMD simulations of a C_{100} melt (close to our C_{120}) at various shear rates. [84] They observed substantial shear thinning at shear rates larger than the inverse rotational diffusion time. Unfortunately, they were unable to observe a Newtonian plateau and experienced problems in extrapolating to zero shear. This is common to NEMD simulations in which large shear rates are needed to obtain significant results.

The above results seem to indicate that many properties of medium long chains may well be described by invoking the Rouse model. This is quite remarkable since the Rouse model assumes that the surrounding chains merely constitute a stochastic background to a chain of harmonically bound beads without excluded volume, and thus is not a very realistic model. It is therefore not at all obvious that a chain which behaves Rouse-like with respect to one property should also behave Rouse-like with respect to another property. It is our aim in this chapter to investigate whether one set of Rouse parameters exists which describes all dynamic properties of a C_{120} melt. In particular we want to include the full zero-shear stress relaxation modulus among the data to be described, and not just the time integrated modulus, i.e. η_0.

After we completed this work, Harmandaris *et al.* published a study which is quite similar

in spirit. [52] Using NEMD simulations, and EMD simulations in the case of a C_{24} melt, they showed that all dynamic processes of C_{24} and C_{78} melts, including shear relaxation processes up to 3 ns, may well be described by the Rouse model. In this chapter we will supply additional evidence, and show that also a C_{120} melt may be described by the Rouse model, at least for processes lasting up to 1 ns. Since all our calculations will be based on EMD simulations, the linear response regime will be guaranteed.

This chapter is organized as follows. In Sec. 3.2 we summarize the simulation model and the methodology used to obtain a well-equilibrated melt. The method of calculation of the various correlation functions and transport properties is summarized in Sec. 3.3. The results are presented and discussed in Sec. 3.4. We summarize our conclusions in Sec. 3.5.

3.2 Simulation model and methodology

MD simulations were performed on four independent boxes of amorphous PE using the GROMOS package. [9] Each box consisted of 12 chains of 120 monomer units [-CH_2-], a system small enough to make calculations computationally feasible, yet large enough to avoid significant interactions of a chain with its periodic images. Moreover, the CH_2 and CH_3 groups are modeled as united atoms (UA) in order to reduce the number of atoms in the actual simulation. Studies by Paul and co-workers have shown the ability of UA models to yield the same dynamic results as more expensive explicit atom models. [100, 102] The simulated systems were all subject to cubic periodic boundary conditions. Bond vibrations and bond angle vibrations were treated by harmonic potentials

$$V(b) = \frac{1}{2} k_b \left(b - b_0\right)^2 \tag{3.1}$$

for all bonds, and

$$V(\theta) = \frac{1}{2} k_\theta \left(\theta - \theta_0\right)^2 \tag{3.2}$$

for all bond angles, where b_0 and θ_0 are the equilibrium bond length and angle. The force constants for bond and bond angle vibrations are k_b and k_θ, respectively. The dihedral rotations were described with the rotational potential of Ryckaert and Bellemans, [119]

$$V(\varphi) = \sum_{n=0}^{5} c_n \cos^n(\varphi). \tag{3.3}$$

The intermolecular interactions and the interactions between atoms separated by four or more atoms in the same molecule were described by Lennard-Jones potentials

$$V(r) = 4\varepsilon \left[(\sigma/r)^{12} - (\sigma/r)^6 \right]. \tag{3.4}$$

Parameters are listed in Table 3.1. We used a 1.15 nm cutoff for the Lennard-Jones interactions. The equations of motion were solved using the leap-frog algorithm with a conservative time step of 1 fs. Simulations of the NVT ensemble were performed using a weak coupling

Parameter	Value	Units
k_b (bond)	3.3475	10^5 kJ mol^{-1} nm^{-2}
b_0	0.153	nm
k_θ (bending)	519.6	kJ mol^{-1} rad^{-2}
θ_0	114.0	deg.
c_0 (torsion)	9.2789	kJ mol^{-1}
c_1	12.156	
c_2	-13.120	
c_3	-3.0597	
c_4	26.24	
c_5	-31.495	
ε (CH_2)	0.3908	kJ mol^{-1}
ε (CH_3)	0.9480	
σ (CH_2)	0.3930	nm
σ (CH_3)	0.3930	

Table 3.1: Force field parameters. Torsion parameters taken from Ryckaert and Bellemans. [119] Other parameters taken from Smit, Karaborni, and Siepmann. [128]

scheme to a temperature bath of 450 K with coupling constant of 0.1 ps. [10] The density was set to 0.7614 g/cm^3, close to the normal pressure density at 450 K. [106] The average pressure from the simulation was $p \approx 54$ atm.

For a correct sampling of the pressure tensor autocorrelation, it is important to have a fully equilibrated melt in which there is no average stress present. This is far from trivial for complex fluids like polyethylene. A number of ways have been suggested by different authors. Forrest and Suter have time-coarse grained the atomic interactions to improve the sampling efficiency. [45] Tschöp *et al.* suggested a spatial-coarse graining for polycarbonates, after which the chemical details are reintroduced into the coarse grained chains. [137] Quite successful in obtaining a well-equilibrated melt is the end-bridging Monte Carlo algorithm, as suggested by Pant and Theodorou, which however yields polydisperse melts because of the connectivity-altering moves. [51, 99] Van der Vegt *et al.* have investigated the influence of three different ways of generating initial configurations on the solubilities of small molecules in amorphous polymer melts. [138] In one of the methods a dilute system is slowly compressed, during which process only the repulsive parts of the nonbonded Lennard-Jones potentials are taken into account. The configurations in this work have been prepared this way. After reintroduction of the full potential, the melt was equilibrated at the final density for 10 ns. The average stress was measured during several simulations of one nanosecond each and found to be small enough to have no influence on the stress-stress correlation functions described in Sec. 3.4.

The production time was 35 ns, the viscosity measurements were done in a subsequent 10 ns run to ensure maximum relaxed systems.

3.3 Calculation of correlation functions and transport properties

We have measured three time-dependent mean square displacements $g_{\rm at}(t)$, $g_{\rm bl}(t)$, $g_{\rm cm}(t)$, which are defined as follows:

$$g_{\rm at}(t) = \frac{1}{n}\sum_{i=1}^{n}\left\langle [\mathbf{r}_i(t)-\mathbf{r}_i(0)]^2\right\rangle, \tag{3.5}$$

$$g_{\rm bl}(t) = \frac{1}{n/20}\sum_{j=1}^{n/20}\left\langle \left[\mathbf{r}_j^{\rm bl}(t)-\mathbf{r}_j^{\rm bl}(0)\right]^2\right\rangle, \tag{3.6}$$

$$g_{\rm cm}(t) = \left\langle [\mathbf{r}^{\rm cm}(t)-\mathbf{r}^{\rm cm}(0)]^2\right\rangle, \tag{3.7}$$

where $\mathbf{r}_i$ is the position of the ith carbon atom, $\mathbf{r}_j^{\rm bl}$ is the position of the jth "blob," as we will explain next, and $\mathbf{r}^{\rm cm}$ is the center of mass of the chain. In *Chapter 4* we will present mean square displacement results of a coarse grained model of polyethylene, in which the smallest particles are blobs. Each blob is supposed to mimic the behavior of the center of mass of a collection of 20 successive carbon atoms. To validate this coarse grained model, we measure $g_{\rm bl}$ in the current atomic simulation. The diffusion coefficient is calculated from the mean square displacement by

$$D = \lim_{t\to\infty}\frac{g_{\rm cm}(t)}{6t}. \tag{3.8}$$

The coherent dynamic structure factor of a single chain can be measured by means of neutron spin echo spectroscopy. It is defined as

$$S(q,t) = \frac{1}{n}\sum_{i=1}^{n}\sum_{j=1}^{n}\left\langle \exp\left\{ i\mathbf{q}\cdot\left[\mathbf{r}_i(t)-\mathbf{r}_j(0)\right]\right\}\right\rangle, \tag{3.9}$$

where the two summations run over the (united) atoms of one chain.

The atomic (molecular) stress tensor is defined as

$$\boldsymbol{\sigma} = -\frac{1}{V}\left[\sum_{i=1}^{n} m_i\mathbf{v}_i\mathbf{v}_i + \sum_{i>j}\left(\mathbf{r}_i-\mathbf{r}_j\right)\mathbf{F}_{ij}\right], \tag{3.10}$$

where $\mathbf{v}$ is the atomic (molecular) velocity, $\mathbf{r}$ is the atomic (molecular center of mass) position, and $\mathbf{F}_{ij}$ is the force exerted on atom (molecular center of mass) i by atom (molecule) j. The molecular stress tensor contains an anti-symmetric part, because the total force on a molecule exerted by another molecule is not directed along the line of centers of the molecules, producing a torque on the molecules. [92] For calculating the shear viscosity we need the symmetric

part. Daivis and Evans [23] have shown that the zero shear relaxation modulus is related to the symmetrized traceless part **P** of the stress tensor $\boldsymbol{\sigma}$ by

$$G(t) = \frac{V}{10k_BT} \langle \mathbf{P}(t) : \mathbf{P}(0) \rangle . \tag{3.11}$$

The double contraction means in practice that we average over five independent contributions: P_{xy}, P_{xz}, P_{yz}, $\frac{1}{2}(P_{xx} - P_{yy})$, and $\frac{1}{2}(P_{xx} - P_{zz})$ [we get no additional information from $\frac{1}{2}(P_{yy} - P_{zz})$ since **P** is traceless]. The viscosity is given by the infinite time integral of Eq. (3.11). It has been proved by Allen that viscosities calculated from the atomic and molecular approach are equal. [4] Several simulation studies have shown this to be correct. [22, 82] The difference between the viscosity calculated from the molecular tensor and that from the atomic tensor is found to converge to zero much faster than the longest relaxation time of the molecule. This was confirmed in test runs of our system in which we calculated the shear relaxation modulus from both atomic and molecular stress tensors. However, the behavior of the atomic stress autocorrelation is dominated by the strong oscillatory behavior due to the bond stretching vibrations. Thus, for practical purposes, the molecular tensor formalism is more efficient since it allows the use of a relatively large sampling time interval. We have chosen to measure the molecular pressure tensor every 50 fs. To make certain that we perform an accurate integration of the data, we have also calculated the integral with a 5 fs interval for the shorter time scales. The two integrals were found to be identical.

3.4 Results and discussion

In this section we will analyze the large time dynamics of the PE melt. We will explore the Rouse model and its boundaries of applicability to real PE chains.

3.4.1 Mean square displacement

In Fig. 3.1 we present the time-dependent mean square displacement results from the simulations. The results have been averaged over four independent boxes, allowing us to estimate the errors. The shortest time behavior ($t \leq 1$ ps) is ballistic and not shown in the graph. After the ballistic regime, we observe two power law regimes $g(t) \propto t^x$ for g_{at} and g_{bl}. The atomic diffusion results reveal an exponent $x = 0.65$ up to 200 ps, after which an exponent $x = 0.57$ sets in. The initial value compares well with the results of molecular dynamics simulations of $C_{100}H_{202}$ melts by Paul, Smith and Yoon. [100] They measured the mean square displacements of central and end monomers of each chain separately, which on average yields an exponent of $x = 0.67$. For the blob diffusion results we measure an exponent $x = 0.75$ up to 400 ps, after which an exponent $x = 0.65$ sets in. These higher exponents should be expected, since in going to the blob level we average over some of the atomic movement (in the ultimate limit of a chain being represented by one blob, g_{bl} and g_{cm} would be the same). For both atomic and blob mean square displacements we expect free diffusion at larger time scales. The chain center of mass diffusion g_{cm} does indeed display free diffusive behavior after $t = 4$ ns. Before this time subdiffusive behavior ($x = 0.80$) is observed. The subdiffusive

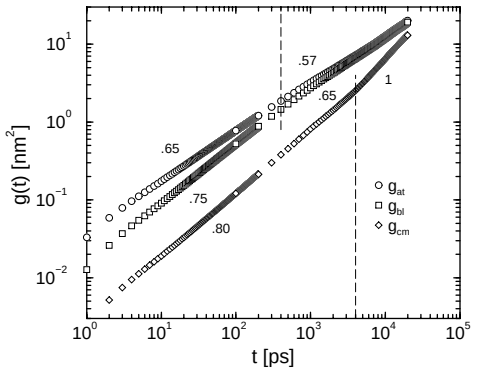

Figure 3.1: Mean square displacement of the atom (circles), blob (squares) and center of mass (diamonds) positions as a function of time on a double logarithmic scale. The numbers are the estimated power-law exponents x. The dashed lines indicate the transition times between the different power-law regimes.

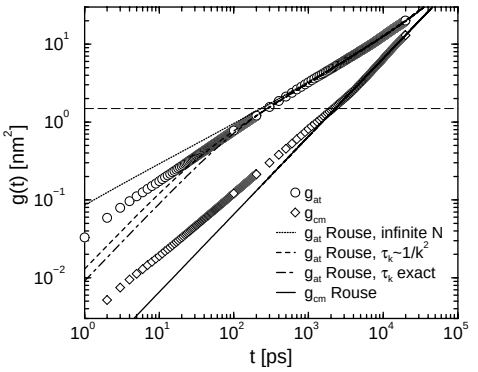

Figure 3.2: Mean square displacement of the atom (circles) and center of mass (diamonds) positions. The lines are fits to the Rouse model. The dotted line is for an infinite Rouse chain ($N \to \infty$, τ_1 = 6.5 ns), the dashed line for a finite Rouse chain, with the approximation $\tau_k \propto 1/k^2$ (N = 20, τ_1 = 7.0 ns), and the dot-dashed line for a finite Rouse chain with the exact expression for τ_k (N = 14, τ_1 = 6.5 ns), see Eq. (2.22). The statistical segment length $b^2 = 1.49$ nm is indicated by the long dashed horizontal line. Above this line the Rouse predictions are correct.

exponent compares well to both simulation [100] and neutron spin echo spectroscopy [101] results of a $C_{100}H_{202}$ melt ($x = 0.83$).

Now we want to investigate how closely the observed mean square displacement results resemble Rouse behavior. In the Rouse model, segmental mean square displacements show a subdiffusive regime $g_{\rm at}(t) \propto t^{1/2}$ before crossing over to free diffusion. However, this is only true in the limit of N going to infinity. For finite N there is a transition from an early t^1 regime to a sublinear exponent. This transition occurs at the fastest relaxation time in the Rouse chain, which is τ_{N-1} in Eq. (2.22). In Fig. 3.2 we present the result of fitting the three independent parameters of the Rouse model to the observed atomic and chain diffusion data. The three fit parameters are the diffusion coefficient of the chain D, the Rouse time τ_1, and the number of statistical segments N. In the Rouse model, the center of mass of a chain will always diffuse freely, so a fit to the long time behavior of $g_{\rm cm}$ will uniquely determine D. We find a self-diffusion coefficient of $D = (1.09 \pm 0.09) \times 10^{-6}$ cm^2/s, which is in excellent agreement with the observations of Harmandaris and co-workers who found $D = (1.16 \pm 0.2) \times 10^{-6}$ cm^2/s for a C_{117} chain, and $D = (1.0 \pm 0.1) \times 10^{-6}$ cm^2/s for a C_{128} chain at the same temperature and approximately the same density as our simulation. [51]

Pearson *et al.* [106] have measured self-diffusion coefficients by means of field gradient NMR at 450 K experimentally for a large range of molecular weights, although not at the weight of C_{120} chains. An interpolation of their data yields $D_{\mathrm{exp}} \approx 0.67 \times 10^{-6}$ cm^2/s. The discrepancy is not specific to our united atom model. It is well known that diffusion coefficients from MD simulations tend to overestimate the self-diffusion coefficient, especially at high packing fractions. For a systematic study, the reader is referred to the work of Dysthe and co-workers. [31]

From the diffusion coefficient, we can calculate the segmental friction coefficient ζ. However, ζ still depends on the size of the statistical segment. One can easily show this by writing $\zeta = m\xi$, in which m is the mass of the statistical segment, and ξ is the friction "frequency." If we apply this to Eq. (2.20) we find $D = k_B T/(Nm\xi) = RT/(M_w\xi)$, where R is the universal gas constant and M_w is the molecular weight of the chain. Since within the Rouse model the diffusion coefficient of a given chain must not depend on how many segments we choose to divide it in, ξ must be a property of the chain *independent* of our choice of statistical segment length (but still dependent on other factors, such as temperature). We find $\xi = (19.0 \pm 1.6)$ ps^{-1} for the friction frequency. Harmandaris et al. have calculated the friction coefficient of a CH_2 monomer, which is then shown to be independent of the chain length for chains longer than C_{70}. If we calculate the monomeric friction coefficient we find $\zeta = (4.45 \pm 0.37) \times 10^{-13}$ kg/s, in accordance with their results. [51] However, we remind the reader that the number of segments N in the Rouse model should not be set equal to the number of monomers n in the chain, since one monomer does not make a statistical segment, as we will show later on.

Now we consider the atomic mean square displacements, shown in Fig. 3.2. The value of the sublinear exponent in the atomic mean square displacement depends on both the Rouse time τ_1 and the number of statistical segments N. It was found that N has little influence on the second regime of $g_{\mathrm{at}}(t)$ (for not too small N), so we used the regime from 1 to 20 ns to fit the Rouse time. Finally we varied N to obtain the best fit for times below 1 ns. Applying the exact expression for the relaxation time spectrum, Eq. (2.22), we obtained $\tau_1 = (6.5 \pm 0.3)$ ns and $N = 14 \pm 2$. Applying the approximation $\tau_k \propto 1/k^2$ [Eq. (2.24)], we obtained slightly different parameters, $\tau_1 = (7.0 \pm 0.3)$ ns and $N = 20 \pm 3$. Since N is found to be relatively low, this approximation fails at short times, so the first set of parameters is the more correct one. For comparison we have also included the results of a fit with an infinite Rouse chain ($N \to \infty$), in which case $\tau_1 = 6.5$ ns and a $t^{1/2}$ regime occurs. Clearly, the deviation of the measured exponent $x = 0.57$ from the ideal value of 0.5 is due to the small number of statistical segments. From this study we can conclude that a statistical segment of polyethylene at 450 K is comprised of about 120/14 = 8.6 monomers. The size of this segment, b^2, is given by the combination of Eqs. (2.20) and (2.22),

$$b^2 = 12ND\tau_1 \sin^2\left(\frac{\pi}{2N}\right) \tag{3.12}$$

which yields $b^2 = 1.49$ nm^2. (If we would have used $N = 20$ and $\tau_1 = 7.0$ ns we would have found $b^2 = 1.13$ nm^2 for a segment comprised of 6 monomers.) It is apparent from Fig. 3.2 that it is this length (rather than a characteristic time) which determines when Rouse theory sets in. When both g_{at} and g_{cm} have moved more than b^2, the Rouse theory predictions co-

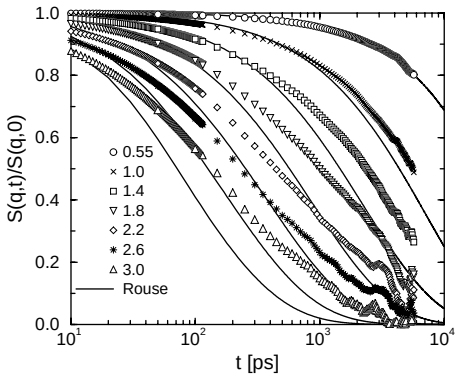

Figure 3.3: Dynamic structure factor for seven different magnitudes of the wave vector. The symbols are the simulation data. The full curves are the Rouse fits, Eq. (2.37).

incide with the molecular dynamics results. Consequently, the atomic results coincide much earlier than the chain center of mass results (after 0.4 and 4 ns respectively). Below these limits the Rouse model fails because of the neglect of molecular stiffness, as was pointed out by Harnau and co-workers. [54, 55] Other factors may be important as well. For instance, Richter *et al.* suggested that an extra (internal) friction term may be necessary to explain experimental results. [112] This has however been questioned by Harnau *et al.* [53, 113] In this chapter we will not elaborate on this matter. Whenever 'chain stiffness' is mentioned, the possibility of these other effects should be kept in mind as well.

3.4.2 Dynamic structure factor

The dynamic structure factor is experimentally the best accessible quantity to check the validity of the Rouse model. The neutron spin echo spectroscopy experiments described in Ref. [101] already formed a critical test of the Rouse model, and our conclusions correspond with those of the authors. In Fig. 3.3 we present the normalized dynamic structure factors for seven wave vectors ranging from $q = 0.55$ nm^{-1} to $q = 3.0$ nm^{-1} together with the Rouse predictions, Eq. (2.37).

The fit parameters were determined as follows: for $q \ll 2\pi/R_e$, where R_e is the end-to-end vector, the wave vector is so small that it only probes the overall diffusion of the chain. Thus we have used the first wave vector to determine D, independent of the mean square displacement measurements. We obtained $D = (1.15 \pm 0.08) \times 10^{-6}$ cm^2/s, which is in prefect agreement with the previous results. The Rouse time τ_1 and the number of segments N are of importance for the larger wave vectors. A combined fit yields $\tau_1 = (6.5 \pm 0.5)$ ns and $N = 15 \pm 5$. The large uncertainty in N stems from the fact that the smallest wave vectors are relatively insensitive to N, while the larger wave vectors cannot be described correctly by any N whatsoever. For $q \geq 1.4$ nm^{-1} the Rouse curves decay too fast compared with the simulation data, leading to underestimated structure factors for large times (but an overestimate for times lower than ~ 50 ps). This value of q corresponds to a half-wavelength of $\pi/q = 2.24$ nm, which is in the same order of magnitude as the statistical segment length b. Again, we conclude that the Rouse model is capable of correctly describing the behavior

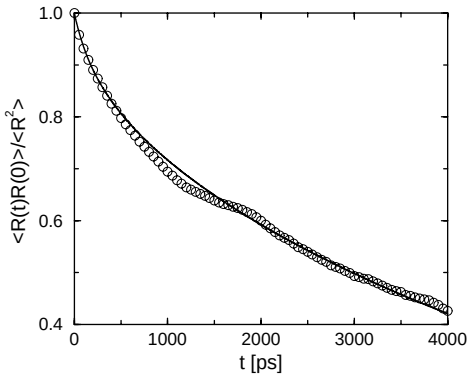

Figure 3.4: Orientational autocorrelation function of the end-to-end vector. The circles are the simulation data, the full curve is the Rouse fit, Eq. (2.30).

of a polymer chain, but only on length scales larger than the statistical segment length. Below this length scale the stiffness of the chain becomes important, leading to a slower decay of the dynamic structure factor.

3.4.3 End-to-end vector

The end-to-end vector measures the position of the last segment with respect to the first segment of a chain, $\mathbf{R}_e = \mathbf{r}_N - \mathbf{r}_1$. For a Gaussian chain, such as the Rouse chain, the average squared magnitude of the end-to-end vector is given by Eq. (2.2), which yields 20.9 nm^2 if we use $N = 14$ and $b^2 = 1.49$ nm^2, and 22.6 nm^2 if we use $N = 20$ and $b^2 = 1.13$ nm^2. In the simulations we measured $\langle R_e^2 \rangle = (23.8 \pm 4.0)$ nm^2, which is in rather good agreement with the Rouse prediction if we take into account that the end-to-end vector is measured from the first to the 120th carbon atom in the atomic case, and between the centers of the first and last statistical segments in case of a Rouse chain.

The dynamic quantity we are interested in is the orientational autocorrelation function for the end-to-end vector $\langle \mathbf{R}_e(t) \cdot \mathbf{R}_e(0) \rangle / \langle R_e^2 \rangle$. It measures the rate at which the chain becomes uncorrelated with itself by means of rotational diffusion. Fig. 3.4 presents the decay of the normalized end-to-end vector autocorrelation function from the simulations including a fit with the Rouse prediction of Eq. (2.30). One can vary both the number of statistical segments N and the Rouse time τ_1 to obtain a best fit. We have used the limiting single exponential behavior to determine the Rouse time and adjusted N to get the best fit for short time behavior. This procedure yields $\tau_1 = (6.0 \pm 0.5)$ ns and $N = 13 \pm 3$, in agreement with the fit parameters obtained from the mean square displacement data. The fit can be made fairly accurate because the end-to-end vector is a property of the entire chain and much larger than the statistical segment length b.

3.4.4 Shear relaxation modulus and viscosity

The shear relaxation modulus $G(t)$ is calculated from the autocorrelation of the stress tensor, Eq. (3.11). As explained in Sec. 3.3 the stress tensor can be determined from an atomic or a

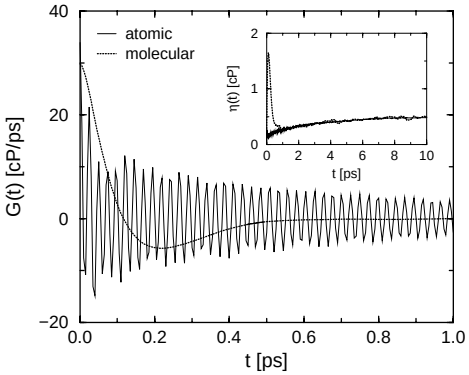

Figure 3.5: Comparison of the short-time behavior of the shear relaxation modulus determined from the atomic (line) and molecular (dotted line) stress tensor. The inset shows the integral up to time t. After 1 ps the atomic and molecular integrals become identical.

molecular point of view. In Fig. 3.5 both results are presented for a sampling interval of 5 fs. The atomic shear relaxation modulus shows strong oscillatory behavior due to fast vibrations of the bonds in the chain, while the molecular shear relaxation modulus is a much smoother function, with a minimum at 0.21 ps. The inset of Fig. 3.5 shows the integrals up to time t,

$$\eta(t) = \int_0^t G(t)\,dt, \tag{3.13}$$

for both shear relaxation moduli. [The shear relaxation modulus itself is given by the slope of $\eta(t)$.] It is seen that the atomic and molecular integrals become identical for t larger than 1 ps, in accordance with the findings of other authors. [22, 82] The limit of Eq. (3.13) for t going to infinity gives the viscosity of the polyethylene melt. The computational demands for these calculations are very large because the stress tensor is a collective property of the system, yielding only one value per time frame (in practice we can use five, as explained in Sec. 3.3). This means that very long runs are needed to obtain enough statistical accuracy. Because of the larger possible integration time step (50 fs), the molecular stress tensor was used to determine $\eta(t)$ for large time scales.

The rate of convergence of the integral of the shear relaxation modulus depends on the relaxation time of the chain. In principle one should integrate up to, say, $2\tau_1$ to reach the plateau value of the integral. This is however quite impossible, so instead of varying the parameters of the Rouse model (N and τ_1) to fit the entire curve, we will use the parameters found before to compare the Rouse predicted integral with the measured integral $\eta(t)$ up to $t = 1$ ns. The measured result, shown in Fig. 3.6, is an average of the results of the four independent simulation boxes, each yielding five independent contributions. We can make a conservative estimate of the error in the average value at each time by treating these 20 contributions at each time as independent data. This way we find estimated errors of 6% at $t = 0.1$ ns up to 17% at $t = 1$ ns. Because the statistical uncertainties are relatively large, we must be careful with our conclusions.

Before testing the Rouse predictions, let us compare our EMD result with the NEMD results of Moore *et al.* on C_{100} chains. [85] They measured transient shear stresses by applying sudden constant shear rates to equilibrated systems. At the high shear rates applied by these authors, the stresses exhibit temporary overshoots above the steady-state values, in

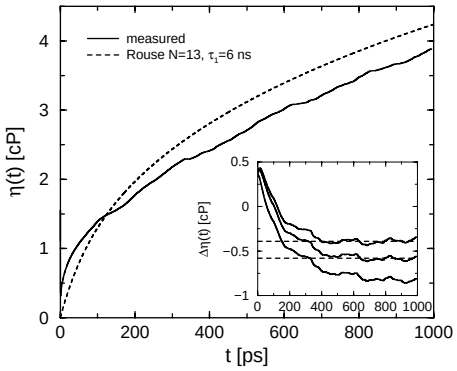

Figure 3.6: The long time behavior of the integral of the shear relaxation modulus determined from the molecular stress tensor (line). The dashed line is the Rouse prediction, Eq. (2.60), for $N = 13$ and $\tau_1 = 6.0$ ns. The inset shows the difference $\Delta\eta(t)$ [see Eq. (3.14)] between measured and Rouse integrals for different sets of parameters. From top to bottom: ($N = 13, \tau_1 = 6.0$ ns), ($N = 14, \tau_1 = 6.5$ ns), and ($N = 20, \tau_1 = 7.0$ ns). For the first two sets, the difference becomes constant after approximately 0.4 ns (dashed lines). From this graph we are unable to determine which of the two sets of parameters provides the best fit.

partial agreement with the Doi-Edwards theory of entangled systems. [30] This seems to indicate that under some conditions aspects of the reptation picture may be applicable, even for chains which are not supposed to be entangled. Notice that our Fig. 3.6 represents the zero-shear limit of their Fig. 1. In this sense the results of Moore *et al.* and our results are complementary.

Let us now compare the results with the Rouse integral, Eq. (2.60). The density of Rouse chains is set equal to the density of chains in the MD system. The result is shown in Fig. 3.6 for $N = 13$ and $\tau_1 = 6.0$ ns. It is immediately apparent that the Rouse curve differs from the measured curve. This should be expected because the initial relaxation modulus $G(t)$ of the polyethylene system does not behave Rouse-like at all, as can be seen in Fig. 3.5. However, the Rouse curve is observed to run parallel with the measured curve after approximately 0.4 ns. This means that the zero-shear relaxation modulus $G(t)$ is perfectly described by the Rouse model in this time regime. Note that 0.4 ns is the time at which the atoms have moved on average over one statistical segment length b. That the two curves really are parallel is best revealed by plotting the difference against time,

$$\Delta\eta(t) = \eta(t) - \eta^R(t) \tag{3.14}$$

and observing that $\Delta\eta$ becomes constant after a certain time. The inset of Fig. 3.6 shows the difference for the three sets of Rouse parameters obtained so far, $N = 13$ and $\tau_1 = 6.0$ ns, $N = 14$ and $\tau_1 = 6.5$ ns, and $N = 20$ and $\tau_1 = 7.0$ ns. Only the first two sets give a constant $\Delta\eta$ within the measured time span, with a limiting value of $\Delta\eta_\infty = -0.39$ cP for $N = 13$ and $\tau_1 = 6.0$ ns, and $\Delta\eta_\infty = -0.58$ cP for $N = 14$ and $\tau_1 = 6.5$ ns. Because of the uncertainty in the data, we are unable to determine which of the two sets of Rouse parameters provides the best fit to the data. In the last set, the Rouse parameters are clearly over-estimated, resulting in an ever decreasing difference curve. If the zero-shear relaxation modulus can perfectly be described by the Rouse model after 1 ns as well, we may estimate the viscosity as

$$\eta = \eta^R + \Delta\eta_\infty \tag{3.15}$$

where η^R is the limit of Eq. (2.60) for t to infinity (8.25 and 8.96 cP respectively for the first two sets). This yields an estimate for the viscosity of respectively $\eta = 7.86$ cP (first set) and $\eta = 8.38$ cP (second set) for our melt of $C_{120}H_{242}$ chains at 450 K. Pearson *et al.* [106] have measured the viscosity of *n*-alkanes and PE as a function of molecular weight at 450 K, although not at the weight of C_{120} chains. An interpolation of their data yields $\eta_{\text{exp}} = 13.5$ cP. As with other MD simulations at high packing fractions the viscosity is somewhat underestimated, [31] in our case by 38% (for the second set). The important result is that we have shown that the shear relaxation modulus $G(t)$ behaves exactly like that of a Rouse chain on time scales between approximately 0.4 and 1.0 ns. A correction $\Delta\eta_\infty$ accounts for the fact that initially a real chain does not behave Rouse-like, but it is relatively small for long chains, in our case only 5 to 6%. Therefore the much applied practice to estimate the viscosity from the longest relaxation time τ_1, Eq. (2.61), seems to be justified. We would however like to place a word of caution: one may not disregard the possibility that $G(t)$ does not behave Rouse-like at times larger than 1 ns. At larger times, contributions from the interactions between different chains may be important, with relaxation times well exceeding the longest intrachain (configurational) relaxation times. A first indication that such processes are important may be found in the transient stress calculations of Moore *et al.* which suggest that entanglements may be important even in the case of C_{100} chains. [85] Additional evidence for this hypothesis will be presented in *Chapter 4* in which we will coarse grain the melt investigated in this chapter in order to reach larger time regimes. We will show that on the largest time scales the stress in the system relaxes more slowly than in the case of a Rouse chain, leading to an increased viscosity as compared to the Rouse model.

3.5 Conclusions

We have performed MD simulations of a polyethylene melt to investigate the validity of the Rouse model predictions for a comphensive set of correlation functions: the mean square displacement, dynamic structure factor, end-to-end vector autocorrelation and zero-shear relaxation modulus. It was found that the chains do indeed behave like Rouse theory predicts, but only on length scales larger than the segment length b. Further, it was found that the different quantities consistently yielded the same set of fit parameters N, D, and τ_1. The deviations between the Rouse model calculations and the experimental and simulation data of short time mean square displacements and large q dynamic structure factors were shown by Harnau and co-workers to be due to the neglect of molecular stiffness [54,55] which becomes prominent on length scales smaller than the statistical segment length. Other effects, such as an extra (internal) friction, may also be of importance on this length scale, as was pointed out by Richter and co-workers. [53, 112, 113]

An important part of this work constituted the calculation of the zero-shear relaxation modulus and viscosity of a melt of chains which is supposed to be described by Rouse dynamics. We have found that a Rouse description of the shear relaxation modulus exactly coincides with the simulation results for time scales between 0.4 and 1.0 ns. This allowed us to extrapolate the integral using Rouse theory, yielding a viscosity of 8.38 cP, underestimating the experimental value by 38%. The correction due to initial differences between Rouse and

simulated shear relaxation modulus is shown to be relatively small. We do not rule out the possibility that at times larger than 1 ns intermolecular contributions to the stress relaxation modulus, caused by ”entanglements”, survive, which will substantially enlarge the calculated viscosity.

4 Uncrossability constraints in mesoscopic polymer melt simulations: Non-Rouse behavior of $C_{120}H_{242}$

An important feature of a melt of long polymers is that the bonds of the chains cannot cross each other. This seemingly simple fact has a great impact on the long time dynamics and rheology of the material. In this chapter we will describe an algorithm that explicitly detects and prevents bond crossings in mesoscopic simulations of polymers. The central idea is to view the bonds as slippery elastic bands which can get entangled. The method is applied to a simulation of a coarse-grained melt of $C_{120}H_{242}$, in which each chain is represented by six blobs. The long time dynamics and zero-shear rate rheology are investigated and the relative importance of uncrossability and chain stiffness is established. As a result of the uncrossability of the chains we observe a subdiffusive exponent in the mean square displacement of the chains, a stretching of the exponential decay of the Rouse mode relaxations, an increase of relaxation times associated with large scales, and a slowing down of the relaxation of the dynamic structure factor. These results are in agreement with the results from the microscopic molecular dynamics simulations in Chapter 3. *Finally an increased viscosity as compared to the Rouse model is observed, which is is attributed to slowly decaying interchain stress components.*[*]

4.1 Introduction

Experimentalists and theoriticians are fascinated by the peculiar dynamics of polymer melts. Rheological experiments reveal a non-trivial molecular weight dependence of the viscosity and the same applies to the diffusion coefficient, which can be measured by field gradient NMR or forward recoil spectrometry techniques. [39, 41, 49, 106] Also, neutron spin echo spectroscopy measurements have revealed a broad spectrum of characteristic times which are associated with relaxations at different length scales. [101, 112, 120] The task of theoriticians is to explain these results in terms of the simplest possible models which still embody the essential features of polymers, like for example that they are long and flexible and that their

[*] The work described in this chapter previously appeared in J. Chem. Phys. **115**(6), 2846 (2001). [97]

covalent bonds cannot be cut or cross. The use of such simple models containing only essential features is justified by experimental observations of universal scaling behavior of (linear) polymers of different chemical structure. This suggests that rheological properties and motions of large parts of the chain may not depend on the details of the polymers except for some species-dependent 'effective' parameters, such as friction coefficients, and structural information may only be needed on the scale of groups of monomers. Two of the best-known models in this category are the Rouse model [118] and the reptation model. [30] The former is supposed to describe the dynamics of relatively low-weight linear polymers. It assumes that the surrounding chains merely constitute a stochastic background to a chain of harmonically bound beads. The latter describes the dynamics of very long chains which are forced to move anisotropically inside effective tubes formed by entanglements with surrounding chains. Still, despite the large amount of literature on these models, many problems remain unsolved. In particular, there is no general consensus of the concept of entanglement length [107] and even the necessity to invoke reptation to explain the experimental results is not without debate (see Ref. [73] for a review on this matter).

Despite their simplicity most polymer models require computer simulations to reveal their macroscopic properties. In the successful model applied by Kremer and co-workers, groups of monomers are represented as pure repulsive Lennard-Jones spheres and the bonded spheres are connected by a finitely extensible non-linear elastic potential (FENE). [66, 107] Alternatively, the polymer may be represented as a freely-jointed chain of hard spheres, [131] or as a chain of ellipsoidal particles. [121,142] In these models, the interactions are chosen explicitly such that bond crossings will be energetically unfavorable. Thus, an essential feature of the polymer chain is incorporated automatically. The range of the repulsive forces in these models is necessarily of the order of the maximum separation of two bonded spheres, which sets a severe limit to the number of monomers which may be represented by one sphere. Actually one would like to have this number as large as possible, and start with detailed molecular dynamics simulations of relatively short polymer chains to determine effective interactions and friction parameters of groups of monomers by averaging out uninteresting degrees of freedom. This so-called coarse-graining of polymers may be done in numerous ways. [1, 7, 137] In this chapter a rather simple coarse-graining procedure is adopted, because interactions will become soft in any case and we think that crucial for obtaining the right rheological properties is not so much the interactions, but the fact that chains are not allowed to cross.[1] Therefore we will give full attention to explicitly obeying the uncrossability constraint.

Up to now, explicit uncrossability constraints have only been implemented for Monte Carlo simulations on cubic and diamond lattices. [125, 126, 135] Simulations on lattices are however typically performed at rather low densities in order to obtain a reasonable acceptance rate of the attempted moves. [66] In order to be able to perform mesoscopic simulations at high densities, we have implemented a routine which explicitly detects and prevents bond crossings in a continuum simulation program called TWENTANGLEMENT (Twente University entanglement). [95]

One can think of many ways to implement an uncrossability constraint. Our method is

1 In the extreme case, a polymer chain has been represented as a single soft ellipsoidal particle. In this case, of course, all entanglement effects are neglected which results in unrealistic dynamics. [87]

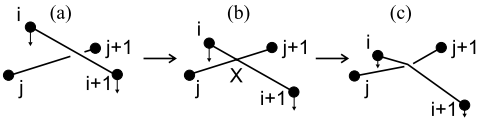

Figure 4.1: The creation of an 'entanglement': (a) two pairs of bonded blobs are closing in on each other. (b) At a certain moment their bonds wil touch. (c) An entanglement is created at the crossing point X, after which the bonds are viewed as slippery elastic bands. The elasticity will slow down the relative speed of the bonds.

based on considering the bonds as elastic bands between the bonded particles. As soon as two of these elastic bands make contact, an 'entanglement' is created which prevents the elastic bands from crossing. This is depicted in Fig. 4.1. To take away any confusion: in the algorithm 'entanglements' are defined as the objects which prevent the crossing of chains. Only a few of these are expected to be entanglements in the usual sense of long-lasting obstacles, slowing down the chain movement. For instance, the $C_{120}H_{242}$ chain is generally considered not to be entangled, yet many 'entanglements' occur in the simulation. For the implementation of the algorithm, the following considerations have been taken into account: (i) the entanglement algorithm should be a simple generalization of the force routine, yet capture the essence of what an entanglement is, i.e. (ii) an entanglement must prevent the crossing of two bonds, (iii) an entanglement should be able to dynamically slide along the backbone of the chain (i.e. not be a permanent crosslink), and (iv) an entanglement should be able to disentangle if the topology of the chain demands so.

The purpose of this chapter is twofold. First, we will explain the assumptions and approximations made for the construction of the entanglement algorithm. Second, the influence of the uncrossability constraint on the dynamic behavior of relatively short coarse-grained polyethylene chains will be investigated. These results will be compared with the microscopic simulations described in *Chapter 3*, with mesoscopic simulations without the uncrossability constraint, and with results from the literature.

This chapter is organized as follows: in Sec. 4.2 we describe the coarse-grained simulation model and give an introduction to the entanglement constraint. Details of the entanglement constraint are given in Sec. 4.3. This section is rather technical, so may be skipped by the reader who is interested in the results only. Sec. 4.4 describes the application of the entanglement constraint to the coarse-grained melt of polyethylene $C_{120}H_{242}$. The method by which the initial box is prepared and the choice of parameters are explained. The results of the simulations are presented and discussed in Sec. 4.5. We summarize the conclusions in Sec. 4.6.

4.2 The simulation model

4.2.1 Coarse-grained interactions

Because the details of a polymer are largely unimportant for its large scale dynamics, the chain will be described in terms of groups of monomers, which we call 'blobs'. The position

$\mathbf{R}$ of each blob is defined as the center of mass position of the λ monomers which together constitute the blob:

$$\mathbf{R} = \frac{1}{M}\sum_{i=1}^{\lambda} m_i \mathbf{r}_i, \tag{4.1}$$

where $\mathbf{r}_i$ is the position and m_i the mass of monomer i, and M is the total mass of the blob. The complementary $3(\lambda-1)$ coordinates per blob of the microscopic system are treated as bath variables, i.e. their effects are taken into account through random forces which perturb the time evolution of the blob positions. A complete separation of time scales is assumed, such that the random force correlations decay much faster than the blob momentum correlations. In this approximation the random force correlations may be represented by delta functions and the equations of motion are of the simplest Langevin type: [1]

$$M\frac{d^2\mathbf{R}_i}{dt^2} = -\nabla_i \chi - \zeta \frac{d\mathbf{R}_i}{dt^2} + \mathbf{F}_i^R. \tag{4.2}$$

where χ is the potential of mean force (PMF) of the blob system, and ζ is the blob friction coefficient. The friction is chosen to be independent of the blob configuration; it is related to the random force $\mathbf{F}_i^R$ through the fluctuation dissipation theorem:

$$\left\langle \mathbf{F}_i^R(t)\cdot\mathbf{F}_j^R(0)\right\rangle = 6kT\zeta\delta_{ij}\delta(t), \tag{4.3}$$

where k is Boltzmann's constant, and T the temperature.

The potential of mean force is defined as

$$\chi(\mathbf{R}^n) = -kT\ln P_n(\mathbf{R}^n). \tag{4.4}$$

Here P_n is the n-blob distribution function which is determined from the microscopic system by averaging over the fast variables. The occurrence of χ in the Langevin equation ensures that the blob distributions in the coarse-grained and microscopic systems will be the same. Unfortunately it is very hard to handle a $3n$-dimensional distribution function, so approximations need to be made. We have made the rather crude assumption that the distribution factorizes into independent non-bonded, bonded, and angular parts according to:

$$P_n(\mathbf{R}^n) = \prod_{i<j} P^{\mathrm{nb}}\left(R_{i,j}\right)\prod_i P^b\left(R_{i,i+1}\right)\prod_i P^\theta(\theta_i). \tag{4.5}$$

Here $\mathbf{R}_{i,j} = \mathbf{R}_i - \mathbf{R}_j$, $R_{i,j} = \left|\mathbf{R}_{i,j}\right|$, and θ_i is the angle between two consecutive bonds, $\cos\theta_i = (\mathbf{R}_{i,i-1}\cdot\mathbf{R}_{i,i+1})/(|\mathbf{R}_{i,i-1}||\mathbf{R}_{i,i+1}|)$. The potential is thus approximated as a sum of non-bonded, bonded and angular energies:

$$\chi(\mathbf{R}^n) = \sum_{i<j}\varphi^{\mathrm{nb}}\left(R_{i,j}\right) + \sum_i \varphi^b\left(R_{i,i+1}\right) + \sum_i \varphi^\theta(\theta_i). \tag{4.6}$$

The first sum is over all non-bonded pairs, the second sum over all bonded blobs and the third sum over all groups of three consecutive blobs. Although in reality the distributions will not be completely independent and indirect correlations between two given blobs via the

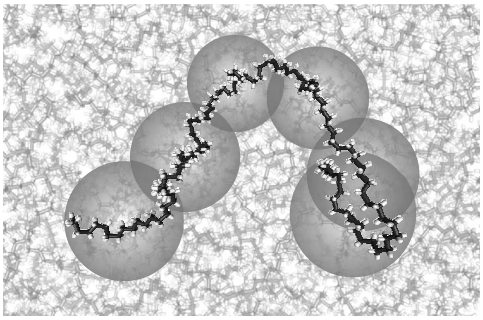

Figure 4.2: A snapshot from the molecular dynamics simulation. In the coarse-grained model, the center of mass of every 20 consecutive monomers will be represented by one blob.

surrounding blobs are important, they have been neglected here since the focus of our work lies with the entanglements.

To determine the distribution functions, molecular dynamics simulations of polyethylene chains of 120 monomers per chain were performed at $T = 450$ K, as decribed in *Chapter 3*. For the number of monomers per blob, λ, the following two considerations were taken into account: (i) λ should be large enough to allow for a significant increase of the integration timestep. For the more monomers together constitute a blob, the larger will be its mass and the softer will be the interactions between the blobs, and consequently the more the timestep can be increased. However, (ii) λ should not be so large that the size of the blobs exceeds the typical diameter of the tube in the reptation picture, or in other words the entanglement length. In that case it would be impossible for the model to display a tube of realistic proportions. A suitable choice seemed to be $\lambda = 20$ CH_2 units, which is still roughly one third of the smallest entanglement length reported in the literature [15]. With this choice of λ each polyethylene chain of 120 monomers was represented by 6 blobs, as shown in Fig. 4.2. The partial PMF's were calculated as minus kT times the logarithm of the measured distributions of blobs and fitted with simple analytical functions, as shown in Fig. 4.3. The non-bonded blob interaction was described by a single repulsive Gaussian pair potential:

$$\varphi^{\mathrm{nb}}(R) = c_0 e^{-\left(R/b_0\right)^2}. \tag{4.7}$$

The bonded blob interaction was split into two parts, a repulsive term φ^{rep}, described by two Gaussians, and an attractive term φ^{att}, described by a single power law:

$$\varphi^{b}(R) = \varphi^{\mathrm{rep}}(R) + \varphi^{\mathrm{att}}(R), \tag{4.8}$$

$$\varphi^{\mathrm{rep}}(R) = c_1 e^{-\left(R/b_1\right)^2} + c_2 e^{-\left(R/b_2\right)^2}, \tag{4.9}$$

$$\varphi^{\mathrm{att}}(R) = c_3 (R)^{\mu}. \tag{4.10}$$

The reason for splitting up the bonded blob interactions will become clear when we apply the uncrossability constraint. The angular potential was described as a function of the cosine of the angle:

$$\varphi^{\theta}(\theta) = c_4 (1 + \cos\theta)^{\nu}. \tag{4.11}$$

The fit parameters c_0 to c_4, b_0 to b_2, μ, and ν are listed in Table 4.1.

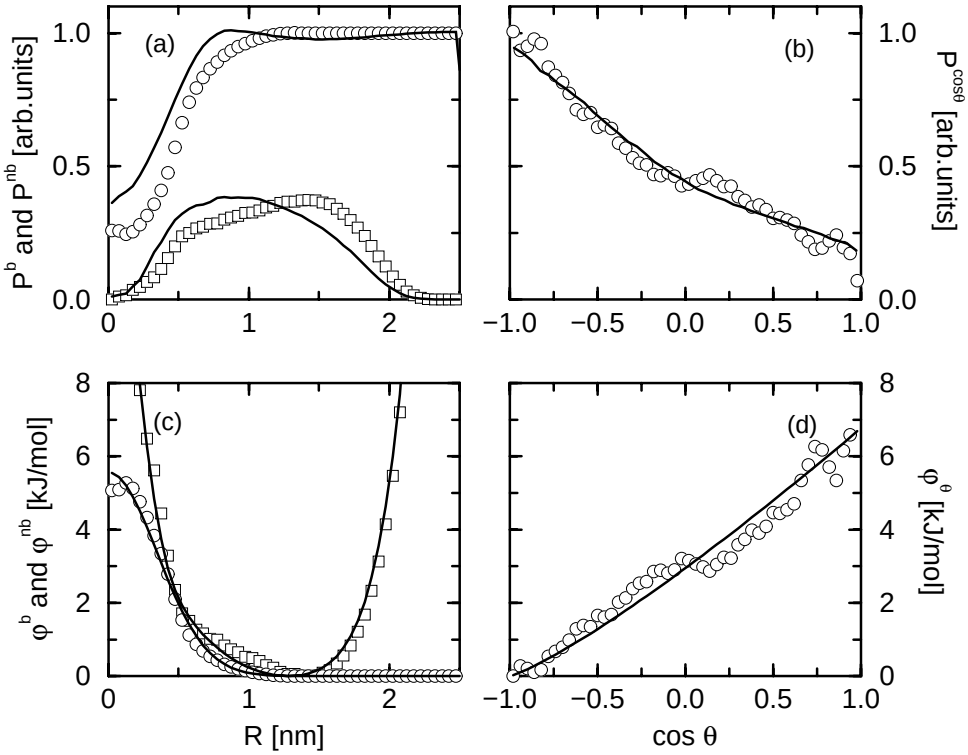

Figure 4.3: Distribution functions and potentials of mean force. Using microscopic simulations, the distribution functions between non-bonded (circles) and bonded (squares) centers of mass of 20 monomer units have been determined [symbols in (a)]. Taking minus kT times the logarithm, partial potentials of mean force are obtained [corresponding symbols in (c)], which are then fitted with simple analytical functions [solid lines in (c), Eqs. (4.7) to (4.10) in the text]. In the same way, the angular potential of mean force has been determined [symbols in (b), symbols and solid line in (d), Eq. (4.11)]. Mesoscopic simulations with these potentials and the uncrossability constraint yield the distributions given by the solid lines in (a) and (b).

Parameter	Value	Units
c_0 (non-bonded)	5.557	kJ mol^{-1}
b_0	0.491	nm
c_1 (bonded)	10.47	kJ mol^{-1}
b_1	0.261	nm
c_2	3.498	kJ mol^{-1}
b_2	0.671	nm
c_3	5.3	10^{-3} kJ mol^{-1} nm$^{-\mu}$
μ	10	
c_4 (angular)	3.011	kJ mol^{-1}
ν	1.2	

Table 4.1: Parameters for the potentials of mean force, obtained from fits of the distribution functions, as explained in the text.

4.2.2 Entanglements

An important consequence of averaging out the bath variables is that the resulting bonded and non-bonded interactions become softer and broaden their range. A comparison with $kT = 3.74$ kJ/mol shows that it becomes likely that two bonds will cross. This is an unphysical process, which will make the model lose all its dynamic properties characteristic for polymer melts. For this reason we have developed an entanglement algorithm, which explicitly detects and prevents bond crossings, and implemented it in a program called TWENTANGLEMENT. [95] The detection of crossings between bonds is achieved by means of a simple geometric argument, details of which will be given in the next section. Once an imminent bond crossing is detected, an entanglement point $\mathbf{X}$ is defined at the crossing site, as in Fig. 4.1(b). As the blobs continue to move, the entanglement point $\mathbf{X}$ shifts, such that it will push both bonds back to their respective sides. This is accomplished by changing the attractive potential φ^{att} between bonded blobs by replacing the blob distance $R_{i,i+1}$ by the *path length* $L_{i,i+1}$ from one blob i to the next *via* the entanglement:

$$L_{i,i+1} = \left|\mathbf{R}_i - \mathbf{X}\right| + \left|\mathbf{X} - \mathbf{R}_{i+1}\right|, \tag{4.12}$$

$$\varphi^{\text{att}}\left(L_{i,i+1}\right) = c_3\left(L_{i,i+1}\right)^{\mu}. \tag{4.13}$$

The entanglement position $\mathbf{X}$ is fixed by requiring that the total attractive potential energy of the entangled bonds $\varphi^{\text{att}}\left(L_{i,i+1}\right) + \varphi^{\text{att}}\left(L_{j,j+1}\right)$ is at its minimum. This is equivalent to requiring equilibrium of forces at the entanglement. In a sense, the original bonds are replaced by slippery elastic bands which go via the entanglements. The finite extensibility of the bands prevents entangled chains from crossing each other. The expression for the path length that is given here is only valid in case of just one entanglement between two pairs

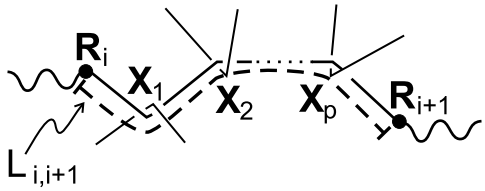

Figure 4.4: Definition of the pathlength $L_{i,i+1}$ between bonded blobs at $\mathbf{R}_i$ and $\mathbf{R}_{i+1}$, Eq. (4.14).

of bonded blobs. The algorithm allows for any number of entanglements between pairs of bonded blobs. To this end the path length concept has been trivially modified. A detailed description of this and other aspects of the entanglement algorithm will be given in the next section.

The replacement of blob distances by path lengths in the bonded part of the potential energy of course changes the structural properties of the model. As shown in Fig. 4.3 however, the mesoscopic distribution functions obtained by this method are hardly different from the ones obtained from the microscopic simulation.

4.3 Detailed description of the entanglement algorithm

4.3.1 Overview

The entanglement algorithm described below can be placed in the force routine of any standard molecular or stochastic dynamics program. A typical update in such a program consists of evaluating the forces that act on the particles, using these to calculate the accelerations of the particles and subsequently updating the particle velocities and positions. The entanglement algorithm in the force routine consists of the following three parts:
1. Given the new blob positions and the order of blobs and entanglements in the chains, move the entanglements to their new positions and calculate the forces that act on the blobs.
2. Detect new entanglements and disentanglements caused by the movements of the blobs and the entanglements.
3. If possible, let entanglements slip across blobs or each other (non-trivial moves).
The details of each of these parts will be described in the following subsections.

4.3.2 Moving entanglements

Suppose entanglements already exist. In the mesoscopic model, the entanglements have no volume and are fully characterized by their positions $\mathbf{X}_k$. As was already mentioned in the previous section, the attractive potential φ^{att} is redefined to be a function of the path length $L_{i,i+1}$. In case the bond runs from blob i, via p consecutive entanglements, to blob $i+1$ (see Fig. 4.4) the path length is defined as:

$$L_{i,i+1} = \left|\mathbf{R}_i - \mathbf{X}_1\right| + \left|\mathbf{X}_1 - \mathbf{X}_2\right| + \ldots + \left|\mathbf{X}_p - \mathbf{R}_{i+1}\right|. \tag{4.14}$$

Since each blob represents a large collection of monomer units, the heavy backbone of the mesoscopic chain will in general move very sluggishly. This is in contrast to an entanglement,

which at the atomic level includes only a few monomer units. Consequently, the timescale with which the entanglement position adjusts itself is much shorter than the timescale with which the polymer backbone is moving. Effectively, on the coarse grained time scale, there will be an equilibrium of forces at the entanglements. Such an equilibrium of forces in a system with n blobs and p entanglements is achieved by the following minimization:

$$\Phi^{\mathrm{att}}(\mathbf{R}^n) = \min_{\mathbf{X}^p} \sum_i \varphi^{\mathrm{att}}\left(L_{i,i+1}(\mathbf{R}^n, \mathbf{X}^p)\right), \tag{4.15}$$

i.e. the entanglement positions are determined by the requirement that the total attractive energy be at its minimum (the blobs are kept at their respective positions). This minimum energy is the contribution Φ^{att} of the attractive part to the total potential energy Φ of the system. The other contributions, Eqs. (4.7), (4.9), and (4.11), are calculated in the usual way from the blob positions, and together constitute the remainder Φ^r of the potential energy, i.e. $\Phi = \Phi^{\mathrm{att}} + \Phi^r$. At each time step the dynamics program will need the forces on the blobs in order to update their velocities and positions. The minimization in Eq. (4.15) does not complicate the evaluation of the force on a blob i since $\left(\partial\Phi^{\mathrm{att}}/\partial\mathbf{X}_k\right) = 0$ at the minimum:

$$\begin{aligned} \mathbf{F}_i &= -\frac{\partial\Phi^{\mathrm{att}}}{\partial\mathbf{R}_i} - \sum_k \left(\frac{\partial\Phi^{\mathrm{att}}}{\partial\mathbf{X}_k}\right)\cdot\left(\frac{\partial\mathbf{X}_k}{\partial\mathbf{R}_i}\right) - \frac{\partial\Phi^r}{\partial\mathbf{R}_i} \\ &= -\frac{\partial}{\partial\mathbf{R}_i}\left(\Phi^{\mathrm{att}} + \Phi^r\right). \end{aligned} \tag{4.16}$$

From the definition of the path length, Eq. (4.14), it is clear that the attractive force $\mathbf{f}_i^{\mathrm{att}}$ on blob i due to the elastic band between blobs i and $i+1$ is always directed along $\mathbf{R}_i - \mathbf{X}_1$:

$$\begin{aligned} \mathbf{f}_i^{\mathrm{att}} &= -\frac{\partial\varphi^{\mathrm{att}}\left(L_{i,i+1}\right)}{\partial\mathbf{R}_i} = -\frac{\partial\varphi^{\mathrm{att}}\left(L_{i,i+1}\right)}{\partial L_{i,i+1}}\frac{\partial L_{i,i+1}}{\partial\mathbf{R}_i} \\ &= -c_3\mu\left(L_{i,i+1}\right)^{\mu-1}\frac{\mathbf{R}_i - \mathbf{X}_1}{\left|\mathbf{R}_i - \mathbf{X}_1\right|}, \end{aligned} \tag{4.17}$$

and, correspondingly, the force due to this elastic band on blob $i+1$ is always directed along $\mathbf{R}_{i+1} - \mathbf{X}_p$, see Fig. 4.4.

It is important to stress that we have constructed a system in which the total energy is conserved. No work is done on the entanglements because the net force is always zero. Also, the entanglements bear no mass and hence have no kinetic energy. However, the Hamiltonian is history dependent. To calculate the forces at time t we need information about the number of entanglements and their positions along the backbones of the chains, which is a result of events at times $t' < t$. In this respect the ensemble is not canonical.

The reader may wonder why the repulsive term of the bonded blob interaction, Eq. (4.9), was not redefined to be a function of the path length, as was realized for the attractive term. The main reason is that the equilibrium position of the entanglement would not be uniquely defined if lower repulsive energies were associated with increased path lengths. Local minima would emerge in which the minimization procedure could be trapped. Moreover, direct

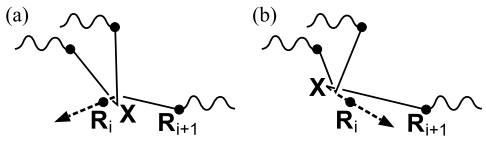

Figure 4.5: The gradient of the attractive energy has a singularity at $\mathbf{R}_i$. Near this point the magnitude of the attractive force on the entanglement $\mathbf{X}$ stays approximately constant, while its direction is given by the unit vector from $\mathbf{X}$ to $\mathbf{R}_i$ [cf. Eq. (4.17)]. This direction changes promptly near $\mathbf{R}_i$ (dashed arrow).

repulsion between the centers of bonded blobs is needed to keep the angular forces from growing too large. A potential defined in terms of angle θ, such as Eq. (4.11), results in a torque between two bonds. If either one of the bond lengths tends to zero, the force on the blob will go infinite, which is highly undesirable.

We end this subsection by mentioning a subtlety involved in the minimization of the attractive energy. Most effective minimization procedures require evaluations of both functions and gradients, i.e. forces. The total force on an entanglement is the sum of the forces along its four arms. Each of these forces is minus the force on its neighbour along the relevant arm. Now, for example, while moving $\mathbf{X}$ in Fig. 4.5 at constant blob positions $\mathbf{R}$, the force on $\mathbf{X}$ has a singularity at $\mathbf{R}_i$, as elucidated in the figure. Notice that the order of objects is not changed in this step of the entanglement algorithm; only in the last step will we check for a possible slip across the blob. Now the above singularity will cause the minimization to converge erroneously if at all. We remedy this problem by adding, at short distances between $\mathbf{X}$ and $\mathbf{R}_i$, an extra repulsive force

$$\mathbf{g}^{\mathrm{add}} = -c_3\mu\left(L_{i,i+1}\right)^{\mu-1}\left(1-\frac{r}{\delta}\right)\frac{\mathbf{R}_i-\mathbf{X}}{\left|\mathbf{R}_i-\mathbf{X}\right|} \qquad (r<\delta) \tag{4.18}$$

$$r = \left|\mathbf{R}_i-\mathbf{X}\right|, \tag{4.19}$$

on the entanglement, and a corresponding force $\mathbf{f}_i^{\mathrm{add}} = -\mathbf{g}^{\mathrm{add}}$ on blob i. At short distances this extra repulsive force on the entanglement counteracts the attractive force $\mathbf{g}^{\mathrm{att}} = -\mathbf{f}_i^{\mathrm{att}}$, and prevents the distance r to become too small. Of course in a next step it must be checked if it is profitable to interchange the order of $\mathbf{X}$ and $\mathbf{R}_i$. A similar procedure must be applied to all pairs of connected objects coming close to each other. The value of δ was chosen equal to 10^{-4} nm, small enough to have a negligible impact on the configurations of the entangled chains, but allowing for a successful convergence of the minimization procedure.

4.3.3 Detecting new (dis)entanglements

In contrast to crosslinks in rubbers, entanglements have a finite lifetime and are continuously appearing and disappearing. In the model that is developed here, a polymer chain is viewed as a succession of objects, be they blobs or entanglements, connected by line segments. During the simulation we keep track of all unattached pairs of line segments which are close together. They may, for instance, be extracted from the blob neighbour list. For each pair of line

segments and at each instant of time the following triple product is calculated:

$$V_{ij} = \left(\mathbf{r}_i - \mathbf{r}_j\right) \cdot \left(\left(\mathbf{r}_{i+1} - \mathbf{r}_i\right) \times \left(\mathbf{r}_{j+1} - \mathbf{r}_j\right)\right), \tag{4.20}$$

in which i and $i+1$ label two consecutive objects along a chain, i.e. define the first line segment. The second line segment is defined by j and $j+1$ [see Fig. 4.1(a)]. Note that the absolute value of the triple product is the volume of the parallelepiped defined by the vectors $\mathbf{r}_{i+1} - \mathbf{r}_i$, $\mathbf{r}_{j+1} - \mathbf{r}_j$, and $\mathbf{r}_i - \mathbf{r}_j$. There are two possibilities for the "volume" V_{ij} to become zero.[2] First, if the distance between the two line segments becomes zero. Second, if the two line segments are parallel. In a molecular or stochastic dynamics simulation the latter possibility can be neglected (the chance of two lines running *exactly* parallel at any time is extremely small, even considering the limited machine precision), so if V_{ij} changes sign from one time to the next, a possible bond crossing has occurred.[3] However, Eq. (4.20) does not distinguish between the physical crossing of two finite line segments and the crossing of two infinite lines. An additional check has to be made to be sure that the crossing is taking place along the physical part of the two finite line segments. In order to calculate the exact crossing point, first the exact time of crossing during the last time step must be calculated. Although in principle this involves solving a third order equation, it is found empirically that solving a linear interpolation of V_{ij} in time gives nearly the same time of crossing. Having determined the positions of the objects at this time, the next task is to find the position $\mathbf{X}$ where the two line segments have crossed [see Fig. 4.1(b)]. To this end define the parameters λ_1 and λ_2 by

$$\begin{aligned} \mathbf{X} &= \mathbf{r}_i + \lambda_1 \left(\mathbf{r}_{i+1} - \mathbf{r}_i\right) \\ &= \mathbf{r}_j + \lambda_2 \left(\mathbf{r}_{j+1} - \mathbf{r}_j\right), \end{aligned} \tag{4.21}$$

i.e. λ_1 defines the crossing point on the line through objects i and $i+1$, with $\lambda_1 = 0$ at object i and $\lambda_1 = 1$ at object $i+1$, and correspondingly for λ_2. These are three equations with two unknowns, λ_1 and λ_2, so any one equation can be dropped and the remaining two be solved (this stems with the fact that the line segments are already confined to a plane in three dimensional space). A physical crossing between the two line segments has occurred if the crossing point lies between both i and $i+1$ and j and $j+1$, i.e.

$$\left(0 < \lambda_1 < 1\right) \wedge \left(0 < \lambda_2 < 1\right). \tag{4.22}$$

The algorithm now proceeds as follows: an entanglement is created, initially at the position $\mathbf{X}$ where the two line segments have crossed each other. In the next time step the minimization of the attractive energy will move the new entanglement to its equilibrium position, and the entanglement will contribute to the elastic forces between chains [Fig. 4.1(c)].

2 A third possibility is that the length of either vector becomes zero. In this rare case impreciseness of the minimization step may lead to false (dis)entanglements. Therefore, if the distance between two connected objects is smaller than ε (introduced in Sec. 4.3.4) it is not allowed to (dis)entangle.

3 Only in an extremely rare case will two line segments simultaneously cross and alter relative orientation during one time step. In that case V_{ij} will not alter sign. We are disregarding entanglements and disentanglements of this kind.

We would like to point out the fact that, in the developed model, two attached (consecutive) line segments can never entangle because the four objects which are connected by an entanglement will all have to be different. If either two objects are the same, the volume V_{ij} between the line segments is always zero and never changes sign.

After an entanglement is created, the associated volume V_{ij} will serve to detect future disentanglements. If the volume V_{ij} of the four objects surrounding an entanglement changes sign from one time to the next, a possible disentanglement has occurred. Additional checks are made in exactly the same way as described for the creation of entanglements, i.e. Fig. 4.1 may also be read backwards.

4.3.4 Non-trivial moves

While searching for its equilibrium position, an entanglement can move freely along the chain between two adjacent objects. At a certain moment, however, the attractive energy would be lower if the entanglement could slip past a blob one position further along the chain backbone, or to the other side of the next entanglement, or, in other words, if the order of objects within a chain would be altered. The order-altering moves are not trivial, but important for a realistic treatment of the entanglement constraints. The algorithm detects if an entanglement has a natural tendency to get close to either one of its adjacent objects by measuring the distance to these objects. If the distance becomes smaller than a prescribed value ε, i.e.

$$\left|\mathbf{r}_i - \mathbf{X}\right| < \varepsilon, \tag{4.23}$$

where $\mathbf{r}_i$ is the position of the adjacent object and ε is sufficiently small compared to the average bond length, a subalgorithm will check order-altering moves. The value of ε was chosen equal to 10^{-2} nm, much smaller than the average bond length of roughly 1.5 nm. The subalgorithm makes the following checks:

1. If the object which is approached is another entanglement go to 2; if it is a blob go to 3.
2. Check if it is physically possible for one entanglement to slip past the other. If it is possible, swap the order in which the entanglements appear in the chain backbone. Otherwise do not swap. Back to main program.
3. If the blob lies at the extremum of a chain, remove the entanglement and go back to the main program. Otherwise go to 4.
4. If a slip past the blob results in an entanglement of a line segment with itself, remove the entanglement (*vide infra*) and go back to the main program. Otherwise go to 5.
5. If a slip past the blob results in disentanglement, remove the entanglement. Otherwise slip the entanglement past the blob. Back to main program.

If the entanglement has survived the slip past the adjacent object, the algorithm will find a new equilibrium position in the next time step. Only one slip per time step is allowed for each entanglement. In the following we will clarify the various checks which are made in the subalgorithm.

Suppose two entanglements are very close to each other, as in Fig. 4.6. The mean position of the two entanglements, $\mathbf{r}_m$, will then be very close to both entanglement positions, $\mathbf{X}_1$ and $\mathbf{X}_2$. Define $\mathbf{s}_1$ to $\mathbf{s}_6$ as the vectors going from $\mathbf{r}_m$ to the surrounding six objects with positions

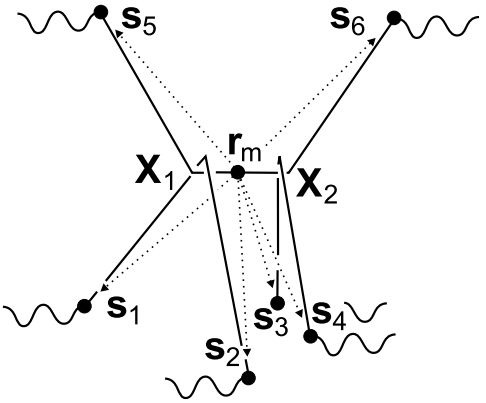

Figure 4.6: Two entanglements at $\mathbf{X}_1$ and $\mathbf{X}_2$ are allowed to slip past each other if the two arms of the first entanglement ($\mathbf{s}_1$ and $\mathbf{s}_2$) can both pass over the two arms of the second entanglement ($\mathbf{s}_3$ and $\mathbf{s}_4$). The reverse case is also possible.

$\mathbf{r}_1$ to $\mathbf{r}_6$, in formula:

$$\mathbf{r}_m = 1/2\left(\mathbf{X}_1+\mathbf{X}_2\right), \tag{4.24}$$

$$\mathbf{s}_i = \mathbf{r}_i-\mathbf{r}_m. \tag{4.25}$$

Now it is assumed that the two entanglements can swap if the two arms connected to the first entanglement, $\mathbf{s}_1$ and $\mathbf{s}_2$, *both* go over the two arms connected to the second entanglement, $\mathbf{s}_3$ and $\mathbf{s}_4$, or the other way around. In the first case we demand that the projections of $\mathbf{s}_3$ and $\mathbf{s}_4$ onto the plane defined by $\mathbf{s}_1$ and $\mathbf{s}_2$ both fall in between $\mathbf{s}_1$ and $\mathbf{s}_2$. To make this mathematically explicit: both $\mathbf{s}_3$ and $\mathbf{s}_4$ must lie in

$$\begin{aligned}\mathscr{R} = \left\{\mathbf{r}\in\mathbb{R}^3 \quad | \quad \mathbf{r} = l_1\mathbf{s}_1+l_2\mathbf{s}_2+l_3\left(\mathbf{s}_1\times\mathbf{s}_2\right),\right.\\ \left. l_1\in\mathbb{R}^+, l_2\in\mathbb{R}^+, l_3\in\mathbb{R}\right\},\end{aligned} \tag{4.26}$$

i.e. any vector $\mathbf{r}$ in $\mathscr{R}$ must have positive components along $\mathbf{s}_1$ and $\mathbf{s}_2$ in the basis $\left\{\mathbf{s}_1,\mathbf{s}_2,\mathbf{s}_1\times\mathbf{s}_2\right\}$. For a given vector $\mathbf{r}$ these components are

$$l_1(\mathbf{r}) = \frac{\left(\mathbf{r}\cdot\mathbf{s}_1\right)s_2^2-\left(\mathbf{r}\cdot\mathbf{s}_2\right)\left(\mathbf{s}_1\cdot\mathbf{s}_2\right)}{s_1^2s_2^2-\left(\mathbf{s}_1\cdot\mathbf{s}_2\right)^2}, \tag{4.27}$$

$$l_2(\mathbf{r}) = \frac{\left(\mathbf{r}\cdot\mathbf{s}_2\right)s_1^2-\left(\mathbf{r}\cdot\mathbf{s}_1\right)\left(\mathbf{s}_1\cdot\mathbf{s}_2\right)}{s_1^2s_2^2-\left(\mathbf{s}_1\cdot\mathbf{s}_2\right)^2}. \tag{4.28}$$

If all four numbers $l_1(\mathbf{s}_3)$, $l_2(\mathbf{s}_3)$, $l_1(\mathbf{s}_4)$, and $l_2(\mathbf{s}4)$ are positive, the entanglements can swap. Now $\mathbf{s}_1\cdot\mathbf{s}_2 = s_1s_2\cos\varphi$, with φ the angle between the two arms $\mathbf{s}_1$ and $\mathbf{s}_2$. Since these are never exactly parallel, the denominators in Eqs. (4.27) and (4.28) are always positive, so only the nominators need to be calculated. As already mentioned, the inverse is also possible: the entanglements can swap if the projections of $\mathbf{s}_1$ and $\mathbf{s}_2$ onto the plane defined by $\mathbf{s}_3$ and $\mathbf{s}_4$ both fall in between $\mathbf{s}_3$ and $\mathbf{s}_4$.

Now suppose the entanglement is near a blob. The subalgorithm checks if this blob is the first or last blob of the chain, because then a slip past this blob means that it is slipping off the

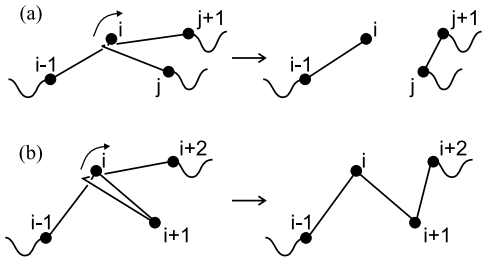

Figure 4.7: (a) A slip past the last blob of a chain results in disentanglement. (b) If a chain is entangled with itself and the loop is shrinking as far as to pass through only one object apart from the entanglement, a self-disentanglement will occur.

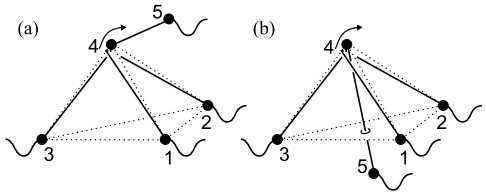

Figure 4.8: (a) The entanglement X slips past blob 4 if the (extension of) the line from blob 4 to object 5 does not cross the 1-2-3 face of the tetrahedron (dotted lines). (b) The chain disentangles if this face is crossed.

end of the chain [Fig. 4.7(a)]. Usually this is not the case and the program checks if a slip past the blob results in an entanglement of two consecutive line segments, as indicated in Fig. 4.7(b). This happens if a chain is entangled with itself, and the loop shrinks as far as to pass through only one object apart from the entanglement. Since all four arms of an entanglement have to end at different objects, the entanglement will simply be released in this case. This is called a self-disentanglement.

Finally it is checked if a slip past a blob results in a disentanglement. Suppose two (parts of) chains are entangled. One (part of the) chain is going from an object at $\mathbf{r}_1$, via the entanglement at $\mathbf{X}$, to an object at $\mathbf{r}_2$, and the other (part of the) chain is going from $\mathbf{r}_3$, via the entanglement, to $\mathbf{r}_4$, as in Fig. 4.8. Due to the very definition of an entanglement it will always be positioned inside the tetrahedron formed by $\mathbf{r}_1$, $\mathbf{r}_2$, $\mathbf{r}_3$, and $\mathbf{r}_4$. Although in principle entanglements may occur in one of many complicated forms, the simplest situation shown in Fig. 4.9(a) is by far the most probable, and we will assume that we will always have to deal with this simple unwinded form. Now suppose the entanglement wants to slip past a blob at $\mathbf{r}_4$. It will depend on the orientation of the line segment between the blob at $\mathbf{r}_4$ and the next object at $\mathbf{r}_5$ whether the entanglement will continue to exists, or must be abolished. Given the unwinded form of the entanglement, it must be abolished if the line segment $\mathbf{r}_5 - \mathbf{r}_4$, or its continuation, passes through the $\mathbf{r}_1$-$\mathbf{r}_2$-$\mathbf{r}_3$ face of the tetrahedron, as in Fig. 4.8(b). In all other cases, as in Fig. 4.8(a), a new entanglement equilibrium position must be searched at the other side. A mathematical criterion is easily obtained by equating the expression for a

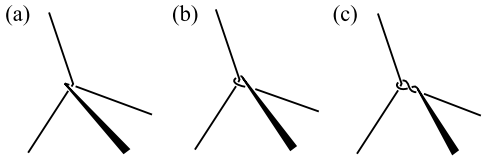

Figure 4.9: The uncrossability constraint does not distinguish between different link windings. Windings (a), (b), and (c) are all equivalent to the algorithm. Obviously types (b) and (c) will be highly improbable.

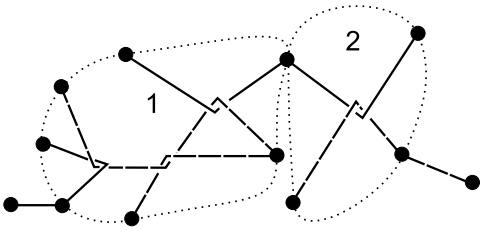

Figure 4.10: The minimization to determine the positions of the entanglements between these four chains can be split up in two independent parts, indicated by the dotted lines.

point in the $\mathbf{r}_1$-$\mathbf{r}_2$-$\mathbf{r}_3$ face of the tetrahedron with the expression for a point along the $\mathbf{r}_5$-$\mathbf{r}_4$ line,

$$\mathbf{r}_3 + l_1\left(\mathbf{r}_1 - \mathbf{r}_3\right) + l_2\left(\mathbf{r}_2 - \mathbf{r}_3\right) = \mathbf{r}_4 + l_3\left(\mathbf{r}_5 - \mathbf{r}_4\right), \tag{4.29}$$

which can be solved for the parameters l_1, l_2 and l_3. A disentanglement will occur only if

$$\left(l_1 > 0\right) \wedge \left(l_2 > 0\right) \wedge \left(l_1 + l_2 < 1\right) \wedge \left(l_3 > 0\right). \tag{4.30}$$

This completes the description of the non-trivial moves.

4.3.5 Increasing the speed of the algorithm

The introduction of the entanglement algorithm in a standard molecular or stochastic dynamics program will cause a lot of computational overhead. The calculations concerning non-trivial moves are quite complicated, but they do not occur very often and do not consume a considerable part of the cpu time. For the detection of new entanglements in principle all line segment pairs must be checked. Much time is saved by looping over the standard list of close neighbours and considering the line segments attached to these particles. The computational costs are then comparable to the costs of evaluating non-bonded forces in a standard program. The slowest part of the entanglement algorithm is the equilibration step where in principle the total attractive energy, Eq. (4.15), has to be minimized. However, the minimization can be split up in several independent parts by recognizing the fact that moving an entanglement on one side of a blob will not influence the attractive energy residing in the bonds which are connected to an entanglement on the other side of the blob (unless there is a path *around* the blob leading to the other entanglement without encountering any other blobs). For instance, in Fig. 4.10 the parts indicated by "1" and "2" can be equilibrated independently. Despite this fact, the minimization can still consume between 70 and 95 percent of the total time spent in the entanglement algorithm, depending on the efficiency of the minimization procedure and the desired accuracy. In this work we demanded a relative energy convergence of 10^{-8}. A stochastic dynamics program using the entanglement algorithm was roughly 10 times slower than the same program without entanglement constraints. The advantage of being able to coarse-grain, however, has more than compensated this unfavourable factor. More important, it is now possible to investigate the influence of the uncrossability constraint on all kinds of dynamic properties by comparing results with and without use of the entanglement algorithm.

4.4 System preparation

4.4.1 Introduction

In Sec. 4.2 we described a possible coarse-graining procedure to arrive at a mesoscopic melt of chains, each represented by $N = 6$ blobs, starting from a microscopic simulation of a $C_{120}H_{242}$ melt. In the remaining part of this chapter the influence of the uncrossability constraint on the dynamics and rheology of this system will be made explicit by comparing results of entangled and unentangled simulations. To discern effects of chain stiffness some additional simulations will be described in which the angular potential was set to zero. In this section we will describe how the initial boxes were created and how the friction coefficient was determined.

4.4.2 Preparation of the initial boxes

For a correct sampling of the pressure tensor autocorrelation it is very important that the initial configuration with which the simulation will be started has no average stress. This puts forward many difficulties for molecular dynamics simulations of microscopic chains. However, unlike microscopic chains, relaxed initial configurations of mesoscopic chains are realized with comparative ease due to the softness of the interactions. Initial configurations of the chains were generated according to the distribution functions obtained from the microscopic simulations (see Fig. 4.3). A total of 120 chains were placed and oriented randomly in each simulation box, at a density $\rho = 0.761$ g/cm^3, which is equal to the microscopic density. The non-bonded interaction parameter (c_0) was set to 1/10th of its final value in order to gently push blobs with large overlap apart, while allowing all bonds to cross each other. After this initial homogenization the non-bonded interaction parameter was gradually increased to reach its final value. After equilibration the initial boxes for the unentangled simulations were ready. An initial box for an entangled simulation was produced by switching on the uncrossability constraint and letting the entanglements form. The total number of entanglements was monitored and observed to reach an equilibrium value (in an average sense) within a few nanoseconds. Because entanglements are continuously created and annihilated the number of entanglements was observed to fluctuate around an average value of 560 with a standard deviation of 40. In *Chapter 5* we will give details of entanglement time correlation functions.

4.4.3 Determination of the friction coefficient

The Langevin equation of motion, Eq. (4.2), contains one parameter, the blob friction coefficient ζ, that has not yet been fixed. It must be emphasized that, apart from the lengths δ and ε in the entanglement algorithm which must be chosen small enough, the friction coefficient is the only free parameter of our model. The Langevin stochastic dynamics method has been used to perform simulations of polymer chains by several other authors among whom Kremer and Grest. [66] These authors effectively established a coupling between the system and a heat bath in order to keep the system at some desired temperature. In order not to influence the chain dynamics too much, they had to choose the friction coefficient much smaller than

the effective friction between the beads of the polymers, which is caused by the mutual interactions and relative motions of the beads and which determines dynamic properties, such as diffusion. In our method however, the system has been coarse-grained to a much higher level and the interactions have become very soft. As a consequence, besides acting as a thermostat, the friction coefficient ζ has acquired the meaning of a *physical* friction. One might ask therefore if the friction model that is applied here (isotropic, delta-correlated friction) is not too much of a simplification. Indeed, somewhat more complicated friction models have been used in the literature, like for example in DPD methods, but also these models don't do justice to all details of the movements on the coarse-grained level. Obviously, finding the right friction model will be a tremendous task (see, for instance, Ref. [1] in which much effort is taken to correctly describe the frictional interactions in a dumbbell of blobs). However, the purpose of this chapter is not to find the best possible friction model, yet to test the entanglement algorithm. It will be shown that the simple approach combined with the entanglement algorithm yields results which already deviate substantially from the Rouse case.

In this chapter the blob friction coefficient was chosen such that the chains center of mass diffusion coefficient D of the entangled mesoscopic system matched the one measured in the microscopic $C_{120}H_{242}$ system. Notice that this is the bare friction coefficient, which goes into the Langevin equation and is not necessarily related to the chains diffusion coefficient D by $\zeta = kT/(ND)$ with $N = 6$ like it would have been for a melt of Rouse chains. In fact from a number of test calculations we deduced that the friction "frequency" $\xi = \zeta/M$, which for a Rouse chain would be independent of the number of monomers used to define a blob, must be chosen equal to 8.0 ps^{-1}, while in *Chapter 3* we found that the Rouse friction frequency of a $C_{120}H_{242}$ chain at 450 K equals 19.0 ps^{-1}. Apparently the intermolecular interactions (specifically the entanglements) introduced a substantial extra friction to the chains. In *Chapter 5* we will present a direct way to calculate ξ from microscopic simulations, leaving no free parameters at all.

The Langevin equation was integrated using the algorithm of Allen [3] (or, equivalently, Van Gunsteren and Berendsen [50]). Given the choice of the friction, a time step $\Delta t = 0.1$ ps was found to be small enough to accurately integrate the equations of motions. The simulations were run up to 4×10^6 time steps corresponding to 0.4 microseconds.

4.5 Results

4.5.1 Mean square displacement

Two time-dependent mean square displacements $g_{\mathrm{bl}}(t)$ and $g_{\mathrm{cm}}(t)$ have been measured and are shown in Fig. 4.11. They are defined as follows:

$$g_{\mathrm{bl}}(t) = \frac{1}{N}\sum_{i=1}^{N}\left\langle [\mathbf{R}_i(t) - \mathbf{R}_i(0)]^2 \right\rangle, \tag{4.31}$$

$$g_{\mathrm{cm}}(t) = \left\langle [\mathbf{R}^{\mathrm{cm}}(t) - \mathbf{R}^{\mathrm{cm}}(0)]^2 \right\rangle, \tag{4.32}$$

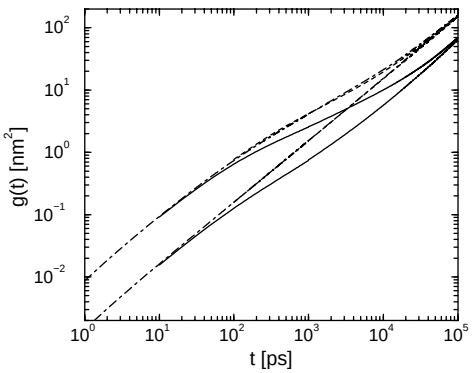

Figure 4.11: Mean square displacements of entangled chains (solid), and unentangled chains with (dot-dashed) or without (dashed) chain stiffness. The upper curves are the mean square displacements of the blobs, Eq. (4.31), the lower curves of the center of mass of the chain, Eq. (4.32).

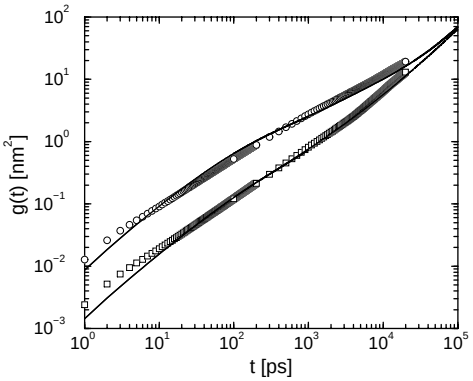

Figure 4.12: Mean square displacements of entangled mesoscopic chains (solid lines) compared with the results of microscopic molecular dynamics simulations (*Chapter 3*). Blob mean square displacements are indicated by circles, chain center of mass mean square displacements by squares.

where $\mathbf{R}_i$ is the position of the ith blob and $\mathbf{R}^{\mathrm{cm}}$ is the center of mass position of the chain of length N. The chains center of mass mean square displacements of the unentangled chains (dashed and dot-dashed lines) are almost perfectly linear with time for all times, as is the case for Rouse chains. Also, the blob mean square displacement of the unentangled chain without angular potential can perfectly be described by the Rouse model (not shown). Adding an angular potential produces only small deviations from the Rouse model, caused by faster relaxations at smaller scales. This will become apparent in the next subsection when the Rouse modes are analyzed. In the entangled case (solid lines), both the blob and center of mass mean square displacements are slowed down considerably after 100 ps.

In Fig. 4.12 the results of microscopic molecular dynamics simulations (symbols) are compared with the entangled mesoscopic results (solid lines). In both cases a sub-linear exponent (t^x, with $x < 1$) in the center of mass mean square displacement is observed. A similar subdiffusive exponent is observed in both simulation [100] and neutron spin echo spectroscopy [101] results of a $C_{100}H_{202}$ melt. Good quantitative agreement of the minimim exponent is obtained for $g_{\mathrm{cm}}(t)$: $x = 0.80$ and $x = 0.77$ for the microscopic and mesoscopic models respectively and $x = 0.83$ for a $C_{100}H_{202}$ chain from literature. [101] The influence of the entanglement algorithm on $g_{\mathrm{bl}}(t)$ seems to be slightly too strong: $x = 0.65$ (microscopic) and $x = 0.56$ (mesoscopic). In view of the crudeness of the coarse-grained interaction model we find this acceptable.

The success of the entanglements and the unimportance of the angular dependent part of the potential in describing the subdiffusive regimes make it highly improbable that these regimes should result from internal, single chain properties.

For long times, the center of mass diffuses freely. From this regime we can determine the self-diffusion coefficient according to

$$D = \lim_{t\to\infty} \frac{g_{\mathrm{cm}}(t)}{6t}. \tag{4.33}$$

Pearson *et al.* have measured self-diffusion coefficients by means of field gradient NMR at 450 K experimentally for a large range of molecular weights, although not for the weight of $C_{120}H_{242}$ chains. [106] An interpolation of their data yields $D_{\mathrm{exp}} \approx 0.67 \times 10^{-6}$ cm^2/s. The microscopic simulation yielded $D = 1.09 \times 10^{-6}$ cm^2/s, overestimating the experimental result a bit. Even though the friction ξ was determined by matching the diffusion coefficient of the entangled mesoscopic model with that of the microscopic model, this matching was not perfect, and a slightly different result was obtained: $D = 0.93 \times 10^{-6}$ cm^2/s. Without the uncrossability constraint much larger diffusion coefficients were measured: $D = 2.56 \times 10^{-6}$ cm^2/s with, and $D = 2.52 \times 10^{-6}$ cm^2/s without angular potential. This is close to the Rouse model predicted diffusion coefficient of $D = 2.78 \times 10^{-6}$ cm^2/s, using $T = 450$ K, $N = 6$, and $\xi = 8$ ps^{-1}.

Of course, the friction coefficients of the unentangled systems might have been varied as well to match the microscopic diffusion coefficient, but then the results would not have agreed with those of the microscopic simulations at shorter time scales. It is the merit of our entangled model that it describes the motions of the chains and parts of them both on the intermediate and on the long time scales. This statement will be substantiated in the following subsections.

4.5.2 Rouse coordinates

It has been shown both experimentally [101] and by computer simulation (see *Chapter 3*) that in some time regimes melts of intermediately long chains can be well described by the simple Rouse model. It is therefore interesting to investigate the systems in terms of Rouse coordinates: [13]

$$\mathbf{X}_k(t) = \frac{1}{N}\sum_{i=1}^{N} \mathbf{R}_i(t) \cos\left[\frac{k\pi}{N}\left(i - \frac{1}{2}\right)\right] \qquad (k = 0, \ldots, N-1) \tag{4.34}$$

Notice that in this subsection $\mathbf{X}_k$ is the normal mode instead of an entanglement position. The motion of the center of mass is given by the zeroth mode, $k = 0$. All other modes are associated with internal motions of the chain, mode k roughly corresponding with motion of a subchain of size N/k. Within the Rouse model each of these modes relaxes independently and exponentially with a relaxation time τ_k,

$$\left\langle \mathbf{X}_k(t) \cdot \mathbf{X}_k(0) \right\rangle / \left\langle \mathbf{X}_k^2 \right\rangle = \exp\left(-t/\tau_k\right), \tag{4.35}$$

$$\tau_k^{-1} = 4W \sin^2\left(\frac{k\pi}{2N}\right), \tag{4.36}$$

where the relaxation rate W is a characteristic frequency of the Rouse model and is given by:

$$W = \frac{3kT}{\zeta b^2}, \tag{4.37}$$

with b the statistical segment length.

Normalized Rouse mode autocorrelation functions for the three systems are shown in Figs. 4.13(a) to (e) for modes $k = 1$ to 5. The first two modes, $k = 1$ and $k = 2$ are slowed down under the influence of the angular potential (from dashed to dot-dashed lines), in qualitative agreement with the semiflexible chain model of Harnau *et al.* [54] They are slowed down even more in case the uncrossibility constraint applies (solid lines). On the other hand, the modes at the smallest scales relax much faster when the chains get some stiffness. Interestingly, these modes relax equaly fast with or without uncrossability constraint. So it seems that the uncrossabililty of chains does not affect the relaxation at small scales. However from Fig. 4.13(f), which shows the relaxations of the entangled system on a semi-logarithmic scale, it is seen that these relaxations are not exponential as predicted by the Rouse model, Eq. (4.35). The reason for this may be that the non-bonded interactions and uncrossibility constraints modify the equations of motion and make them highly nonlinear. [126] As a consequence the Rouse modes can no longer be considered as normal modes of the chains and may no longer relax exponentially.

To quantify the non-exponentiality, the Rouse mode autocorrelation functions were fitted with stretched exponentials,

$$\left\langle \mathbf{X}_k(t) \cdot \mathbf{X}_k(0) \right\rangle / \left\langle \mathbf{X}_k^2 \right\rangle = \exp\left[-(t/\tau_k^*)^{\beta_k} \right], \tag{4.38}$$

where the relaxation times τ_k^* and stretching parameters β_k depend on mode number k. The fit parameters for the three systems are given in Table 4.2. Two observations can be made. (i) The deviations from exponential behavior ($\beta_k = 1$) become larger with increasing mode number, i.e. smaller scales relax increasingly non-exponentially. This is in contradiction with the results of Richter *et al.* [112] who did not find any hint of stretching in the internal modes, yet in accordance with the results of Shaffer [126] who placed polymers on a lattice and applied uncrossability constraints. To clear this ambiguity, more experimental evidence of the existence or non-existence of stretched relaxations will be needed. (ii) Including chain stiffness and uncrossability both make the deviations from exponential behavior become larger, resulting in $\beta_k = 0.77$ for modes 3, 4 and 5 in the entangled system. The stretching parameters of Shaffer compare to ours, about 0.75 for the largest mode numbers, although in his case there was less difference between β_k values of crossing and non-crossing polymers. A possible explanation for this smaller difference may be that polymers on a lattice are already more restricted in their motion than polymers in continuum models, so there will be a less pronounced difference between crossing and non-crossing polymers.

In analogy with Shaffer's work the effective Rouse mode relaxation times were determined as time integrals over the normalized relaxation functions as the macroscopic stress relaxation is governed by these integrals. However, instead of integrating Eq. (4.38) using the fit parameters, the measured relaxation functions were integrated directly to account for any deviations of the true curves from the fitted curves:

$$\tau_k^{\text{eff}} = \int_0^\infty \left\langle \mathbf{X}_k(t) \cdot \mathbf{X}_k(0) \right\rangle / \left\langle \mathbf{X}_k^2 \right\rangle dt. \tag{4.39}$$

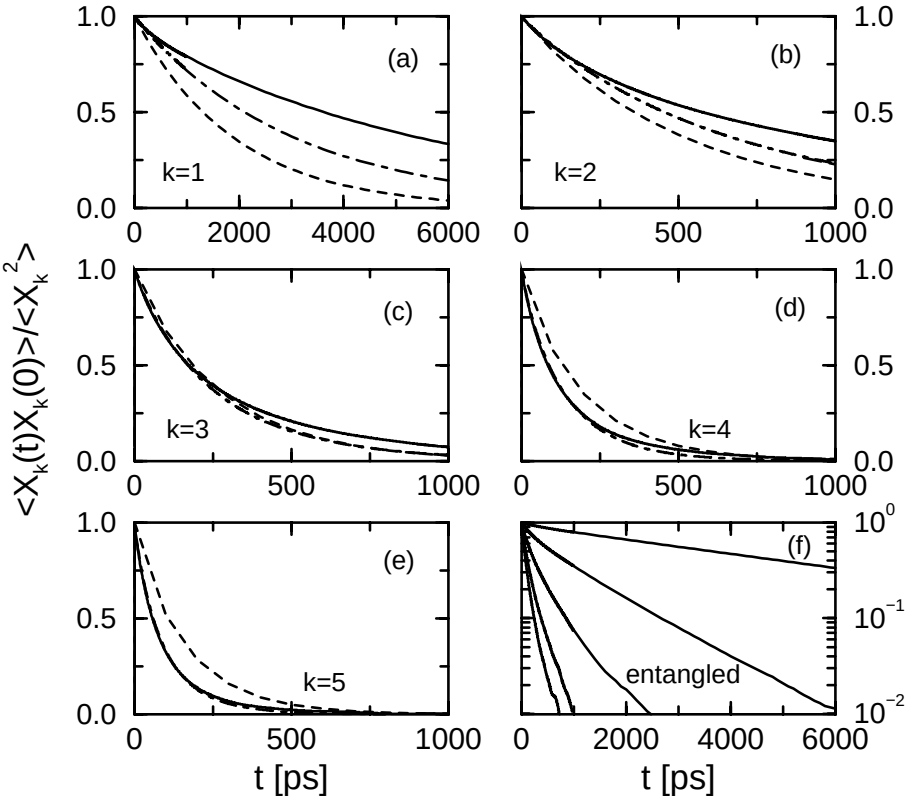

Figure 4.13: Rouse mode autocorrelation functions of entangled chains (solid), and unentangled chains with (dot-dashed) or without (dashed) chain stiffness, for mode numbers 1 (a) to 5 (e). The results of the entangled chains are plotted on a semi-logarithmic scale in (f), demonstrating non-exponential relaxation.

system	k	$\langle \mathbf{X}_k^2 \rangle$ (nm^2)	τ_k^* (ps)	β_k	τ_k^{eff} (ps)	W_k^{eff} (ns^{-1})
unentangled	1	0.725	1920	1.00	1920	1.94
not stiff	2	0.190	520	0.98	525	1.91
	3	0.094	270	0.96	275	1.82
	4	0.062	185	0.95	195	1.71
	5	0.050	155	0.94	165	1.63
unentangled	1	1.110	3100	1.00	3100	1.20
stiff	2	0.227	670	0.96	680	1.47
	3	0.084	250	0.92	270	1.85
	4	0.044	135	0.90	155	2.15
	5	0.031	90	0.87	110	2.44
entangled	1	0.919	5650	0.94	5515	0.68
stiff	2	0.192	940	0.80	1065	0.94
	3	0.074	280	0.77	345	1.45
	4	0.040	130	0.77	165	2.02
	5	0.028	80	0.77	110	2.44

Table 4.2: Amplitude, fit with a stretched exponent, Eq. (4.38), effective relaxation time and effective relaxation rate as a function of Rouse mode number for the three different systems.

In analogy to Eq. (4.36) we define the effective Rouse rate

$$W_k^{\text{eff}} = \left[4\tau_k^{\text{eff}} \sin^2\left(\frac{k\pi}{2N}\right) \right]^{-1}, \tag{4.40}$$

which in the case of Rouse chains is a constant. Effective relaxation times and rates are listed in Table 4.2. As can be seen in Fig. 4.14, the relaxation rates of the unentangled system without chain stiffness (dashed line) are slightly decreasing with increasing mode number. Because the decrease is relatively small, the relaxation time distribution of this system is essentially Rouse-like. As was already noted, a stiffening of the chain (dot-dashed line) causes slower relaxation of the large scale modes and a faster relaxation of the small scale modes. The uncrossability constraint makes the large scale modes even slower, but leaves the small scale modes unaffected (solid line). We can compare these results with the work of Richter *et al.* who have analyzed dynamic structure factors from neutron spin echo experiments in terms of relevant theoretical approaches. [112] They argued that a stiffening of the chain is essential but a stiffness correction alone is not enough. Using a realistic value of the stiffness of the chain, their calculations showed that the relaxation times decrease too slowly with increasing mode number to reproduce the experimentally observed dynamic structure factors. These results were questioned by Harnau, [53] but Richter *et al.* argued in response that additional (internal) friction terms may be necessary to explain the experimental results. [113] Our results suggest an alternative additional mechanism. The uncrossability

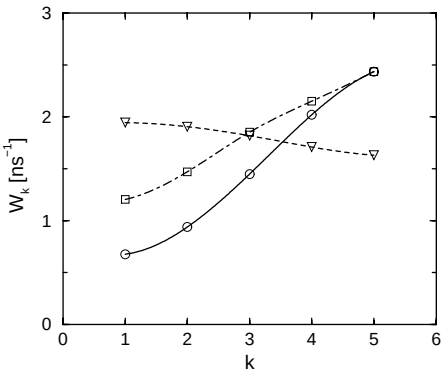

Figure 4.14: Effective Rouse relaxation rates as a function of mode number, Eq. (4.40), for entangled chains (circles), and unentangled chains with (squares) or without (triangles) chain stiffness. The lines are guides to the eye.

interactions between different (parts of) chains increase the relaxation times of the large scale modes, even for chains which are generally considered not to be entangled.

The crossing over of relaxation rates is often associated with the entanglement length N_e. In Ref. [115] Richter *et al.* argue that the modes with $k \geq N/N_e$ are not modified by the entanglement constraints, while modes with $k < N/N_e$ are strongly slowed down. Their Fig. 7 may be compared with our Fig. 4.14. In our case the crossing over occurs at $k \approx 3$, i.e. the entanglement length of our model appears to be approximately $6/3 = 2$ blobs. This corresponds in the microscopic (polyethylene) chain to a length of C_{40}. The values reported in the literature have been going up and down, mainly because the definition of entanglement length was (and still is) unclear. Richter *et al.* derived $N_e = 136$ monomers, i.e. C_{136}, from their dynamic structure factor measurements, [109] and Carella *et al.* measured $N_e = 65$ monomers from rheological measurements. [15] Our result is in any case smaller than those from the literature, but this is due to the fact that this estimate is not derived from dynamic structure factor measurements, nor from rheology. We will return to this point in *Chapters 5* and *6*.

4.5.3 Dynamic structure factor

The coherent dynamic structure factor can be measured by means of neutron spin echo spectroscopy. In the experiments conducted by Richter and co-workers protonated chains were dissolved in a deuterated matrix. [101,112,120] Because the scattering lengths of protons and deuterons differ, they were able to extract the single chain coherent dynamic structure factor. It can be calculated from

$$S(q,t) = \frac{1}{N_s} \sum_{i=1}^{N_s} \sum_{j=1}^{N_s} \left\langle \exp\left\{ i\mathbf{q} \cdot \left[\mathbf{r}_i(t) - \mathbf{r}_j(0) \right] \right\} \right\rangle, \tag{4.41}$$

where $\mathbf{q}$ is the scattering wave vector and the double summation is over all N_s scattering centers of one chain. Because our chains have been coarse-grained, detailed microscopic information about positions of the hydrogens is lost. However, to a good approximation the blob positions $\mathbf{R}_i(t)$ can still be used in Eq. (4.41) to calculate the microscopic dynamic

structure factor, provided the wavelength of the scattering wave vector is large compared to the bond length of bonded blobs. As Fig. 4.3 shows, the maximum bond length is of the order of 2 nm, so q will have to be small compared to 3 nm^{-1}.

The results for five different scattering vectors are shown in Fig. 4.15 for all three mesoscopic systems (solid lines). Dynamic structure factors were also calculated for corresponding Rouse chains (dotted lines). For each system the following three Rouse parameters were used: the measured effective first relaxation time τ_1^{eff} (Table 4.2), the measured diffusion coefficient D, and $N = 6$ [see Eqs. (2.37), (2.20), and (2.22)]. For the unentangled system without angular potential, Fig. 4.15(a), the measured curves coincide perfectly with the Rouse curves for all but the largest q vector. This confirms the observation made before that this system can be viewed as essentially Rouse-like. If the chain is made stiffer, Fig. 4.15(b), the smallest q vector result coincides with the Rouse curve, but all larger q vector results relax slower than the Rouse curves, as was already pointed out by Harnau *et al.* [54, 55] If the uncrossability constraint is applied, Fig. 4.15(c), again the first q vector result coincides with the Rouse curve. All larger q curves not only relax slower, but also do not run parallel to the corresponding Rouse curves. These flattened curves imply a slower relaxation of $S(q,t)$ for large enough times.

In Fig. 4.16 the results of the entangled mesoscopic model (solid lines) are compared with the results determined from the microscopic simulations described in *Chapter 3* (symbols). In that chapter it was found that an optimized Rouse fit yielded $\tau_1 = 6.5$ ns, $D = 1.15 \times 10^{-6}$ cm^2/s, and $N = 15$. This Rouse result is indicated in Fig. 4.16 by the dotted lines. As already mentioned, the present works friction ξ was determined by matching the diffusion coefficient of the mesoscopic model with that of the microscopic model, but because of inaccuracy of the interpolation a slightly smaller diffusion coefficient was obtained. As a result all small q dynamic structure factor results are slightly above the microscopic results. Despite this inaccuracy, it is clear that the entangled mesoscopic model yields results which are far more better than the Rouse predictions. The results for q equal to 0.55, 1.0 and 1.4 nm^{-1} are in perfect agreement with the microscopic chain. The results for both of the large q values, 1.8 and 2.2 nm^{-1}, suffer from the lack of microscopic detail. In all cases, the slopes are in agreement with the microscopic results, from which we conclude that our model captures the physics much better than the Rouse model.

4.5.4 Shear relaxation modulus and viscosity

In a non-periodic system, the stress tensor in the presence of entanglements may be given by

$$\boldsymbol{\sigma} = -\frac{1}{V}\left[\sum_{i=1}^{n} M\mathbf{V}_i\mathbf{V}_i + \mathbf{R}_i\mathbf{F}_i\right] - \frac{1}{V}\left[\sum_{k=1}^{p} \mathbf{X}_k\mathbf{G}_k\right]. \tag{4.42}$$

The first bracketed term is the standard expression for the stress tensor in a non-periodic system of n particles without entanglements: $\mathbf{V}_i$ is the velocity and $\mathbf{F}_i$ the force on particle i. The second bracketed term contains the sum of all products of entanglement positions $\mathbf{X}_k$ and corresponding forces $\mathbf{G}_k$. This term may be added because the total force on each entanglement is zero. In the presence of entanglements, the attractive forces appear as pair interactions

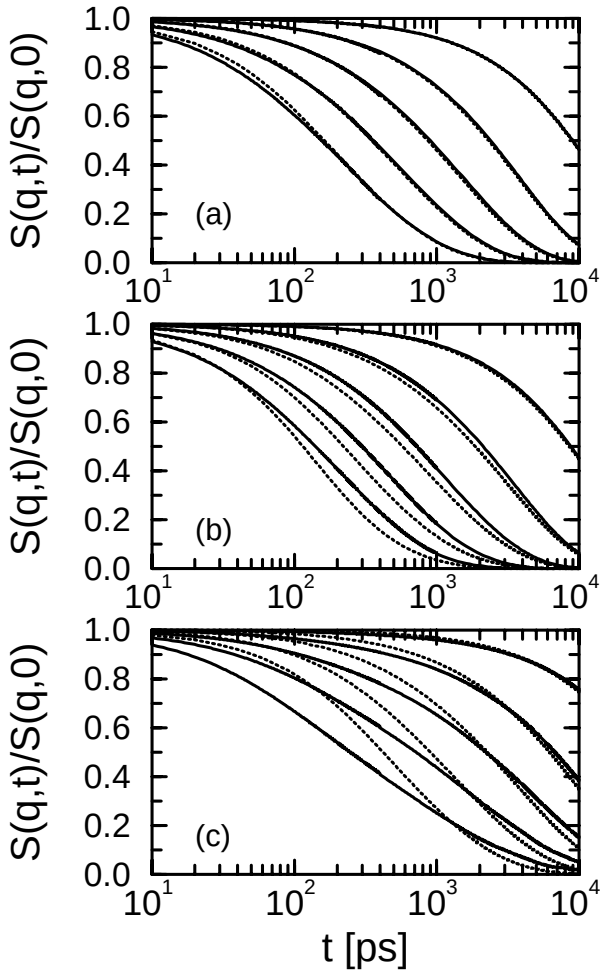

Figure 4.15: Single chain dynamic structure factors of entangled chains (c), and unentangled chains with (b) or without (a) chain stiffness (solid lines). In each picture the q values are, from top to bottom: 0.55 nm^{-1}, 1.0 nm^{-1}, 1.4 nm^{-1}, 1.8 nm^{-1}, and 2.2 nm^{-1}. The dotted lines show the fit with the corresponding ($N = 6$) Rouse model, using the longest effective relaxation time τ_1^{eff}.

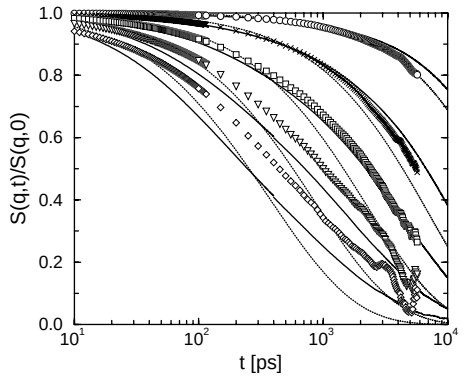

Figure 4.16: Single chain dynamic structure factors of entangled mesoscopic chains (solid lines) compared with the results of microscopic molecular dynamics simulations (symbols) and the optimized Rouse fit of *Chapter 3* (dotted lines). The q values shown are 0.55 nm^{-1}, 1.0 nm^{-1}, 1.4 nm^{-1}, 1.8 nm^{-1}, and 2.2 nm^{-1}.

between nearest neighbours along the chains, be they blobs or entanglements [see Eq. (4.17) and the discussion following this equation]. Since these pair interactions obey Newtons third law we may apply the usual transformation to a periodic system in order to calculate the contribution of the attractive forces to the stress tensor. The remaining contributions to the stress tensor, due to the angular, non-bonded and repulsive interactions between bonded blobs, are related to the blob positions only, and can be calculated in the usual way.

The zero shear relaxation modulus is related to the symmetrized traceless part $\mathbf{P}$ of the stress tensor $\boldsymbol{\sigma}$ by [23]

$$G(t) = \frac{V}{10kT} \langle \mathbf{P}(t) : \mathbf{P}(0) \rangle . \tag{4.43}$$

The double contraction means that in practice we can average over five independent contributions: P_{xy}, P_{xz}, P_{yz}, $\frac{1}{2}(P_{xx} - P_{yy})$, and $\frac{1}{2}(P_{yy} - P_{zz})$. Fig. 4.17 shows the integrals of the zero shear relaxation modulus up to time t,

$$\eta(t) = \int_0^t G(t)\, dt, \tag{4.44}$$

for the three mesoscopic models, together with the Rouse predicted integrals using the effective first Rouse times τ_1^{eff} (dotted lines). The unentangled system without chain stiffness (dashed line) follows the Rouse curve quite well, so the viscosity equals that of the corresponding Rouse chain, i.e. 2.5 cP. With chain stiffness (dot-dashed line) the integral systematically lies beneath the Rouse result. This can be explained by the fact that the viscosity of a Rouse melt is proportional to the sum of all relaxation times (see the Appendix of *Chapter 3*). The Rouse curve in Fig. 4.17 was calculated using a relaxation time spectrum obtained from the first, largest scale relaxation time, but as it was shown before the small scale modes actually have shorter relaxation times. Still, the increased chain stiffness has increased the viscosity to approximately 3.6 cP. The result of the entangled system is quite remarkable (solid line). Initially it follows the Rouse prediction up to $t = 5$ ns, but then continues to increase where the Rouse prediction is already converged. The following mechanism may explain this result: initially the stress due to intrachain interactions predominates the stress

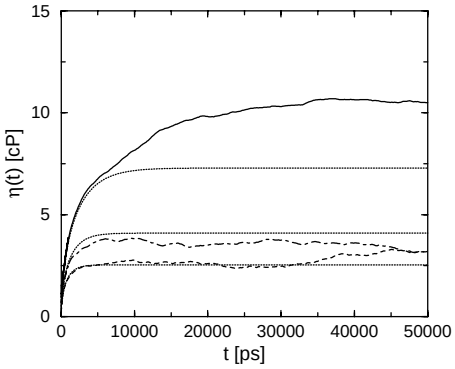

Figure 4.17: Integral of the zero shear relaxation modulus up to time t, Eq. (4.44), of entangled chains (solid), and unentangled chains with (dot-dashed) or without chain stiffness (dashed). The dotted lines show the Rouse integrals determined by using the longest effective relaxation time τ_1^{eff}.

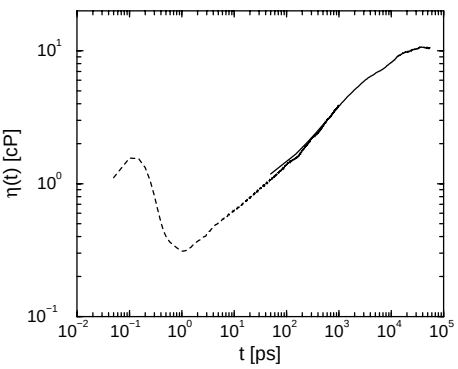

Figure 4.18: Integral of the zero shear relaxation modulus up to time t of the entangled mesoscopic model (solid) and from microscopic molecular dynamics simulations (dashed) on a double-logarithmic scale.

due to interchain interactions and the relaxation is rather Rouse-like. However, after the intrachain stress has relaxed, the interchain stress still remains. This interchain stress relaxes slower than the slowest intrachain relaxation, i.e. slower than τ_1. This interchain stress will eventually bring about the plateau modulus for longer chains.

Fig. 4.18 shows the integrals of both the microscopic and entangled mesoscopic systems on a double-logarithmic scale. Here the strength of the coarse-grained simulation combined with the entanglement algorithm is apparent: after a comparable run time of a few months, the microscopic simulations reached correlation times up to 1 ns, while the coarse-grained simulations reached up to 50 ns (notice that the coarse-grained system contained ten times as many chains). At medium long times the mesoscopic results are nicely following the microscopic results, so we have confidence that the coarse grained model can predict the viscosity. From the asymptotic value of the integral we estimate the viscosity of a $C_{120}H_{242}$ chain at 450 K to be $\eta \approx 10.5$ cP. This is in good agreement with (interpolated) experimental results of Pearson *et al.*, who found $\eta_{\text{exp}} \approx 13.5$ cP. [106]

4.6 Conclusions

We have investigated the influence of uncrossability constraints on the dynamics of coarse-grained polymer melts. In the first part of this work we have described how such a constraint may be implemented in a continuum simulation model. We next have applied our method to a $C_{120}H_{242}$ melt, represented by chains composed of six blobs. In order to investigate the importance of various aspects of our model, we have simulated two other systems, both with-

out the uncrossability constraint: one with and one without chain stiffness. We have found that the uncrossability constraint is essential to reproduce microscopic dynamic correlation functions. We summarize our findings in the following points:
1. Neither one of the unentangled systems shows a subdiffusive exponent in the mean square displacement of the center of mass of the chain; the entangled system does. The subdiffusive exponent must be caused by uncrossability interactions with the surrounding chains.
2. The Rouse mode autocorrelation functions of the unentangled system without chain stiffness are rather Rouse-like. The other two systems clearly display a stretching of the exponential decay, which becomes most pronounced for the smallest scales in the entangled system ($\beta = 0.77$). For stiff chains, the effective relaxation rates of small scale modes increase and those of large scale modes decrease, in agreement with semiflexible chain models. The uncrossability constraint causes an even slower relaxation of the large scale modes.
3. The single chain dynamic structure factor of the unentangled system without chain stiffness displays a Rouse-like decay. The incorporation of chain stiffness yields slower decaying curves, but this is not enough to reproduce the microscopic data. For q values smaller than 1.8 nm^{-1} the results of a microscopic simulation are well-reproduced by the entangled system. Results for larger q values can not be reproduced because the coarse-grained simulations suffer from a lack of microscopic detail.
4. The shear relaxation modulus of the unentangled system without chain stiffness behaves Rouse-like. The inclusion of chain stiffness has some effect because the relaxation spectrum is modified. In the entangled system an initial Rouse-like relaxation is observed. After $t = 5$ ns the chain relaxes more slowly than a Rouse chain. This must be due to a very slow interchain stress relaxation caused by the uncrossability of chains. This interchain stress is dominated by the intrachain stress relaxation at shorter times. The viscosity found for this system ($\eta \approx 10.5$ cP) is close to experimental findings.

In *Chapter 5* we will increase the chain length N to investigate the scaling of dynamic properties. We will pay attention to the entanglement length and investigate how a plateau in the shear relaxation modulus develops with increasing N.

5 Time and length scales of polymer melts studied by coarse-grained molecular dynamics simulations

We present coarse-grained molecular dynamics simulations of linear polyethylene (PE) melts, ranging in chain length from C_{80} to C_{1000}. The employed effective potentials, frictions, and random forces are all derived from detailed molecular dynamics simulations, leaving no adjustable parameters. Uncrossability constraints are introduced in the coarse-grained model to prevent unphysical bond crossings. The dynamic and zero-shear rate rheological properties are investigated and compared with experiment and other simulation work. In the analysis of the internal relaxations we identify a new length scale, called the slowing down length N_s, which is smaller than the entanglement length N_e. The effective segmental friction rapidly increases around N_s leading, at constant density, to a transition in the scaling of the diffusion coefficient from $D \sim N^{-1}$ to $D \sim N^{-2}$, a transition in the scaling of the viscosity from $\eta \sim N$ to $\eta \sim N^{1.8}$, and conspicuous non-exponential relaxation behavior. These effects are attributed to strong local kinetic constraints caused by both chain stiffness and interchain interactions. The onset of non-local (entanglement) effects occurs at a chain length of C_{120}. Full entanglement effects are observed only above C_{400}, where the shear relaxation modulus displays a plateau and the single chain coherent dynamic structure factor agrees with the reptation model. In this region the viscosity scales as $\eta \sim N^{3.6}$, the tube diameter is $d \approx 5.4$ nm, the entanglement molecular weight is $M_e \approx 1700$ g/mol, and the plateau modulus is $G_N^0 \approx 2.4$ MPa, all in good agreement with experimental data.[*]

5.1 Introduction

Long-chain polymer liquids are well-known for their peculiar viscoelastic behavior. The relaxation of stress after a step shear strain at first occurs in a liquidlike fashion, but soon, at least if the molecular weight is sufficiently large, a plateau is reached very similar to what is found in solids and rubbers. In the long run, the remaining stress of course relaxes, as

[*] The work described in this chapter previously appeared in J. Chem. Phys. **117**(2), 925 (2002). [98]

it must in a liquid. The range of time scales associated with these relaxations can be enormous. On the shortest time scales, processes such as atomic bond vibrations and torsional jumps are important, whereas the longest time scales are associated with the escape of chains from entanglements with other, surrounding chains. This escaping time depends strongly on molecular weight and scales approximately with the molecular weight to the power of 3.4, irrespective of the chemical details of the polymer.

Because of the enormously large relaxation times, conventional atomistic molecular dynamics simulations of long-chain polymer melts are practically impossible. Such simulations have been performed only for medium long chains up to about 150 monomers. [51, 52, 82–84, 96, 100–102] At first glance these simulations seem to indicate that the dynamics and rheology of medium long chains may well be described by the Rouse model. [118] Yet the applicability of this inherently single chain model has been questioned in literature, especially as far as the rheology is concerned, because an important part of the shear stress is observed to arise from the intermolecular interactions. [35, 43, 47] In *Chapter 4*, we have shown that interchain interactions are important in the shear relaxation of $C_{120}H_{242}$.

In order to simulate dynamical and rheological behavior of long chains one has to resort to coarse-grained models. [48, 63, 66, 68, 97, 107, 130, 131] Usually, the interactions between two coarse objects, called blobs from now on, are chosen such that bond crossings will be energetically unfavorable. The range of the repulsive forces is then necessarily of the order of the maximum separation of two bonded blobs. If one wants to avoid using physically unrealistic models, this sets a severe limit to the number of monomers which may be represented by one blob. Moreover, no systematic method exists to calculate model parameters on the coarse level from atomistic, i.e., chemically realistic simulations. Of course one may fix time and length scales by mapping/adjusting simulation to experimental results, but usually it is doubtful with these models whether one and the same set of mapping parameters is able to describe all experimental data. In *Chapter 4* we proposed a model whose parameters were calculated from a short molecular dynamics simulation. A friction 'frequency' ξ, though, had to be obtained by trial and error while adjusting the results of a mesoscopic simulation with those of an atomistic simulation in the time regime where both are applicable. In the Appendix of this chapter we present a direct way to calculate ξ from microscopic simulations, thereby turning the whole procedure into an "*ab initio*" calculation. Obviously *ab initio* is not meant in a quantum-chemical sense, but in the sense that we start at the lowest relevant scale for statistical simulations. In statistical physics the interactions between the constituent particles are considered to be a prescribed basic ingredient. (There are two reasons to do *ab initio* quantum-chemical simulations like, e.g., Car and Parrinello simulations: first, if one is interested in restructuring of electronic densities, and second, in cases when no simple interaction model can be formulated and one is obliged to calculate forces on the fly.)

In this chapter we present the results of various dynamic properties of polyethylene, obtained by simulations on 7 processors of an SGI Origin 2000 system (UNITE) for more than one year. We will focus on the determination of characteristic length scales, particularly the entanglement length, and try to gain insight in the origin of these length scales.

5.2 Method

5.2.1 Coarse-grained interactions and uncrossability of chains

In the simulation a blob represents the center of mass of λ consecutive monomers. The fundamental difference with some other polymer simulation models, such as the FENE model of Kremer *et al.*, [66] is that λ may be chosen arbitrarily and is not determined afterwards by a mapping procedure to relate the simulation results to experimental values. This is possible because the interaction model is not fixed *a priori*, but derived without any adjustable parameters from short microscopic simulations of the material under consideration. The number of monomers per blob is however not completely arbitrary. If spherical interactions are assumed, λ should not be so large that the size of the blob exceeds the typical diameter of the tube in the reptation picture. In that case, it would be impossible for the model to display a tube of realistic proportions. For practical purposes, λ must not be too small either. In the first place, much is gained if λ is as large as possible to allow for a large integration time step. Secondly, λ must be large enough to be able to treat the complementary $3(\lambda-1)$ coordinates per blob of the microscopic constituents as bath variables, i.e., to take their effects into account through random forces which perturb the time evolution of the blob positions. If the random forces decorrelate much faster than the blob momenta, the random force correlations may be represented by delta functions (Markov approximation) and the equations of motion are of the simplest Langevin type:

$$M\frac{d^2\mathbf{R}_i}{dt^2} = -\nabla_i\chi - M\xi\frac{d\mathbf{R}_i}{dt} + \mathbf{F}_i^R, \tag{5.1}$$

where $\mathbf{R}_i$ is the position of blob i, M is its mass, and ξ is the blob friction frequency, related to the random force $\mathbf{F}^R$ through the fluctuation dissipation theorem. In Eq. (5.1) we have implicitly assumed that the friction on each blob is isotropic and independent of the positions of the other blobs, in which case the friction is a scalar quantity. In *Appendix 5.A* we describe how this quantity can be calculated from short atomistic simulations. The free energy χ, which is the potential of mean force, can be calculated from

$$\chi(\mathbf{R}^n) = -kT\ln P_n(\mathbf{R}^n). \tag{5.2}$$

Here P_n is the n-blob distribution function which is determined from the microscopic system by averaging over the bath variables. It is assumed that this distribution can be factorized into independent pairwise and angular parts. At first sight this assumption may seem rather crude, and better methods to estimate the effective interactions are available, such as the method described by McCoy an Curro, [78] who mapped explicit atom onto united atom potentials. However, this method may run into problems if applied to polymers, because two non-bonded blobs which are nevertheless part of the same chain are not independent entities; the interactions between two such blobs are not determined by interactions between the atoms of these blobs alone.[1] Fortunately, the long time dynamics and rheology of polymer chains is dominated not so much by the details of the interactions, but by the fact that chains can not cross each other.

1 H. Fukunaga, personal communication.

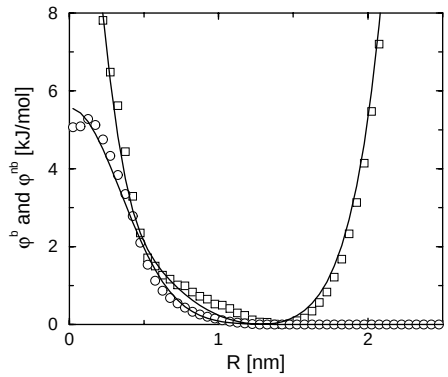

Figure 5.1: The potential of mean force between nonbonded (circles) and bonded (squares) blobs. These potentials were obtained from the distribution functions measured in atomistically detailed molecular dynamics simulations of $C_{120}H_{242}$ at the same temperature and density as the current simulations. The solid lines are fits with simple analytical functions, as described in *Chapter 4*.

Now, in this work we will investigate polyethylene melts at a temperature of 450 K and a constant density of 0.761 g/cm^3. In *Chapter 4* we argued that a suitable level of coarse-graining for this material is $\lambda = 20$, which is well below any reported entanglement length. In atomistic molecular dynamics simulations of a melt of $C_{120}H_{242}$ chains the blob distibution functions were measured. From these we calculated the interaction potentials. The interactions between pairs of bonded and pairs of nonbonded blobs are shown in Fig. 5.1. Because the degree of coarse-graining is so high, the blobs are rather 'empty' and the interactions between blobs are very soft. Consequently, in the mesoscopic simulations based on the above Langevin equation, without additional measures unphysical bond crossings will be probable. To prevent this from happening, an uncrossability constraint is applied. The idea behind this constraint is to consider the bonds between consecutive blobs to be elastic bands. As soon as two of these elastic bands make contact, an 'entanglement' is created at the crossing position $\mathbf{X}$ which prevents the elastic bands from crossing. This is accomplished by defining the attractive part of the potential between bonded blobs i and $i+1$ to be a function of the path length $L_{i,i+1}$ of the bond, going from one blob (i) to the next ($i+1$) *via* the intermediate entanglement:

$$L_{i,i+1} = \left|\mathbf{R}_i - \mathbf{X}\right| + \left|\mathbf{X} - \mathbf{R}_{i+1}\right|. \tag{5.3}$$

See Fig. 5.2 for a sketch of this situation. The position of the entanglement is determined by the requirement that there is always an equilibrium of forces at the entanglement. Of course more than one entanglement per bond is allowed. Details about this and more about the uncrossability constraint can be found in *Chapter 4*.

We stress that the entanglements are created and annihilated according to the dynamics of the system itself and no network structure is imposed *a priori*. The uncrossability constraints are called 'entanglements' for simplicity, but they are not the classic entanglements which form a network of effective tubes and attribute to the long time stress. This work is therefore conceptually very different from work of, e.g., Masubuchi *et al.* [76] who coarse-grained at the level of segments between consecutive entanglements, therefore imposing a network of primitive chains. In Subsec. 5.3.1 we will focus on the characteristics of the uncrossability constraints.

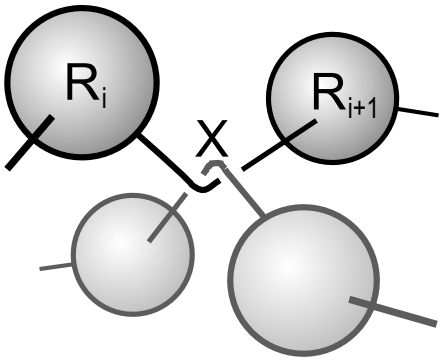

Figure 5.2: Sketch of two "entangled" parts of chains. At an earlier time, the bonds between the two depicted pairs of blobs tried to cross each other. This caused the uncrossability constraint to insert an "entanglement" at the crossing point. Since then the attractive part of the potential between bonded blobs is a function of the path length from blob i, via the entanglement at **X**, to blob $i+1$.

Species	N	n_{chain}	L [nm]	$\langle R_g^2 \rangle$ [nm^2]	$\langle R_e^2 \rangle$ [nm^2]
C_{80} / B_4	4	180	7.61	1.51	10.2
C_{120} / B_6	6	120	7.61	2.51	16.3
C_{200} / B_{10}	10	100	8.49	4.05	25.3
C_{400} / B_{20}	20	80	9.93	9.05	54.9
C_{600} / B_{30}	30	80	11.37	14.9	91.8
C_{800} / B_{40}	40	80	12.51	21.6	132.2
C_{1000} / B_{50}	50	80	13.48	27.2	167.3

Table 5.1: Polymer species, number of blobs N per chain, number of chains n_{chain}, length L of the simulation box, the mean square radius of gyration $\langle R_g^2 \rangle$, and mean square end-to-end distance $\langle R_e^2 \rangle$ of the systems studied.

5.2.2 Equilibration and characterization of the systems under study

In this chapter we investigate melts of seven different chain lengths, ranging from $C_{80}H_{162}$ to $C_{1000}H_{2002}$, hereafter referred to as B_4 to B_{50}, after the number of blobs representing one chain. An overview of the systems is given in Table 5.1. In order to avoid significant interactions of a chain with its periodic images, the number of chains in each system was chosen such that the length of the periodic simulation box was at least the root mean squared end-to-end distance of a polymer chain. A similar criterion was adopted by Kremer and Grest. [66] To check finite size effects, they analyzed a melt of FENE chains of length 200 (comparable to our B_{30}) for two system sizes, one with 20 and one with 100 chains. Although the static dimensions of the chains depended slightly on the system size, all dynamic results for both system sizes were found to be the same within the statistical errors. We are therefore confident that the sizes of the systems studied in this work are sufficiently large.

Unlike microscopic chains, well-equilibrated initial configurations of mesoscopic chains can be realized with comparative ease due to the softness of the interactions and the possibility to relax the configurations *before* imposing the uncrossability constraint. Initial configurations of the chains were generated according to the distribution functions obtained from microscopic simulations and were placed and oriented randomly in the simulation box. The repulsive force between nonbonded blobs was initially set to 1/10th of its final value in order to gently push blobs with large overlap apart, while allowing all bonds to cross each other. After this initial homogenization, the nonbonded force was gradually increased to reach its final value. The melts were then equilibrated for at least one rotational relaxation time. This was possible because the longest relaxation times of crossing chains are much shorter than those of non-crossing chains. Finally, the uncrossability constraint was switched on. The number of entanglements was monitored and observed to reach an equilibrium value (in an average sense) within a few nanoseconds for *all* systems. Non-diagonal components of the stress tensor were also monitored and found to be zero on average.

To check whether the equilibration of the chain structure was successful at all relevant length scales, the Rouse modes of the chains were studied. For a finite chain of length N these are given by [13]

$$\mathbf{X}_k = \frac{1}{N}\sum_{j=1}^{N} A_{kj}\mathbf{R}_j \qquad (k = 0,\ldots,N-1), \tag{5.4}$$

where A_{kj} is defined as

$$A_{kj} = \cos\left[\frac{k\pi}{N}\left(j-\frac{1}{2}\right)\right]. \tag{5.5}$$

The zeroth Rouse mode is the position of the center of mass of the chain. All other modes describe the internal configuration of the chain, mode number k describing a wavelength corresponding to a subchain of N/k blobs. According to Rouse theory, the amplitudes should obey the scaling relation

$$\left\langle \mathbf{X}_k^2 \right\rangle = \frac{b^2}{8N\sin^2\left(\frac{k\pi}{2N}\right)}. \tag{5.6}$$

We calculated $\left\langle \mathbf{X}_k^2 \right\rangle \cdot 8N\sin^2\left(\frac{k\pi}{2N}\right)$ for each chain length and mode number. According to Eq. (5.6), for an ideal chain this should be constant and equal to the square of the statistical segment length b. Our chains however are not ideal, mainly because of the angular potential which gives them some stiffness. The stiffness will have the strongest effect on the smallest length scales, but no effect on the very large length scales where ideal random walk statistics should be obeyed. More importantly, if the systems are well-equilibrated, we expect that the data of all the chains collapse onto one single curve if it is plotted against the natural scale N/k. As can be seen in Fig. 5.3, this is indeed the case. From the limiting value we can estimate the statistical segment length to be $b^2 \approx 3.3$ nm^2. As can be seen in Table 5.1, the mean square end-to-end distance and mean square radius of gyration of the longest chains obey random walk statistics, i.e., $\left\langle R_e^2 \right\rangle = Nb^2$ and $\left\langle R_g^2 \right\rangle = \frac{1}{6}Nb^2$. In view of the above, we are confident that all starting configurations have relaxed sufficiently.

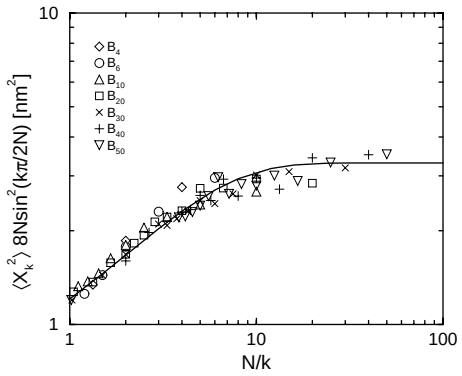

Figure 5.3: Rouse amplitudes vs N/k for several values of k and N. The results are scaled such that the data would fall on a horizontal line for ideal chains. The line is a guide to the eye.

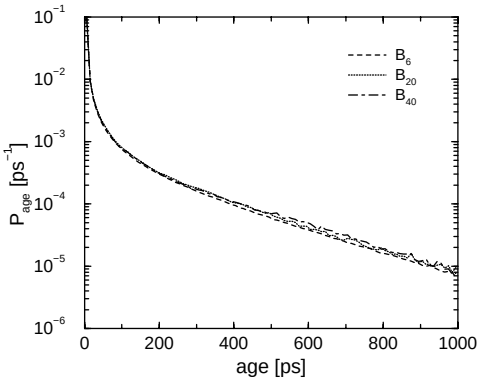

Figure 5.4: Probability that an "entanglement" (uncrossability constraint) dies at a given age. Effective entanglements, which contribute to the long time stress, are rare but more common than one would estimate from this plot (see text).

5.3 Results

5.3.1 Entanglement characteristics

During the simulations the chains try to cross each other in which case the uncrossability constraint creates entanglements. Entanglements are also annihilated because chains slip off the ends of other chains, they unknot, or simply because chains move apart again. Obviously, the number of entanglements is not constant but fluctuating in time. The long-time average number of entanglements however was found to be constant and equal to 2.5 entanglements per bond in all systems. Many of these entanglements were short-lived. Accordingly, only a few contributed significantly to long time interactions between different chains and therefore to the long time stress. To quantify this, we present in Fig. 5.4 the probability P_{age} of an entanglement to reach a certain 'age'. Age is defined here as the time interval between the creation and annihilation of a certain entanglement. There are two prominent features in the plot of P_{age}: (*i*) After a sharp initial drop the probability decreases exponentially with age. From the slope in the semilogarithmic plot we derive a characteristic decay time of 230 ps. (*ii*) Somewhat surprisingly, also at the long life times, all curves coincide. This proves that even B_6 behaves as a chain, not as a small molecule. Apparently the influence of the chain ends on the life time of uncrossability constraints is very small.

We expect a larger influence of the chain ends on the *effective* number of entanglements which do get old and contribute significantly to the long time stress. The calculation of the number of such effective entanglements is however complicated by the fact that in determining the age we have disregarded the possibility that two entangled chains, due to some fluctuation, move apart for a very short time after which they entangle again at approximately

the same location. Although this would be the same entanglement effectively, it is treated as a new entanglement in the calculation of P_{age}. In this work we will not try to correct for this, for instance by allowing two parts of chains to be separated for a specified maximum time interval and maximum relative displacement, because new and non-trivial variables would need to be introduced. Instead, we will calculate the effective number of entanglements from the influence they have on the dynamic and rheological properties. In the following subsections we will focus on these properties and find that only one in every 15 entanglements will be effective in creating a 'tube', i.e., we will find that the classic entanglement length of our model polyethylene is $N_e \approx 6$ blobs.

5.3.2 Slowing down of Rouse mode relaxations

In Sec. 5.2 we checked the equilibration of the chain structure by analyzing the Rouse mode amplitudes, Eqs. (5.4) to (5.6). We will now focus on the time dependence of these Rouse modes because they reveal the relaxation dynamics at different length scales. Within the Rouse model, for ideal chains, each of the modes relaxes independently and exponentially with a relaxation time τ_k,

$$C_k(t) \equiv \left\langle \mathbf{X}_k(t) \cdot \mathbf{X}_k(0) \right\rangle / \left\langle \mathbf{X}_k^2 \right\rangle = \exp\left(-t/\tau_k\right), \tag{5.7}$$

$$\tau_k^{-1} = 4W \sin^2\left(\frac{k\pi}{2N}\right), \tag{5.8}$$

where the relaxation rate W is a characteristic frequency of the Rouse model and is given by:

$$W = \frac{3kT}{M\xi b^2}. \tag{5.9}$$

For realistic polymer chains, however, it is not expected that the Rouse modes are the normal modes (in a dynamic sense; the static cross-correlations *are* zero), because the nonbonded interactions and uncrossability constraints modify the equations of motion and make them highly nonlinear. [114, 126] As a consequence, the Rouse modes may no longer relax exponentially. As was already observed in other simulation work, [100–102, 126, 129] we find that the Rouse mode autocorrelations of polymer chains can better be described by a stretched exponential form,

$$C_k(t) = \exp\left[-\left(t/\tau_k^*\right)^{\beta_k}\right], \tag{5.10}$$

where the relaxation times τ_k^* and stretching parameters β_k depend on mode number k and on the chain length. The Rouse modes were measured and fitted to Eq. (5.10) by calculating minus the natural logarithm of the normalized autocorrelations and plotting them on a double-logarithmic scale. A typical example is given in Fig. 5.5, where this procedure has been applied to several Rouse modes of the B_{30} system. Consistent with Eq. (5.10) straight lines result, with a slope equal to β_k and an intercept (at some time $t > 0$) proportional to $1/\tau_k^*$. In Fig. 5.6 we show the original data, together with the fits from Fig. 5.5, on a semilogarithmic scale. Notice that the fits do well in describing the data and that the non-exponentiality of

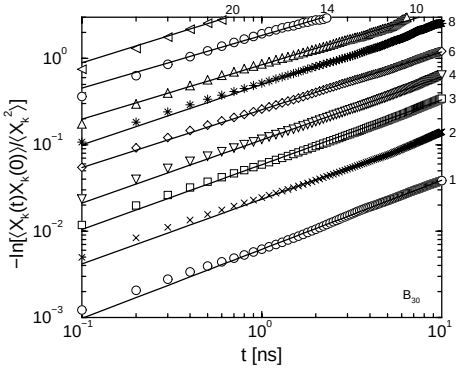

Figure 5.5: Rouse mode relaxations in the B_{30} system, scaled as $-\ln\left[C_k(t)\right]$ on a double logarithmic scale to extract the stretching parameters β_k. Solid lines are the fits. Mode numbers are given along the top and right side of the plot.

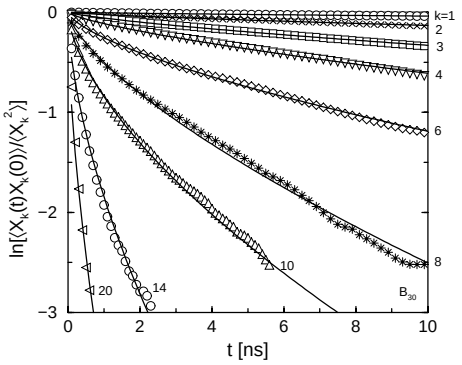

Figure 5.6: Rouse mode relaxations in the B_{30} system, scaled as $\ln\left[C_k(t)\right]$ on a linear scale, showing the non-exponentiality of the simulation data. Solid lines are the fits. The fit quality for $k = 1$ is better appreciated in Fig. 5.5.

the data is strongest around $k = 14$. In Fig. 5.7 we have plotted β_k for all chain lengths and all mode numbers against the mode wavelenth N/k. The data more or less collapse on to the same curve, at least for $N > 6$ and N/k smaller than about 6. At the smallest length scales β_k is approximately 0.7. Then a minimum of approximately 0.5 occurs around $N/k \approx 2$, after which β_k increases again to a value of approximately 0.8 at the largest scale of each chain.

The non-exponential relaxation of the Rouse modes is not specific to our model. Shaffer placed polymers on a lattice and applied uncrossability constraints. [126] He also found deviations from exponential behavior, very similar to what we find. Shaffer interpreted the devation of β_k from unity to reflect the severity of kinetic constraints. He suggested that the results may also be interpreted in the framework of the coupling model of Ngai and coworkers, in which the degree of non-exponentiality is associated with the cooperativity that is required for configurational relaxation in the presence of entanglement constraints. [88–90] With these interpretations in mind, Fig. 5.7 suggests that the effect of kinetic constraints and/or the required cooperativity is most severe around $N/k \approx 2$. We will introduce a separate symbol for this length scale: N_s, where the 's' stands for 'slowing down', because the dynamics of the chain is strongly slowing down at this length scale. Notice that we do not interpret this length scale as the entanglement length N_e from classic reptation theory.

The slowdown of dynamics at various length scales becomes clearly perceptible if we analyze the Rouse mode relaxation times. Note that the parameter τ_k^* is not very useful in itself because the instant relaxation rate at any time t depends on all three t, τ_k^* and β_k. In analogy with Shaffer's work, we calculate the effective relaxation times as time integrals over

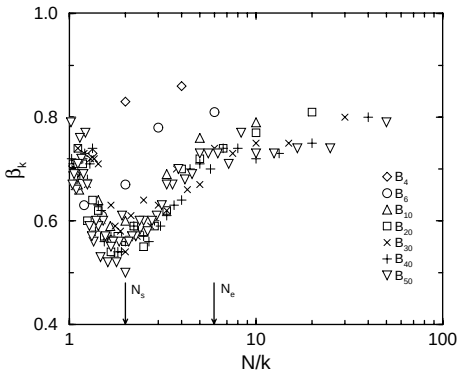

Figure 5.7: Stretching parameters β_k vs N/k for several values of k and N. A distinct minimum is observed at $N/k = N_s \approx 2$.

the normalized relaxation functions. From Eq. (5.10) we find:

$$\tau_k^{\text{eff}} = \int_0^\infty C_k(t)\,dt = \int_0^\infty \exp\left[-(t/\tau_k^*)^{\beta_k}\right] dt = \frac{\tau_k^*}{\beta_k}\Gamma\left(1/\beta_k\right), \tag{5.11}$$

where $\Gamma(x)$ is the gamma function. The corresponding effective Rouse rate is defined as

$$W_k^{\text{eff}} = \left[4\tau_k^{\text{eff}} \sin^2\left(\frac{k\pi}{2N}\right)\right]^{-1}, \tag{5.12}$$

which, in the case of Rouse chains, is a constant and equal for all chain lengths. In Fig. 5.8(a) we have plotted the effective Rouse rates for all chain lengths and all mode numbers against the mode wavelength N/k. It is interesting to see that the data of each chain length follow the same 'universal' curve until they depart to reach a plateau at a value which differs for each chain length. The universal curve has the following characteristics:

1. Initially the effective Rouse rate is constant, which means that the effective relaxation times scale like predicted in Eq. (5.8). This regime is very small, only up to about 1.5 blobs. In this respect we can say that only the very small length scales behave Rouse-like.

2. Then there is a sharp drop in the effective Rouse rate. The curve has an apparent minimal slope of -2 in the neighbourhood of N_s. This means that the effective relaxation times scale like $\tau_k^{\text{eff}} \sim (N/k)^4$ in this regime.

3. A regime with slope -1 starts at about $1.5N_s$ and ends when a plateau is reached. The effective relaxation times in this regime scale like $\tau_k^{\text{eff}} \sim (N/k)^3$.

Both the second and third regimes are quite distinct from the predictions of both Rouse ($\sim N^2/k^2$) and reptation ($\sim N^3/k^2$) models. We will return to this in the discussion. The occurrence of a plateau in the W_k^{eff} data is in agreement with the reptation model although other models which also predict a plateau cannot be ruled out, such as the generalized Rouse approach by Hess. [57] The original reptation theory predicts that the relaxation time of a Rouse

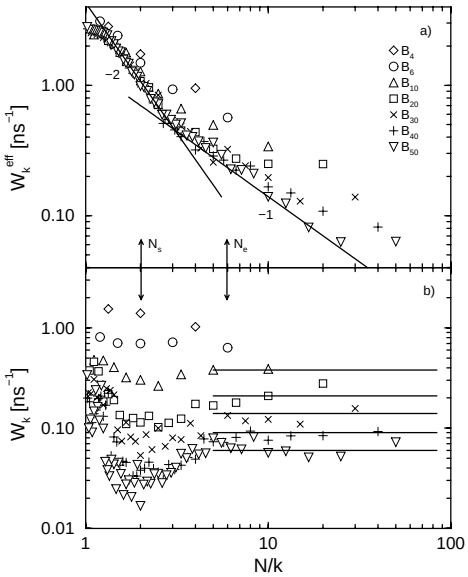

Figure 5.8: Effective Rouse relaxation rates (a) and terminal Rouse relaxation rates (b) vs N/k for several values of k and N. The lines in (a) show the scaling regimes $\tau_k^{\text{eff}} \sim N^4/k^4$ and $\tau_k^{\text{eff}} \sim N^3/k^3$. The lines in (b) show the $\tau_k^l \sim N^{3.5}/k^2$ scaling for scales larger than N_e, in agreement with reptation theory.

mode k with $N/k > N_e$ is enhanced by a factor $3N/N_e$ compared to the Rouse model, [30] i.e., the plateau of W_k should decrease proportional to N^{-1}. The plateau values in Fig. 5.8(a) decrease somewhat faster, approximately with $N^{-1.5}$. This can be explained by including contour length fluctuations in the reptation theory. [30] The chain ends have a large effect on the relaxation times in chains which are not far above the entanglement length, such as our chains.

5.3.3 Disentanglement times

Contrary to what we would expect, the plateau in Fig. 5.8(a) is restricted to the first few modes, even for the longer chains. The same observation was made by Shaffer. [126] We should keep in mind, however, that we have calculated effective relaxation times, Eq. (5.11), which are largely dominated by the relaxations at short times, where the correlations still differ appreciably from zero. If we want to obtain information about their long time behavior, we are forced to investigate the correlation functions themselves. According to reptation theory, the Rouse mode correlation functions decay exponentially, with characteristic times $\tau_k \sim N^3/k^2$, at times larger than the time τ_r it takes for the chain to relax along its own primitive path, and for values of k such that $N/k > N_e$. In the original application of the reptation model τ_r was assumed to be the Rouse time τ_R of a hypothetical chain which does not feel the tube constraints. We shall refrain from this interpretation and continue to use τ_r for the time when reptation sets in. Since at times larger than the disentanglement time τ_d each chain will have found a completely new environment, the Rouse mode correlation functions will decay exponentially at these times, and consequently $\tau_r \leq \tau_d$. The Rouse

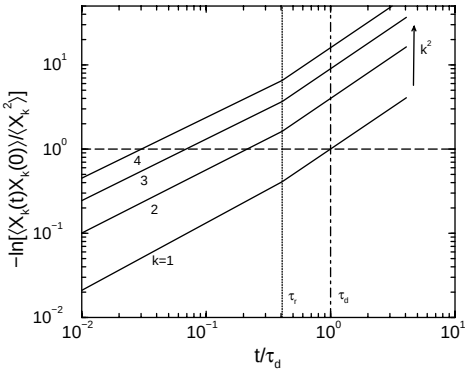

Figure 5.9: Relaxation of the Rouse modes (schematically) for different mode numbers. The chain has relaxed along the primitive path at τ_r, after which all modes relax exponentially. At the disentanglement time τ_d the relaxation of the first mode is by definition $1/e$ (dashed line). The long time relaxation times scale as $1/k^2$ with mode number.

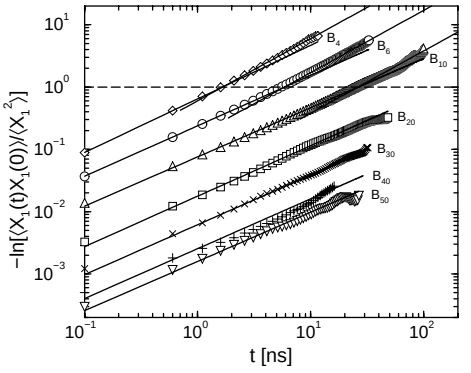

Figure 5.10: Relaxation of the first Rouse mode for different values of N (symbols). The data is scaled in the same way as in Fig. 5.5. Solid lines are fits to the relaxation regime $t < \tau_r$, with slope $\beta_1 = 0.8$ (except for the B_4 system), and the regime $t > \tau_r$, with slope 1, respectively. The horizontal dashed line indicates where $C_1(t) = 1/e$.

mode correlation functions then behave according to

$$C_k(t) = \begin{cases} \exp\left[-\left(t/\tau_k^*\right)^{\beta_k}\right] & \text{for } t < \tau_r, \\ \exp\left[-\left(t/\tau_k^l\right)\right] & \text{for } t > \tau_r, \end{cases} \tag{5.13}$$

where τ_k^l is the terminal (long time) relaxation time. The exponential decay time of the first mode is the above mentioned disentanglement time, i.e., $\tau_1^l = \tau_d$. $C_k(t)$ then decays as schematically depicted in Fig. 5.9. Notice that at time $t = \tau_d$, $C_1(t)$ has decayed to $1/e$ of its original value at $t = 0$. $C_k(t)$ with mode numbers k larger than 1 decay faster.

We expect that for the shorter chains, although already strongly influenced by entanglements, the primitive paths are still too short for reptation to be applicable, and that consequently "τ_r" $\approx \tau_d$. Only for very long chains will τ_r substantially differ from τ_d. In Fig. 5.10 we investigate the relaxation of the first Rouse mode of each chain length. The data for $N < 20$ clearly display a crossover from a short time relaxation with $\beta_1 \approx 0.8$ to a long time exponential relaxation. For each of these chain lengths, the two asymptotes intersect at $-\ln C_1(t) = 1$ (dashed line in Fig. 5.10), i.e., when the normalized autocorrelation has decayed to $1/e$. So indeed we find that for these chain lengths we have $\tau_r = \tau_d$, i.e., the chain has never completely relaxed along its primitive path until a new environment is found. For $N \geq 6$ times τ_r are certainly larger than the Rouse times τ_R of unentangled chains. Values of τ_R can be estimated from the work in *Chapter 4* where we investigated chains which were able to cross each other. The effective Rouse rate of large scale modes was found to be $W \approx 1.2$ ns^{-1}. This yields estimates of τ_R listed in the second column of Table 5.2. Only for

N	τ_R	k=1	2	3	4	5	6	7	8	9	10	15	19	29	39	49
4	1.42	1.62	0.29	0.10												
6	3.10	5.67	1.05	0.34	0.14	0.09										
10	8.5	25.3	4.99	1.83	0.84	0.39	0.21	0.15	0.11	0.10						
20	34	140	38	16.6	8.0	3.9	2.7	1.68	1.02	0.61	0.47	0.13	0.09			
30	76	559	162	52	24.0	11.6	10.2	5.9	3.4	2.5	1.86	0.49	0.21	0.10		
40	135	1687	359	121	61	27.3	20.5	12.7	9.1	5.6	5.3	1.59	0.57	0.14	0.09	
50	211	3367	925	346	128	73	34	23.4	17.8	10.9	7.2	2.37	1.33	0.27	0.11	0.09

Table 5.2: Calculated Rouse times τ_R (ns) of crossing chains and effective relaxation times τ_k^{eff} (ns) of non-crossing chains for various mode numbers k.

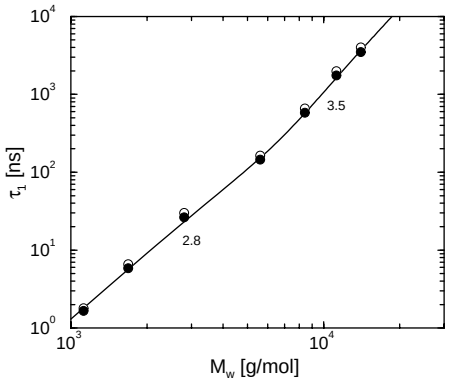

Figure 5.11: Estimated disentanglement times τ_d (filled circles) and effective relaxation times (open circles) as estimated by Eq. (5.11) vs molecular weight M_w. The solid line is a guide to the eye.

$N = 4$ there is agreement between τ_r and τ_R. For both $N = 6$ and $N = 10$ the non-exponential decay persists much longer than τ_R. We assume that the same will hold for $20 \leq N \leq 50$, although no rigorous proof can be given, because the exponential time regime could not be reached. Still, all these chain lengths show the same stretching parameter, $\beta_1 = 0.8$ (solid lines in Fig. 5.10). A deviation is visible in the data of the B_{40} system. Because this deviation is not visible when $N = 30$ nor when $N = 50$, we expect that it is incidental and will disappear after longer averaging. An upper limit of τ_d can be estimated by extrapolating $-\ln C_1(t)$ up to the time where it is equal to 1 (see Fig. 5.9). Since our longest chain length is only about 8 times the entanglement length τ_r will not be very different from τ_d and consequently the real disentanglement time will by very close to this estimate. The scaling of the estimated τ_d with molecular weight is investigated in Fig. 5.11 (filled circles). Two regimes can be distinguished, with scaling exponents 2.8 and 3.5 respectively. The latter value is markedly larger than the pure reptation prediction of 3, but in agreement with the theory if contour length fluctuations are taken into account.

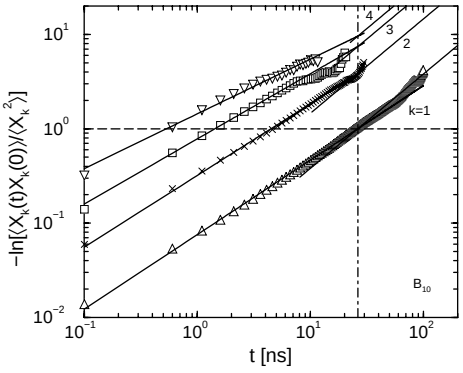

Figure 5.12: Relaxation of modes $k = 1$, 2, 3, and 4 for $N = 10$ (symbols). The data is scaled in the same way as in Fig. 5.5. Solid lines are fits and extrapolations to the relaxation regimes $t < \tau_r$ and $t > \tau_r$ respectively. The horizontal line indicates where $C_k(t) = 1/e$, the vertical dot-dashed line is at $t = \tau_r$.

Next we investigate the long time relaxation of intermediate modes. A typical plot is given in Fig. 5.12 where $k = 1$, 2, 3, and 4 results of the B_{10} system are shown. Although statistical uncertainties arise in the data when $C_k(t) \approx 0$, we clearly find that for each mode $k > 1$ the non-exponential behavior persists far beyond the time when $C_k(t) = 1/e$. We are unable to follow the relaxation into the exponential regime, but we assume that the non-exponential behavior persists up to τ_r, as was stated in Eq. (5.13). The terminal relaxation time τ_k^l of Rouse mode k can be derived from known τ_k^* and β_k data by equating the two regimes in Eq. (5.13) at $t = \tau_r$, resulting in:

$$\tau_k^l = \tau_r \left(\frac{\tau_k^*}{\tau_r} \right)^{\beta_k}. \tag{5.14}$$

The reptation scaling $\tau_k \sim N^3/k^2$ must be valid in the regime $t > \tau_r$. This is checked in Fig. 5.8(b), where we plot the Rouse mode relaxation rates based upon the terminal relaxation times. Indeed, a broad reptation-like plateau is observed for each chain length if $N/k > N_e \approx 6$. A small dip occurs at scales below the entanglement length N_e, with a minimum around $N_s \approx 2$, consistent with the observations made before on the stretching parameter β_k. Contrary to Fig. 5.8(a), the Rouse rates do not converge to some universal curve at the smallest scales. This indicates that Eq. (5.13) does not hold for scales far below N_e. This will have no practical consequences in future applications of Eq. (5.13), however, because the correlation functions of these smallest scale modes are completely negligible in the time regime $t > \tau_r$.

Effective relaxation times can be calculated again as integrals over $C_k(t)$, but now in two parts, one before τ_r and one after. These effective relaxation times are given in Table 5.2 and were actually used to calculate the effective Rouse rates in Fig. 5.8(a). It should be noted, that these relaxation rates are essentially equal to those calculated with Eq. (5.11) for mode numbers two and higher, because the contribution to the integral for times $t > \tau_r$ is negligibly small. Only the effective relaxation time of the first mode is somewhat overestimated by Eq. (5.11), as can be seen in Fig. 5.11.

5.3.4 Slowing down of diffusion

In the previous subsections we have analyzed the internal relaxations of the polymer chains. Now we will investigate the mobility of blobs and centers of mass. Before we do this, we will summarize the reptation model predictions. In the reptation model the effects of the surrounding chains on the dynamics of a polymer chain are incorporated effectively by forcing a Rouse chain to move inside a tube formed by entanglements with other chains. A constant friction with the background and no other constraints besides the tube are assumed. At short times, a blob doesn't know about any tube constraints. The mean square displacement of a blob, defined as

$$g(t) = \frac{1}{N}\sum_{i=1}^{N}\left\langle [\mathbf{R}_i(t) - \mathbf{R}_i(0)]^2 \right\rangle, \tag{5.15}$$

will therefore behave Rouse-like and scale like $t^{1/2}$. (We note that for even shorter times, shorter than the fastest relaxation time of the chain τ_0, $g(t)$ is proportional to t.) When the blob has moved a distance comparable to the tube diameter, the only way for the chain to relax further is along the primitive path. This is supposed to happen at the entanglement time τ_e. The chain next moves, still in a Rouse-like fashion, but now along a quasi one-dimensional path, leading to the famous $t^{1/4}$ power law for the mean square displacement of the blobs. After a certain time τ_r the chain has relaxed along its tube. In the reptation model this time is the Rouse time τ_R. Next, assuming that the tube does not change appreciably, an overal diffusion along the tube is predicted, leading to a second $t^{1/2}$ regime. Finally, after the disentanglement time τ_d, the chain has managed to escape its old tube and create a new one, and the blobs start to diffuse.

It is generally believed now that the reptation model, in its essentials, correctly picks up the physical behavior of polymer melts. This will be confirmed in the following subsections where we will show that 'coarse' quantities, such as the shear relaxation modulus, can well be described by the reptation model. The constant friction approximation, however, is too strict. In reality, as we have seen in the previous subsections, an increasing effective friction is associated with increasing length scales. The increase is strongest around N_s. Because $N_s < N_e$ we expect that the blobs effectively slow down even *before* they have moved a tube diameter distance. The typical time scale τ_s at which this may happen can be estimated from Fig. 5.8(a) and Eq. (5.12) by assuming it to be the effective relaxation time of a subchain of length N_s. This yields a 'slowing down time' $\tau_s \approx 0.47$ ns. In Fig. 5.13, the blob mean square displacement of several chain lengths is plotted against time. Although for $N \geq 20$ we did not reach the diffusion limit, it is clear that longer chains are increasingly slowed down. For B_{50} an effective minimal slope of about 0.4 is measured. Perhaps less clear is the onset of this regime, which agrees with the predicted slowing down time τ_s. The preceding regime, where normal Rouse behavior ($g(t) \sim t^{1/2}$) is observed, turns out to be quite narrow, however. This is a consequence of the fact that we have coarse-grained relatively far, making the fastest relaxation time of the chain come close to the slowing down time τ_s. If we had coarse-grained even further, combining 40 instead of 20 monomers into one blob, this $t^{1/2}$ regime would not have been observed at all. The fastest relaxation time, according to Eq.

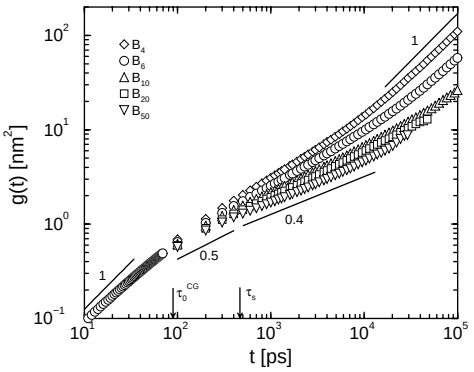

Figure 5.13: Blob mean square displacement $g(t)$ vs t averaged over all blobs for five different values of N. The fastest possible relaxation time in the coarse-grained system, Eq. (5.16), is indicated by the arrow labelled with τ_0^{CG}. The slowing down time is indicated by the arrow labelled with τ_s.

(5.12), is given by:

$$\tau_0^{\mathrm{CG}} = \tau_{N-1}^{\mathrm{eff}} = \left[4W_{N-1}^{\mathrm{eff}} \sin^2\left(\frac{(N-1)\,\pi}{2N} \right) \right]^{-1} \approx \left[4W_{N-1}^{\mathrm{eff}} \right]^{-1}, \tag{5.16}$$

where we have added the superscript 'CG' to indicate that it depends on the level of coarse-graining. The approximation in Eq. (5.16) is valid in case N is large compared to unity. From Fig. 5.8(a) we estimate: $W_{N-1}^{\mathrm{eff}} \approx 2.8$ ns^{-1}, which yields $\tau_0^{\mathrm{CG}} \approx 0.09$ ns. This is in good agreement with the transition from t^1 to $t^{1/2}$, as observed in Fig. 5.13.

The observed minimal slope of 0.4 is not as low as the reptation prediction of 0.25. There are two reasons, which are both related to averaging. First, in going from the atomistic to the blob level we average over some of the atomic movement. Since the mean square displacement of a blob is always less than the mean square displacement of a more detailed particle, but relatively larger differences occur at shorter times, the scaling laws of the blobs are less pronounced than one would expect for more detailed particles. [96] Secondly, we have averaged over all the blobs. It is well known that, because of contour length fluctuations, the entanglement constraints are more easily released at the chain ends than at the inner section of a chain. This was shown in simulations of the FENE polymer model by Kremer and Grest. [66] The pure reptation result will only hold for very long chains where the influence of the chain ends is relatively unimportant. Recently, Pütz *et al.* performed simulations of up to 10000 beads per chain, in which case a minimal slope of 0.26 was observed with great clarity. [107] Our chain lengths are clearly not yet in this long chain limit.

More evidence for the existence of the slowing down length N_s can be found in the molecular weight dependence of the self-diffusion coefficient D. In Fig. 5.14 results by several authors, who performed simulations of *n*-alkanes and polyethylenes, are combined. The open circles are constant density ($\rho = 0.766$ g/cm^3) simulation results of C_6 to C_{66} alkanes at $T = 448$ K by Mondello *et al.* [82, 83] The open square is a constant density ($\rho = 0.777$ g/cm^3) simulation result of C_{100} by Paul *et al.* [100] The latter has been corrected from $T = 509$ to 450 K, in the same way as described in Ref. [100] by using the result for the temperature dependence of the friction as obtained from an analysis of a C_{90} system by Pearson et al., $\xi \sim \exp[1326/(T-149)]$. [106] The closed circles are results from this work, the cal-

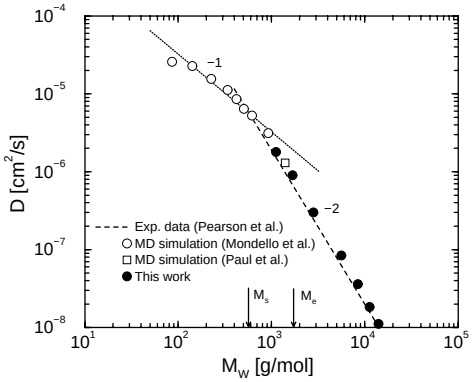

Figure 5.14: Diffusion coefficient D vs molecular weight M_w for polyethylene from different simulation studies (open symbols) and experiment (long dashed line) compared to the present simulation results (closed circles). All simulations were carried out at constant density. The crossover between two scaling regimes is indicated by the arrow labelled with M_s.

culation of which will be explained further on. The diffusion coefficient scales approximately like M_w^{-2} for the larger molecular weights. The low molecular weight data of Mondello *et al.* is more or less consistent with M_w^{-1}. We expect that the agreement with the Rouse model prediction is only fortituous in this regime where chain end effects dominate, as was shown by Harmandaris *et al.* [51, 52] Nevertheless, the crossing over between these two regimes occurs at a molecular weight which is found to correspond well to the slowing down length, $M_s = N_s M \approx 560$ g/mol. Notice that all calculations were performed at approximately the same density, therefore ruling out the possibility that the increase in the effective friction is a density effect.

Pearson *et al.* have measured D in alkane and polyethylene melts at $T = 450$ K. [106] They found that the entire range from $M_w = 600$ to 120000 follow a power law

$$D^{\mathrm{exp}} = 1.65/M_w^{1.98} \qquad (\mathrm{cm}^2/\mathrm{s}) \tag{5.17}$$

This fit is also plotted in Fig. 5.14 (dashed line). It is important to note that the experimental density is not constant, but increasing with molecular weight. However, the experimental density levels off to a value of 0.766 g/cm^3 relatively fast; from $M_w = 600$ onward the increase is less than 5 percent. [106] We can therefore rule out density effects to explain the scaling in this experimental range, and the results can directly be compared with constant density simulations. It is clear from Fig. 5.14 that the simulation results agree well with Eq. (5.17). Below $M_w = 600$ there *is* a large increase in the experimental density, making the effective friction subject to density effects. This explains why the experimental scaling in this regime does not agree with constant density simulation results, such as those of Mondello *et al.* [82, 83]

Pearson *et al.* corrected for the increase in friction factor in order to effectively keep the same distance from the glass transition temperature. He then observed a transition in the scaling of D at a molecular weight which was more in agreement with the entanglement weight M_e from rheological measurements. [106] In this work, however, we put ourselves to the viewpoint that the remaining increase of friction at constant density is a physical effect (we will not try to analyze whether it is a free volume effect or otherwise) that must be reproduced by any realistic simulation model. Indeed, the experimental data is reproduced,

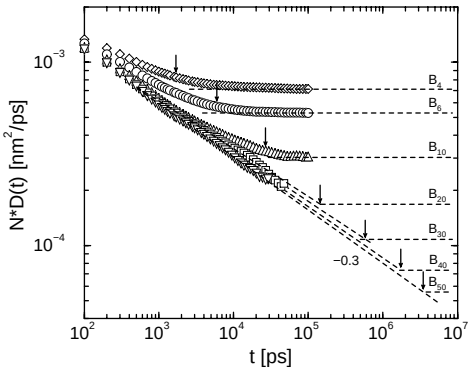

Figure 5.15: Center of mass mean square displacement, scaled such as to represent a time-dependent diffusion coefficient $D(t)$, Eq. (5.19). The dashed lines show the extrapolations to the disentanglement times τ_d (arrows). The symbols are the same as in Fig. 5.13.

and we do not see a transition at M_e. In most other constant density simulation work the transition in D is wrongfully interpreted as the entanglement molecular weight, which may explain some of the discrepancies that arise when comparing with rheology. We will return to this in the discussion.

Now we will explain how the diffusion coefficients were calculated. To this end we will define the mean square displacement of the center of mass $\mathbf{R}^{\mathrm{cm}}$ of a chain:

$$g_{\mathrm{cm}}(t) = \left\langle \left[\mathbf{R}^{\mathrm{cm}}(t) - \mathbf{R}^{\mathrm{cm}}(0)\right]^2 \right\rangle. \tag{5.18}$$

According to the Rouse model, $g_{\mathrm{cm}}(t) = 6Dt$ for all times and $D \sim N^{-1}$. A real chain however will be severely hindered by the interactions with surrounding chains, leading to subdiffusive behavior. According to the reptation model, $g_{\mathrm{cm}}(t) \sim t$ up to the entanglement time τ_e, followed by $g_{\mathrm{cm}}(t) \sim t^{1/2}$ up to τ_r $(= \tau_R)$. Subsequently the chain diffuses along the quasi-one dimensional Gaussian tube contour which results in three dimensional diffusive motion of its center of mass with $D \sim N^{-2}$. We generalize the diffusion coefficient to a time-dependent diffusion coefficient, according to

$$D(t) = g_{\mathrm{cm}}(t)/6t, \tag{5.19}$$

with limiting value $D = \lim_{t\to\infty} D(t)$. The deviation from the Rouse model becomes most distinct if we plot $ND(t)$ against correlation time. This is shown in Fig. 5.15. If the Rouse model were valid, all data would be constant and fall on top of each other. This is clearly not the case; subdiffusive behavior is observed, and it apparently sets in even before τ_s, which was also observed in the work of Kremer. [66] The early subdiffusive behavior occurs for all chain lengths, including chains which are shorter than the entanglement length. This can be explained as a "correlation hole" effect in the polymer mode-coupling (PMC) theory of Schweizer. [122] In this theory an explicit nonlinear coupling of the collective fluid density fluctuations with the segmental density field of a probe (Rouse) polymer is introduced. The combined effect of chain connectivity and the correlation hole (induced by excluded volume interactions of the probe chain with the polymer matrix) cause the effective *inter*molecular interactions to be very long ranged, on the order of the radius of gyration of the polymer

chain. This leads to a slow center of mass frictional memory decay and to subdiffusive behavior of $g_{\rm cm}(t)$. In fact, PMC theory predicts anomalously slow short time diffusion without *a priori* introducing the phenomenological tube concept. For relatively short times and chain lengths PMC theory explains the observed subdiffusive behavior well. For very long chains $g_{\rm cm}(t) \sim t^{9/16}$ is predicted, close to the reptation result. It will therefore be very difficult to discriminate between these theories by analyzing mean square displacement data.

In Fig. 5.15, the minimal slope of $g_{\rm cm}(t)$ is observed to decrease with increasing chain length. However, even for our largest chain lengths the $t^{1/2}$ regime of the reptation model is not strictly followed (nor the $t^{9/16}$ regime of PMC theory). For the chain lengths studied here the picture of a chain diffusing freely along a Gaussian primitive path is too strict and only some broad crossover to diffusion with an averaged slope (0.7 for B_{50}) remains. As said before, only the chain lengths $N < 20$ actually reached the diffusive regime. It is clearly seen that for these chain lengths the transitions from subdiffusive to diffusive behavior (horizontal lines in Fig. 5.15) occur at the calculated times τ_r (arrows in Fig. 5.15), where the Rouse modes crossover from non-exponential to exponential relaxation behavior. For the other chain lengths ($20 \leq N \leq 50$), we have assumed that the crossover occurs at τ_r, which we have put equal to the estimated τ_d values. This is how we obtained the diffusion coefficients D, which by the nature of the approximation may be slightly underestimated.

5.3.5 Entanglement time from shear relaxation

We will now turn our attention to the rheologic properties of polymer melts. Much theoretical and simulation effort has been spent to predict or reproduce the zero shear relaxation modulus $G(t)$, which measures the relaxation of stress after applying a small step shear strain. Experimentally, its Fourier transform is measured by applying small oscillatory shear, yielding the storage and loss moduli, $G'(\omega)$ and $G''(\omega)$. A prominent feature of viscoelastic liquids is the plateau that appears in $G(t)$, signifying the elastic part of the relaxation behavior that sets in after a liquid-like initial relaxation. The initial relaxation is generally believed to more or less follow the Rouse model, [30]

$$G(t) = \frac{ckT}{N} \sum_{k=1}^{N-1} \exp\left(-2t/\tau_k\right), \tag{5.20}$$

where c is the number concentration of blobs. The crossover time between the Rouse and the plateau regime is identified as the entanglement time τ_e. In the reptation picture, the beads of the chain hit the tube wall at this time. In most simulation work, however, it has proved to be difficult to directly observe a plateau in $G(t)$.

The shear relaxation modulus was determined by autocorrelating non-diagonal elements of the stress tensor, as explained in Sec. 4.5.4. The result for the B_4 system is shown in Fig. 5.16. Because the measuring time was finite, scattering of the data occurs at the largest correlation times where the relaxation modulus is close to zero. To assess the proximity to zero of the scattered data on a logarithmic scale, the positive data is represented by open circles and the negative data by closed circles. Where the number of open and closed circles are exactly balanced, the shear relaxation modulus is expected to be zero. The reader should

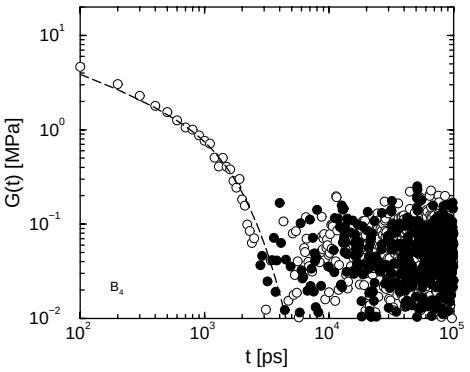

Figure 5.16: Shear relaxation modulus of the B_4 system. Absolute values of negative data are represented by filled circles. The long dashed line is the Rouse model prediction, Eq. (5.20).

be aware, however, that the closed circles are plotted in front of the open circles, which is why the closed circles may *appear* to dominate the open circles. Note that no effect is seen at the previously found slowing down time, $\tau_s \approx 0.47$ ns. In fact no entanglement effect is seen at all, and the data can very well be described by the Rouse model result, Eq. (5.20) and dashed line in Fig. 5.16. Here we replaced τ_k with the measured effective relaxation time τ_k^{eff}, Eq. (5.11). In Fig. 5.17 we present the results for the systems with chain lengths $6 \leq N \leq 50$, in the same way as Fig. 5.16 (except for the solid lines; these will be explained later). Notice that already for B_6 a hump emerges after $t \approx 6$ ns which splits off the Rouse prediction (dashed line). In *Chapter 4*, we attributed this to a very slow relaxation of the interchain stress, i.e., the hump indicates that we are in the transition region from unentangled to entangled dynamics. If we look at the other results in Fig. 5.17, we can observe how the hump evolves with increasing chain length. Although the data for $N = 20$ and 30 may not be regarded conclusive (some oscillations remain), a rubbery plateau is observed for the two longest chain lengths studied, with hardly any negative data remaining.

Because the onset of entanglement effects is found in the B_6 system, we estimate the entanglement length to be $N_e \approx 6$. Also, we assume that the entanglement time is around the time at which the hump emerges: $\tau_e \approx 6$ ns. This entanglement time seems to be reasonable for $N > 6$ as well (arrows in Fig. 5.17). The estimates of entanglement time and length are internally consistent if τ_e is interpreted as the relaxation time of a chain of length N_e: $\tau_1^{\text{eff}}(N_e) \approx 5.7$ ns from Fig. 5.8(a). It is also very important that they are consistent with experimental results. It is encouraging to see that an entanglement molecular weight $M_e = 2000$ is predicted from neutron spin echo experiments on polyethylene by Richter *et al.* and Schleger *et al.*, [114, 120] corresponding to $N = 7$ blobs. Also, they predict an entanglement time of $\tau_e \approx 5$ ns at the slightly higher temperature of 509 K, in very good agreement with our observations. Most estimates of N_e from rheology are based on the magnitude of the plateau modulus instead of the onset of entanglement effects in $G(t)$. In the next subsection we will determine the value of the plateau modulus and compare with rheological experiments.

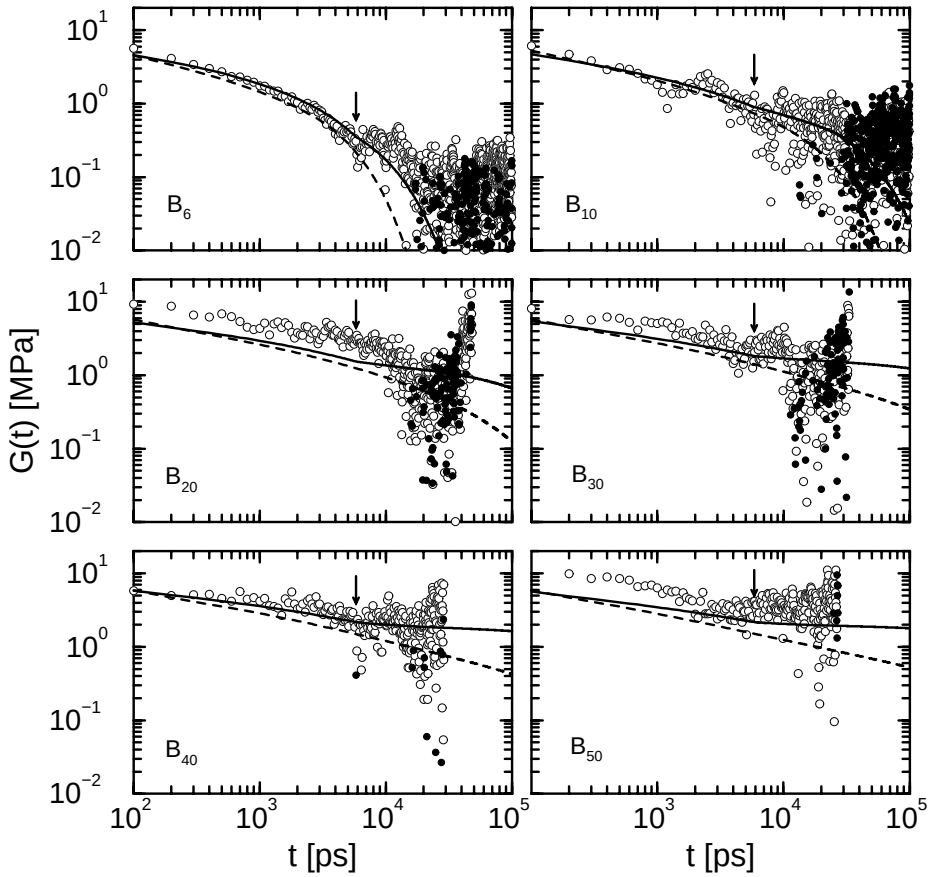

Figure 5.17: Shear relaxation modulus of the systems with $6 \leq N \leq 50$, represented in the same way as Fig. 5.16. Arrows indicate the estimated entanglement time τ_e. The solid lines are predictions from a mixed Rouse and reptation approach, Eq. (5.24).

5.3.6 Entanglement length from plateau modulus and viscosity

Let us consider the shear relaxation modulus $G(t)$ again (Fig. 5.17). For short times, $t < \tau_e$, the chain does not feel the entanglement constraints and behaves like a three dimensional Rouse chain. It is usually assumed that the chains are Gaussian on all scales, i.e., that Eq. (5.6) applies, and that the modes relax exponentially at all times, together leading to Eq. (5.20). Real chains, as we have seen, behave differently. The agreement may be improved by explicitly accounting for the measured mode amplitudes, relaxation times, and stretching parameters. According to Eq. (2.54), leaving the equilibrium mode amplitudes *and* relaxations explicit, we find:

$$G(t) = \frac{c}{N} E \sum_{k=1}^{N-1} \langle \mathbf{X}_k^2 \rangle \sin^2\left(\frac{k\pi}{2N}\right) \exp\left[-2\left(\frac{t}{\tau_k^*}\right)^{\beta_k}\right] \qquad (t < \tau_e), \tag{5.21}$$

where E is proportional to the (entropic) spring constant. The value of E is unknown, but we assume that the pure Rouse model result, Eq. (5.20), is valid for t approaching zero. This leads to

$$E = (N-1)\,kT \left[\sum_{k=1}^{N-1} \langle \mathbf{X}_k^2 \rangle \sin^2\left(\frac{k\pi}{2N}\right)\right]^{-1}. \tag{5.22}$$

For times $t > \tau_e$ the entanglement constraints are felt. According to the pure reptation model, the stress at time t is proportional to the fraction $\Psi(t)$ of the original tube that is still part of the tube at time t:

$$\Psi(t) = \sum_{k=\text{odd}} \frac{8}{k^2\pi^2} \exp\left(-\frac{k^2 t}{\tau_d}\right). \tag{5.23}$$

According to Eq. (5.23) a well-defined plateau will emerge in the shear relaxation modulus if the chains are long enough. The summation is done over all odd k modes, usually with no upper limit. However, we expect that in reality only the first $k_{\max} \approx \text{int}(N/N_e)$ modes will contribute to the reptational part of the stress relaxation. The remaining modes correspond to scales which are smaller than the entanglement length, and are therefore expected to contribute to the stress relaxation in a Rouse-like fashion. Combining Eqs. (5.21) to (5.23), explicitly accounting for the measured relaxation times and stretching parameters in the reptational part also, we obtain the following prediction for the stress relaxation:

$$\begin{aligned} G(t) \;=\; & F \sum_{k=\text{odd}}^{k_{\max}} \frac{8}{k^2\pi^2} \exp\left[-\left(\frac{t}{\tau_k^*}\right)^{\beta_k}\right] \\ & + \frac{c}{N} E \sum_{k=k_{\max}+1}^{N-1} \langle \mathbf{X}_k^2 \rangle \sin^2\left(\frac{k\pi}{2N}\right) \exp\left[-2\left(\frac{t}{\tau_k^*}\right)^{\beta_k}\right] \qquad (t > \tau_e), \end{aligned} \tag{5.24}$$

where β_k must be replaced with 1 and τ_k^* replaced with τ_k^l if $t > \tau_r$. The constant F is determined in the usual way, by equating $G(t)$ right before [Eqs. (5.21) and (5.22)] and after [Eq. (5.24)] τ_e. The predicted results are shown as solid lines in Fig. 5.17. Although the

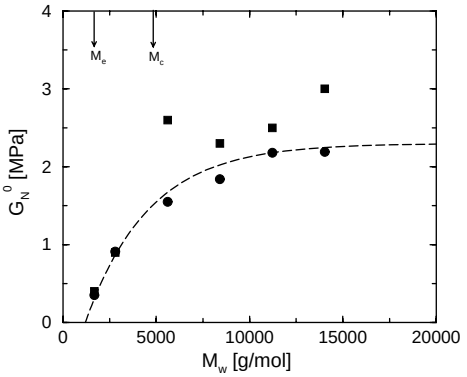

Figure 5.18: Plateau modulus G_N^0, estimated from the simulation data (squares) and the mixed Rouse and reptation prediction, Eq. (5.24) (circles) vs molecular weight M_w. The dashed line is a guide to the eye.

simulation data cannot rigourously proof the validity of Eq. (5.24), the agreement is found to be rather good. The simulation results of B_{20} and B_{50} are somewhat too high, but we expect that longer averaging would have yielded results which are closer to the predicted lines.

The plateau modulus G_N^0 can be estimated from the value of the shear relaxation modulus at the entanglement time, $G_N^0 \approx G(t = \tau_e)$. The estimated plateau values are plotted against molecular weight in Fig. 5.18. Clearly, the crossover from unentangled to entangled dynamics is made within the range of chain lengths studied: after the entanglement molecular weight of $M_e \approx 1700$ the plateau modulus quickly rises until it levels off to a molecular weight independent value which is in good agreement with the experimental value of 2.4 MPa. [40] To our knowledge this is the first time that the experimental plateau modulus of a specific polymer species has been reproduced with such good agreement by means of molecular dynamics simulations.

In rheological practice, the entanglement molecular weight is calculated from the plateau modulus: [30]

$$M_{e,p} = \frac{4}{5}\frac{\rho RT}{G_N^0}, \tag{5.25}$$

in which R is the universal gas constant. We have added a subscript p to indicate that M_e is estimated from the plateau modulus. Using this, we find $M_{e,p} \approx 960$ ($N_{e,p} \approx 3.4$), which is between our previous estimate $M_e \approx 1700$ from the onset of entanglement effects in the shear relaxation modulus, and the slowing down molecular weight $M_s \approx 560$ from the Rouse mode and mean square displacement analysis. We will return to this in the discussion.

The zero-shear viscosity can be calculated by integration of the shear relaxation modulus,[2]

$$\eta = \int_0^\infty G(t)\,dt. \tag{5.26}$$

Direct integration of the measured $G(t)$ data was possible for $N < 20$. A comparison between

2 Analogous to *Chapter 3* a small amount of 1.5 cP was added to account for the difference between the initial shear relaxation of atomistically detailed and coarse-grained systems.

N	d^{NSE} [nm]	G_N^0 [MPa]	η^{Rouse} [Pa s]	η [Pa s]	η^{exp} [Pa s]	D [10^{-6} cm^2/s]	D^{exp} [10^{-6} cm^2/s]
4			0.004	0.005 (0.005)	0.006	1.8	1.5
6		0.35	0.008	0.011 (0.011)	0.013	0.90	0.68
10		0.91	0.019	0.033 (0.032)	0.034	0.30	0.25
20	6.9 ± 0.9	1.55	0.056	0.20	0.17	0.084	0.063
30	5.3 ± 0.4	1.84	0.14	0.88	0.73	0.036	0.028
40	5.2 ± 0.5	2.18	0.30	2.95	2.09	0.018	0.016
50	5.8 ± 0.5	2.19	0.51	5.98	4.68	0.011	0.010
Exp.	5.3 ± 0.7	2.4					

Table 5.3: Tube diameter d^{NSE} from fits to the dynamic structure factor, plateau modulus G_N^0, viscosity η^{Rouse} based on the Rouse expression, Eq. (5.20), and viscosity η based on a mixed Rouse-reptation approach, Eq. (5.24) (viscosities determined by direct integration of $G(t)$ are between brackets), experimental viscosity η^{exp}, [106] diffusion coefficient D from the simulation, and experimental diffusion coefficient D^{exp}. [106] The last row gives experimental values for d^{NSE} for chain lengths B_{40} to B_{90}, [140] and the limiting plateau modulus for very long chains. [40]

the viscosities predicted by the Rouse approach, Eq. (5.20), and the mixed Rouse-reptation approach, Eq. (5.24), learns that the latter does a much better job in reproducing these values (see Table 5.3). We will therefore rely on the mixed approach to predict the viscosities of the chain lengths $N \geq 20$. The results are shown in Fig. 5.19 (filled circles). Results by several other authors are given in Fig. 5.19 as well. The open circles are the constant density simulation results of C_6 to C_{66} alkanes by Mondello *et al.* [82, 83] The open square is a constant density ($\rho = 0.75$ g/cm^3) non-equilibrium dynamics simulation result of C_{100} by Moore et al. [84] Here we used their preliminary value of about 7.2 cP, obtained at the lowest

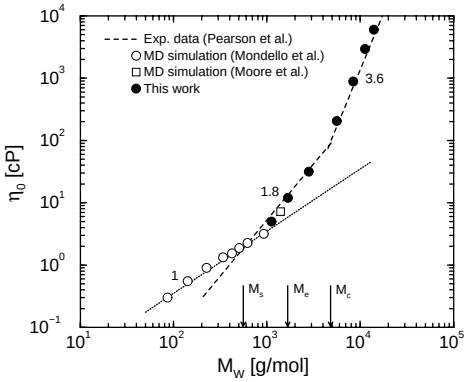

Figure 5.19: The zero shear viscosity η_0 vs molecular weight M_w for polyethylene from different simulation studies (open symbols) and experiment (long dashed lines) compared to the present simulation results (closed circles). All simulations were carried out at constant density. The weights corresponding to different length scales are indicated by arrows.

shear rate of $\dot{\gamma} = 1.5 \cdot 10^8$ s^{-1}, which is expected to be in the linear regime. Pearson *et al.* [106] found that at low molecular weight, $M_w < M_c \approx 5000$, the viscosity is well described by the power law

$$\eta = 2.1 \cdot 10^{-5} M_w^{1.8} \qquad \text{(cP)}, \tag{5.27}$$

while at high molecular weight, $M_w > M_c$, the M_w dependence is much stronger:

$$\eta = 3.76 \cdot 10^{-12} M_w^{3.64} \qquad \text{(cP)}. \tag{5.28}$$

The crossover between the two regimes is determined by the critical molecular weight M_c, which, like the entanglement molecular weight M_e, is characteristic of the polymer species. We can understand the origin of M_c by noticing that at this molecular weight the plateau has almost fully developed, while at the same time τ_d has grown large enough for the reptation part to dominate the Rouse part of the integral of $G(t)$. However, the role of M_c may not be as fundamental as that of M_e: no characteristic time scale is connected with M_c and it is always equal to "a few times" M_e, enough for the entanglement effects to fully mature. For a more in-depth analysis of M_c the reader is referred to Ref. [40].

Pearson's fits, Eqs. (5.27) and (5.28), are plotted as dashed lines in Fig. 5.19. Notice the agreement between our simulation predictions and experiment. The results of Mondello *et al.* [82,83] show an initial regime where the viscosity scales with M_w, in agreement with pure Rouse model predictions. The crossing over to the $M_w^{1.8}$ regime occurs at the slowing down molecular weight M_s, i.e., at the same weight as where a crossing occurred in the scaling of the diffusion coefficient. Again, the results of Mondello *et al.* do not agree with those of Pearson *et al.* because they refer to different densities. Experimentally, there is a large increase in density in the region $M_w < M_s$, causing a faster than Rouse scaling of the viscosity. Trying to validate reptation theory, Pearson corrected the viscosity to the value it would have had if the friction factor had been constant (long chain limit). In that case the $M_w^{1.8}$ region disappeared and a new Rouse-like region was observed up to the critical molecular weight M_c. Given the agreement between our results and the experimental viscosities, and given the fact that above $M_w \approx 1000$ the density hardly changes, we can only conclude that Pearson's analysis must be on the wrong track.

5.3.7 Tube diameter from dynamic structure factor

The coherent dynamic structure factor can be measured by means of neutron spin echo spectroscopy. In the experiments conducted by Richter and coworkers, protonated chains were dissolved in a deuterated matrix. [109, 111, 112, 114, 120] Because the scattering lengths of protons and deuterons differ, they were able to extract the single chain coherent dynamic structure factor,

$$S(q,t) = \frac{1}{N_{sc}} \sum_{i=1}^{N_{sc}} \sum_{j=1}^{N_{sc}} \left\langle \exp\left\{ i\mathbf{q} \cdot \left[\mathbf{r}_i(t) - \mathbf{r}_j(0) \right] \right\} \right\rangle, \tag{5.29}$$

where $\mathbf{q}$ is the scattering wave vector and the double summation is over all N_{sc} scattering centers of one chain. Because our chains have been coarse-grained, detailed microscopic

information about positions of the hydrogens is lost. However, it was shown in *Chapter 4* that, to a good approximation, the blob positions $\mathbf{R}_i$ can still be used in Eq. (5.29) to calculate the microscopic dynamic structure factor, provided the wavelength of the scattering wave vector is large compared to the bond length of bonded blobs. As the maximum bond length is of the order of 2 nm, q will have to be small compared to 3 nm^{-1}. The results for five different scattering vectors, $0.55 \leq q \leq 2.2$ nm^{-1}, are shown in Fig. 5.20 (symbols) for all chain lengths $N \geq 6$. We will now investigate to what extent this data is compatible with the Rouse and reptation models.

It was shown in *Chapter 4* that the simulation results of the B_6 system do not agree with the pure Rouse model predictions. However, one might expect that the agreement improves if the mean square displacement of the center of mass and the mode amplitudes, relaxation times, and stretching parameters are taken explicitly into account, as we have done in the previous subsection. Inverting Eq. (5.4) and inserting in Eq. (5.29) yields:

$$\begin{aligned} S(q,t) &= \frac{1}{N}\exp\left\{-\frac{q^2}{6}\left\langle\left[\mathbf{R}^{\mathrm{cm}}(t)-\mathbf{R}^{\mathrm{cm}}(0)\right]^2\right\rangle\right\} \\ &\times\left\{\sum_{i=1}^{N}\sum_{j=1}^{N}\exp\left[-\frac{2q^2}{3}\sum_{k=1}^{N-1}\left\langle\mathbf{X}_k^2\right\rangle\left(\left[A_{ki}-A_{kj}\right]^2+2A_{ki}A_{kj}\left[1-C_k(t)\right]\right)\right]\right\}, \end{aligned} \tag{5.30}$$

where it is assumed that the blob displacements are Gaussianly distributed and the Rouse modes remain orthogonal. A_{ki} and $C_k(t)$ are defined by Eqs. (5.5) and (5.13). The results from Eq. (5.30) are shown as dashed lines in Fig. 5.20. For all chain lengths, the fit for the smallest wave vector ($q = 0.55$ nm^{-1}) is reasonably good. This wave vector is always small compared to $2\pi/R_g$, so only the overall center of mass motion is probed. Because this motion is explicitly introduced in Eq. (5.30), the good agreement comes as no surprise. The other wave vector results are in less good agreement. The modified Rouse prediction is observed to always underestimate the simulation results. This observation is in agreement with recent simulation and neutron spin echo work on unentangled 1,4-polybutadiene. [129] Smith *et al.* compared the dynamic structure factor results with a Rouse expression, modified in the same spirit as Eq. (5.30). They found that the failure of the Rouse model does not lie primarily in the predicted mode amplitudes or relaxation times, yet in the non-Gaussianity of segmental displacements. The non-Gaussianity is caused by chain-stiffness at the smallest scales and, more importantly, by intermolecular interactions at larger scales.

Above a certain chain length, the effects of intermolecular interactions become dominant in the form of entanglements. De Gennes [27] has formulated an expression for the single chain coherent dynamic structure factor, valid for times beyond τ_e and wave vectors much larger than the inverse end-to-end distance, i.e., $qR_e \gg 1$:

$$\begin{aligned} \frac{S(q,t)}{S(q,0)} &= \left\{1-\exp\left[-(qd/6)^2\right]\right\}\exp\left(t/\tau_{\mathrm{loc}}\right)\mathrm{erfc}\left(\sqrt{t/\tau_{\mathrm{loc}}}\right) \\ &+\exp\left[-(qd/6)^2\right]\sum_{k=1}^{k_{\max}}\frac{A\sin^2(\alpha_k)}{\alpha_k^2\left(\mu^2+\alpha_k^2+\mu\right)}\exp\left(-\frac{4\alpha_k^2 t}{\pi^2\tau_d}\right), \end{aligned} \tag{5.31}$$

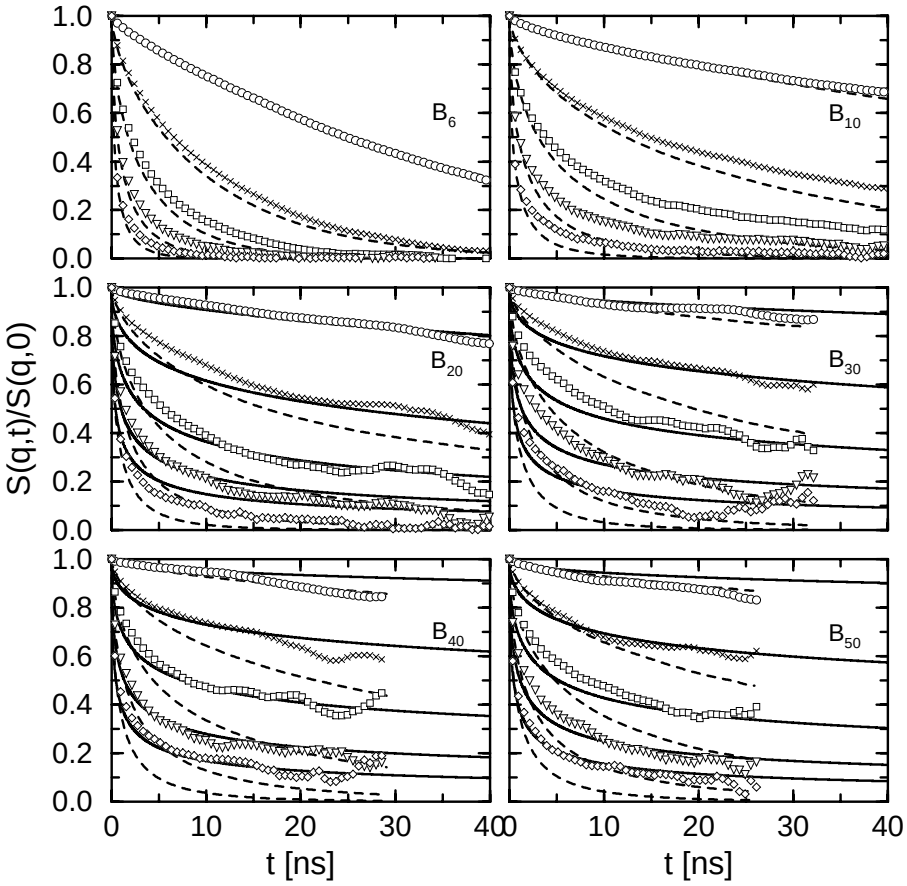

Figure 5.20: Single chain coherent dynamic structure factors of the simulated chains. The q values shown are 0.55 nm^{-1} (circles), 1.0 nm^{-1} (crosses), 1.4 nm^{-1} (squares), 1.8 nm^{-1} (triangles), and 2.2 nm^{-1} (diamonds). Dashed lines are Rouse model predictions, Eq. (5.30), solid lines are fits to the reptation model, Eq. (5.31).

where α_k are positive solutions of the transcedental equation

$$\alpha_k \tan \alpha_k = \mu = \frac{q^2 N b^2}{12}, \tag{5.32}$$

and A is a normalization factor for the second term in Eq. (5.31). The first term describes the decay of correlations due to the smearing out of the (initially localized) chain throughout its tube. This is called local reptation. The associated q-dependent time scale τ_{loc} is given by

$$\tau_{\text{loc}} = \frac{36}{W b^4 q^4}. \tag{5.33}$$

To calculate τ_{loc} is not trivial, because both the Rouse rate W and the effective statistical segment length b depend on the length scale. We can estimate these quantities by assuming that the length scale probed by a wave vector corresponds to the end-to-end distance of a subchain of some effective number (N_{eff}) of blobs, i.e., $N_{\text{eff}}(q) b_{\text{eff}}^2(q) \approx (2\pi/q)^2$. Using Fig. 5.3 we find that the effective number of blobs for the smaller scales are: $N_{\text{eff}}(2.2) \approx 3.6$ for $q = 2.2$ nm^{-1}, $N_{\text{eff}}(1.8) \approx 4.8$, and $N_{\text{eff}}(1.4) \approx 7.0$, with effective statistical segment lengths $b_{\text{eff}} = 1.52$, 1.60, and 1.69 nm, respectively. From Fig. 5.8(a) the effective Rouse rates at these length scales are estimated as $W = 0.43$, 0.32, and 0.25 ns^{-1} respectively. This is very fortunate, for the product Wb^4 turns out to be almost constant: 2.27, 2.08, and 2.03 nm^4/ns respectively. In our subsequent calculations we have used the average value of 2.1 nm^4/ns.

The second term in Eq. (5.31) describes the slow, global creep of the chain inside its tube, known as reptational diffusion. This process depends on the disentanglement time τ_d, which is known from the previous subsection. The summation is done over different reptational modes, and should therefore stop at $k_{\max} \approx \text{int}(N/N_e)$, while in the literature a value of either $N-1$ or ∞ is used. The difference, however, is small. It is important that the disentanglement times of long chains (say $N \geq 20$) are much larger than the entanglement time $\tau_e \approx 6$ ns. This causes a plateau to emerge at intermediate times $\tau_e < t < \tau_d$. It should be noted that in the original theory by De Gennes [27] the height of this plateau was determined by a prefactor $\left[1 - (qd/6)^2\right]$, in which it was assumed that $qd \ll 1$. To allow for larger q values this prefactor is interpreted, in analogy with Schleger *et al.*, [120] as the first two terms in the Taylor series of $\exp\left[-(qd/6)^2\right]$.

The fits using Eq. (5.31) are shown as solid lines in Fig. 5.20. Since all other parameters were known from previous measurements, the tube diameter d served as the only fit parameter. For each chain length a joint fit for all q and $t > \tau_e$ was done. The dynamic structure factor results of the B_6 and B_{10} chains could not be described by Eq. (5.31) in any way. The results of the B_{20} system could be fitted reasonably well, except for the highest q value. The fit quality for the longer chains ($N > 20$) is good, particularly if we take into account that the chains are not extremely far in the entangled regime (only 5 to 8 times N_e). In a similar way, Pütz *et al.* have measured the dynamic structure factor of their FENE model chains. [107,108] They also found good agreement with reptation theory for chain lengths above 550, which is about 8 times N_e, if the proper [108] entanglement length is used (see the discussion, Sec. 5.4).

With this data, however, we are not able to distinguish between De Gennes' reptation model and other models which also predict a plateau, such as the rubberlike model of des Cloizeaux [18] or the model of Ronca. [117] Schleger *et al.* were able to show that experiment clearly favors the reptation model. [120] This was possible because they measured up to times as large as 175 ns. The correlation times of our simulations did not reach so far, but we have shown that the dynamic structure factor results are at least compatible with reptation. The tube diameters which follow from the fits are given in Table 5.3. Notice that roughly the same tube diameter d is found for chain lengths $N = 30$, 40 and 50. Some scatter in the data of d occurs, but the average of $d \approx 5.4$ nm for the three largest chain lengths is in very good agreement with the results of Wischnewski *et al.* who found $d = 5.3 \pm 0.7$ nm for a similar molecular weight range, but at a slightly higher temperature. [140]

5.4 Discussion

In this work we have studied the time and length scales which determine the transition from unentangled to entangled dynamical behavior by means of coarse-grained molecular dynamics simulations. What have we learned from these simulations? First, we found clear evidence for stretched exponential relaxation of the Rouse modes. Our simulations show that the stretching parameter β_k depends on the length scale under consideration, but a constant value of 0.8 is observed for the first Rouse mode of each chain length between 6 and 50. If this value would remain the same for much longer chains, this would open up a way to roughly estimate the disentanglement times of long chains from relatively short simulations. As τ_r starts to deviate from τ_d, this estimate becomes increasingly worse. Moreover, there is, no guarantee that the value of 0.8 will persist indefinitely for longer chains. This must be investigated in future work.

It must be remarked that the non-exponential relaxation of the Rouse modes comes as no surprise. Stretching was already observed in *Chapter 4*, but we did not pay attention to the fact that relaxation after τ_r is exponential, obtaining averaged estimates of the stretching parameters, which were somewhat closer to unity. Also, Richter *et al.* [114] suggested some years ago that the assumption of exponential decay for the Rouse modes may be too rough for higher molecular weight chains, which was confirmed by computer simulations. [100–102, 126, 129] However, the physical origin of the stretching is not entirely clear. Because stretching is observed at length scales below the entanglement length, a successful theory of polymer dynamics must not only include entanglement effects but possibly also other intermolecular correlations and chain stiffness effects. In this respect it is important to mention polymer mode-coupling theory [122] which predicts an intermediate time regime of non-exponential relaxation of the normal mode time correlation functions.

For the range of chain lengths studied here, we have made a rather detailed analysis of the scaling of the effective relaxation times with chain length N and mode number k. When plotted against N/k we find three universal regimes. In the first regime the effective relaxation times scale as predicted by the Rouse model, Eq. (5.8). The second regime is relatively small, but a distinct $(N/k)^4$ scaling can be observed around N_s. This k-dependence (k^{-4}) was predicted by Kavassalis and Noolandi in their Generalized Rouse Model (GRM), if we inter-

pret their N_e as our N_s, but they find a different N-dependence (N^3). [60] Alternatively, the bending force model of Harnau *et al.* [54] could be used in an effort to explain the observed scaling as a stiffness effect. In *Chapter 4* we found that a stiffening of the chain caused both faster relaxation of the small scale modes and slower relaxation of the large scale modes. However, as was already pointed out by Richter *et al.*, [112] a stiffness correction alone is not enough. Using realistic values of the stiffness, the relaxation times decrease too slowly with increasing mode number. In *Chapter 4* we showed that the uncrossability of chains is an important factor in the internal relaxation of a polymer chain. It has a large influence on the relaxation times of all scales but the very smallest. From the deviation of the stretching parameters from unity, Fig. 5.7, we deduce that the kinetic constraints, caused by the uncrossability constraints, are most severe at length scales of the order of N_s. Although at this length scale we can not yet speak of global entanglement effects (in the sense of confined dynamics inside a tube), there are strong local effects leading to a rapid increase of effective friction. The universality of the curves show that the magnitude of this effective friction depends on the absolute length scale and not on the chain length itself. This is also the case for the third regime, where the effective relaxation times scale like $(N/k)^3$. The third regime starts at about $1.5N_s$, i.e., C_{60}. While we can not rule out the possibility that the scaling of the second regime only shows up in this particular coarse-grained model, the physical reality of the third scaling regime is supported by similar observations in other simulation models. [65,100–102,126] In all these simulations the density was kept constant. If the density is allowed to decrease with decreasing chain length, e.g., by simulating under normal pressure, the scaling of the relaxation times in each of these regimes is expected to be different. However, the characteristic length scales at which the transitions occur may still be observed. Indeed, Harmandaris *et al.* [51, 52] performed atomistically detailed NVT simulations of polyethylene at $P = 1$ atm, and found a clear increase of the friction coefficient between C_{40} and C_{60}. After the three universal regimes a final regime sets in where the effective relaxation times scale with $N^{3.5}$ and k^{-2}, in agreement with reptation theory if contour length fluctuations are included. Note that the smallest length scale where this final regime applies closes in on the largest available length scale ($= N$) with increasing chain length. They will merge at some very large chain length unless the observed scaling laws change beyond the range of chain lengths studied here.

If focus is laid on the terminal relaxation times, instead of effective relaxation times, the observed scaling is compatible with the reptation model for all length scales beyond N_e.

The effect of the increased friction around the length scale N_s shows up in the mean square displacement of blobs $g(t)$ as a transition from initial Rouse-like $t^{1/2}$ behavior to a smaller power law exponent. In our case the exponent is about 0.4 for the B_{50} system, but lower values may be reached if longer chains are used and the average is taken over inner blobs to exclude the influence of the more mobile chain ends. [66, 107] It is important to note that this transition occurs at an earlier time than the entanglement time. Likewise, the scaling of the diffusion coefficient with chain length (at constant density) displays a transition at N_s, not at N_e. If we study the mean square center of mass displacement $g_{\mathrm{cm}}(t)$, it becomes clear that the center of mass motion of a chain is strongly influenced by the uncrossability constraints. A subdiffusive regime is observed up to the time τ_r, which, because of the relatively short chain lengths studied here, almost coincides with the disentanglement time τ_d. To illustrate the

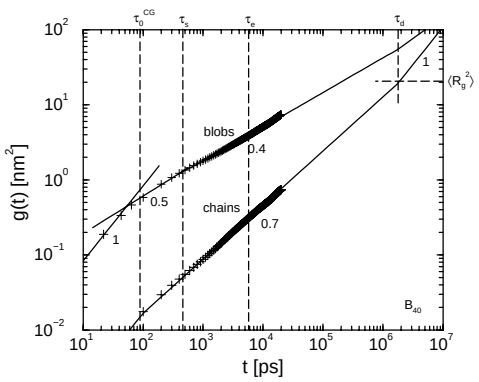

Figure 5.21: Blob and center of mass mean square displacement data of the B_{40} system (plus). Extrapolation (solid lines) to $t = \tau_d$ yields a center of mass mean square displacement equal to $\langle R_g^2 \rangle$. Different time scales are indicated by dashed lines.

consistency of putting τ_r equal to τ_d for the longer, but still not very long chain lengths, we have plotted in Fig. 5.21 the mean square displacement of the center of mass of a B_{40} chain and its extrapolation with slope 0.7. The extrapolation at $t = \tau_d$ exactly equals the mean square radius of gyration R_g^2, in agreement with the fact that the chain must have escaped its original tube at $t = \tau_d$. We note that in order for $g_{\rm cm}(\tau_d) = R_g^2$ to hold, the diffusion coefficient D must be proportional to R_g^2/τ_d, in which case a stronger than N^{-2} dependence is predicted. Indeed, a least squares fit to a power law of the data of $20 \leq N \leq 50$ gives $D \sim N^{-2.2}$, which is in agreement with recent results giving $D \sim N^{-2.28\pm0.05}$ for different polymer species. [72, 134]

The advantage of coarse-graining bottom-up is that it allows for a direct comparison with atomistic simulations and experimental values, without any need of mapping to theoretical or phenomenological models. In *Chapter 4* we showed the good agreement between the coarse-grained and atomistic simulations and in this chapter we showed the good agreement with experimental values. In Table 5.4 the entanglement parameters found in our work are summarized and compared with rheological and NSE data. The tube diameter for polyethylene as estimated from $S(q,t)$ ($d \approx 5.4$ nm) agrees well with experimental values for a similar molecular weight range. For very long chains, assuming that $d^2 \approx N_e b^2$, we expect a tube diameter of $d^{\rm NSE} \approx \sqrt{6 \cdot 3.3} = 4.4$ nm, in agreement with (but slightly underestimating) the experimental value. [140] The plateau modulus yields an entanglement molecular weight which is about half of the estimate from $S(q,t)$, also in agreement with experimental observations. The reason why $M_{e,p}$ may differ from M_e was discussed by Tanaka *et al.* [133] They argued that $M_{e,p}$, defined by Eq. (5.25) is not a pure entanglement parameter, and may therefore not be the same as M_e, which is a parameter specifying the reptation/tube model.

Besides comparing with experimental work, we can also compare with other simulation work. The best studied simulation model of the last decade has been the FENE model of Kremer, Grest, and co-workers. [66, 68, 107] One of the remaining puzzles of this model is the discrepancy between the entanglement length N_e calculated from the mean square displacement and from the single chain coherent dynamic structure factor. Pütz *et al.* wonder why $S(q,t)$ should give different results from $g(t)$ since "they both are single chain quantities and measure the same motion." [107] However, the coherent dynamic structure factor measures

	Simulation	Experiment
τ_e (ns)	6	5
M_e (g/mol)	1700	2000
$M_{e,p}$ (g/mol)	960	920
d^{NSE} (nm)	5.4	5.3

Table 5.4: Entanglement parameters for PE from this simulation study ($T = 450$ K) and experiment. Experimental τ_e and M_e are estimates from NSE experiments at $T = 509$ K (Ref. [120]). Experimental $M_{e,p}$ is estimated from G_N^0, Eq. (5.25), including factor 4/5 at $T = 443$ K (Ref. [41]). Experimental d^{NSE} is for a M_w range 12000 to 25000; $d \approx 4.6$ nm for $M_w = 36000$ (Ref. [140]).

the motion of a q-dependent number of chain segments surrounding the original position of a given segment. It is therefore sensitive to relative motions on a q dependent scale. On the other hand, the mean square displacement $g(t)$ measures the absolute motion of a single segment in space, and is therefore much more sensitive to local changes of the effective friction, resulting in a somewhat earlier slowing down. Thus, we suggest that the claimed entanglement length from $g(t)$ is actually the slowing down length N_s. (In this respect it is important to note that their simulations were also performed at constant density.) Pütz *et al.* deduced from the mean square displacement of (inner) segments an entanglement length (now slowing down length) of 35 segments for $N = 700$ and 28 segments for $N = 10000$. [107] The transition in the scaling of the diffusion coefficient with chain length also occurs around $N = 35$ (see their Fig. 8 in Ref. [66]). Fitting the single chain coherent dynamic structure factor $S(q,t)$ of the reptation model to their simulation data they find $d^{\mathrm{NSE}} = 12.9\sigma$ for $N = 700$ and $d^{\mathrm{NSE}} = 9.6\sigma$ for both $N = 2000$ and $N = 10000$. The $S(q,t)$ data of $N = 10000$ was found indistinguishable from that of $N = 2000$, [108] from which may be concluded that finite chain length effects have no discernable effects beyond $N = 2000$. [139] Again assuming that $d^2 \approx N_e b^2$, this yields an entanglement length of $N_e^{\mathrm{NSE}} \approx (9.6/1.28)^2 = 56$ for very long chains. These estimates yield a ratio N_s/N_e^{NSE} of about 0.5 to 0.6, in rough agreement with the value of 0.33 expected for our simulation model in the case of very long chains. A second characteristic ratio to compare both models is $N_{e,p}/N_e^{\mathrm{NSE}}$. Pütz *et al.* estimated G_N^0 from the normal stress decay in a step strain elongation. [107] The outcome depended somewhat on the applied stress-strain formula, but an average yielded $N_{e,p} = 72$ (65 - 83). Thus the ratio $N_{e,p}/N_e^{\mathrm{NSE}}$ was found to be approximately 1.3, while our result is about 0.6. This should be compared to the experimental result of about 0.5 which can be calculated from the values in Table 5.4. It is encouraging to find that our model predicts a proportionality between these length scales which agrees with experiment.

We end this section with a remark concerning computation times. Large computational overhead is introduced by the rather complicated uncrossability constraint. Still, there is a clear speed-up compared with atomistically detailed simulations as is exemplified by the fact

that we are able to reach larger correlation times with equal computational effort. The FENE model mentioned above, using conventional schemes, also reaches such large speed-ups, or even larger ones. [66,107] We think, however, that our model, since it is built on an undulging atomistic model, encompasses time and length scales in a much more realistic way than the FENE model in which several monomers are mapped into an unrealistically hard bead. In the limit of very long chains this objection will become less important, while at the same time the FENE calculations will most probably be much faster than the TWENTANGLEMENT calculations.

5.5 Summary

The general picture that emerges from this work is that the dynamics of medium long chain lengths (C_{400} - C_{1000}) is in approximate agreement with reptation theory, with fluctuating contour length corrections when necessary, but that the approximation of a primitive path moving with great freedom in a tube is too strict. The chains are interacting with their neighbours on every length scale, down to the slowing down length N_s, leading to non-exponential relaxation for as long as it takes a chain to escape its original environment. Only after time τ_r, equal to τ_d in the case of our moderately long chains, and for mode numbers smaller than $k_{\max} = \mathrm{int}(N/N_e)$, exponential relaxation occurs. This can effectively be accounted for by explicitly introducing into the reptation model results the measured relaxation behavior of the reptating modes. The same must be done with those modes whose length scales are smaller than the entanglement length, and which must be treated like Rouse modes. Proper care also has to be taken of the fact that the chains are not Gaussian, caused by stiffness and other sources of non-harmonicity. These effects can in some cases be handled by using measured mode amplitudes instead of pure Rouse amplitudes.

We want to stress that in our approach we started from the bottom, i.e., all coarse-grained parameters were determined "*ab initio*" from short atomistic molecular dynamics runs of polyethylene. The choice of the number of monomers in one blob, $\lambda = 20$, was arbitrary within certain bounds, as explained in Sec. 5.2. Other values, such as $\lambda = 10$ or $\lambda = 30$ could have been used, leading to different blob interactions, but they should lead to the same dynamic behavior. We find very good agreement with experimental data on polyethylene, which we think is to a large extent due to the way we have introduced the entanglements in our model. In contrast, if the uncrossability of chains is realized by combining relatively hard spheres into flexible chains, the proportionalities between different length scales may not be the same as those that occur in real polymer systems. Chemically realistic polymers are flexible only at large length scales when the beads will be almost empty and consequently very soft. These objections will become less important if one is interested only in very long time scales in very long polymer chains, in which case other, more conventional, coarse-grained simulations may become preferable.

We hope that the present work will aid in the understanding of the dynamics and rheology of polymer melts. It will certainly be interesting to extend this simulation model to even longer chains, possibly of different polymer species, and to investigate the non-linear properties under shear.

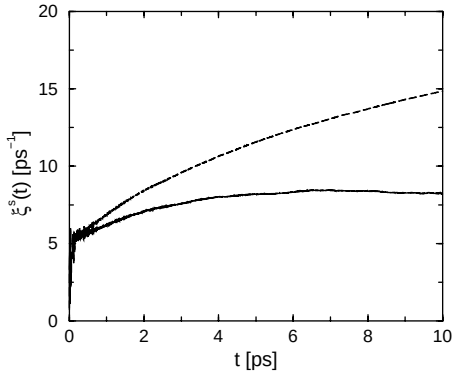

Figure 5.22: Scalar friction from integration of the autocorrelation of the constraint force (dashed line) and autocorrelation of the random force (solid line), Eq. (5.A.1). A value of 8 ps^{-1} was used in the coarse-grained simulations.

5.A Appendix. Determination of the friction factor

In the coarse-grained approach the fast fluctuating interactions between the microscopic constituents are represented by a random forces and frictions. Assuming that the friction on each blob is isotropic and independent of the positions of the other blobs, it can be calculated from:

$$\xi(t) = \frac{\beta}{M}\int_0^t d\tau \left\langle F_\alpha^R(\tau) F_\alpha^R(0)\right\rangle, \tag{5.A.1}$$

where $\beta = 1/kT$ and F_α^R is the x, y, or z-component of the random force on a blob. The friction can be calculated from a microscopic molecular dynamics run. [1] To this end, a constraint force is added to fix the position of one blob relative to the center of mass of the box. Part of this force at each instant balances the mean force due to interactions with other blobs, while the remaining part balances the fluctuating random force due to the bath variables. The issue now is to isolate the latter part. Simply subtracting the long time average from the constraint force will not give the correct random force, because on the longer time scales the mean force also fluctuates, albeit at a much lower frequency. A way to estimate the maximum frequency with which the mean force oscillates is to search for the maximum curvature within one kT from the free energy minimum:

$$M\omega_{\max}^2 \simeq \left(\nabla^2\chi\right)_{\max}. \tag{5.A.2}$$

Applying this to the interaction model for our coarse-grained polyethylene blobs, we found $\omega_{\max} \simeq 0.06$ rad/ps. The constraint force was measured for five nanoseconds in a simulation of $C_{120}H_{242}$. The constraint force data was Fourier transformed and frequencies $\omega < \omega_{\max}$ were removed. The autocorrelation, Eq. (5.A.1), was determined by squaring and Fourier transforming back to the time domain. Different blobs were fixed in different runs, to account for varying friction factors at different positions along the chain. However, it was found that these friction factors do not differ much for C_{120}. The averaged result is given in Fig. 5.22 (solid line). Notice that the friction levels off to a value of about 8 ps^{-1} after about 5 ps of correlation time, which was the value used in all our coarse-grained simulations. The 5 ps correlation time is sufficiently small compared to the smallest mean force oscillation period (about 100 ps), so the assumption that the blobs are slow compared to the bath

variables (Markov approximation) seems to be justified. Fig. 5.22 also shows the integrated autocorrelation of the constraint force itself (dashed line). In this case the friction factor becomes much larger, consistent with the fact that now also the interactions between the blobs, especially between blobs on different chains, are included in the friction. This leads to the well-known Einstein result for the diffusion coefficient,

$$D = \frac{kT}{NM\xi}, \tag{5.A.3}$$

where N is the number of blobs in a chain. In *Chapter 3* it was found that the friction frequency corresponding to the measured diffusion coefficient of a C_{120} chain must be 19.0 ps^{-1}, which is consistent with our present results.

6 A time-integrated estimate of the entanglement molecular weight in polymer melts in agreement with the one determined by time-resolved measurements

We propose definitions for the entanglement molecular weight M_e which can be derived from different independent time-resolved measurements, such as the single-chain dynamic structure factor and the zero-shear relaxation modulus. Using these definitions, measurements in simulations of polyethylene consistently yield the same *estimate of the entanglement molecular weight. This value of M_e can not be derived directly from time-integrated properties, such as the diffusion coefficient, viscosity, or the shear plateau modulus. However, using a dynamic scaling hypothesis, the density of dynamic units making up the temporary network can be derived from a combination of diffusion coefficient and viscosity, without specifying a precise mechanism for entanglement polymer motion. We show that the molecular weight corresponding to one of these dynamic units is consistent with values of M_e derived from the time-resolved measurements, but not consistent with the empirical estimate from the value of the shear plateau modulus.*[*]

6.1 Introduction

The peculiar dynamics and viscoelastic behavior of polymer melts is often rationalized by viewing the melt as a temporary network. This network arises as a result of mutual uncrossability of the constituent chains, which effectively confines the chains in "tubes" from which they can only escape through the process of reptation. Since the longest characteristic times increase extremely fast with molecular weight, relaxation processes occur on an enormous range of time and length scales. It is therefore not surprising that a host of experimental techniques is used to study the dynamic properties of polymer melts on all relevant time and length scales. Sufficiently generic system properties can routinely be measured by more than just one experiment. In these cases, experiments of different nature often lead to mutually inconsistent conclusions. This is particularly true for the determination of the entanglement molecular weight M_e. In this chapter, we will show that such inconsistencies need

[*] The work described in this chapter has been submitted to Macromolecules

not arise. When focus is laid on various time-resolved experiments, a consistent value for M_e emerges. Moreover, we will present a particular combination of time-integrated quantities, which yields exactly the same value for M_e.

Before going into details, we will explain the distinction between the two abovementioned types of experiments. Time-resolved experiments measure the dynamics of the system with sufficiently small time resolution to be able to probe a relevant time dependent correlation function before it reaches its long time limit. Examples are neutron spin echo (NSE) spectroscopy, [120] measuring the coherent dynamic structure factor, proton and deuteron field-cycling NMR relaxometry, [61] probing the segment tangent vector correlation function, and NMR field-gradient diffusometry (when applied to relatively short time scales), [42] probing the mean-squared displacement of segments. On the other hand, time-integrated experiments either integrate over a long time or measure the long time limit of some correlation function, which amounts to integrating its time derivative. Examples are measurements of the shear viscosity [103, 106] or plateau modulus, [40] both by means of rheometry, and measurements of self-diffusion coefficients, e.g., by means of NMR field-gradient diffusometry, [103, 106] forward recoil spectroscopy, [21] or scanning infrared microscopy. [124]

Now, starting with a polymer model, it is usually possible to express experimentally accessible quantities in terms of a limited set of microscopic parameters (like Kuhn step length, friction coefficient, and entanglement length). Reversal of the procedure, i.e., deriving the limited set of parameters from experimental data, must be done with caution because the model will possibly not be perfect. Particularly when time-integrated measurements are interpreted, there is the danger of getting incorrect microscopic parameters, because the data do not contain enough detailed information. Still, it is highly desirable to be able to estimate the microscopic parameters from time-integrated measurements because of the relative simplicity of such experiments.

6.2 Time-resolved results

In this section we will show that from the analysis of different time-resolved results a consistent value for the entanglement molecular weight emerges, which is why we perceive this value as the "true" entanglement molecular weight. We will clarify our point by the example of polyethylene (PE) melts at 450 K. We will refer to experimental work and to the results of molecular dynamics simulations of PE melts at a temperature of 450 K and density $\rho = 0.761$ g/cm^3, reported in *Chapter 5*.

The entanglement molecular weight has been derived in the following ways:

1. Richter *et al.* [110, 120, 141] have performed NSE experiments on high molecular weight PE melts. For the single-chain coherent dynamic structure factor, they found very good agreement with the predictions of the reptation model. A simultaneous fit could be made for several values of the wave vector q using a slightly adapted version [98, 120, 141] of an expression formulated by de Gennes, [27] with the tube diameter d as the only fit parameter. This allowed them to extract the tube diameter d very accurately: at a temperature of 509 K, a tube diameter of about 4.6 nm was found.

Although in the original tube model it was assumed that the tube diameter is more or less independent of temperature, in reality this is only approximately true. The conformations are different between 509 K and 450 K, leading to different local structures and different tube diameters. In their 1993 paper, [110] Richter *et al.* investigated the temperature dependence of the tube diameter and found that it increases slowly with temperature. In a range of temperatures, including the two above, d was found to be proportional to $\exp\left[(1.2\pm0.2)\cdot10^{-3}T\right]$. Using this formula, one finds a slightly smaller tube diameter, $d = 4.3$ nm, at the lower temperature of 450 K at which we have performed our molecular dynamics simulations. In these simulations, like in the experiments of Richter, the single-chain coherent dynamic structure factor was found to be in good agreement with the tube model for times larger than the entanglement time (*vide infra*). A simultaneous fit for several values of q yielded $d = 5.4$ nm in the molecular weight range $M_w = 8-14$ kg/mol. These results are in good agreement with results of Richter *et al.* in the same range om molecular masses. [141] The reason for the apparent increase of d is the fact that, in the quoted molecular weight range, the chains are still very much influenced by contour length fluctuations. Richter *et al.* have successfully shown that, on correcting for these contour length fluctuations, the resulting tube diameter does not significantly depend on the chain length. [141] In other words, the corrected tube diameter is found to be in agreement with the tube diameter of asymptotically long chains ($d = 4.3$ nm at 450 K).

Now, assuming that d^2 equals the average squared end-to-end distance of a chain with molecular weight $M_w = M_e$, i.e.,

$$d^2 = \left\langle R_e^2(M_e)\right\rangle, \tag{6.1}$$

one finds $M_e = 1.7$ kg/mol for polyethylene at a temperature $T = 450$ K. This is our first estimate of the entanglement molecular weight. Some criticism may be cast on the usage of the average end-to-end distance in Eq. (6.1). Some authors claim that d must equal two times the radius of gyration of a chain with molecular weight $M_w = M_e$. Assuming a Gaussian distribution of the particles, this would amount to $d^2 = 2/3\left\langle R_e^2(M_e)\right\rangle$. Notice that this prefactor of 2/3 would actually lead to a *larger* estimate for the entanglement molecular weight because the tube diameter is already fixed by the experimental results. As we will see in the next section, this would therefore worsen the agreement with the estimate from the value of the plateau modulus. We will substantiate this prefactor of 1 by comparing with the other time-resolved quantities.

2. In the simulations we found that the shear relaxation modulus $G(t)$, which describes the relaxation of stress after a small shear step, can be described well by the Rouse model [30] for melts of relatively low molecular weight polyethylene. For molecular weights larger than 1.7 kg/mol an initially Rouse-like stress relaxation substantially slows down at larger time scales. Therefore, if we define the entanglement molecular weight as the lowest molecular weight where deviations from Rouse-like stress relaxation occur, we find 1.7 kg/mol as the entanglement molecular weight.

3. For all chain lengths, the slowing down of $G(t)$ sets in at 6 ns, which time in the usual tube/reptation model [30] is identified as the entanglement time τ_e. We define the entanglement molecular weight as the molecular weight of a chain whose longest relaxation time is equal to τ_e,

$$\tau_e = \tau_1(M_e). \tag{6.2}$$

   In the previous chapter, the relaxation times of various chain lengths have been investigated. Using Eq. (6.2), we again find an entanglement molecular weight of $M_e = 1.7$ kg/mol.

4. Finally, the characteristics of both the short-time and the long-time Rouse-mode correlation functions change drastically when $M_w/k = M_e$, with k the Rouse-mode number and $M_e = 1.7$ kg/mol again [see Figs. 5.7 and 5.8(b)].

Thus, we find that time-resolved measurements consistently give the same value for M_e, independent of the type of experiment. The entanglement molecular weight can be estimated from the tube diameter [via Eq. (6.1)], from the entanglement time [via Eq. (6.2)], by careful investigation of the onset of deviations from Rouse-behavior in the shear relaxation modulus, or by careful investigation of the relaxation behavior of the Rouse-modes.

6.3 Time-integrated results

In practice, the entanglement molecular weight is often determined [30] from the experimental value of the plateau modulus G_N^0:

$$M_{e,p} = \frac{4}{5}\frac{\rho N_A k_B T}{G_N^0}, \tag{6.3}$$

where N_A is Avogadro's number, k_B is Boltzmann's constant, T is the temperature, and ρ is the polymer melt density (we have added a subscript p to indicate that M_e is estimated from the plateau modulus). Fetters *et al*. [40] measured the value of the plateau modulus in PE melts at a density of $\rho = 0.768$ g/cm^3 and temperature $T = 443$ K, close to the conditions of the molecular dynamics simulations. Using Eq. (6.3) (including the prefactor 4/5) they found $M_{e,p} = 0.92$ kg/mol. This is much lower than the previously found 1.7 kg/mol from the time-resolved measurements.

Notice that Eq. (6.3) uses a rather arbitrary prefactor of 4/5 from the Doi-Edwards model. [30] Using different models, different prefactors may be found. However, the prefactor never exceeds unity. Even when this largest prefactor of 1 is used, the entanglement molecular weight from the plateau modulus ($M_{e,p} = 1.15$ kg/mol in that case) can not be brought into agreement with the estimate from the time-resolved measurements. It may even be that there is no unique relation between M_e and G_N^0. Indeed, as was already noticed by Tanaka *et al*., [133] $M_{e,p}$ defined by Eq. (6.3) is not a pure entanglement parameter, and may therefore not be the same as the "true" entanglement molecular weight as it occurs in the tube/reptation model. To estimate the latter, one needs to measure a physical quantity that is sensitive to

density fluctuations occurring in a tube, such as the single-chain coherent dynamic structure factor. [120]

Also, there is no straightforward way to extract the entanglement molecular weight from the molecular weight dependence of time-integrated quantities such as the viscosity η or the self-diffusion coefficient D. The reptation model predicts a transition in the scaling of D from M_w^{-1} to M_w^{-2} at the entanglement molecular weight. However, both experiment [103, 106] and simulation (see *Chapter 5*) have revealed that the molecular weight region in which D scales like M_w^{-2} (and even faster [72]) clearly starts *before* M_e. No transition is observed at the molecular weight M_e itself, not under constant pressure nor under constant density conditions. This fact has not always been recognized in other polymer simulation work, yielding underestimated values of M_e, as shown in *Chapter 5*. The reason why the transition does not occur at M_e is that there are additional molecular relaxation processes besides those in the original reptation model, as was already noticed by Pearson *et al*. [103] Similarly, the exponent in the scaling of the viscosity η has a transition at a molecular weight, which is much *larger* than M_e. This molecular weight is usually referred to as the critical molecular weight M_c (4 - 5 kg/mol for PE [106]). It is evident that, if one insists on estimating M_e from time-integrated data, one should aim for combinations of observables which do not rely on the precise mechanism for the polymer motion.

Oostwal and Odijk introduced a dynamic scaling hypothesis, which applies to both semidilute and concentrated solutions and to polymer melts. [94] We have repeated their arguments in Appendix 6.A. The main result is that ν, the effective number of dynamic units per unit volume making up the temporary network, can be related to a combination of the viscosity, self-diffusion coefficient, and a characteristic scale of the polymer [see Eq. (6.A.4)]. The dynamic scaling hypothesis does not supply exact prefactors. However, taking into consideration a limiting case the prefactor can be fixed, leading to the following result:

$$\nu = \frac{36\eta D}{k_B T \left\langle R_e^2 \right\rangle}. \tag{6.4}$$

The limiting case, motivating the prefactor of 36 is the following. Melts of unentangled, short polymers are known to behave like Rouse chains. The viscosity of a Rouse chain is given by [30]

$$\eta = \frac{\pi^2}{12} \frac{c k_B T}{N} \tau_R, \tag{6.5}$$

where N is the number of segments per chain, c is the number of segments per unit volume, and τ_R is the Rouse time, which is given by

$$\tau_R = \frac{\zeta N^2 b^2}{3\pi^2 k_B T}, \tag{6.6}$$

where ζ is the segmental friction coefficient and b is the segment size. The latter two quantities can be eliminated in favor of the diffusion coefficient $D = k_B T / N\zeta$ and the mean square end-to-end distance $\left\langle R_e^2 \right\rangle = Nb^2$:

$$\tau_R = \frac{\left\langle R_e^2 \right\rangle}{3\pi^2 D}. \tag{6.7}$$

polymer	M_w (kg mol^{-1})	$\langle R_e^2 \rangle$ (nm^2)	η (Pa s)	D (10^{-10} m^2 s^{-1})	ν (nm^{-3})
$C_{80}H_{162}$	1.12	10.2	0.005	1.8	0.51
$C_{120}H_{242}$	1.69	16.3	0.011	0.90	0.35
$C_{200}H_{402}$	2.81	25.3	0.033	0.30	0.23
$C_{400}H_{802}$	5.61	54.9	0.20	0.084	0.18
$C_{600}H_{1202}$	8.42	91.8	0.88	0.036	0.20
$C_{800}H_{1602}$	11.23	132	2.95	0.018	0.23
$C_{1000}H_{2002}$	14.03	167	5.98	0.011	0.23

Table 6.1: Molecular characteristics and density of effective dynamic units for polyethylene at 450 K. Mean square end-to-end distance, zero shear viscosity, and self-diffusion coefficient are taken from molecular dynamics simulations, see *Chapter 5*. All these simulations were performed at constant density, $\rho = 0.761$ g cm^{-3}. ν is the density of effective dynamic units making up the temporary network, calculated according to Eq. (6.4) in the main text.

Now, in a melt of short polymers, each individual chain acts as an independent spring. This is true because short chains are unentangled. Therefore, in the limit of short chain lengths, the effective number of dynamic units per unit volume is equal to the number of chains per unit volume, i.e., $\nu = c/N$. Combination of Eqs. (6.5) and (6.7) leads to Eq. (6.4).

We now generalize Eq. (6.4) by stating that it is valid for melts of polymers of any length. After all, the dynamic scaling hypothesis is valid for polymers of any length. For polymer melts of increasingly large molecular weight, we expect that ν becomes constant. In Table 6.1, the results of constant density ($\rho = 0.761$ g/cm3) simulations of PE melts at 450 K are reported (see *Chapter 5*). The fact that ν indeed becomes more or less constant for large enough molecular weights, indicates the presence of a characteristic length for the effective dynamic units. The corresponding characteristic mass $\rho N_A/\nu$ is conceptually very similar to the entanglement molecular weight, and for a melt obeying reptation actually equals M_e. [94] In Fig. 6.1, $\nu/\rho N_A$ is plotted against molecular weight. In this scaling, the vertical axis represents the inverse of the molecular weight corresponding to one effective dynamic unit. The low molecular weight data is observed to be close to $1/M_w$ (solid line), signifying the fact that in this regime indeed the individual chains are the dynamic units. This is a justification of the *quantitative* validity of Eq. (6.4). At higher molecular weight, the data clearly deviate from the $1/M_w$ line. After a dip, they approach a value which is consistent with the entanglement molecular weight found from time-resolved measurements, i.e., 1.7 kg/mol, see the long-dashed line in Fig. 6.1. On the other hand, if the empirical estimate based on the plateau modulus would have been the actual weight of an effective dynamic unit, the data in Fig. 6.1 would have to stabilize to the value indicated by the dotted line, calculated according to Eq. (6.3) ($M_{e,p} = 0.92$ kg/mol. Even when the maximum prefactor of one is used in Eq. (6.3) instead of the Doi-Edwards prefactor of 4/5, the estimate from the plateau modulus remains at variance with estimates from time-resolved measurements and ν

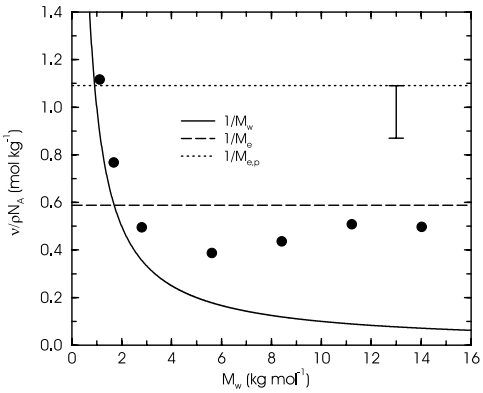

Figure 6.1: Inverse molecular weight of an effective dynamic unit in a polyethylene melt at 450 K as a function of polymer molecular weight: circles are results from molecular dynamics simulations, see *Chapter 5*. The solid line represents the inverse polymer weight, in which case the individual chains are the dynamic units. The long-dashed line represents the inverse entanglement molecular weight, obtained from time-resolved measurements ($M_e = 1.7$ kg/mol). The dotted line represents the inverse of the empirical estimate based on the value of the plateau modulus [Eq. (6.3)]; the lower part of the error bar indicates the value from Eq. (6.3) when a prefactor of one is used instead of the Doi-Edwards prefactor of 4/5.

(see the error bar). (It is important to be able to recognize when the value of ν has stabilized. This will depend on many factors, of which the polydispersity of the sample is an important one. [103])

6.4 Discussion and conclusion

Let us note that the combination of viscosity and self-diffusion coefficient was already investigated by Pearson *et al*. [103,106] No attempt was made, however, to derive the entanglement molecular weight from the high molecular weight data. Rather, they used the empirical value based on the plateau modulus to test the reptation theory prediction

$$(\eta D)_l = (\eta D)_s (M_w/M_e), \tag{6.8}$$

with the subscript l referring to long chains and s to short chains. As we have reviewed, it was shown by Oostwal and Odijk that such a relation is to be expected to hold true on much more general grounds. The fact that a *scaling* like Eq. (6.8) holds is, in itself, not a validation of reptation theory.

However, we have shown that the density of effective dynamic units ν obtained by the combination of viscosity and self-diffusion coefficient becomes a constant for large values of M_w, and that this constant corresponds to a value of M_e in agreement with time-resolved experiments, when the outcome of these experiments are interpreted in terms of the tube/reptation model. This is indeed extra motivation for the validity of the reptation model. The strict relationship between the entanglement molecular weight and the plateau modulus, as it occurs in reptation theory, has to be released.

Such a subtlety was not known to Pearson. In retrospect, deriving M_e from Pearson's data, we find an M_e close to 1.7 kg/mol, in agreement with our simulation results and the neutron

spin echo experiments of Richter *et al*. [120, 141] and not with $M_{e,p}$ obtained from the value of the plateau modulus. More theoretical work will be needed to fully understand the exact relationship between the value of the plateau modulus and the value of the entanglement molecular weight as it occurs in the tube/reptation model.

Acknowledgment

We would like to thank Theo Odijk for bringing Ref. [94] to our attention.

6.A Appendix. Dynamic scaling hypothesis

Suppose we know both the mean square extension R^2 and the self-diffusion coefficient of a polymer chain. The relation

$$D \equiv \frac{R^2}{\tau} \tag{6.A.1}$$

defines a time scale τ during which a test chain diffuses over a distance R. The probability of two test chains initially occupying essentially the same domain of size R^3 to still overlap at a later time t, decays rapidly to zero after a time of order τ. Stated differently, the correlation of the network at time t with the original network at time $t = 0$, decays rapidly for $t > \tau$. As a consequence, stresses induced by a small shear strain applied at $t = 0$ will quickly disappear at times $t > \tau$. Oostwal and Odijk make this statement operational by assuming that there is really only one time scale involved in both processes, i.e. diffusion and stress relaxation, which leads to the scaling relation introduced previously by de Gennes: [26]

$$\eta \approx E\tau. \tag{6.A.2}$$

We will consider this equation as the definition of E, which has the dimension of a modulus, but does not necessarily equal the plateau modulus G_N^0. Still, it has to be interpreted in terms of a temporary elastic network presumed to exist for times shorter than $O(\tau)$. Therefore, it can be used to define ν, the effective number of dynamic units per unit volume making up the temporary network:

$$E \equiv k_B T \nu. \tag{6.A.3}$$

Combining Eqs. (6.A.1) - (6.A.3), we eliminate the unknown time scale τ:

$$\nu \approx \frac{\eta D}{k_B T R^2}. \tag{6.A.4}$$

Notice that, as also stressed by Oostwal and Odijk, Eq (6.A.4) is obtained without specifying the detailed dynamics of the surrounding fluctuating network of other chains, nor specifying whether the test chain diffuses in or out of an effective tube, or any other mechanism.

7 Coarse-grained molecular dynamics simulations of polymer melts in transient and steady shear flow

By use of nonequilibrium simulations the coarse-grained model of polyethylene, developed in the previous chapters, is subjected to a planar Couette flow. Both transient and steady state nonlinear flow properties are investigated for shear rates varying from 30 to 3000 μs^{-1} and chain lengths varying from $C_{80}H_{162}$ to $C_{800}H_{1602}$. We report rheological data (shear viscosity, normal stress differences) and structural data (chain dimensions and the order tensor), and compare them with experimental results, where available. The locations of maxima and magnitudes of overshoots in the shear stress and normal stress difference are in agreement with experimental results. We also observe an undershoot in the transient extinction angle, and a decrease of the steady state extinction angle with shear rate, both of which are in very good agreement with recent experiments. Two rheological "rules", the stress-optical rule and the Cox-Merz rule, are tested. It is shown that the extinction angle, as calculated from stress components, remains equal to the optical extinction angle even for high shear rates, where the stress-optical rule is no longer strictly valid.

7.1 Introduction

Coarse-grained molecular dynamics simulations provide a powerful tool to investigate the microscopic origins of the rheological behavior of complex fluids. In *Chapter 5* we have investigated coarse-grained polymer melts by use of equilibrium simulation techniques, and found good agreement with experimental results in the limit of zero shear rates. The good agreement was not accidental, but due to the way the coarse-grained friction and interaction model were derived from an underlying microscopic (atomistic) model. It was found that the interactions between coarse-grained sites are rather soft, which without additional measures would lead to unrealistic bond crossings and too fast dynamics. This accellerated dynamics might have been slowed down by artificially changing the friction, but this would probably have improved just one quantity, while aggravating the other. For example, it is known that for high molecular weight polymer melts the combination $\eta D/\langle R_e^2 \rangle$ is a constant (see *Chapter 6*). In a system of crossable chains the product ηD is invariant under changes of the

friction ξ. Since obviously $\langle R_e^2 \rangle$ is also independent of ξ, the product $\eta D / \langle R_e^2 \rangle$ can not be changed by just changing the friction. To preserve the physical reality of the coarse-grained model, a constraint was introduced to prevent bond crossings. Because of this combination of 'bottom-up' coarse-graining and the guaranteed uncrossability of chains, the time and length scales which occurred in the coarse-grained simulations were all in the right proportions. We found good agreement with experimental diffusion and viscosity results, as well as neutron scattering spectroscopy.

Encouraged by the success of this method, we now address the nonlinear properties of our polymer simulation model. We will investigate nonlinear rheological properties of both unentangled and entangled polymer melts. The longest chain lengths that we will study have molecular weight $M_w > M_c$, i.e., well into the entangled regime where the zero-shear viscosity scales approximately as $\eta_0 \propto M_w^{3.4}$. Note that the pure reptation prediction, $\eta_0 \propto M_w^3$, only occurs in even longer chains ($M_w > 100 M_e$), in which case "ab initio" coarse-grained simulations of the rheological properties are practically impossible.

Experimental data for the nonlinear viscoelasticity of unentangled and moderately entangled polymer melts are hardly available because of the difficulty to reach the associated high shear rates (at least under controlled circumstances). This is one motivation to perform computer simulations. Another motivation is the fact that computer simulations can provide valuable information about the relation between the rheology at the macrosopic level and the molecular processes at the microscopic level. For example, the often used stress-optical rule, which states a proportionality between the stress tensor and the refractive index tensor of a polymer melt, can be tested because both properties can be measured independently in the simulation.

Several theoretical models have been proposed, [30,33,58,71,81] all with their successes and shortcommings. The Doi-Edwards tube model, for example, greatly overpredicts the phenomenon of shear thinning, even to the degree of predicting a nonmonotonic variation of shear stress with shear rate, not seen in experiments on well-characterized polymer melts. The problem arises from the nearly perfect alignment of the tubes along the flow direction. (Notice that for entangled wormlike surfactant solutions such a perfect alignment is suppressed by the continual breakup and recombination of the worms [16]). Marrucci solved this problem to a significant extent by adding a new ingredient in the theory of polymer melt rheology, which plays a crucial role in the nonlinear range: convective constraint release (CCR). [74] CCR is the mechanism by which topological constraints are not only affinely displaced, but also removed by the nonthermal motion between chains. The relative motion can be induced either directly by a velocity gradient, or indirectly by chain retraction following a 'fast' deformation, i.e., with a rate larger than the reciprocal Rouse time. Open problems still remain, however. One of them is the incomplete fulfilment of the Cox-Merz rule. [75] This provides another motivation for performing computer simulations: the results of computer simulations can be used to test the predictions, and aid in the improvement, of molecular theories of polymer melt flow.

This chapter is organized as follows: The simulation model is presented in Sec. 7.2. The results are presented and discussed in Sec. 7.3. This section is divided in three subsections. In subsection 7.3.1 we will focus on the transient response upon startup of fast steady shear. We will analyze the characteristic over- and undershoot in stress and the transient chain elonga-

tion and orientation. Next, in subsection 7.3.2, we will present the steady shear flow results. We will analyze the development of the nonlinear viscosity and normal stress coefficients with shear rate and molecular weight. We will also measure the steady state extinction angle and test the stress-optical rule. In subsection 7.3.3 we will test the Cox-Merz rule against a mixed Rouse-reptation expression for the linear shear relaxation modulus that was introduced in *Chapter 5*. In Sec. 7.4 we will summarize our conclusions.

7.2 Model and simulation method

7.2.1 Coarse-grained interactions and uncrossability

In this study we have used the same coarse-grained molecular dynamics simulation model of linear polyethylene (PE) as presented in *Chapters 4* and *5*. In short, each coarse-grained particle (blob) represents the center of mass of $\lambda = 20$ consecutive monomers. Because of the coarse-graining, alongside the mean forces, friction and random forces emerge in the equations of motion. It was found that the random forces decorrelate much faster than the blob momenta, which leads to an equation of motion of the simple Langevin type;

$$M\frac{d^2\mathbf{R}_i}{dt^2} = \mathbf{F}_i^S - M\xi\frac{d\mathbf{R}_i}{dt} + \mathbf{F}_i^R, \tag{7.1}$$

where $\mathbf{R}_i$ is the position of blob i, M is its mass, and ξ is the blob friction frequency, related to the random force $\mathbf{F}^R$ through the fluctuation-dissipation theorem. $\mathbf{F}_i^S$ is the systematic part of the force on blob i, which is derived from the free energy or potential of mean force associated with the configuration:

$$\mathbf{F}_i^S = -\nabla_i\chi, \tag{7.2}$$

$$\chi(\mathbf{R}^n) = -k_BT\ln P_n(\mathbf{R}^n). \tag{7.3}$$

Here P_n is the n-blob distribution function. Both the systematic interaction and the friction parameters were derived from a microscopic molecular dynamics simulation of PE at a temperature of 450 K and a constant mass density of $\rho = 0.761$ g/cm^3, in a cubic simulation box with periodic boundary conditions.

As already mentioned in the introduction, since so many monomers are combined into one blob, the blobs are rather empty and the systematic interactions between blobs are very soft. Consequently, in the mesoscopic simulations, without additional measures, unphysical bond crossings may occur. To prevent this from happening, an uncrossability constraint (TWENTANGLEMENT) is applied. The idea behind this constraint is to consider the bonds between consecutive blobs to be elastic bands. As soon as two of these elastic bands make contact, an "entanglement" is created at the crossing position $\mathbf{X}$ which prevents the elastic bands from crossing. This is accomplished by defining the attractive part of the potential between bonded blobs i and $i+1$ to be a function of the path length $L_{i,i+1}$ of the bond, going from one blob (i) to the next ($i+1$) via the intermediate entanglement,

$$L_{i,i+1} = \left|\mathbf{R}_i - \mathbf{X}\right| + \left|\mathbf{X} - \mathbf{R}_{i+1}\right|. \tag{7.4}$$

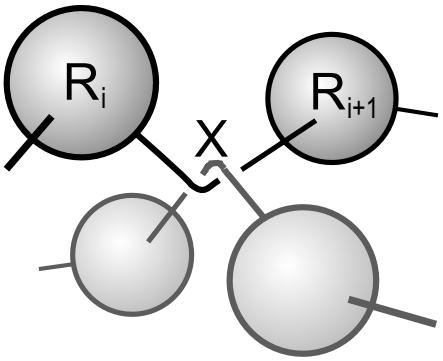

Figure 7.1: Sketch of two "entangled" parts of chains. At an earlier time, the bonds between the two depicted pairs of blobs tried to cross each other. This caused the uncrossability constraint to insert an "entanglement" at the crossing point. Since then the attractive part of the potential between bonded blobs is a function of the path length from blob i, via the entanglement at $\mathbf{X}$, to blob $i+1$.

See Fig. 7.1 for a sketch of this situation. The position of the entanglement is determined by the requirement that there is always equilibrium of forces at the entanglement. Of course more than one entanglement per bond is allowed. Details about this and more about the uncrossability constraint can be found in *Chapter 4*.

7.2.2 Simulating shear flow

In this chapter we study the nonlinear viscoelastic properties of our polymer simulation model. To this end we apply a planar Couette (shear) flow to our box, the velocity field being given by

$$\mathbf{u}(\mathbf{r}) = \dot{\gamma}\, r_y \widehat{\mathbf{e}}_x, \tag{7.5}$$

where $\dot{\gamma}$ is the shear rate and $\widehat{\mathbf{e}}_x$ is the unit vector parallel to the x-axis. In a simulation, the effect of shear flow can be taken into account through the SLLOD algorithm [5,6] which, in a form modified for the Langevin equation, is:

$$\frac{d\mathbf{R}_i}{dt} = \frac{\mathbf{P}_i}{M} + \dot{\gamma}\, R_{iy} \widehat{\mathbf{e}}_x, \tag{7.6}$$

$$\frac{d\mathbf{P}_i}{dt} = \mathbf{F}_i^S - \dot{\gamma}\, P_{iy} \widehat{\mathbf{e}}_x - \left(\frac{\sum_i \mathbf{F}_i^S \cdot \mathbf{P}_i - \dot{\gamma}\, P_{ix} P_{iy}}{\sum_i \mathbf{P}_i^2} \right) \mathbf{P}_i - \xi \mathbf{P}_i + \mathbf{F}_i^R. \tag{7.7}$$

Here $\mathbf{P}_i$ is the peculiar momentum of blob i. The term between brackets serves to keep the peculiar kinetic energy $\sum \mathbf{P}_i^2 / 2M$ exactly constant in case there are no friction or random forces ($\xi = 0$). In other words, all fluctuations in the temperature of the system under shear will be caused by the friction and random forces. This may become important when the shear rate $\dot{\gamma}$ is large compared with the friction frequency ξ or when the systematic forces are relatively large. This is, however, not the case for our simulations. To explain this, we have to elucidate the two different possible uses of the Langevin equation.

The Langevin stochastic dynamics method has been used to perform simulations of polymer chains by several authors among whom are Kremer and Grest. [66] These authors effectively established a coupling between the system and a heat bath in order to keep the system at some desired temperature. In order not to influence the chain dynamics too much, they had to choose the friction frequency ξ much smaller than the effective friction due to systematic interactions between the beads in the model, which determines dynamic properties, such as diffusion. In our work, however, the systems have been coarse-grained to a much larger level and the interactions have become very soft. As a consequence, besides acting as a thermostat, the friction has acquired the meaning of a *physical* friction. In fact, the friction frequency ξ is so large that, if a simple leap-frog or velocity-Verlet algorithm [5] would be used, it would limit the length of the integration step by $\Delta t \ll 1/\xi$. To overcome this limitation, in our previous work, we have adopted the Brownian dynamics algorithm of Allen, in which the effects of the friction and stochastic forces in Eq. (7.1) are "pre-integrated" under the assumption that the systematic forces may be interpolated linearly during each time step (for $\xi \to 0$ this results in a second order Verlet algorithm). [4] This way, the integration step is again limited by the maximum curvature of the systematic interactions. However, such a pre-integration is not so easy to perform when shear is present, see Eqs. (7.6) - (7.7). Fortunately, there is a way out. Inserting Eq. (7.6) in Eq. (7.7) one finds

$$M\frac{d^2\mathbf{R}_i}{dt^2} = \mathbf{F}_i^S - M\xi^{\text{eff}}\left(\frac{d\mathbf{R}_i}{dt} - \dot{\gamma} R_{iy}\widehat{\mathbf{e}}_x\right) + \mathbf{F}_i^R, \tag{7.8}$$

$$\xi^{\text{eff}} = \xi + \left(\frac{\sum_i \mathbf{F}_i^S \cdot \mathbf{P}_i - \dot{\gamma} P_{ix}P_{iy}}{\sum_i \mathbf{P}_i^2}\right). \tag{7.9}$$

In our case, the friction frequency is large ($\xi = 8$ ps^{-1}) and the systematic forces and shear rates (maximal 0.003 ps^{-1}) relatively small. Therefore, to a good approximation $\xi^{\text{eff}} = \xi$. Notice that Eq. (7.8) can be interpreted as follows: the forces which act on a blob under shear are the systematic forces, the friction forces, where the velocities must be taken relative to the shear field, and the random forces. The latter two forces have the same characteristics as in equilibrium. In this work we have used the abovementioned algorithm of Allen, in which we treat the term $\mathbf{F}_i^S + M\xi\,\dot{\gamma} R_{iy}\widehat{\mathbf{e}}_x$ as the systematic force on a blob. We have checked the stability of this algorithm by measuring the temperature, defined through the peculiar kinetic energy $\sum \mathbf{P}_i^2/2M$, where $\mathbf{P}_i$ is given by Eq. (7.6). This yielded good results (450 K, as desired).

We conducted the simulations for systems consisting of n_{chain} linear polymers made of N blobs confined in a sheared box with Lees-Edwards boundary conditions, [5] where N was taken to be 4, 6, 10, 20, 30, and 40 (these systems will be referred to as B_4, B_6, etc.), and n_{chain} was 180, 120, 100, 80, 80, and 80, respectively. These are both unentangled and entangled systems, since $N_e \approx 6$ blobs. The mass density was kept at 0.761 g/cm^3. Well-equilibrated systems from our previous work (*Chapter 5*) were used as initial states and the shear field was suddenly switched on at $t = 0$. This allowed measurement of both transient response upon onset of shear and steady state. The shear rates were taken to be 30, 100, 300, 1000, and 3000 μs^{-1}, except for $N = 40$, where the shear rate 30 μs^{-1} was estimated to be too small to reach steady state within the production time (about 3 months of computation on an SGI

Origin 2000 system, one processor for each system). The stress tensor $\sigma_{\alpha\beta}$ is calculated by

$$\sigma_{\alpha\beta} = -\frac{1}{V}\sum_{i=1}^{N_{\rm tot}}\left(MV_{i\alpha}V_{i\beta} + R_{i\alpha}F^S_{i\beta}\right), \tag{7.10}$$

where V is the volume of the simulation box, $N_{\rm tot}$ is the total number of blobs, $V_{i\alpha} = P_{i\alpha}/M$ is the α component of the peculiar velocity of blob i, $R_{i\alpha}$ the α component of $\mathbf{R}_i$, and $F^S_{i\beta}$ the β component of the systematic force on blob i arising from the potential energy. In order to estimate the error in the measurement of the stress, in some of the systems independent starting configurations were generated by continuing equilibrium simulations for a time longer than the largest relaxation time. After this, the shear field was turned on for a second measurement.

7.3 Results and discussion

We will now present and discuss the results from the nonequilibrium simulations. We will first focus on the transient response, then on the steady state properties. At the end of this section, we will test the Cox-Merz rule, which equates the nonlinear steady state viscosity to the Fourier transform of the zero-shear relaxation modulus.

7.3.1 Transient response upon startup of steady shear

Startup stress

In equilibrium, the average stress tensor is diagonal and the diagonal components are all equal to each other, $\sigma_{\alpha\alpha} = -P$, where P is the isotropic pressure. This means that the non-diagonal components $\sigma_{\alpha\beta}$ are zero on average. The first and second normal stress differences, defined as

$$N_1 = \sigma_{xx} - \sigma_{yy}, \tag{7.11}$$
$$N_2 = \sigma_{yy} - \sigma_{zz}, \tag{7.12}$$

are also zero on average. Obviously the situation is different as soon as the system is sheared, i.e., is brought in a nonequilibrium situation. Fig. 7.2 shows the time dependence of various components of the stress tensor in the B_{10} system (equivalent to $C_{200}H_{402}$) when a shear flow with constant shear rate $\dot{\gamma} = 1000\ \mu s^{-1}$ is started at time $t = 0$. Several qualitative observations can be made. Both the *xz*- and *yz*-components of the stress tensor remain zero, as should be expected for a shear field which is symmetric with respect to the *xy*-plane. The *xy*-component of the stress tensor is clearly not zero and passes through a very weak maximum before becoming stationary. At the given shear rate, the first normal stress difference is much larger than σ_{xy} and also displays a very weak maximum, but occurring at a later time. The second normal stress difference is much smaller than the first normal stress difference and its sign is negative, in agreement with experimental observations. Such normal stress differences give rise to quite peculiar viscoelastic effects, collectively known as Weissenberg effects. [12]

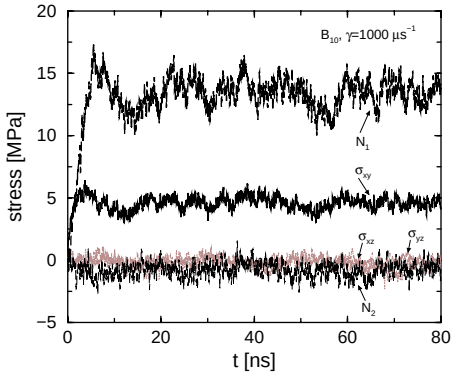

Figure 7.2: Time dependence of various stress components in the B_{10} system (equivalent to $C_{200}H_{402}$) in starting up a shear flow with shear rate $\dot{\gamma}$= 1000 μs^{-1}.

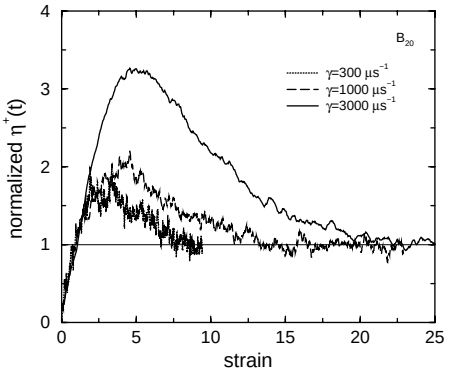

Figure 7.3: Transient growth of viscosity normalized by the steady state viscosity as a function of total strain after startup of steady shear flow in the B_{20} system, for shear rates $\dot{\gamma}$= 300, 1000, and 3000 μs^{-1}. The dimensionless shear rates (Deborah numbers) are 42, 140, and 420, respectively.

It is generally believed that the overshoots in the stress components occur because the polymer resists the chain stretch induced by the onset of fast flow, an effect which diminishes once the chains become oriented towards the flow direction. The Doi-Edwards tube model predicts that the maximum overshoot in the *xy*-stress occurs at a total strain $\gamma = \int \dot{\gamma}\, dt = \dot{\gamma}\, t$ value of 2. It is well known that at high shear rates the strain at which the maximum in the overshoot occurs actually increases with shear rate. [104, 105] This is also predicted, at least qualitatively, by other reptation-like theories which include the convective constraint release mechanism. [33, 58, 81] The increase of the overshoot is investigated for the B_{20} system (equivalent to $C_{400}H_{802}$) in Fig. 7.3. Here, we plot the transient growth of viscosity upon onset of shear, $\eta^+(t)$, against total strain γ for three different shear rates. The transient viscosity is defined as

$$\eta^+(t) = \frac{\sigma_{xy}(t)}{\dot{\gamma}}, \tag{7.13}$$

where the plus signifies the fact that the shear is suddenly turned on at $t = 0$. The results in Fig. 7.3 are all normalized by their respective steady state values. All shear rates correspond to Deborah numbers $\dot{\gamma}\,\tau_d$ much larger than one. Here, τ_d is the largest relaxation time of the chain. At these high shear rates, not only the maximum overshoot increases with shear rate, but indeed also the strain $\gamma_{\max}$ at which the maximum occurs. In Fig. 7.4 we present the maximum overshoot and the strain at maximum overshoot against Deborah number (filled triangles). These results are in good agreement with experiments on solutions in tricresyl phosphate of nearly monodisperse polystyrene by Hua, Schieber, and Venerus (open circles). [58]

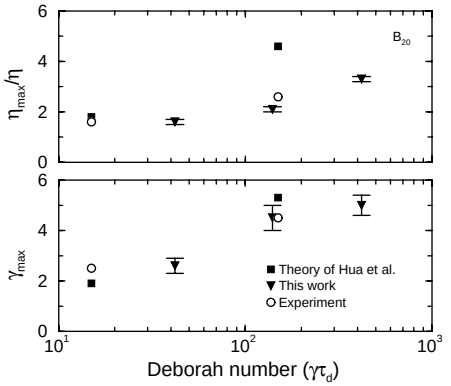

Figure 7.4: Maximum overshoot in the transient viscosity (top figure) and the strain γ_{max} at which the maximum occurs (lower figure) against Deborah number. Filled triangles are for the B_{20} system from this work, open circles are experimental results by Hua, Schieber, and Venerus. [58] Filled squares are predictions from the theory of the same authors.

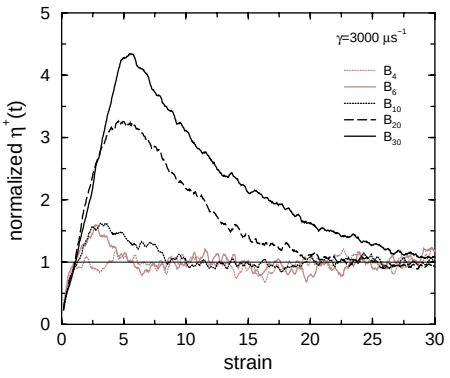

Figure 7.5: Transient growth of viscosity normalized by the steady state viscosity as a function of total strain after startup of steady shear flow for different chain lengths at shear rate $\dot{\gamma}$= 3000 μs^{-1}. The dimensionless shear rates (Deborah numbers) are 5, 17, 76, 420, and $1.7 \cdot 10^3$, respectively.

The degree of entanglement of their sample was approximately $Z = M_w/M_e = 7$, comparable with ours. It is important to notice that most theories greatly overpredict the magnitude of the overshoot at these high shear rates. In the theory of Hua *et al.*, an overshoot of 4.6 is predicted for the above Deborah number of 150 (filled square in the top Fig. 7.4), whereas experimental observations are closer to 2.6.

Instead of varying the shear rate, we can also vary the chain length. In Fig. 7.5, we investigate the development of the transient growth of viscosity with chain length. The development of the overshoot with increasing chain length is similar to the development of the overshoot with increasing shear rate: both the maximum overshoot and the strain at which the maximum occurs increase with chain length. This may have been expected since increasing the shear rate and increasing the chain length both lead to an increase of the Deborah number.

Next, we turn our attention to the transient first normal stress difference N_1. The first normal stress coefficient is related to N_1 by

$$\Psi_1^+(t) = \frac{N_1(t)}{\dot{\gamma}^2}, \tag{7.14}$$

where again the plus signifies the fact that the shear is suddenly turned on at $t = 0$. In Fig. 7.6 we plot the transient growth of the first normal stress coefficient Ψ_1^+, normalized by its steady state value, against total strain γ for the same system and shear rates as in Fig. 7.3. The overshoot is weaker than in the case of the viscosity, in agreement with experiment. [104]

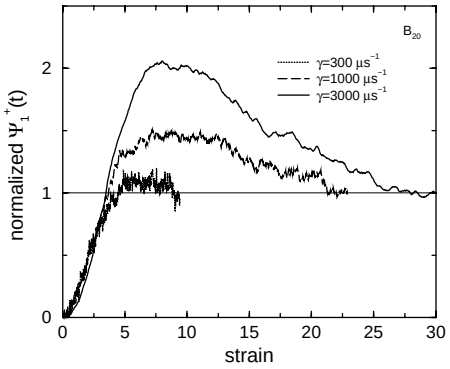

Figure 7.6: Transient growth of the first normal stress coefficient normalized by the steady state value as a function of total strain after startup of steady shear flow for the same system and shear rates as in Fig. 7.3.

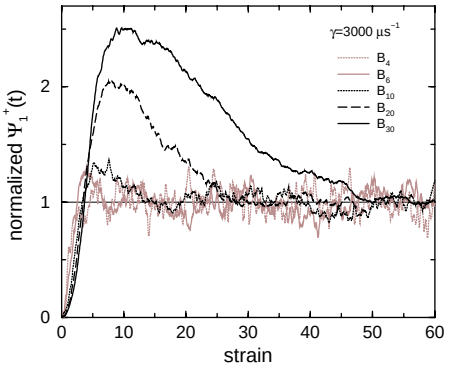

Figure 7.7: Transient growth of the first normal stress coefficient normalized by the steady state value as a function of total strain after startup of steady shear flow for the same chain lengths and shear rate as in Fig. 7.5.

At $\dot{\gamma}$= 300 μs^{-1} (dotted line) only very weak overshoot in Ψ_1^+ can be observed, while η^+ already has a maximum overshoot of 1.5. Moreover, where overshoot in Ψ_1^+ can be observed, it occurs at roughly twice the strain value compared with the overshoot in η^+. Also, the time required to reach steady state is roughly twice as long for Ψ_1^+. In Fig. 7.7 we investigate the development of the transient growth of the first normal stress coefficient with chain length for the same systems and shear rate as in Fig. 7.5. Again, the development of the overshoot with chain length is similar to the development with shear rate.

Transient elongation and orientation

When a shear flow with constant shear rate is started, the polymer chains deform and orient towards the flow direction. The elongation of the polymer is characterized by the *xx*-component of the mean square gyration tensor $\langle \mathbf{R} \rangle$: [6]

$$\langle \mathbf{R} \rangle = \frac{1}{n_{\text{chain}} N} \sum_{p=1}^{n_{\text{chain}}} \sum_{i=1}^{N} \left(\mathbf{R}_{pi} - \mathbf{R}_{pg} \right) \left(\mathbf{R}_{pi} - \mathbf{R}_{pg} \right). \tag{7.15}$$

Here $\mathbf{R}_{pi}$ represents the position of the *i*th blob on the *p*th chain, and $\mathbf{R}_{pg}$ is the position of the center of mass of the *p*th chain. Notice that the trace of $\mathbf{R}$ is the mean square radius of gyration. Fig. 7.8 shows the time dependence of the *xx*-component of the mean square gyration tensor in the B_{10} system for all applied shear rates, as well as the *yy*- and *zz*-components for the largest shear rate, $\dot{\gamma}$= 3000 μs^{-1}. Initially all components are equal to one third of the equilibrium mean square radius of gyration, which is $1/3 \times 4.05$ nm^2 (horizontal thin line, see *Chapter 5*). Fig. 7.8 indicates that when the shear flow starts, $\langle R_{xx} \rangle$ increases dramatically for the highest shear rates. At the same time the *yy*- and *zz*-component of the mean square

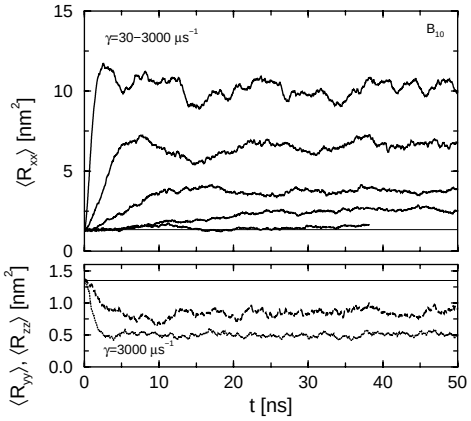

Figure 7.8: Diagonal components of the mean square radius of gyration tensor in a B_{10} melt after startup of steady shear flow. Solid lines in the top figure, from bottom to top of the figure, are the *xx*-components for shear rates 30, 100, 300, 1000, and 3000 μs^{-1}. Dotted and dashed lines in the lower figure are the *yy*- and *zz*-components, respectively, for $\dot{\gamma}$= 3000 μs^{-1}. The thin horizontal line is one third of the equilibrium mean square radius of gyration.

gyration tensor decrease, the *yy*-component somewhat more than the *zz*-component. Such a large decrease of $\langle R_{yy} \rangle$ and $\langle R_{zz} \rangle$ does not occur at the lower shear rates (not shown).

The orientation of the polymers is characterized by the order tensor **S**:

$$\mathbf{S} = \frac{3}{2}\left(\langle \mathbf{uu} \rangle - \frac{1}{3}\mathbf{I} \right), \tag{7.16}$$

$$\langle \mathbf{uu} \rangle = \frac{1}{n_{\text{chain}}\,(N-1)} \sum_{p=1}^{n_{\text{chain}}} \sum_{i=2}^{N} \frac{\mathbf{R}_{pi} - \mathbf{R}_{p,i-1}}{\left| \mathbf{R}_{pi} - \mathbf{R}_{p,i-1} \right|} \frac{\mathbf{R}_{pi} - \mathbf{R}_{p,i-1}}{\left| \mathbf{R}_{pi} - \mathbf{R}_{p,i-1} \right|}, \tag{7.17}$$

where **I** is the unit tensor. In an isotropic system, all components of the order tensor equal zero. In a nonisotropic system, the eigenvector belonging to the largest eigenvalue (the order parameter) of the order tensor gives the preferential orientation of the bonds. The angle between this eigenvector and the flow direction ($\hat{\mathbf{e}}_x$) is the flow alignment angle χ. It is given by

$$\tan 2\chi = \frac{2S_{xy}}{S_{xx} - S_{yy}}. \tag{7.18}$$

Because the bonds align with the flow direction, the optical properties of the polymer melt are also influenced; the refractive index of the material is no longer isotropic, but must be represented by a tensor, the refractive index tensor. The anisotropies in the refractive index tensor are caused by anisotropies in the polarizability of the material. Birefringence experiments can be used to measure the flow alignment angle experimentally. The flow alignment angle is also referred to as the extinction angle.

Fig. 7.9 shows the time dependence of the flow alignment angle in the B_{20} system for three different shear rates. The flow alignment angle decreases from approximately 45° to a lower angle, which decreases with increasing shear rate. The 45° angle is expected for systems in the linear regime. For example, for a Rouse chain undergoing a small *xy*-strain, the chain is preferentially oriented along the line $x = y$. Notice the undershoot in the predicted flow alignment angle at the highest shear rates, in agreement with experimental observations

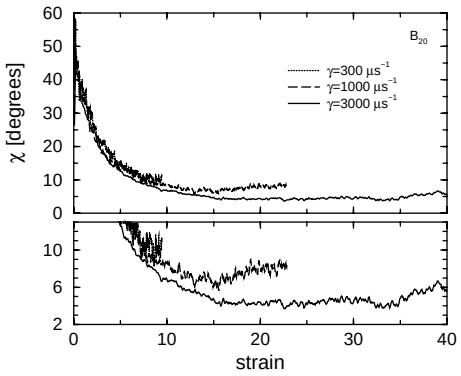

Figure 7.9: Transient flow alignment angle in the B_{20} system as a function of total strain after startup of steady shear flow with shear rates $\dot{\gamma}$= 300, 1000, and 3000 μs^{-1}, corresponding to Deborah numbers 42, 140, and 420, respectively. In the lower figure, the verticale scale is magnified.

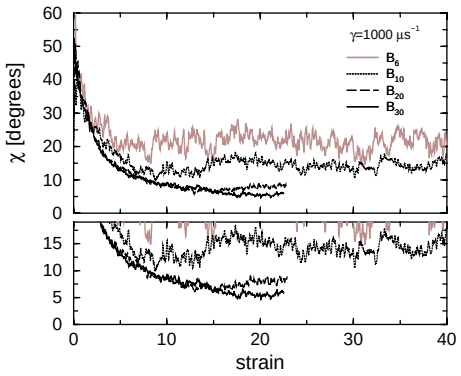

Figure 7.10: Transient flow alignment angle as a function of total strain after startup of steady shear flow for different chain lengths at shear rate $\dot{\gamma}$= 1000 μs^{-1}. The dimensionless shear rates (Deborah numbers) are 6, 25, 140, and 560, respectively. In the lower figure, the verticale scale is magnified.

[58, 81, 91] and theoretical predictions. [33, 58, 81] In the beforementioned experiments of Hua *et al.* [58] on solutions of polystyrene, with a Deborah number of 150, the undershoot occurred at a strain of approximately 16, in agreement with our results (dashed curve in Fig. 7.9). In Fig. 7.10 the influence of the molecular weight on the transient flow alignment angle is investigated. The results are plotted against total strain for different chain lengths, while the shear rate is kept constant at 1000 μs^{-1}. For $N \geq 10$ undershoots are present, though perhaps not always clearly visible.

7.3.2 Steady shear flow

Some time after startup of the shear flow, a steady state is reached. In this subsection we will study the steady state viscometric and optical properties.

Viscometric properties

Experiments [8] on highly entangled chains show that, over a wide range of shear rates $\dot{\gamma}$ above the inverse disentanglement time $1/\tau_d$, the steady shear stress σ_{xy} is nearly constant. The first normal stress difference N_1 increases more rapidly with shear rate than does the shear stress over the same range of shear rates. Moreover, the slopes of σ_{xy} and N_1 vs. $\dot{\gamma}$ increase with decreasing molecular weight. In our simulations the longest chains are not so highly entangled, so we do not expect to observe the nearly constant stress. However, the more rapid increase of the first normal stress difference may be observed, as well as the

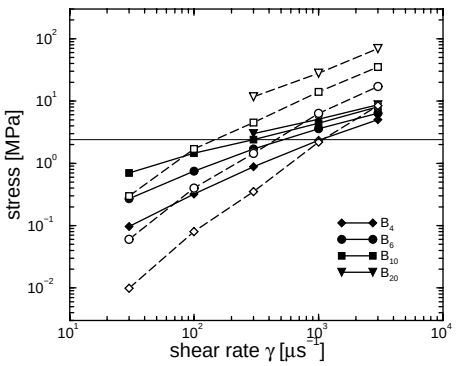

Figure 7.11: Steady state values of the shear stress σ_{xy} (filled symbols) and first normal stress difference N_1 (open symbols) as a function of shear rate $\dot{\gamma}$ for the B_4, B_6, B_{10}, and B_{20} systems (equivalent to $C_{80}H_{162}$ to $C_{400}H_{802}$). The thin horizontal line is the estimate of the (linear) plateau modulus from equilibrium simulations, *Chapter 5*.

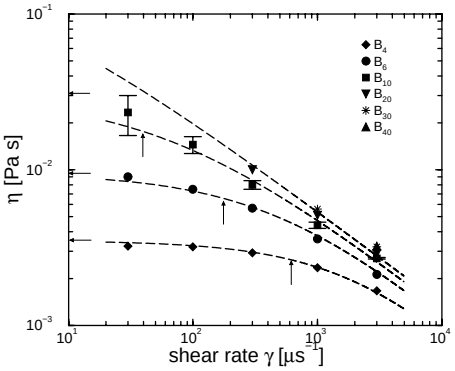

Figure 7.12: Steady state shear viscosity η as a function of shear rate $\dot{\gamma}$ for different chain lengths. The error bars for the B_{10} data originate from the standard deviations in the average *xy* stress component, and are typical for viscosity measurements in the other systems. The dashed curves are guides to the eye. Arrows under the curves indicate the inverse longest relaxation times of the B_4, B_6, and B_{10} systems. Horizontal arrows at the left scale indicate the zero-shear viscosities, obtained in equilibrium simulations (*Chapter 5*) of the same systems.

increase of the slopes with decreasing molecular weight. Fig. 7.11 shows the steady shear stress and first normal stress difference versus shear rate $\dot{\gamma}$. Clearly, the slopes are decreasing with increasing chain length and the slope of N_1 vs. $\dot{\gamma}$ is always larger than that of σ_{xy}. In the B_{20} system, steady state was not yet fully reached for $\dot{\gamma} \leq 100\ \mu s^{-1}$, making it impossible to make a reliable estimate of the steady state stress. The same applies for $\dot{\gamma} \leq 300$ in the B_{30} system and $\dot{\gamma} \leq 1000$ in the B_{40} system.

The shear-rate dependent viscosity η is determined from the steady state shear stress:

$$\eta = \lim_{t \to \infty} \frac{\sigma_{xy}}{\dot{\gamma}}. \tag{7.19}$$

The limit $t \to \infty$ must not be taken literaly; it just signifies the fact that all transient effects must be ignored. In Fig. 7.12 the shear viscosity is plotted versus shear rate. At low shear rates, the viscosity should approach a constant value, the zero-shear viscosity. The arrows at the left scale indicate the zero-shear viscosities of B_4, B_6, and B_{10} from our previous equilibrium simulations in *Chapter 5*.[1] The arrows under the curves indicate the inverse

1 The small amount that was added in *Chapter 5* to account for the difference between initial shear relaxation of

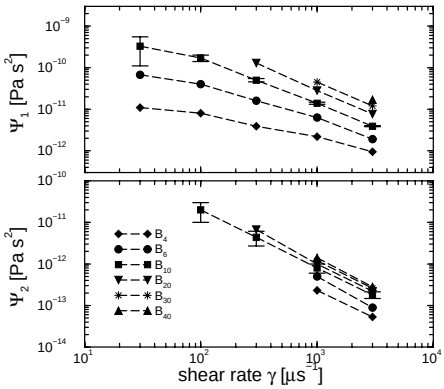

Figure 7.13: Steady state first normal stress difference Ψ_1 (top figure) and second normal stress difference Ψ_2 (lower figure) as a function of shear rate $\dot{\gamma}$ for different chain lengths. The error bars for the B_{10} data originate from the standard deviations in the average relevant stress components, and are typical for normal stress measurements in the other systems.

longest relaxation times $1/\tau_d$, also from our previous equilibrium simulations. Only for B_4, and almost for B_6, the linear regime is reached. For both chain lengths, the linear plateau is in good agreement with the zero-shear viscosity from the previous equilibrium simulations. Notice that the transition to the linear plateau is determined by the inverse longest relaxation time, but that this transition is not very sharp; the viscosity keeps increasing for $\dot{\gamma} < 1/\tau_d$. The same holds for the curve for the B_{10} system, although the way of plotting is slightly misleading. In fact, the curve was made with the viscosity at zero shear constrained to the equilibrium simulation value and the point of maximum inflection at $1/\tau_d$.

At higher shear rates, shear thinning is observed. The viscosities of the samples of length $N = 10$ and larger all approach a common curve independent of molecular weight. In the plot the data for $N = 20$ and larger are hardly discernible. This is in agreement with experimental observations [132] and other simulation work. [6, 68, 69] The slope of the curve is approximately -0.6, in agreement with observations in simulation work by Kröger and Hess. [68] Experimentally, the slope is closer to -0.85, [132] but this is for highly entangled chains. We expect that, as molecular weight increases, the slope of σ_{xy} in Fig. 7.11 becomes smaller, and the slope of the viscosity curve comes closer to the experimental value.

The first normal stress coefficient Ψ_1 and the second normal stress coefficient Ψ_2 are determined from the steady state first and second normal stress differences:

$$\Psi_1 = \lim_{t\to\infty} \frac{N_1}{\dot{\gamma}^2}, \tag{7.20}$$

$$\Psi_2 = \lim_{t\to\infty} \frac{N_2}{\dot{\gamma}^2}. \tag{7.21}$$

In Fig. 7.13 the first and second normal stress coefficients are plotted against shear rate. A linear plateau can be recognized in the Ψ_1 data of B_4 at small shear rates. All larger chain lengths are in the nonlinear regime for all shear rates studied. The first normal stress coefficients of the samples of length $N = 20$ and higher all approach a common curve independent

atomistically detailed and coarse-grained systems is now omitted.

of molecular weight. This is also observed in other simulation work. [6] The slope of the curve is approximately -1.1. The data for the second normal stress coefficient is less complete because the relative noise in N_2 increases rapidly as the strain rate decreases. At the highest shear rates accurate measurements of Ψ_2 were still possible. In this region the slope of the curves is approximately -1.5.

In the development of the theory of polymers in shear flow, much interest goes to the normal stress ratio, $-\Psi_2/\Psi_1$. Which value this ratio should approach for small shear rates, is still a matter of debate. [75] Different theories predict different ratios, ranging from 1/7 to 2/7. Unfortunately, because of the large noise in the N_2 measurements at low shear rates, these simulations can not give a definite answer either. However, we can estimate the ratios at higher shear rates, in the nonlinear regime. For the B_{10} system, the normal stress ratio decreases from 0.12 ± 0.04 for $\dot{\gamma} = 100\ \mu s^{-1}$ to 0.046 ± 0.006 for $\dot{\gamma} = 3000\ \mu s^{-1}$. Similar values in the nonlinear regime have been observed in experiments [93] and in the simulation work of Aoyagi and Doi. [6]

Steady state extinction angle

In subsection 7.3.1 we have seen that the flow alignment angle or extinction angle χ decreases from 45° to a lower value, which decreases with increasing shear rate. For long chains and high shear rates an undershoot in χ was predicted. After some time, however, the extinction angle remains constant. According to the Doi-Edwards theory, the steady state extinction angle falls to zero very fast for Deborah numbers larger than one, i.e., the chains become almost perfectly aligned with the flow field when the shear rate becomes much larger than the inverse disentanglement time. Exactly this is the reason, why the Doi-Edwards theory predicts excessive shear thinning of the viscosity at high shear rates. Experimentally, [58, 80] the steady state extinction angle decreases more gradually with shear rate. As already mentioned in the Introduction, the idea of convective constraint release serves to explain this observation. When the flow is fast compared with the inverse disentanglement time, constraints surrounding a given chain are quickly swept away, leaving the chain much more free to relax than is possible in pure reptation. [81]

Although, the steady state extinction angle strictly is a function of both the shear rate and the chain length, the dominant factor is the Deborah number. In Fig. 7.14 we show a plot of the steady state extinction angle (or flow alignment angle) χ of our simulation model as a function of the Deborah number $\dot{\gamma}\,\tau_d$. Indeed, the results fall more or less on one curve. Also plotted are the results of experiments on nearly monodisperse entangled polystyrene solutions by Hua, Schieber, and Venerus. [58] We find a very good agreement between our simulation results and experiment. Note that for B_{30} and B_{40}, at the highest shear rate of $\dot{\gamma} = 3000\ \mu s^{-1}$, the average chain size is larger than the size of the cubic box. Finite box-size effects limit the minimum flow alignment angle to about 5 degrees.

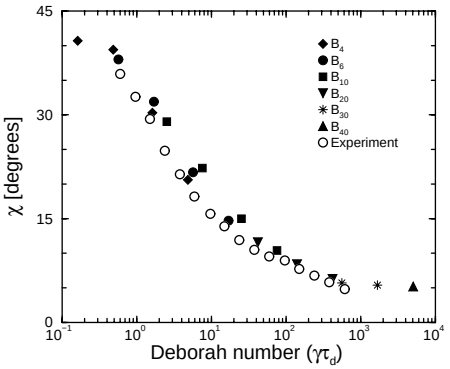

Figure 7.14: Steady state extinction angle χ as a function of Deborah number $\dot{\gamma}\,\tau_d$ for different chain lengths. The open circles are experimental results by Hua, Schieber, and Venerus [58] of a solution in tricresyl phosphate of nearly monodisperse polystyrene.

The stress-optical rule

Considering a system of temporary entanglements connected by entropic springs, the stress tensor $\boldsymbol{\sigma}$ is proportional to the order tensor $\mathbf{S}$:

$$\bar{\boldsymbol{\sigma}} = C\mathbf{S}. \tag{7.22}$$

$\bar{\boldsymbol{\sigma}}$ is the traceless part of the stress tensor, since in general the relationship between the traces of $\boldsymbol{\sigma}$ and $\mathbf{S}$ is not as simple as stated above. Since the order parameter is directly related to the refrective index tensor, this is equivalent to the stress-optical rule.

In a simulation, the stress-optical rule can be tested because both the stress and the order tensor can be measured independently. In Fig. 7.15 we plot the stress-order ratio against the shear rate for three components: σ_{xy}/S_{xy}, $N_1/(S_{xx}-S_{yy})$, and $N_2/(S_{yy}-S_{zz})$. From the Figure it is clear that for the first two of these components, the ratio becomes constant for low shear rates. Moreover, the constant of proportionality is the same, $C \approx 28$ MPa, for these components. Thus, we find that the stress-optical rule is valid for small shear rates. For higher shear rates, the ratios increase and the stress-optical rule is violated, as was already verified in the simulations of Kröger *et al.* [69] The ratio $N_2/(S_{yy}-S_{zz})$ seems to be always lower than that of the other components. However, this ratio can not be evaluated for the lowest shear rates, so no conclusion can be drawn for the validity of the stress-optical rule for the second normal stress difference.

In experimental work, the stress-optical rule is usually employed to derive the flow alignment (or extinction) angle from stress measurements:

$$\tan 2\chi^{\text{stress}} = \frac{2\sigma_{xy}}{N_1}, \tag{7.23}$$

where we have added the superscript "stress" to distinguish it from the directly measured flow alignment angle χ, Eq. (7.18). In Fig. 7.16 we have plotted the stress based flow alignment angle versus the "real" flow alignment angle. We find that the agreement is very good, even though we have seen that the stress-optical rule is not strictly valid for high shear rates (Deborah numbers of up to order 1000 occur). The reason for this can be found in Fig.

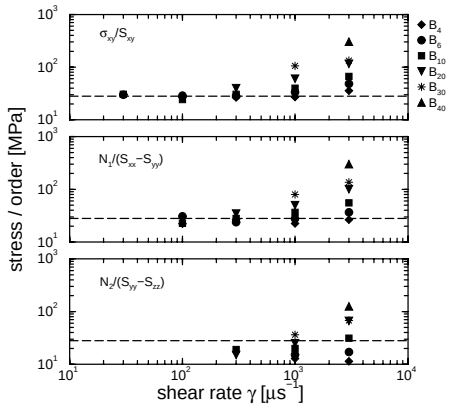

Figure 7.15: Test of the stress-optical rule. Different components of the stress tensor divided by corresponding components of the order tensor are plotted against shear rate $\dot{\gamma}$ for different chain lengths. The components are: xy (top figure), $xx-yy$ (middle figure), and $yy-zz$ (lowest figure). Dashed lines indicate a constant of proportionality of $C = 28$ MPa.

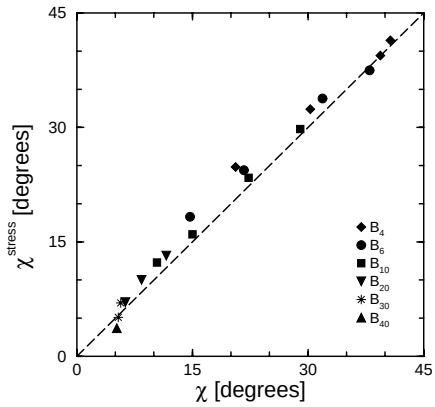

Figure 7.16: Steady state extinction angle estimated from stress tensor components, $\chi^{\text{stress}} = 1/2\tan^{-1}\left(2\sigma_{xy}/N_1\right)$, versus the "real" steady state extinction angle, $\chi = 1/2\tan^{-1}\left(2S_{xy}/\left(S_{xx}-S_{yy}\right)\right)$ for different chain lengths.

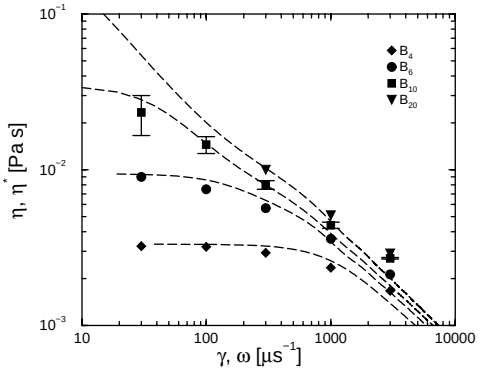

Figure 7.17: Steady state shear viscosity η versus shear rate $\dot{\gamma}$ (symbols), and complex viscosity η^* versus frequency ω (dashed lines) for different chain lengths. The complex viscosity is obtained by Fourier transforming the mixed Rouse-reptation expression for the linear shear relaxation modulus $G(t)$, Eq. (5.24).

7.15, where we see that the ratio σ_{xy}/S_{xy} increases approximately just as fast with shear rate as the ratio $N_1/(S_{xx}-S_{yy})$. Therefore the equality of χ and χ^{stress} is valid over a much larger range of shear rates than the stress-optical rule. The disagreement between χ and χ^{stress} is largest for the smallest chain lengths, $N = 4$ and 6. This could have been expected, since the approximation of the polymer as a collection of entropic springs (on which the proportionality between stress and order is based) is only valid for very long chains. The downturn at $\chi \approx 5$ degrees is caused by the finite box-size effects, as explained before.

7.3.3 The Cox-Merz rule

It is an experimental fact that the observed behavior in concentrated polymer solutions and polymer melts is in very good agreement with the empirical Cox-Merz rule. [12,20,59,74,75] This (rather mysterious) rule states that there is a relation between the nonlinear steady state shear viscosity and the complex viscosity obtained in the linear regime:

$$\eta\left(\dot{\gamma}\right) = \left|\eta^*(\omega)\right|_{\omega=\dot{\gamma}}, \tag{7.24}$$

where

$$\eta^*(\omega) = \frac{G^*(\omega)}{i\omega} = \int_0^\infty e^{-i\omega t} G(t)\, dt. \tag{7.25}$$

G^* is called the complex modulus and is essentially the Fourier transform of the linear shear relaxation modulus $G(t)$. In *Chapter 5* we have shown that $G(t)$, to a good approximation, can be viewed as a sum of Rouse-type relaxations for mode numbers k larger than N/N_e and reptation-type relaxations for the lower mode numbers [Eq. (5.24] at times larger than the entanglement time τ_e. We will now test whether this expression is in agreement with the Cox-Merz rule. In Fig. 7.17 we plot both the steady state shear viscosities (symbols) and the magnitude of the Fourier transform of the mixed Rouse-reptation $G(t)$ (dashed lines) against shear rate and frequency, respectively. The wiggles in the dashed curves are a consquence of the strict separation between Rouse-type and reptation-type relaxation of the lowest modes for times $t < \tau_e$ and $t > \tau_e$. Nevertheless, the agreement is very satisfactory for all shear

rates lower than $\dot{\gamma} = 3000\ \mu s^{-1}$. A deviation at very high shear rates is in agreement with other observations in which the Cox-Merz rule was found to underpredict the viscosity. See, for example, Ref. [12]. At shear rates much higher than $3000\ \mu s^{-1}$, the predictions of the coarse-grained model will become unrealistic anyway, because the fastest relaxation time of the model is $\tau_0^{CG} \approx 0.09$ ns, as we have seen in *Chapter 5*. Much faster relaxations can occur in real polyethylene melts, down to the picosecond time scale.

7.4 Conclusions

We have used a coarse-grained simulation model, developed in the previous chapters, to investigate the transient and steady state nonlinear flow properties of unentangled and moderately entangled polyethylene melts. We found that the model's predictions agrees very well with various kinds of rheological experiments for shearing flow:

1. The simulation model predicts transient overshoot for both the shear stress and the normal stress difference at high shear rates. The locations of the maxima and the magnitudes of the the overshoots are in good agreement with experiment.

2. The simulation model predicts an undershoot of the extinction angle during startup of steady shear flow at high shear rates. The strain at which the undershoot occurs is in good agreement with experiment.

3. The slopes of the steady state shear stress and normal stress difference versus shear rate increase with decreasing molecular weight. The viscosities and normal stress coefficients all approach common curves independent of molecular weight at high shear rates. These findings are also in agreement with experiment.

4. Because of convective constraint release, the steady state extinction angle decreases more gradually with shear rate than predicted by the Doi and Edwards model. The actual decrease is in very good agreement with experiment.

We have been able to test the stress-optical rule and found that it is valid, but only for low and moderate shear rates. Interestingly, the extinction angle, as calculated from stress components, remains equal to the "real" (optical) extinction angle even for very high shear rates, where the stress-optical rule no longer strictly applies. Apparently, the ratio of shear stress and first normal stress difference remains equal to the corresponding ratio in the order tensor, even at very high shear rates.

Finally, the Cox-Merz rule was tested for our coarse-grained model. We found that the nonlinear viscosity can well be predicted by using this rule, but not at the highest shear rates.

Summary and outlook

Summary

In this thesis we report on computer simulations of polymer melts. Polymers in a melt can be viewed as long molecules which coil around each other and hinder each other's motions: they are "entangled". Entanglements occur because bonds between two adjacent atoms in a polymer chain can never be crossed by other such bonds. The goal of our study was to simulate and to understand the dynamical and rheological behavior resulting from this entanglement effect. Because of its relative simplicity, we have chosen polyethylene (PE) as our primary system of interest.

In *Chapter 3* we report on molecular dynamics (MD) simulations of a melt of relatively short $C_{120}H_{242}$ chains. Using the atomistic MD force fields, the uncrossability of bonds is automatically guaranteed because of the extremely high energy barier that has to be overcome if two bonds want to cross. Unfortunately, MD simulations are computationally very demanding. The rapid internal motions of the molecules make it necessary to calculate the interactions at femtosecond (10^{-15} s) intervals. As a consequence, simulations of even the relatively small system of C_{120} chains took a few months to complete. From these simulations we learned that various dynamic quantities, as measured in the C_{120} system, can consistently be described by the Rouse model (see *Chapter 2*) using a single set of fit parameters, provided the length scales involved are larger than the statistical segment length.

The longest characteristic time scale that occurs in a system of C_{120} chains is about 6 nanoseconds, which is well within reach of atomistic MD simulations. However, the longest time scale increases rapidly with chain length, and already equals several microseconds for a C_{1000} chain. Moreover, the system size must increase as well to avoid significant overlap of a chain with itself via the periodic boundary conditions. Hence, fully atomistic simulation of the dynamics and rheology of long polymer chains is quite impossible with current-day computer power. In order to increase the time and length scales accessible in simulations, it is necessary to describe the polymers on a more coarse-grained level. If the degree of coarse-graining is larger, a particular chain is represented by less coarse particles (called "blobs") and the integration time step can be increased. However, as long as the coarse-grained interactions are modelled as spherical interactions, it is important that the size of a blob does not exceed the entanglement length, since otherwise no realistic entanglement effects can arise. Taking these considerations into account, we decided to represent the center of mass of 20 consecutive CH_2 groups by one blob.

In *Chapter 4* we derived the coarse-grained interactions between these blobs from the underlying atomistic model. The resulting interactions are so soft that the uncrossability of bonds is no longer automatically met. To prevent such unphysical bond crossings a new uncrossability constraint, the TWENTANGLEMENT algorithm, was introduced, details of which are also given in *Chapter 4*. The idea behind this constraint is to consider the bonds be-

tween consecutive blobs to be elastic bands. As soon as two of these elastic bands make contact, an "entanglement" is created at the crossing point which prevents the elastic bands from crossing.

The advantage of coarse-graining bottom-up, from the atomistic to the mesoscopic scale, is that all time and length scales are incorporated automatically and in their right proportions. Indeed, in *Chapter 4* we found very good agreement between the dynamic results of the atomistic MD simulations of C_{120} and the coarse-grained simulations of B_6. We observed a subdiffusive exponent in the mean square displacement of the chains, a stretching of the exponential decay of the Rouse modes, and a slowing down of the relaxation of the single chain coherent dynamic structure factor. Both the uncrossability of chains and their stiffness at smaller scales were found to be essential for these effects to occur. Interestingly, the shear relaxation modulus initially behaves Rouse-like, but after $t = 5$ nanoseconds, the stress in the system relaxes more slowly than in a system of Rouse chains. This was attributed to a very slow interchain stress relaxation caused by the uncrossability of chains.

In *Chapter 5* we studied the dynamical and rheological behavior of melts of chains ranging from C_{80} to C_{1000} (4 to 50 blobs). We found that the dynamics of chain lengths C_{400} - C_{1000} is in approximate agreement with reptation theory for large time scales, but that the approximation of a Rouse-like primitive path moving with great freedom in a tube is too strict. A better picture would be that of a primitive path that is interacting with the neighbouring chains on every length scale up to the entanglement length N_e. This is especially clear in Fig. 5.7, where the degree of non-exponentiality of the relaxation of internal modes is largest for scales below the entanglement length N_e. In fact we identified a new length scale, called the slowing down length N_s, which is smaller than the entanglement length N_e. The effective segmental friction increases rapidly around N_s, leading, at constant density, to a transition in the scaling of the diffusion coefficient from $D \sim N^{-1}$ to $D \sim N^{-2}$ and a conspicious non-exponential relaxation behavior. These effects were attributed to strong local kinetic constraints caused by both chain stiffness and interchain interactions. The onset of non-local (entanglement) effects occurs at a chain length of C_{120}, as exemplified by deviations from Rouse behavior of the shear relaxation modulus. Full (rheological) entanglement effects were observed only above C_{400}, where the shear relaxation modulus displays a plateau and the single chain coherent dynamic structure factor agrees with the reptation model. The results for the tube diameter and the plateau modulus, as well as diffusion coefficients and viscosities were found to be in good agreement with experiment.

In *Chapter 6* we derived the entanglement length from a combination of the diffusion coefficient D and the zero-shear viscosity η_0, depite the fact that these transport properties individually do not display a transition in their scaling exponents at the entanglement length. The result is consistent with estimates from time-resolved measurements in *Chapter 5*, but not consistent with empirical estimates from the value of the plateau modulus G_N^0.

Finally in *Chapter 7*, as an application of our coarse-grained model, we studied the nonlinear flow properties of polyethylene melts by subjecting the model to a planar Couette flow. In steady state, typical effects such as shear thinning of the viscosity and a decrease of the extinction angle with shear rate were measured. Also transient effects, such as the characteristic overshoot in the shear stress and an undershoot in the transient extinction angle upon onset of shear flow, were measured and found to be in good agreement with experiments.

Outlook

In polymer melts, and in most other complex systems, relaxations of configurations and stress occur on a very broad range of time and length scales. If our goal is to understand these relaxations from a microscopic point of view, computer simulations now and in the future can provide valuable information to both validate certain ideas (theories) and to improve them. However, as we have seen above, microscopic simulations of complex systems are usually limited by the availability of computing power. Since science will always push at the frontiers of what is possible, we expect that the technique of coarse-graining microscopic interactions to a mesoscopic scale will play an increasingly important role in both academic and industrial research. However, before the coarse-graining technique can be applied as routinely as the atomistic MD simulation technique nowadays, some difficulties will have to be overcome. For example, no systematic coarse-graining method exists up to this day. The optimization of the parameters occurring in a coarse-grained model may be performed with different target functions in mind. One may aim to describe as good as possible the static structure of the system, or some thermodynamic function, or even some dynamic function. Unfortunately, we have to deal here with the law of *conservation of misery*: improving the agreement with one target function usually implies deteriorating the agreement with other quantities. In other words, it is impossible to get everything right. The situation may be improved by including interactions beyond the level of pairwise additive and angular interactions, but this has not yet been studied systematically. An additional complication is that the coarse-grained interactions generally are state-point dependent, i.e., the interactions can not be assumed to be transferable to a different temperature, density, or composition of the system. [86]

In the work described in this thesis, the coarse-grained interactions were based on radial and angular distribution functions at a specified density and temperature (structural criterion), and the friction was determined from the autocorrelation of the constraint force needed to keep a blob at a fixed position (dynamic criterion). The resulting pressure (a thermodynamic quantity) was much lower than in the corresponding microscopic system. However, the focus of this thesis was not on the thermodynamics of polymer melts, but on the dynamics and rheology. We generally found very good agreement with dynamical and rheological experimental results. Apparently, and this is an advantage, the dynamics and rheology of polymer melts are not very sensitive to the details of the interactions. This does not imply that the magnitudes of the interactions do not matter. Rather, the precise form does not matter as long as the attractions and repulsions between bonded blobs are of the right magnitudes and as long as all other interactions (angular, non-bonded) are accounted for in the right relative proportions. We therefore expect that the dynamical and rheological properties of many more polymer systems can be calculated by a coarse-graining method similar to the one performed in this work. Usually the degree of coarse-graining will be high, in which case the uncrossability of bonds must explicitly be included in the equations of motion, as was done in this thesis.

Samenvatting in begrijpelijk Nederlands

In dit proefschrift beschrijven we computersimulaties van polymeervloeistoffen. Polymeren zijn zeer lange moleculen, bestaande uit zeer vele, maar identieke, repeterende eenheden. Elke repeterende eenheid, een monomeer, bestaat uit enkele atomen, meestal koolstof- en waterstofatomen, maar soms ook andere. U kunt zich zo'n monomeer voorstellen als een soort kraal en het polymeer als een kralensnoer. Stelt u zich nu eens voor dat u met uw vinger door een bak met losse kralen roert. Dit gaat redelijk gemakkelijk. Vervolgens probeert u met uw vinger door een bak met kralensnoeren te roeren. Ondanks het feit dat we precies dezelfde kralen gebruiken, gaat dit veel moeilijker. De reden is natuurlijk dat de kralensnoeren achter elkaar blijven haken; als we een kralensnoer willen bewegen sleurt hij meteen vele andere kralensnoeren met zich mee. Misschien kunt u zich zelfs voorstellen dat hoe langer de kralensnoeren zijn, deste moeilijker het roeren zal gaan. Dat is precies de reden waarom een vloeistof van lange polymeren veel stroperiger (meer visceus) is dan een vloeistof van korte polymeren.

Nu hebben deze polymeervloeistoffen nog een bijzondere eigenschap: als de polymeren lang genoeg zijn vertonen ze tijdelijk elastisch gedrag. Dat wil zeggen, als u een druppel polymeervloeistof snel probeert te vervormen, heeft hij de neiging zijn oorspronkelijke vorm weer aan te nemen, net als een rubber balletje. Aan de andere kant, als u de druppel langzaam vervormt, keert hij niet meer terug naar zijn oorspronkelijke vorm. Samenvattend: polymeervloeistoffen zijn zowel visceus als elastisch, afhankelijk van de snelheid waarmee u de vloeistof vervormt. Daarom worden ze ook wel viscoelastische vloeistoffen genoemd. Uit puur wetenschappelijk oogpunt is het heel interessant om deze eigenschappen te proberen te begrijpen. Er zijn echter ook praktische redenen. Polymeren worden veel gebruikt in onze maatschappij – denk aan plastic verpakkingsmateriaal, isolatiemateriaal, onderdelen in electronische apparatuur, toepassingen in de medische wereld, etc. Voor de verwerking van polymeren is het heel belangrijk dat we precies begrijpen waarom ze deze materiaaleigenschappen hebben, en ook hoe die eigenschappen precies afhangen van de samenstelling van het monomeer en de lengte van het polymeer.

In dit proefschrift proberen we de materiaaleigenschappen te begrijpen door te kijken naar de beweging, oftewel dynamica, van de polymeren. Tegenwoordig is het mogelijk om de dynamica van atomen en moleculen heel gedetailleerd na te bootsen op een computer. Het voordeel van zo'n computersimulatie is dat de polymeerbewegingen heel precies bekeken kunnen worden, vaak nog beter dan met de meeste experimenten mogelijk is. Ook is het mogelijk met behulp van computersimulaties theorieën over de dynamica van polymeermoleculen te toetsen en, als het nodig is, aan te passen met nieuw verkregen inzichten. Een nadeel van een dergelijk gedetailleerde computersimulatie is dat hij ontzettend veel tijd kan kosten. Dit komt omdat atomen in verhouding tot hun eigen afmetingen ontzettend snel bewegen maar in een vloeistof ook heel vaak met elkaar botsen, waardoor ze heel vaak van

richting veranderen. Als men de dynamica van de atomen natuurgetrouw wil simuleren, zal men daarom heel kleine tijdstapjes moeten maken: elk tijdstapje mag niet veel langer duren dan een femtoseconde, dat is een miljoenste deel van een miljardste deel van een seconde! In hoofdstuk drie hebben we deze methode gebruikt om de dynamica van een vloeistof van $C_{120}H_{242}$ ketens te onderzoeken. We hebben deze berekeningen enkele maanden lang uitgevoerd op een van de snelste computers van deze tijd. Desondanks was de totale tijdsduur waarover we de ketens op deze wijze hebben kunnen volgen maar 50 nanoseconde, dat is 0.000000050 seconde. Gelukkig was het mogelijk om bijna alles over de dynamica te weten te komen in die ogenschijnlijk korte tijd, omdat de onderzochte C_{120} ketens relatief kort zijn en zich snel aanpassen aan nieuwe omstandigheden.

Wanneer men langere ketens wil volgen in de tijd wordt het veel moeilijker. Ten eerste zijn er dan veel meer ketens nodig om een goede representatie van een vloeistof te krijgen. Hierdoor duurt het uitrekenen van elk tijdstapje veel langer. Ten tweede passen lange ketens zich veel langzamer aan aan nieuwe omstandigheden. Bestudering van de dynamica van dergelijke lange polymeren met bovengenoemde gedetailleerde simulaties zou daarom vele tientallen jaren in beslag nemen. Zo lang willen we niet wachten en dat is gelukkig ook niet nodig. Het blijkt namelijk dat de dynamica en materiaaleigenschappen ook heel goed te beschrijven zijn met een minder gedetailleerd model. In hoofdstuk vier leggen we uit hoe groepen van wel twintig aaneengesloten monomeren vervangen kunnen worden door slechts één zachte bal (we noemen het een ‘blob’). Omdat er veel minder van dergelijke blobs nodig zijn, én omdat we veel grotere tijdstappen kunnen maken – de blobs bewegen veel trager dan individuele atomen – kan de klus toch in redelijke tijd geklaard worden. We hebben hiervoor wel een probleem moeten overwinnen: de blobs zijn zo ontzettend zacht dat de polymeren zonder moeite dwars door elkaar kunnen vliegen. Echte polymeren, bestaande uit echte atomen, kunnen natuurlijk niet dwars door elkaar vliegen. Het feit dat ze achter elkaar blijven haken geeft ze juist de bijzondere materiaaleigenschappen – denk maar aan de bak gevuld met kralensnoeren. Daarom hebben we een rekenmethode ontwikkeld die ervoor zorgt dat in een simulatie met zachte blobs, de ketens toch niet door elkaar vliegen.

In hoofstukken vijf en zes onderzoeken we de dynamica van lange ketens. We vinden dat de viscositeit van de vloeistof en de beweeglijkheid van de ketens, dankzij de nieuwe rekenmethode, goed overeenkomen met experimentele gegevens. We vinden ook dat een bekende theorie voor polymeerdynamica, de zogenaamde reptatie theorie, redelijk goed op gaat als niet al te precies naar de details van de beweging gekeken wordt. Echter, als wel iets preciezer gekeken wordt, komen allerlei afwijkingen naar voren die vooral veroorzaakt worden door het feit dat de ketens op kleine schaal enigszins stijf zijn en ook op die kleine schaal al met elkaar interacteren. Dit wordt door de reptatie theorie genegeerd. Dit heeft gevolgen voor korte en middellange polymeren, maar wordt minder belangrijk voor extreem lange polymeren.

Tenslotte bekijken we in hoofdstuk zeven het gedrag van onze polymeervloeistoffen wanneer ze in een hele snele stroming gebracht worden. Ook nu vinden we goede overeenstemming met experimentele resultaten. In de simulaties beschikken we echter over meer gedetailleerde informatie dan in experimenten waardoor we opnieuw de mogelijkheid hebben om allerlei theorieën, en ook vuistregels, te testen.

Dankwoord

En dan nu het meest gelezen deel van elk proefschrift: het dankwoord. Voor mij persoonlijk is dit zo ongeveer het moeilijkste deel van het proefschrift. Ik weet namelijk hoe slecht mijn geheugen is, waardoor ik waarschijnlijk veel mensen zal vergeten te bedanken voor hun steun, inzet, of gewoon voor de gezelligheid gedurende de afgelopen vier jaren. Deze mensen bied ik bij voorbaat mijn excuses aan. Ter compensatie zal ik ze vereren met mijn allereerste dank: dank jullie wel!

Degene die in wetenschappelijk opzicht ongetwijfeld mijn grootste dank verdient is Wim Briels. Wim, ik had me geen betere promotor en begeleider voor kunnen stellen dan jij. Ik heb veel van je geleerd en waardeer de ruime mate waarin je me hebt vrij gelaten in de uitvoering van het onderzoek. Op momenten dat het onderzoek vast dreigde te lopen kwam je altijd met stimulerende ideeën en wist mij weer te enthousiasmeren voor een stevige rekenpartij. Jouw aandeel in de resultaten van dit onderzoek is onmiskenbaar.

Ook de andere (oud-)leden van de groepen Computational Chemistry en Computational Dispersion Rheology wil ik bedanken. Mijn speciale dank gaat uit naar Wouter den Otter, mijn kamergenoot gedurende de laatste twee jaren van mijn AIO-schap. Ik heb genoten van de vele malen dat we wis- of natuurkundige probleempjes aan elkaar hebben voorgelegd. Probleempjes die vaak weinig of niets te maken hadden met ons onderzoek, maar toch onze aandacht dagenlang konden vasthouden. Ook bedank ik Harald Tepper en Reinier Akkermans voor de prikkelende discussies, en vooral voor alles wat zich na het werk afspeelde. Ik herinner me met name de zwoele avonden in Granada en de koele sneeuwwandelingen in Han-sur-Lesse. Verder bedank ik Martin van der Hoef, Dick Feil, Bob Hoomans, en Albert van den Noort voor de vele discussies, met name rond de koffietafel. I would like to thank Tanya Tolpekina, Sergey Shkulipa, Wladimir Shchettinin and Yuguo Tao for making my stay at the CDR group a pleasant one and for offering me an insight in Ukrainean and Chinese culture and language.

Van de studenten wil ik met name Léon van Heijkamp and Peter Kindt bedanken, die ik heb mogen begeleiden bij hun afstudeeropdrachten. Ik hebt de samenwerking altijd als zeer prettig ervaren en ik hoop dat jullie er hetzelfde over denken.

Natuurlijk is er meer in het leven dat wetenschap alleen. Ik wil Michel, Bertil, Geert, Marten, Marco, Henri, Sandra en de rest van de ‘Monolith- en Global-clan’ bedanken voor de broodnodige afleiding in de vorm van film-, concert- en vooral feestbezoeken. Ook Marko & Marko wil ik bedanken voor de gezellige avondjes uit.

Op deze plaats wil ik ook mijn ouders bedanken die mij altijd hebben gesteund en elke keuze hebben gerespecteerd die ik heb gemaakt in het leven. Ik denk dat jullie invloed op mijn ontwikkeling tot wetenschapper groter is geweest dan jullie zelf vermoeden. Ook mijn broertje Alexander en zusje Marjolijn wil ik bedanken voor het altijd warme welkom dat ik voel als ik weer eens in Steenwijk kom.

Mijn grootste dank gaat uit naar Astrid. Astrid, jouw liefde, steun en begrip zijn de laatste jaren erg belangrijk voor mij geweest. Ook na zware dagen op het werk ging ik altijd met

plezier weer naar huis in het vooruitzicht jou weer te zien. Ik hoop dat we nog lang van elkaar kunnen genieten.

Johan Padding Enschede, december 2002

Bibliography

[1] R.L.C. Akkermans and W.J. Briels, *Coarse-grained dynamics of one chain in a polymer melt*, J. Chem. Phys. **113**, 6409 (2000).

[2] R.L.C. Akkermans and W.J. Briels, *A structure-based coarse-grained model for polymer melts*, J. Chem. Phys. **114**, 1020 (2001).

[3] M.P. Allen, *Brownian dynamics simulation of a chemical reaction in solution*, Mol. Phys. **40**, 1073 (1980); *Algorithms for Brownian dynamics*, Mol. Phys. **47**, 599 (1982).

[4] M.P. Allen, *Atomic and molecular representations of molecular hydrodynamic variables*, Mol. Phys. **52**, 705 (1984).

[5] M.P. Allen and D.J. Tildesley, *Computer simulation of liquids* (Clarendon, Oxford, 1987).

[6] T. Aoyagi and M. Doi, *Molecular dynamics simulation of entangled polymers in shear flow*, Comput. Theor. Polym. Sci. **10**, 317 (2000).

[7] J. Baschnagel, K. Binder, P. Doruker, A.A. Gusev, O. Hahn, K. Kremer, W.L. Mattice, F. Müller-Plathe, M. Murat, W. Paul, S. Santos, U.W. Suter, and V. Tries, *Bridging the Gap Between Atomistic and Coarse-Grained Models of Polymers: Status and Perspectives*, Adv. Polym. Sci. **152**, 41 (2000).

[8] M. Bercea, B. Peiti, B. Dimionescu, and P. Navard, *Shear rheology of semidilute poly(methylmethacrylate) solutions*, Macromolecules **26**, 7095 (1993).

[9] H.J.C. Berendsen and W.F. van Gunsteren, *GROMOS Reference Manual* (University of Groningen, Groningen, 1987).

[10] H.J.C. Berendsen, J.P.M. Postma, W.F. van Gunsteren, A. Di Nola, and J.R. Haak, *Molecular dynamics with coupling to an external bath*, J. Chem. Phys. **81**, 3684 (1984).

[11] K. Binder and W. Paul, *Monte Carlo Simulations of Polymer Dynamics: Recent Advances*, J. Polym. Sci. B: Polym. Phys. **35**, 1 (1997).

[12] R.B. Bird, R.C. Armstrong, and O. Hassager, *Dynamics of Polymeric Liquids* 1 (Wiley, New York, 1977).

[13] W.J. Briels, *Theory of Polymer Dynamics*, Lecture Notes, Uppsala (1994). The full text can be downloaded from *http://www.tn.utwente.nl/cdr/PolymeerDictaat/*.

[14] D. Brown, J.H.R. Clarke, M. Okuda, and T. Yamazaki, *A large scale molecular dynamics study of chain configurations in the n=100 alkane melt*, J. Chem. Phys. **104**, 2078 (1996).

[15] J.M. Carella, W.W. Graessley, and L.J. Fetters, *Effects of Chain Microstructure on the Viscoelastic Properties of Linear Polymer Melts: Polybutadienes and Hydrogenated Polybutadienes*, Macromolecules **17**, 2775 (1984).

[16] M.E. Cates, *Reptation of living polymers: dynamics of entangled polymers in the presence of reversible chain-scission reactions*, Macromolecules **20**, 2289 (1987); *Nonlinear viscoelasticity of wormlike micelles (and other reversibly breakable polymers)*, J. Phys. Chem. **94**, 371 (1990).

[17] D. Chandler, *Introduction to modern statistical mechanics* (Oxford University Press, Oxford, 1987). [Chapter 8. *Statistical mechanics of non-equilibrium systems*]

[18] J. des Cloizeaux, *Dynamic form function of a long polymer constrained by entanglements in a polymer melt*, J. Phys. I **3**, 1523 (1993).

[19] J. des Cloizeaux, *Theory of Polymer Melts and Applications*, Macromol. Symp. **81**, 1 (1994).

[20] W.P. Cox and E.H. Merz, J. Polym. Sci., Part B: Polym. Phys. **28**, 619 (1958).

[21] B. Crist, P.F. Green, R.A.L. Jones, and E.J. Kramer, *Self-diffusion of hydrogenated polybutadiene by forward recoil spectroscopy*, Macromolecules **22**, 2857 (1989).

[22] S.T. Cui, P.T. Cummings, and H.D. Cochran, *The calculation of the viscosity from the autocorrelation function using molecular and atomic stress tensors*, Mol. Phys. **88**, 1657 (1996).

[23] P.J. Daivis, and D.J. Evans, *Comparison of constant pressure and constant volume nonequilibrium simulations of sheared model decane*, J. Chem. Phys. **100**, 541 (1994).

[24] P.G. De Gennes, *Reptation of a polymer chain in the presence of fixed obstacles*, J. Chem. Phys. **55**, 572 (1971).

[25] P.G. De Gennes, *Dynamics of fluctuations and spinodal decomposition in polymer blends*, J. Chem. Phys. **72**, 4756 (1980).

[26] P.G. De Gennes, *Scaling Concepts in Polymer Physics* (Cornell University Press, Ithaca, New York, 1979).

[27] P.G. De Gennes, *Coherent scattering by one reptating chain*, J. Physique **42**, 735 (1981).

[28] P.G. De Gennes, *Fragile objects. Soft matter, hard science, and the thrill of discovery*, (Springer-Verlag, New York, 1996).

[29] M. Doi, J. Polym. Sci. **21**, 667 (1983).

[30] M. Doi and S.F. Edwards, *The Theory of Polymer Dynamics* (Clarendon, Oxford, 1986).

[31] D.K. Dysthe, A.H. Fuchs, and B. Rousseau, *Fluid transport properties by equilibrium molecular dynamics. III. Evaluation of united atom interaction potential models for pure alkanes*, J. Chem. Phys. **112**, 7581 (2000).

[32] A. Einstein, *Die von der molekularkinetischen Theorie der Wärme geforderte Bewegung von in ruhenden Flüssigkeiten suspendierten Teilchen*, Ann. Phys. **17**, 549 (1905).

[33] J. Fang, M. Kröger, and H.C. Öttinger, *A thermodynamically admissible reptation model for fast flows of entangled polymers. II. Model predictions for shear and extensional flows*, J. Rheol. **44**, 1293 (2000).

[34] N. Fatkullin and R. Kimmich, *Nuclear spin-lattice relaxation dispersion and segment diffusion in entangled polymers. Renormalized Rouse formalism*, J. Chem. Phys. **101**, 822 (1994).

[35] N. Fatkullin and R. Kimmich, *The intra- and intermolecular basis of the zero-shear viscosity in unentangled polymers*, JETP Lett. **69**, 762 (1999).

[36] N.F. Fatkullin, R. Kimmich, and M. Kroutieva, *The Twice-Renormalized Rouse Formalism of Polymer Dynamics: Segment Diffusion, Terminal Relaxation, and Nuclear Spin-Lattice Relaxation*, J. Exp. Theor. Phys. **91**, 150 (2000).

[37] N. Fatkullin, *Viscoelastic properties of linear polymer melts as effect of broken axial symmetry and mutual uncrossability of macromolecules*, J. Non-Cryst. Solids **307-310**, 824 (2002).

[38] J. D. Ferry, *Viscoelastic Properties of Polymers*, third edition (Wiley, New York, 1980).

[39] L.J. Fetters, D.J. Lohse, and W.W. Graessley, *Chain Dimensions and Entanglement Spacings in Dense Macromolecular Systems*, J. Polym. Sci. B: Polym. Phys. **37**, 1023 (1999).

[40] L.J. Fetters, D.J. Lohse, S.T. Milner, and W.W. Graessley, *Packing Length Influence in Linear Polymer Melts on the Entanglement, Critical, and Reptation Molecular Weights*, Macromolecules **32**, 6847 (1999).

[41] L.J. Fetters, D.J. Lohse, D. Richter, T.A. Witten, and A. Zirkel, *Connection between Polymer Molecular Weight, Density, Chain Dimensions, and Melt Viscoelastic Properties*, Macromolecules **27**, 4639 (1994).

[42] E. Fischer, R. Kimmich, N. Fatkullin, and G. Yatsenko, *Segment diffusion and flip-flop spin diffusion in entangled polyethyleneoxide melts: A field-gradient NMR diffusometry study*, Phys. Rev. E **62**, 775 (2000).

[43] M. Fixman, *Stress relaxation in polymer melts and concentrated solutions*, J. Chem. Phys. **95**, 1410 (1991).

[44] P.J. Flory, *Statistical Mechanics of Chain Molecules* (Wiley, New York, 1969).

[45] B.M. Forrest, and U.W. Suter, *Accelerated equilibration of polymer melts by time-coarse-graining*, J. Chem. Phys. **102**, 7256 (1995).

[46] J. Gao and J.H. Weiner, *Stress relaxation in a polymer melt of freely-rotating chains*, J. Chem. Phys. **97**, 8698 (1992).

[47] J. Gao and J.H. Weiner, *Computer Simulation of Viscoelasticity in Polymer Melts*, Macromolecules **25**, 1348 (1992).

[48] J. Gao and J.H. Weiner, *Simulated polymer melt stress relaxation. I. Plateau behavior*, J. Chem. Phys. **103**, 1614 (1995).

[49] C.B. Gell, W.W. Graessley, and L.J. Fetters, *Viscoelasticity and Self-Diffusion in Melts of Entangled Linear Polymers*, J. Polym. Sci. B: Polym. Phys. **35**, 1933 (1997).

[50] W.F. van Gunsteren and H.J.C. Berendsen, *Algorithms for brownian dynamics*, Mol. Phys. **45**, 637 (1982).

[51] V.A. Harmandaris, V.G. Mavrantzas, and D.N. Theodorou, *Atomistic Molecular Dynamics Simulations of Polydisperse Linear Polyethylene Melts*, Macromolecules **31**, 7934 (1998).

[52] V.A. Harmandaris, V.G. Mavrantzas, and D.N. Theodorou, *Atomistic Molecular Dynamics Simulation of Stress Relaxation upon Cessation of Steady-State Uniaxial Elongational Flow*, Macromolecules **33**, 8062 (2000).

[53] L. Harnau, *Comment on "From Rouse dynamics to local relaxation: A neutron spin echo study on polyisobutylene melts"* [*J. Chem. Phys. 111, 6107 (1999)*], J. Chem. Phys. **113**, 11396 (2000).

[54] L. Harnau, R.G. Winkler, and P. Reineker, *On the dynamics of polymer melts: Contribution of Rouse and bending modes*, Europhys. Lett. **45**, 488 (1999).

[55] L. Harnau, R.G. Winkler, and P. Reineker, *Comment on "Chain Motion in an Unentangled Polyethylene Melt: A Critical Test of the Rouse Model by Molecular Dynamics Simulations and Neutron Spin Echo Spectroscopy"*, Phys. Rev. Lett. **82**, 2408 (1999).

[56] M.F. Herman, B. Panajotova, and K.T. Lorenz, *A quantitative theory of linear chain polymer dynamics in the melt. I. General scaling behavior*, J. Chem. Phys. **105**, 1153 (1996); *A quantitative theory of linear chain polymer dynamics in the melt. II. Comparison with simulation data*, J. Chem. Phys. **105**, 1162 (1996).

[57] W. Hess, *Generalized Rouse theory for entangled polymeric liquids*, Macromolecules **21**, 2620 (1988).

[58] C.C. Hua, J.D. Schieber, and D.C. Venerus, *Segment connectivity, chain-length breathing, segmental stretch, and constraint release in reptation models. III. Shear flows*, J. Rheol. **43**, 701 (1999).

[59] G. Ianniruberto and G. Marrucci, *On compatibility of the Cox-Merz rule with the model of Doi and Edwards*, J. Non-Newtonian Fluid Mech. **65**, 241 (1996).

[60] T.A. Kavassalis and J. Noolandi, *A New Theory of Entanglements and Dynamics in Dense Polymer Systems*, Macromolecules **21**, 2869 (1988).

[61] R. Kimmich, N. Fatkullin, R.-O. Seitter, and K. Gille, *Chain dynamics in entangled polymers: Power laws of the proton and deuteron spin-lattice relaxation dispersions*, J. Chem. Phys. **108**, 2173 (1998).

[62] A. Kopf, B. Dünweg, and W. Paul, *Dynamics of polymer "isotope" mixtures: Molecular dynamics simulation and Rouse model analysis*, J. Chem. Phys. **107**, 6945 (1997).

[63] T. Kreer, J. Baschnagel, M. Müller, and K. Binder, *Monte Carlo Simulation of Long Chain Polymer Melts: Crossover from Rouse to Reptation Dynamics*, Macromolecules **34**, 1105 (2001).

[64] K. Kremer, *Statics and Dynamics of Polymeric Melts: A Numerical Analysis*, Macromolecules **16**, 1632 (1983).

[65] K. Kremer, G.S. Grest, and I. Carmesin, *Crossover from Rouse to reptation dynamics – A molecular-dynamics simulation*, Phys. Rev. Lett. **61**, 566 (1988).

[66] K. Kremer and G.S. Grest, *Dynamics of entangled linear polymer melts: A molecular-dynamics simulation*, J. Chem. Phys. **92**, 5057 (1990).

[67] K. Kremer and G.S. Grest, *Simulations for Structural and Dynamic Properties of Dense Polymer Systems*, J. Chem. Soc. Faraday Trans. **88**, 1707 (1992).

[68] M. Kröger and S. Hess, *Rheological Evidence for a Dynamical Crossover in Polymer Melts via Nonequilibrium Molecular Dynamics*, Phys. Rev. Lett. **85**, 1128 (2000).

[69] M. Kröger, W. Loose, and S. Hess, *Rheology and structural changes of polymer melts via nonequilibrium molecular dynamics*, J. Rheol. **37**, 1057 (1993).

[70] W. Kuhn, Kolloid Z. **87**, 3 (1939); Z. Physik. Chem. **B42**, 1 (1939).

[71] A.E. Likhtman, S.T. Miller, and T.C.B. McLeish, *Microscopic Theory for the Fast Flow of Polymer Melts*, Phys. Rev. Lett. **85**, 4550 (2000).

[72] T.P. Lodge, *Reconciliation of the Molecular Weight Dependence of Diffusion and Viscosity in Entangled Polymers*, Phys. Rev. Lett. **83**, 3218 (1999).

[73] T.P. Lodge, N.A. Rotstein, and S. Prager, *Dynamics of entangled polymer liquids: do linear chains reptate?*, Adv. Chem. Phys. **79**, 1 (1990).

[74] G. Marrucci, *Dynamics of entanglements: A nonlinear model consistent with the Cox-Merz rule*, J. Non-Newtonian Fluid Mech. **62**, 279 (1996).

[75] G. Marrucci, G. Ianniruberto, *Open problems in tube models for concentrated polymers*, J. Non-Newtonian Fluid Mech. **82**, 275 (1999).

[76] Y. Masubuchi, J.-I. Takimoto, K. Koyama, G. Ianniruberto, G. Marrucci, and F. Greco, *Brownian simulations of a network of reptating primitive chains*, J. Chem. Phys. **115**, 4387 (2001).

[77] V.G. Mavrantzas, T.D. Boone, E. Zervopoulou, and D.N. Theodorou, *End-Bridging Monte Carlo: A Fast Algorithm for Atomistic Simulation of Condensed Phases of Long Polymer Chains*, Macromolecules **32**, 5072 (1999).

[78] J.D. McCoy and J.G. Curro, *Mapping of Explicit Atom onto United Atom Potentials*, Macromolecules **31**, 9362 (1998).

[79] D.A. McQuarrie, *Statistical Mechanics* (Harper and Row, New York, 1976). [Chapter 21. *The time-correlation function formalism*]

[80] D.W. Mead and R.G. Larson, *Rheooptical study of isotropic solutions of stiff polymers*, Macromolecules **23**, 2524 (1990).

[81] D.W. Mead, R.G. Larson, and M. Doi, *A Molecular Theory for Fast Flow of Entangled Polymers*, Macromolecules **31**, 7895 (1998).

[82] M. Mondello, and G.S. Grest, *Viscosity calculations of n-alkanes by equilibrium molecular dynamics*, J. Chem. Phys. **106**, 9327 (1997).

[83] M. Mondello, G.S. Grest, E.B. Webb III, and P. Peczak, *Dynamics of n-alkanes: Comparison to Rouse model*, J. Chem. Phys. **109**, 798 (1998).

[84] J.D. Moore, S.T. Cui, H.D. Cochran, and P.T. Cummings, *A molecular dynamics study of a short-chain polyethylene melt. I. Steady-state shear*, J. Non-Newtonian Fluid Mech. **93**, 83 (2000).

[85] J.D. Moore, S.T. Cui, H.D. Cochran, and P.T. Cummings, *A molecular dynamics study of a short-chain polyethylene melt. II. Transient response upon onset of shear*, J. Non-Newtonian Fluid Mech. **93**, 101 (2000).

[86] F. Müller-Plathe, *Coarse-Graining in Polymer Simulation: From the Atomistic to the Mesoscopic Scale and Back*, Chem. Phys. Chem. **3**, 754 (2002).

[87] M. Murat and K. Kremer, *From many monomers to many polymers: Soft ellipsoid model for polymer melts and mixtures*, J. Chem. Phys. **108**, 4340 (1998).

[88] K.L. Ngai, R.W. Rendell, A.K. Rajagopal, and S. Teitler, Ann. NY Acad. Sci. **484**, 150 (1986).

[89] K.L. Ngai and J. Skolnick, *Correspondence between the coupling model predictions and computer-simulations – Diffusion of a probe polymer in a matrix having different degrees of polymerization*, Macromolecules **24**, 1561 (1991).

[90] K.L. Ngai, S.L. Peng, and J. Skolnick, *Generalized Fokker-Planck approach to the coupling model and comparison with computer-simulations*, Macromolecules **25**, 2184 (1992).

[91] J.P. Oberhauser, L.G. Leal, and D.W. Mead, *The response of entangled polymer solutions to step changes of shear rate: signatures of segmental stretch?*, J. Polym. Sci., Part B: Polym. Phys. **36**, 265 (1998).

[92] R.D. Olmsted, and R.F. Snider, *Symmetry of the pressure tensor in macromolecular fluids*, J. Chem. Phys. **65**, 3423 (1976).

[93] D.J. Olson, E.F. Brown, and W.R. Burghardt, *Second normal stress difference relaxation in a linear polymer melt following step-strain*, J. Polym. Sci., Part B: Polym. Phys. **36**, 2671 (1998).

[94] M. Oostwal and T. Odijk, *Novel dynamic scaling hypothesis for semidilute and concentrated solutions of polymers and polyelectrolytes*, Macromolecules **26**, 6489 (1993).

[95] J.T. Padding and W.J. Briels, *TWENTANGLEMENT User's manual*, Twente University, 2000.

[96] J.T. Padding and W.J. Briels, *Zero-shear stress relaxation and long time dynamics of a linear polyethylene melt: A test of Rouse theory*, J. Chem. Phys. **114**, 8685 (2001).

[97] J.T. Padding and W.J. Briels, *Uncrossability contraints in mesoscopic polymer melt simulations: Non-Rouse behavior of $C_{120}H_{242}$*, J. Chem. Phys. **115**, 2846 (2001).

[98] J.T. Padding and W.J. Briels, *Time and length scales of polymer melts studied by coarse-grained molecular dynamics simulations*, J. Chem. Phys. **117**, 925 (2002).

[99] P.V.K. Pant, and D.N. Theodorou, *Variable Connectivity Method for the Atomistic Monte Carlo Simulation of Polydisperse Polymer Melts*, Macromolecules **28**, 7224 (1995).

[100] W. Paul, G.D. Smith, and D.Y. Yoon, *Static and Dynamic Properties of a n-C100H202 Melt from Molecular Dynamics Simulations*, Macromolecules **30**, 7772 (1997).

[101] W. Paul, G.D. Smith, D.Y. Yoon, B. Farago, S. Rathgeber, A. Zirkel, L. Willner, and D. Richter, *Chain Motion in an Unentangled Polyethylene Melt: A Critical Test of the Rouse Model by Molecular Dynamics Simulations and Neutron Spin Echo Spectroscopy*, Phys. Rev. Lett. **80**, 2346 (1998).

[102] W. Paul, D.Y. Yoon, and G.D. Smith, *An optimized united atom model for simulations of polymethylene melts*, J. Chem. Phys. **103**, 1702 (1995).

[103] D.S. Pearson, L.J. Fetters, W.W. Graessley, G. Ver Strate, and E. von Meerwall, *Viscosity and self-diffusion coefficient of hydrogenated polybutadiene*, Macromolecules **27**, 711 (1994).

[104] D.S. Pearson, E.A. Herbolzheimer, G. Marrucci, and N. Grizzuti, *Transient behavior of entangled polymers in high shear rates*, J. Polym. Sci., Part B: Polym. Phys. **29**, 1589 (1991).

[105] D.S. Pearson, A.D. Kiss, and L.J. Fetters, *Flow-induced birefringence of concentrated polyisoprene solutions*, J. Rheol. **33**, 517 (1989).

[106] D.S. Pearson, G. Ver Strate, E. von Meerwall, and F.C. Schilling, *Viscosity and Self-Diffusion Coefficient of Linear Polyethylene*, Macromolecules **20**, 1133 (1987).

[107] M. Pütz, K. Kremer, and G.S. Grest, *What is the Entanglement Length in a Polymer Melt?*, Europhys. Lett. **49**, 735 (2000).

[108] M. Pütz, K. Kremer, and G.S. Grest, *Reply to the Comment by A. Wischnewski and D. Richter on "What is the entanglement length in a polymer melt?"*, Europhys. Lett. **52**, 721 (2000).

[109] D. Richter, R. Butera, L.J. Fetters, J.S. Huang, B. Farago, and B. Ewen, *Entanglement Constraints in Polymer Melts. A Neutron Spin Echo Study.*, Macromolecules **25**, 6156 (1992).

[110] D. Richter, B. Ewen, L.J. Fetters, J.S. Huang, and B. Farago, *On the dynamics of dense polymer systems*, Progr. Colloid Polym. Sci. **91**, 130 (1993).

[111] D. Richter, B. Farago, R. Butera, L.J. Fetters, J.S. Huang, and B. Ewen, *On the Origins of Entanglement Constraints*, Macromolecules **26**, 795 (1993).

[112] D. Richter, M. Monkenbusch, J. Allgeier, A. Arbe, J. Colmenero, B. Farago, Y.C. Bae, and R. Faust, *From Rouse dynamics to local relaxation: A neutron spin echo study on polyisobutylene melts*, J. Chem. Phys. **111**, 6107 (1999).

[113] D. Richter, M. Monkenbusch, W. Pykhout-Hintzen, A. Arbe, and J. Colmenero, *Response to "Comment on 'From Rouse dynamics to local relaxation: A neutron spin echo study on polyisobutylene melts' "* [*J. Chem. Phys. 113, 11396 (2000)*], J. Chem. Phys. **113**, 11398 (2000).

[114] D. Richter, L. Willner, A. Zirkel, B. Farago, L.J. Fetters, and J.S. Huang, *Onset of Topological Constraints in Polymer Melts: A Mode Analysis by Neutron Spin Echo Spectroscopy*, Phys. Rev. Lett. **71**, 4158 (1993).

[115] D. Richter, L. Willner, A. Zirkel, B. Farago, L.J. Fetters, and J.S. Huang, *Polymer Motion at the Crossover from Rouse to Reptation Dynamics*, Macromolecules **27**, 7437 (1994).

[116] H. Risken, *The Fokker-Planck Equation. Methods of Solution and Applications*, Second Edition (Springer-Verlag, Berlin Heidelberg, 1989).

[117] G. Ronca, *Frequency spectrum and dynamic correlations of concentrated polymer liquids*, J. Chem. Phys. **79**, 1031 (1983).

[118] P.E. Rouse, *A Theory of the Linear Viscoelastic Properties of Dilute Solutions of Coiling Polymers* , J. Chem. Phys. **21**, 1273 (1953).

[119] J.-P. Ryckaert and A. Bellemans, Mol. Phys. **44**, 68 (1981).

[120] P. Schleger, B. Farago, C. Lartigue, A. Kollmar, and D. Richter, *Clear Evidence of Reptation in Polyethylene from Neutron Spin-Echo Spectroscopy*, Phys. Rev. Lett. **81**, 124 (1998).

[121] G. Schöppe and D.W. Heermann, *Alternative off-lattice model with continuous backbone mass for polymers*, Phys. Rev. E. **59**, 636 (1999).

[122] K.S. Schweizer, *Microscopic theory of the dynamics of polymeric liquids – General formulation of a mode mode-coupling approach*, J. Chem. Phys. **91**, 5802 (1989); *Mode-coupling theory of the dynamics of polymer liquids – Qualitative predictions for flexible chain and ring melts*, J. Chem. Phys. **91**, 5822 (1989).

[123] K.S. Schweizer and G. Szamel, *Crossover to entangled dynamics in polymer solutions and melts*, J. Chem. Phys. **103**, 1934 (1995).

[124] J. von Seggern, S. Klotz, and H.-J. Cantow, *Reptation and constraint release in linear polymer melts: an experimental study*, Macromolecules **24**, 3300 (1991).

[125] J.S. Shaffer, *Effects of chain topology on polymer dynamics: Bulk melts*, J. Chem. Phys. **101**, 4205 (1994).

[126] J.S. Shaffer, *Effects of chain topology on polymer dynamics: Configurational relaxation in polymer melts*, J. Chem. Phys. **103**, 761 (1995).

[127] J. Skolnick, R. Yaris, and A. Kolinski, *Phenomenological theory of the dynamics of polymer melts. I. Analytic treatment of self-diffusion*, J. Chem. Phys. **88**, 1407 (1988); *Phenomenological theory of the dynamics of polymer melts. II. Viscoelastic properties*, J. Chem. Phys. **88**, 1418 (1988).

[128] B. Smit, S. Karaborni, and J.I. Siepmann, *Computer simulations of vapor-liquid phase equilibria of n-alkanes*, J. Chem. Phys. **102**, 2126 (1995).

[129] G.D. Smith, W. Paul, M. Monkenbusch, and D. Richter, *On the non-Gaussianity of chain motion in unentangled polymer melts*, J. Chem. Phys. **114**, 4285 (2001).

[130] S.W. Smith, C.K. Hall, and B.D. Freeman, *Large-scale molecular dynamics study of entangled hard-chain fluids*, Phys. Rev. Lett. **75**, 1316 (1995).

[131] S.W. Smith, C.K. Hall, and B.D. Freeman, *Molecular dynamics study of entangled hard-chain fluids*, J. Chem. Phys. **104**, 5616 (1996).

[132] R.A. Stratton, *The dependence of non-Newtonian viscosity on molecular weight for 'monodisperse' polystyrene*, J. Colloid Interface Sci. **22**, 517 (1966).

[133] M. Tanaka, K. Iwata, and N. Kuzuu, *High-precision computer simulations of entangled polymer chains: 1. Determination of entanglement parameters of bond-fluctuation model*, Comput. Theor. Polym. Sci. **10**, 299 (2000).

[134] H. Tao, T.P. Lodge, and E.D. von Meerwall, *Diffusivity and Viscosity of Concentrated Hydrogenated Polybutadiene solutions*, Macromolecules **33**, 1747 (2000).

[135] Y. Termonia, *A Creep Compliance Simulation Study of the Viscosity of Entangled Polymer Melts*, Macromolecules **29**, 2025 (1996).

[136] V. Tries, W. Paul, J. Baschnagel, and K. Binder, *Modeling polyethylene with the bond fluctuation model*, J. Chem. Phys. **106**, 738 (1997).

[137] W. Tschöp, K. Kremer, J. Batoulis, T. Bürger, and O. Hahn, *Simulation of polymer melts. I. Coarse-graining procedure for polycarbonates*, Acta Polymer. **49**, 61 (1998); *Simulation of polymer melts. II. From coarse-grained models back to atomistic description* Acta Polymer. **49**, 75 (1998).

[138] N.F.A. van der Vegt, W.J. Briels, M. Wessling, and H. Strathmann, *Free energy calculations of small molecules in dense amorphous polymers. Effect of the initial guess configuration in molecular dynamics studies*, J. Chem. Phys. **105**, 8849 (1996).

[139] A. Wischnewski and D. Richter, *Comment on "What is the entanglement length in a polymer melt?" by M. Pütz, K. Kremer, and G.S. Grest*, Europhys. Lett. **52**, 719 (2000).

[140] A. Wischnewski, D. Richter, M. Monkenbusch, L. Willner, B. Farago, G. Ehlers, and P. Schleger, *Reptation in polyethylene-melts with different molecular weights*, Physica B **276-278**, 337 (2000).

[141] A. Wischnewski, M. Monkenbusch, L. Willner, D. Richter, A.E. Likhtman, T.C.B. McLeish, and B. Farago, *Molecular Observation of Contour-Length Fluctuations Limiting Topological Confinement in Polymer Melts*, Phys. Rev. Lett. **88**, 058301 (2002).

[142] K.M. Zimmer, A. Linke, and D.W. Heermann, *Ellipsoidal potential parameterization for bisphenol-A polycarbonate*, Macromol. Theor. Simul. **5**, 1065 (1996).